

# **An Investigation on the Fatigue Performance of Hydraulic Gate Rollers**

by

**Abdul Nabi Lashari**

A Thesis submitted to the Faculty of Graduate Studies of  
The University of Manitoba  
in partial fulfilment of the requirements of the degree of

**Doctor of Philosophy**

Department of Civil Engineering  
University of Manitoba  
Winnipeg, Manitoba, Canada

Copyright © 2009 by Abdul Nabi Lashari

THE UNIVERSITY OF MANITOBA  
FACULTY OF GRADUATE STUDIES  
\*\*\*\*\*  
COPYRIGHT PERMISSION

**An Investigation on the Fatigue Performance  
Of Hydraulic Gate Rollers**

By

**Abdul Nabi Lashari**

A Thesis/Practicum submitted to the Faculty of Graduate Studies of The University of  
Manitoba in partial fulfillment of the requirement of the degree

Of

**Doctor of Philosophy**

Abdul Nabi Lashari©2009

Permission has been granted to the University of Manitoba Libraries to lend a copy of this thesis/practicum, to Library and Archives Canada (LAC) to lend a copy of this thesis/practicum, and to LAC's agent (UMI/ProQuest) to microfilm, sell copies and to publish an abstract of this thesis/practicum.

This reproduction or copy of this thesis has been made available by authority of the copyright owner solely for the purpose of private study and research, and may only be reproduced and copied as permitted by copyright laws or with express written authorization from the copyright owner.

## **Acknowledgement**

The author would like to express his deepest gratitude to his advisor Dr. Dimos Polyzois. In addition to his support and friendship over the past years, he has provided the unwavering source of inspiration, determination, and leadership that was so essential for the successful execution of this research project.

The author would like to express his sincere thanks to committee members Dr. Nipon Rattanawangcharoen and Dr. Jack Cahoon for their help, constructive comments, and encouragements throughout the research. Sincere thanks are also due to external examiner Dr. Iraj H. P. Mamaghani (University of North Dakota, USA) for reviewing this thesis and providing useful feedback.

The author also expresses his special thanks to Messrs Moray McVey and Grant Whiteside for their valuable assistance during the construction of test set-up and cyclic testing of the specimens.

This research project was sponsored by Manitoba Hydro, which is greatly acknowledged. The help, assistance, and cooperation provided by the Project Monitors Messrs Greg Friesen and Don Spangelo of Manitoba Hydro are highly appreciated.

Finally, the love, patience, help, and support of my wife Nabila Maya cannot be praised enough; to her this report is dedicated.

## Abstract

Manitoba Hydro is Canada's largest hydro utility company currently owning fourteen hydropower-generating stations with a total capacity of over 7500 MW. Both emergency intake gates and spillway gates are used in each. These are fixed-wheel gates with wheels mounted on both sides that roll on roller path plates. Environmental corrosion along with high wheel loads cause differences in the profile of the roller path surface. Combined with the relatively high torsional stiffness of the gate end girders, a condition of wheel load redistribution occurs where some wheels are relieved of load while others are loaded beyond their maximum design values. These loads can be as high as two to three times larger as the original design loading. Failure of one wheel could jeopardize the overall operation of the gate. Furthermore, the frequent opening and closing of these gates result in changes in the stress profile in both wheels and roller paths that, potentially, could lead to failure. Currently, design guidelines for gate wheels and roller paths do not consider the fatigue life of these elements. It is this lack of knowledge in the structural performance of gate wheels, which constitutes the basis of the present research investigation.

An experimental investigation was carried out at the University of Manitoba in Winnipeg, Canada, which involved the testing of three wheels and six plates under cyclic loading. One of the wheels,  $R_1$ , was made of cast iron while the other two wheels,  $R_2$  and  $R_3$ , were made of high carbon steel. The material in two of the roller path plates,  $P_1$  and  $P_2$ , was medium carbon steel with no heat treatment. The material in the other four plates,

P<sub>3</sub> to P<sub>6</sub>, was heat-treated stainless steel. Eight cyclic tests were conducted, two on each of Rollers R<sub>1</sub> and R<sub>2</sub> and four on Roller R<sub>3</sub>. The wheels were subjected to radial compressive loads of approximately 753 kN to 903 kN that remained fairly constant while the wheels were “rolled” over the roller paths for a number of cycles that also varied from 200,000 to a million cycles. At the end of each cyclic test, the test setup was dismantled and indentation profiles were measured in roller paths. Scanning electron microscope tests were also conducted on all specimens to measure the extent of damage in specimens.

A finite element (FE) analysis was conducted on a three-dimensional contact stress model of a roller and a plate using the ANSYS<sup>®</sup> finite element program. The stress-based multi-axial theory was used to assess the fatigue life of rollers and roller paths. Very high strains were observed in Roller R<sub>1</sub>, whereas, much lower strains were found in Rollers R<sub>2</sub> and R<sub>3</sub> as compared to Roller R<sub>1</sub>. Likewise, high strains were observed in Plates P<sub>1</sub> and P<sub>2</sub>, whereas, lower strains were found in Plates P<sub>3</sub>-P<sub>6</sub>. Large visible cracks were observed in Roller R<sub>1</sub> and in Plates P<sub>1</sub> and P<sub>2</sub>, whereas, no sign of any crack or damage was observed in Rollers R<sub>2</sub> and R<sub>3</sub> and in Plates P<sub>3</sub>-P<sub>6</sub>. Plates P<sub>1</sub> and P<sub>2</sub> exhibited a maximum indentation of 1.48 mm and 1.21 mm, respectively, after one million and 0.82 million cycles, while the stainless steel heat-treated plates suffered a much smaller surface indentation, which ranged from 0.02 mm to 0.12 mm after 400,000 cycles. The test results demonstrated that the cast iron wheel and Plates P<sub>1</sub> and P<sub>2</sub> performed very poorly under fatigue loading while high carbon steel Rollers R<sub>2</sub> and R<sub>3</sub> performed extremely well.

The FE results indicated that high stress values in contact areas, both in rollers and in plates, were critical. The maximum values of all types of stresses were found in these zones. The trend of stresses found in the contact area of roller and plate were consistent with those found in the literature. Laboratory test results and FE results were in good agreement.

The fatigue lives of Roller  $R_1$  and Plates  $P_1$  and  $P_2$ , under the influence of both normal and tangential forces, was half a million cycles. The fatigue lives of Rollers  $R_2$  and  $R_3$  and Plates  $P_3$ - $P_6$  were very high as compared to those of Roller  $R_1$  and Plate  $P_1$ . Laboratory test results, visual inspection and SEM results of rollers and plates supported the fatigue analysis results. High principal compressive and tensile contact stresses under the influence of both normal and tangential forces, evidenced by both FE results and literature review, were the main cause of fatigue failure of roller and plate. High contact stresses are fatal to the fatigue life of rollers and plates.

## Table of Contents

Abstract.....	iii
<b>CHAPTER 1</b>	<b>INTRODUCTION</b>
1.1 General.....	1
1.2 Research Objectives.....	4
1.3 Thesis Outline.....	4
<b>CHAPTER 2</b>	<b>LITERATURE RIVIEW</b>
2.1 Review of Current Design Standards.....	6
2.2 Previous Work at the University of Manitoba.....	9
2.3 Contact Stresses.....	12
2.4 Metal Fatigue.....	21
2.5 Basic Fracture Mechanic Concept.....	23
2.6 Contact Fatigue.....	24
<b>CHAPTER 3</b>	<b>EXPERIMENTAL PROGRAM</b>
3.1 General.....	28
3.2 Brinell Hardness Tests.....	31
3.3 Test Set-up.....	31
3.3.1 Pump.....	38
3.3.2 Hydraulic Actuator.....	39
3.3.3 Roller Path Plate.....	42
3.3.4 Rollers.....	44
3.4 Instrumentation.....	47
3.5 Testing Procedure.....	49
3.6 Frequency of the Cyclic Testing.....	51
3.7 Indentation Measurement.....	51
3.8 Scanning Electron Microscope.....	53
3.9 Material Properties.....	56

## CHAPTER 4                    EXPERIMENTAL RESULTS AND DISCUSSION

4.1 General.....	60
4.2 Brinell Hardness Tests.....	60
4.3 Radial Compressive Load.....	62
4.4 Strains in Roller $R_{1A}$ .....	64
4.5 Strains in Roller $R_{1B}$ .....	74
4.6 Strains in Roller $R_2$ .....	78
4.7 Strains in Roller $R_3$ .....	82
4.8 Strains in Plates $P_1$ and $P_2$ .....	84
4.9 Strains in Plates $P_3$ and $P_4$ .....	86
4.10 Strains in Plates $P_5$ and $P_6$ .....	87
4.11 Indentation Measurements.....	89
4.12 Inspection of Specimens.....	89
4.13 Scanning Electron Microscope.....	93
4.14 Summary.....	98

## CHAPTER 5                    FINITE ELEMENT ANALYSIS

5.1 Introduction.....	103
5.2 Finite Element Model.....	103
5.3 Boundary Conditions.....	107
5.4 Finite Element Results.....	107
5.4.1 Program $R_1P_1$ with External Load of 838 kN.....	107
5.4.1.1 Cast Iron Roller $R_1$ .....	108
5.4.1.2 Plates $P_1$ and $P_2$ .....	117
5.4.2 Program $R_1P_1$ with External Load of 734 kN.....	121
5.4.3 FEA of Rollers $R_2$ and $R_3$ .....	121
5.5 Comparison between FE Results and Laboratory Test Results.....	122
5.6 Summary.....	127



## List of Figures

1.1 Vertical lift fixed-wheel gate-downstream elevation.....	2
1.2 End section of the vertical lift fixed-wheel gate (a) Normal load, all wheels bearing evenly (b) Overload, bottom wheel not bearing.....	3
2.1 Curves showing variation in principal stresses, maximum shear stress, and octahedral shear stress with variation in distance from the contact surface.....	14
2.2 Line contact between cylindrical bodies.....	15
2.3 Tangential and normal forces over the contact area.....	16
2.4 Effect of tangential force on principal stresses.....	18
2.5 Effect of tangential force on maximum shear stresses.....	19
2.6 Effect of tangential force on octahedral shear stress.....	20
2.7 Schematic diagram of crack initiation and subsequent crack growth, first along the slip line and then at right angles to the principal tensile stress.....	23
2.8 A crack in an infinitely wide plate.....	24
2.9 Anatomy of a race spall in a ball bearing (a) Typical delta shape with the apex at the origin (b) Profiles of the spall.....	26
2.10 “Shelly” rail spall from wheel-rail contact fatigue.....	26
3.1 A section through centre line of the Cast Iron Roller $R_1$ showing nomenclature and dimensions.....	29
3.2 Cast Iron Roller $R_1$ and heat treated high carbon steel Roller $R_3$ .....	30
3.3 A typical roller path plate.....	30
3.4 Top view of the test set-up.....	32
3.5 Cross section of the test set-up (section A-A).....	33
3.6 Large base plate of steel fixture (section B-B).....	34
3.7 Roller in steel fixture (section C-C).....	35
3.8 Steel Plate 2 attached with the strong concrete wall (section D-D).....	36
3.9a Front view of the test set-up.....	37
3.9b Arial view (front portion) of the test set-up.....	37
3.9c Side view of the test set-up.....	37
3.10 Hydraulic actuator.....	39

3.11 Universal joints provided in the piston rod of the hydraulic actuator.....	40
3.12 Small steel frame attached with the hydraulic actuator.....	40
3.13 Mechanical limit switch.....	41
3.14 Bars through the strong floor.....	42
3.15 Typical roller path plate attached with large supporting Plate 1.....	43
3.16 High strength solid round bars.....	44
3.17 Front and side view of the large steel fixture.....	45
3.18 Teflon plate and a solid steel shaft.....	45
3.19 Roller in contact with roller path plate.....	46
3.20 Spreader steel beams and hydraulic jacking system.....	47
3.21 Typical strain gauge layout and nomenclature.....	48
3.22 Data acquisition system and a Pentium III computer.....	49
3.23 Thermocouple on rim surface where strain gauges were installed.....	50
3.24 Digital thermometer and a thermocouple.....	50
3.25 Indentation depth test set-up.....	52
3.26 Scanning Electron Microscope.....	53
3.27 Roller R <sub>3</sub> being cut using abrasive water-jet technology.....	54
3.28 Water-jet cutting.....	55
3.29 Typical control samples for SEM.....	55
3.30 Pore surface structure of cast iron Roller R <sub>1</sub> (X200).....	57
3.31 Pore structure of heat treated high carbon steel Roller R <sub>3</sub> (X200).....	57
3.32 Pore structure of roller path Plate P <sub>1</sub> (X200).....	58
3.33 Surface pore structure of stainless steel Plate P <sub>3</sub> , (X200).....	58
4.1 BHN vs. radial distance below rolling surface.....	61
4.2 Strain versus time for high strength Bar 1, Test R <sub>1A</sub> , after 1 <sup>st</sup> cycle.....	62
4.3 Radial compressive load vs. time in Roller R <sub>1A</sub> , after 1 <sup>st</sup> cycle.....	63
4.4 Radial compressive load vs. number of cycles in Roller R <sub>1A</sub> .....	63
4.5 Enlarged view of the rim where strain gauges were installed.....	64
4.6 Strain vs. time for gauge 9 in Roller R <sub>1A</sub> after 1 <sup>st</sup> cycle.....	66
4.7 Location of gauge 9 in Roller R <sub>1A</sub> , during 1 <sup>st</sup> complete cycle.....	66
4.8a Strain vs. number of cycles for gauge 5 in Roller R <sub>1A</sub> .....	69

4.8b Strain vs. number of cycles for gauge 6 in Roller R <sub>1A</sub> .....	69
4.8c Strain vs. number of cycles for gauge 7 in Roller R <sub>1A</sub> .....	69
4.9a Strain vs. number of cycles for gauge 9 in Roller R <sub>1A</sub> .....	70
4.9b Strain vs. number of cycles for gauge 11 in Roller R <sub>1A</sub> .....	70
4.9c Strain vs. number of cycles for gauge 12 in Roller R <sub>1A</sub> .....	70
4.10 Strain vs. number of cycles for gauge 13 in Roller R <sub>1A</sub> .....	71
4.11a Maximum principal strain in Roller R <sub>1A</sub> .....	73
4.11b Minimum principal strain in Roller R <sub>1A</sub> .....	73
4.11c Maximum shearing strain in Roller R <sub>1A</sub> .....	73
4.12a Strain vs. number of cycles for gauge 7 in Roller R <sub>1B</sub> .....	76
4.12b Strain vs. number of cycles for gauge 9 in Roller R <sub>1B</sub> .....	76
4.13a Maximum principal strain in Roller R <sub>1B</sub> .....	77
4.13b Minimum principal strain in Roller R <sub>1B</sub> .....	77
4.13c Maximum shearing strain in Roller R <sub>1B</sub> .....	77
4.14a Strain vs. number of cycles for gauge 8 in Roller R <sub>2A</sub> .....	81
4.14b Strain vs. number of cycles for gauge 10 in Roller R <sub>2A</sub> .....	81
4.15a Roller R <sub>1</sub> Side A after cyclic loading.....	90
4.15b Roller R <sub>1</sub> Side B after cyclic loading.....	90
4.16 Roller R <sub>2A</sub> after 220,000 cycles of repeated loading.....	91
4.17a A typical roller plate before cyclic testing.....	92
4.17b Roller path Plate P <sub>1</sub> after cyclic testing.....	92
4.17c Roller path Plate P <sub>2</sub> after cyclic testing.....	92
4.18 Roller R <sub>1</sub> , control specimen, using SEM.....	93
4.19 Roller R <sub>1A</sub> , inside surface perpendicular to the tested contact surface showing depth of damage, using scanning electron microscope.....	94
4.20 Roller R <sub>1A</sub> , inside surface perpendicular to the tested contact surface showing depth of damage, using an optical microscope, (X200).....	94
4.21 Roller R <sub>1B</sub> , inside surface perpendicular to the tested contact surface showing depth of damage, using an optical microscope, (X200).....	95
4.22 Roller R <sub>2</sub> , control specimen, using SEM.....	95
4.23 Tested surface area of Roller R <sub>2A</sub> using an optical microscope, (X200).....	95

4.24 Roller R <sub>3</sub> , control specimen, using SEM.....	96
4.25 Tested surface area of Roller R <sub>3</sub> , using an optical microscope, (X200).....	96
4.26 Control specimen, Plate P <sub>1</sub> , using SEM.....	96
4.27 Tested contact surface area of Plate P <sub>1</sub> , using SEM.....	97
4.28 Plate P <sub>2</sub> , inside surface perpendicular to the tested contact surface showing depth of damage, using an optical microscope (X200).....	97
4.29 Plate P <sub>3</sub> , control specimen, using SEM.....	98
4.30 Tested contact surface area of Plate P <sub>5</sub> , using an optical microscope, (X200).....	98
5.1 One-eighth of a roller along with one quarter of a roller path plate.....	104
5.2 Hexahedral shape of elements in roller.....	106
5.3 Boundary conditions.....	108
5.4 Contour plot of principal stress $\sigma_1$ in Roller R <sub>1</sub> .....	110
5.5 Contour plot of principal stress $\sigma_2$ in Roller R <sub>1</sub> .....	110
5.6 Contour plot of principal stress $\sigma_3$ in Roller R <sub>1</sub> .....	111
5.7 Three paths created in Roller R <sub>1</sub> .....	112
5.8 Principal stresses on a path along the x-axis in Roller R <sub>1</sub> .....	112
5.9 Path plots of principal and octahedral shear stresses in the y-axis in Roller R <sub>1</sub> .....	115
5.10 Path plots of $\sigma_e$ , $\sigma_i$ , and $\sigma_o$ in the y-axis in Roller R <sub>1</sub> .....	116
5.11 Principal stresses on a path along the z-axis (rolling direction) in Roller R <sub>1</sub> .....	116
5.12 Path plots of $\sigma_e$ , $\sigma_i$ , $\tau_{max}$ , and octahedral stresses along the z-axis in Roller R <sub>1</sub> .....	117
5.13 Contour plot of principal stress $\sigma_1$ in Plate P <sub>1</sub> .....	118
5.14 Principal stresses on a path along the y-axis in Plate P <sub>1</sub> .....	119
5.15 Principal stresses on a path along the z-axis (rolling direction) in Plate P <sub>1</sub> .....	120
5.16 Path plots of $\sigma_e$ , $\sigma_i$ , $\tau_{max}$ , and octahedral stresses along the z-axis in Plate P <sub>1</sub> .....	120
5.17 Location of strain gauges 9, 14, and 18 on Roller R <sub>1</sub> and Plates P <sub>1</sub> and P <sub>2</sub> .....	123
5.18 F.E. Strain along a line in global y-axis passing through the location of gauge 9.....	124
5.19 Path plot along a line in global y-axis where gauge 14 was installed.....	125
5.20 Path plot along a line in global y-axis where gauge 18 was installed.....	126
6.1 Normalized amplitude-mean diagram (Dowling 2007).....	134
6.2 Movement of point P in roller.....	137

## List of Tables

2.1 Values of contact stresses between two long cylindrical bodies sliding against each other while in line contact under normal and friction forces.....	20
3.1 Stroke length, frequency and speed for rollers.....	52
3.2 Number of samples and nomenclature for SEM testing.....	56
3.3 Material properties of rollers and roller path plates.....	59
4.1 Radial compressive load applied on all rollers.....	65
4.2 Micro strains in Roller $R_1$ .....	68
4.3 Principal and maximum shearing micro strains in rollers.....	75
4.4 Micro strains in Roller $R_2$ .....	79
4.5 Micro strains in Roller $R_{3A}$ on Roller Path Plate $P_5$ .....	82
4.6 Micro strains in Roller $R_{3B}$ on Roller Path Plate $P_6$ .....	83
4.7 Micro strains in roller path Plates $P_1$ and $P_2$ .....	85
4.8 Micro strains in roller path Plates $P_3$ and $P_4$ .....	86
4.9 Micro strains in roller path Plate $P_5$ .....	87
4.10 Micro strains in roller path Plate $P_6$ .....	88
4.11 Summary of laboratory test results.....	102
5.1 Maximum stresses in MPa in rollers and in roller path plates.....	114
5.2 Comparison between FE results and laboratory test results.....	126
6.1 Fatigue properties of rollers and roller path plates.....	136
6.2 Fatigue life of specimens under worst-case scenario.....	140

## 1.1 General

This chapter introduces the main topic of this doctoral thesis and highlights the need for conducting research on hydraulic gate rollers and roller path plates. Background information and lack of knowledge concerning fatigue life of rollers are discussed. Finally, the research objectives and the outline of this doctoral thesis are clarified.

Manitoba Hydro is Canada's largest hydro utility company currently owning fourteen hydropower-generating stations with a total capacity of over 7500 MW (Polyzois and Lashari 2006). Each hydroelectric generating station has two types of gates: emergency intake gates and spillway gates. These two types of gates have a very distinct purpose, although they provide the same basic function of holding back high volumes of water. The purpose of the emergency intake gate is to cut off the flow of water to the turbine during maintenance procedures or in case of malfunction. Spillway gates, on the other hand, are in place to regulate the elevation of the body of water both upstream and downstream. The type of gates used at Manitoba Hydro generating stations are fixed-wheel gates. The only exceptions to this are the intake gates at the Great Falls, which have a roller train system (Doucet 2000).

Fixed-wheel gates have been extensively used in many water-resource development projects all over the world. Many types of gates have been invented and have become

unpopular, but fixed-wheel gates have remained as one of the most widely used type of gates with many applications. The term fixed-wheel gate applies to a rectangular gate with wheels mounted on the gate, as contrasted with an earlier type using roller chains independent of the gate leaf (Sagar 1989). As shown in Fig. 1.1, the hydrostatic load is transferred through a skin plate, onto a structural system of diaphragms, horizontal girders, and vertical end girders that are supported on wheels (Polyzois et al. 1995). The water thrust on the gate is transferred by the wheels to the roller path plates in the gate slots, fastened to track bases embedded in concrete of the structure, and the wheels rotate on the track as the gate is operated. The advantage of providing wheels is that the frictional forces to be surmounted during gate operation are relatively of much smaller magnitude as compared to sliding friction in slide gates, and enables the gate to be self-closing under gravity without a push force from the hoist (Sagar 1989).

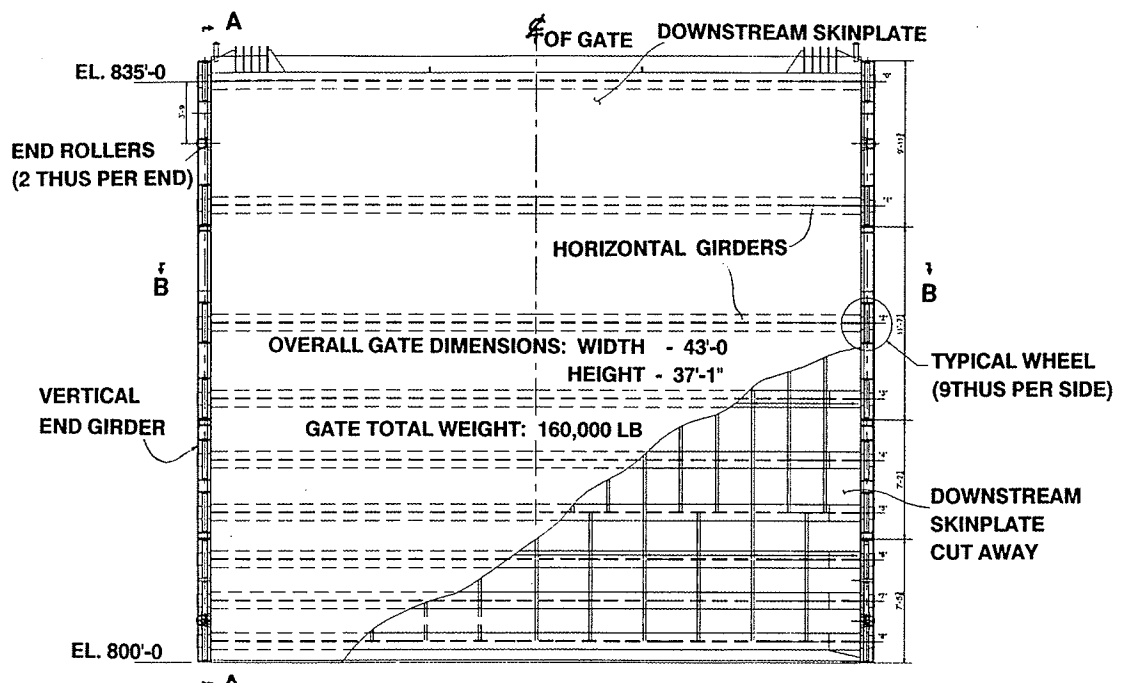


Fig. 1.1 Vertical lift fixed-wheel gate-downstream elevation (Polyzois et al. 1995)

Consequently, the wheel is a critical component of the gate assembly. Environmental corrosion and high wheel loads cause differences in the profile of the roller path surface. Combined with the relatively high torsional stiffness of the gate end girders, a condition of wheel load redistribution occurs where some wheels are relieved of load and other wheels are loaded beyond the maximum values for which they have been designed. As shown in Fig 1.2, these loads can be as much as two to three times larger than the original design loading. Failure of one wheel could jeopardize the overall operation of the gate (Polyzois et al. 1995).

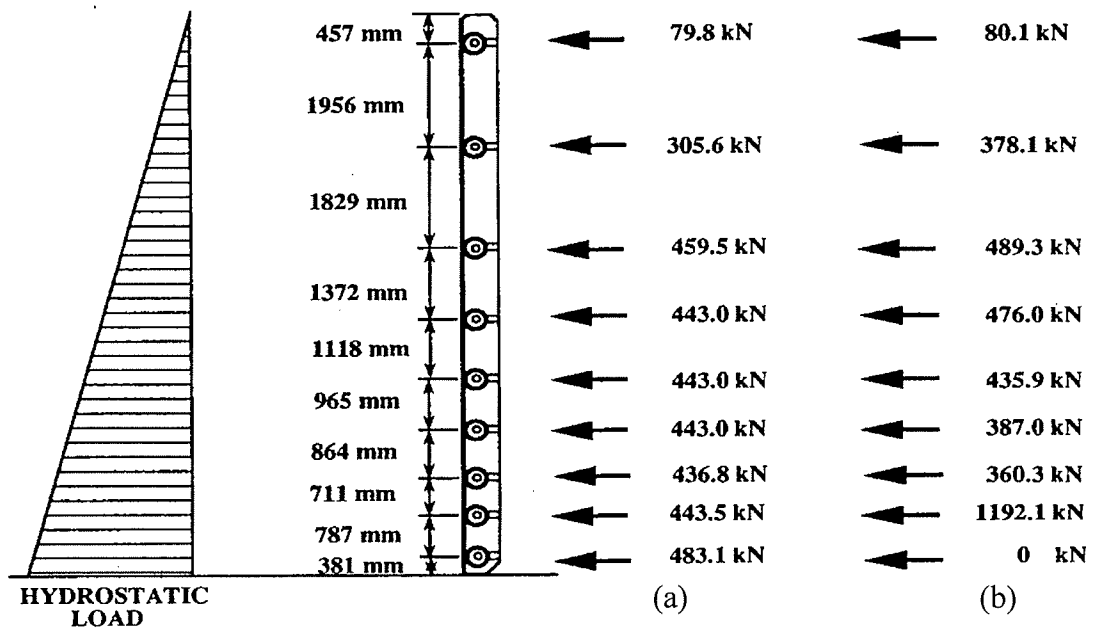


Fig. 1.2 End section of the vertical lift fixed-wheel gate (a) Normal load, all wheels bearing evenly (b) Overload, bottom wheel not bearing (Polyzois et al. 1995)

While the design of various gate structural components is carried out based on established national standards, the design of gate rollers<sup>1</sup> involves the use of an empirical formula, based on Brinell hardness, to obtain the initial roller diameter and the tread

<sup>1</sup>A roller is defined as a cylindrical solid with a height to width (aspect) ratio of less than or equal to unity. The rollers tested in this research program are actually wheels. Because Manitoba Hydro refers to them as rollers in their specification documents, the term “roller” has also been used in this thesis.

width (Noonan and Strange 1934). Tread surface Hertzian contact stresses and subsurface shear stresses are computed using methods developed by Thomas and Hoersch (1930). Although the Noonan and Strange (1934) formula was based on tests involving small-diameter cylindrical forged steel rollers, it has been subsequently adopted for the design of large-diameter crowned wrought-steel wheels, some in excess of 760 mm (30 in.) in diameter. The applicability of this formula to crowned wheels is questionable. Furthermore, this formula provides no information on the fatigue life of rollers or the relationship between the safe working loads and ultimate load capacity of the wheels, thereby making the safe wheel capacity unknown (Polyzois and Muzyczka 1994).

## **1.2 Research Objectives**

The main objectives of research reported in this thesis were:

- (a) To review current design standards of rollers used by Manitoba Hydro;
- (b) To test rollers and roller path plates under fatigue loading;
- (c) To perform finite element analysis of rollers and roller path plates;
- (d) To assess fatigue life of rollers and roller path plates; and,
- (e) To recommend design guidelines.

## **1.3 Thesis Outline**

The following is a brief description of the contents of each chapter in the thesis:

**Chapter 2** covers the literature review related to current design standards of rollers; previous work done by Muzyczka (1992) at the University of Manitoba; and, various theories dealing with the metal fatigue and contact fatigue of steel rollers.

**Chapter 3** describes in detail laboratory tests conducted on rollers and roller path plates under cyclic loading. A unique test set up was designed and developed in order to evaluate the fatigue performance of rollers and roller path plates. The details of each component of the test set up are mentioned using detailed diagrams. This chapter also describes the scanning electron microscope (SEM) testing program conducted on pieces taken from rollers and roller path plates after the completion of laboratory cyclic testing.

**Chapter 4** presents detailed discussions on the results obtained using laboratory testing of rollers and roller path plates under fatigue loading and scanning electron microscope testing.

**Chapter 5** encompasses the analysis of the rollers and roller path plates using ANSYS<sup>®</sup> finite element software and results obtained are compared with those obtained through laboratory testing.

**Chapter 6** covers details on the metal fatigue theory and fatigue life assessment of rollers and roller path plates.

**Chapter 7** summarizes the whole thesis with a retrospective view on the research study and draws conclusions from the work. Recommendations for the design guidelines are also highlighted in this chapter.

### 2.1 Review of Current Design Standards

The current design practice in Manitoba Hydro (1986) calls for crowned wheels to be designed in accordance with the criteria outlined by Skinner (1957) in his ASCE Paper No. 3000 "Fixed Wheel Gates for Penstock Intakes." These criteria were developed on the basis of work conducted by Noonan and Strange (1934) who devised an experimental procedure to study the relationship between the load on cylindrical steel rollers and deformation or permanent set of the rollers. As a result of their work, a method for evaluating the critical stress causing permanent set in steel rollers was developed. The critical stress,  $\sigma_{cr}$ , was expressed in terms of the Brinell hardness number (BHN) as follows (Polyzois and Muzyczka 1993):

$$\sigma_{cr} = 24.5 \cdot \text{BHN} - 2200 \quad (\text{psi per inch diameter per inch width}) \quad 2.1$$

The critical stress<sup>1</sup> is then equated to the projected area of the cylinder (product of the cylinder diameter and tread length). Knowing the critical stress, for a given diameter of a roller, the required tread width may be computed. The Noonan and Strange (1934) experiments were based on the assumptions that testing of plates to find the load at which they will become permanently deformed by hardened steel rollers is analogous to the testing of metal by means of a hardness machine and follows from conclusions reached by Wilson (1927). The testing involved solid steel rollers ranging in size from 38 mm (1.5 in.) to 254 mm (10 in.) in diameter with a height-to-width aspect ratio ranging from 0.25 to 0.5. For design purposes, the authors recommended that a safety factor of 2 is

---

<sup>1</sup>A sample calculation illustrating the application of Eq. 2.1 is included in Appendix A.

adequate since failure in the rollers is local. The empirical Eq. 2.1 presented by Skinner (1957) originated from work done by Noonan and Strange (1934) on behalf of the U.S. Bureau of Reclamation (Muzyczka 1992).

There are, however, important limitations to the work of Noonan and Strange (1934). Their experimental work involved only solid cylindrical rollers and roller plates made of stainless steels, commercial grades of steel and bronze. It is therefore questionable whether the results of this study are applicable to crowned cast iron and carbon steel wheels. Also, the diameter of typical vertical lift gate wheels used in hydro-electric generating stations range from 685.5 mm (27 in.) to 838 mm (33 in.) with aspect ratios of 20 to 25. These wheels are considerably larger and have relatively thinner webs than those tested by Noonan and Strange (1934). The authors clearly stated that the valid range of applicability of Eq. 2.1 was for rollers less than 254 mm (10 in.) in diameter. Skinner's work (1957) was an attempt to validate the work by Noonan and Strange (1934) for large diameter wheels. His work dealt with gate wheels fabricated from A57 wrought iron. Skinner (1957) also reported that the stress in the tread was the governing factor in gate wheel design and also recommended that a safety factor of 2 be applied to Eq. 2.1 for a wheel over load condition and a safety factor of 3 be applied on the critical stress for normal wheel loads (Muzyczka 1992). While the empirical expression given by Eq. 2.1 was used to size a roller, the design against failure was based on the maximum shear stress theory (Thomas and Hoersh 1930), which states that the maximum shear stress,  $V_u$ , developed when two bodies are in direct contact is one third the maximum compressive stress,  $C_u$ , at the point of contact (Roark 1989); i.e.,

$$V_u = \frac{C_u}{3} \quad 2.2$$

The shear resistance of the wheels, however, varies with the type of material used and must be determined experimentally. A simple approach would be to relate shear strength to hardness, since hardness can be easily obtained. However, most of the information available involves the relationship between the tensile strength of steel and hardness (Polyzois and Muzyczka 1994). Lieson and Jurinal (1963) developed the following relationship between the ultimate tensile strength,  $T_u$ , and the BHN for plain carbon steel:

$$T_u = 500 \cdot \text{BHN} \quad (\text{psi}) \quad 2.3$$

The applicability of Eq. 2.3 was limited to a range between 200 to 350 BHN, with greater variation in the ultimate tensile strength exhibited for high BHN. Lieson and Jurinal (1963) also presented the following relationship between the ultimate tensile strength,  $T_u$ , and the BHN for cast iron:

$$T_u = 0.294 \cdot \text{BHN} - 29.4 \quad (\text{ksi}) \quad 2.4$$

Eq. 2.4 was limited to materials whose BHN ranged from 150 to 300. A number of other relationships between tensile strength and BHN have also been developed for cast iron (Angus 1976). There is no direct relationship between the ultimate shear strength,  $V_u$ , and hardness. Rather, the relationships between the shear and tensile strength and between the tensile strength and hardness have been used to derive a relationship between shear strength and hardness (Polyzois and Muzyczka 1994). For low carbon steel the shear to tensile strength ratio is (Davis et al. 1982):

$$\frac{V_u}{T_u} = 0.7 \quad 2.5$$

Combining Eqs. 2.3 and 2.5, the following relationship between the ultimate shear strength and BHN was obtained:

$$V_u = 0.7(500 \cdot \text{BHN}) = 350 \cdot \text{BHN} \quad (\text{psi}) \quad 2.6$$

Using the relationship of Eq. 2.6, Skinner (1957) established the maximum elastic shear strength for wrought steel with BHN of 255. Thus, Eq. 2.6 became:

$$V_u = 350 \cdot \text{BHN} \leq 350 \cdot 255 \approx 90,000 \quad (\text{psi}) \quad 2.7$$

According to the current design procedure for cast iron wheels, the maximum shear stress due to the applied loads, computed from Eq. 2.2, must be less than or equal to the ultimate shear stress given by Eq. 2.7. This, however, is the maximum elastic shearing stress suggested by Skinner (1957) for wrought steel wheels. It is thus questionable whether the same limit can be applied to cast iron wheels (Polyzois and Muzyczka 1994).

## **2.2 Previous Work at the University of Manitoba**

An experimental program (Muzyczka 1992), sponsored by Manitoba Hydro, was undertaken in 1991 at the University of Manitoba to study the performance characteristics of large diameter cast iron wheels and to determine their failure capacity under static loading conditions. Eleven 685.5 mm (27 in.) diameter cast iron wheels obtained from a spillway gate at the McArthur Falls Generating Station were tested to failure under radial and a combination of radial and lateral loads. The test parameters included the orientation of the radial load with respect to the handling holes, and the presence or absence of a lateral load. The material properties of the wheels were established through standard test coupons taken from one wheel. The material, geometry and profile of eleven 685.5 mm (27 in.) diameter cast iron wheels tested by Muzyczka (1992) were same as to those of the 838 mm (33 in.) diameter cast iron roller tested under cyclic loading in this doctoral

research program. In developing failure criteria for the cast iron wheels, Muzyczka (1992) considered two wheel orientations: (a) the line of action of the radial load was between the handling holes, and (b) a handling hole was in direct line of action of the applied radial load. To account for the presence of a lateral load, a modification to the vertical load capacity was made utilizing the information obtained through testing. Failure of wheels loaded through the handling holes was due to sudden cracking initiating at the hole locations. This may be attributed to the high concentration of tensile stress around the hole. However, the wheels loaded between the holes failed by shelling, a mode of failure associated with the presence of high shear stresses (Mitsuda and Bouling 1989). The failure criteria for wheels loaded between the handling holes were based on the maximum shear stress theory, which requires that the maximum shear stress be less or equal to the shear strength of the material. According to the results obtained from the coupon testing, the average measured shear strength to tensile strength ratio was determined to be (Polyzois and Muzyczka 1994):

$$\frac{V_u}{T_u} = 1.39 \quad 2.8$$

Substituting Eq. 2.8 into 2.4, the following relationship between shear strength and BHN was obtained (Polyzois and Muzyczka 1994):

$$V_u = 0.409 \cdot \text{BHN} - 40.9 \quad (\text{ksi}) \quad 2.9$$

The ultimate shear strength of a cast iron material given by Eq. 2.9 was established on the basis of the ultimate tensile strength-BHN relationship, which is valid between 150 and 300 BHN (Lieson and Jurinal 1963). Using 300 as an upper limit to the BHN of cast iron, Eq. 2.9 becomes (Polyzois and Muzyczka 1994):

$$V_u = 0.409 \cdot \text{BHN} - 40.9 \leq 81.8 \quad (\text{ksi}) \quad 2.10$$

To obtain the theoretical load capacity for the case where the load is applied through handling hole, a bilinear approximation of the stress-strain curve obtained through tension coupon tests was used along with the load-strain relationships obtained through the FE analysis, as follows (Polyzois and Muzyczka 1994):

$$P_t = P_y + a k (\varepsilon_t + \varepsilon_y) \quad 2.11$$

Where  $P_t$  = theoretical failure load (N);  $P_y$  = yield load at which inelastic behavior begins =  $k E_y$  (N);  $a = E_t/E$ ;  $E, E_t$  = modulus of elasticity and tangent modulus, respectively;  $\varepsilon_t = (k_{cr}/k) \varepsilon_{cr}$ ;  $k_{cr}, k$  = slope of linear load-strain relationship at the edge of the hole and at a point located 4 mm from the hole, respectively (N/mm/mm);  $\varepsilon_{cr}$  = ultimate strain obtained from the bilinear stress-strain curve (mm/mm); and  $\varepsilon_y$  = yield strain obtained from the bilinear stress-strain curve (mm/mm). A lateral force of 29% of the radial load reduced the capacity of the wheel by approximately 50%. To account for the presence of a lateral load, a linear reduction of the vertical force capacity was proposed. This linear reduction, given by the following expressions, was developed on the basis of test results. For wheels loaded through the handling hole, the ultimate load capacity,  $P_t$ , in the presence of a lateral load,  $P_L$ , was established as (Polyzois and Muzyczka 1994):

$$P_t = P_r - 4.87P_L \quad (\text{kN}) \quad 2.12$$

Similarly, for loading between holes, the ultimate load was defined as:

$$P_t = P_r - 0.43P_L \quad (\text{kN}) \quad 2.13$$

Where  $P_r$  = radial load capacity of the wheels in the absence of any lateral force. For wheels loaded between handling holes,  $P_r$  = load that will cause a maximum shear is given by Eq. 2.10. For wheels loaded through the handling holes, the load is given by Eq. 2.11 (Polyzois and Muzyczka 1994).

### **2.3 Contact Stresses**

Contact stresses are caused by the pressure of one solid on another over limited areas of contact. Members are designed on the basis of stress in the main body of the member, that is, in portions of the body not affected by the localized stresses at or near a surface of contact between bodies. Most failures of members are associated with stresses and strains in portions of the body far removed from the points of application of the loads. Nevertheless, the contact stresses created when surfaces of two bodies are pressed together by external loads are the significant stresses. The stresses on or somewhat beneath the surface of contact are the major cause of failure of one or both of the bodies. For example, contact stresses may be significant at the area (1) between a locomotive wheel and the railroad rail; (2) between a roller or ball and its race in a bearing; (3) between the teeth of a pair of gears in mesh; (4) between the cam and valve tappets of a gasoline engine; etc (Boresi et al. 1993). The contact stresses are often cyclic in nature and are repeated a very large number of times, often resulting in a fatigue failure that starts as a localized fracture (crack) associated with localized stresses. The fact that contact stresses frequently lead to fatigue failure largely explains why these stresses may limit the load-carrying capacity of the members in contact and hence may be the significant stresses in the bodies. For instance, a railroad rail sometimes fails as a result of contact stresses. Failure starts as a localized fracture in the form of a minute transverse crack at a point in the head of the rail somewhat beneath the surface of contact between the rail and locomotive wheel, and progresses outwardly under the influence of the repeated wheel loads until the entire rail cracks or fractures. On the other hand, bearings and gear teeth sometimes fail as a result of formation of pits (pitting) at the surface of

contact. The bottom of such pit is often located approximately at the point of maximum shear stress. Steel tappets have been observed to fail by initiation of microscopic cracks at the surface that then spread and cause flaking. Chilled cast-iron tappets have failed by cracks that start beneath the surface, where the shear stress is highest, and spread to the surface, causing pitting failure. The principal stresses at or on the contact area between two curved surfaces that are pressed together are greater than at a point beneath the contact area, whereas the maximum shear stress is usually greater at a point a small distance beneath the contact surface (Boresi et al. 1993).

Fig. 2.1 depicts the curves showing variation in principal stresses, maximum shear stress, and octahedral shear stress with variation in distance  $z$  from the contact surface of two semicircular solid disks made of elastic material with  $\frac{B}{A} = 1.24$  and the Poisson's ratio of 0.25. The constants  $A$  and  $B$  depend on the principal radii of curvature of the two elastic bodies in contact. In this figure, the coefficients of  $\frac{b}{\Delta}$  are plotted as abscissas and the values of  $\frac{kz}{b}$  to the point at which the stresses occur are plotted as ordinates, where  $k$  is the ratio of semi-minor axis  $b$  to semi-major axis  $a$  of ellipse of contact (Seely and Smith 1955). The expression for  $\Delta$  is given below:

$$\Delta = \frac{1}{A+B} \left( \frac{1-\nu_1^2}{E_1} + \frac{1-\nu_2^2}{E_2} \right) \quad 2.14$$

Where,  $E_1$  and  $E_2$  and  $\nu_1$  and  $\nu_2$  are elastic modulus and Poisson's ratio of the two elastic bodies in contact, respectively. The curves in Fig. 2.1 representing  $\sigma_{xx}$ ,  $\sigma_{yy}$ , and  $\sigma_{zz}$  show that their largest values occur at the centre of the surface of contact and that all three

stresses decrease as  $z$  increases. The principal stress having the greatest magnitude at every point is  $\sigma_{zz}$  and its maximum value is  $\sigma_{\max} = \frac{0.67b}{\Delta}$  (Seely and Smith 1955).

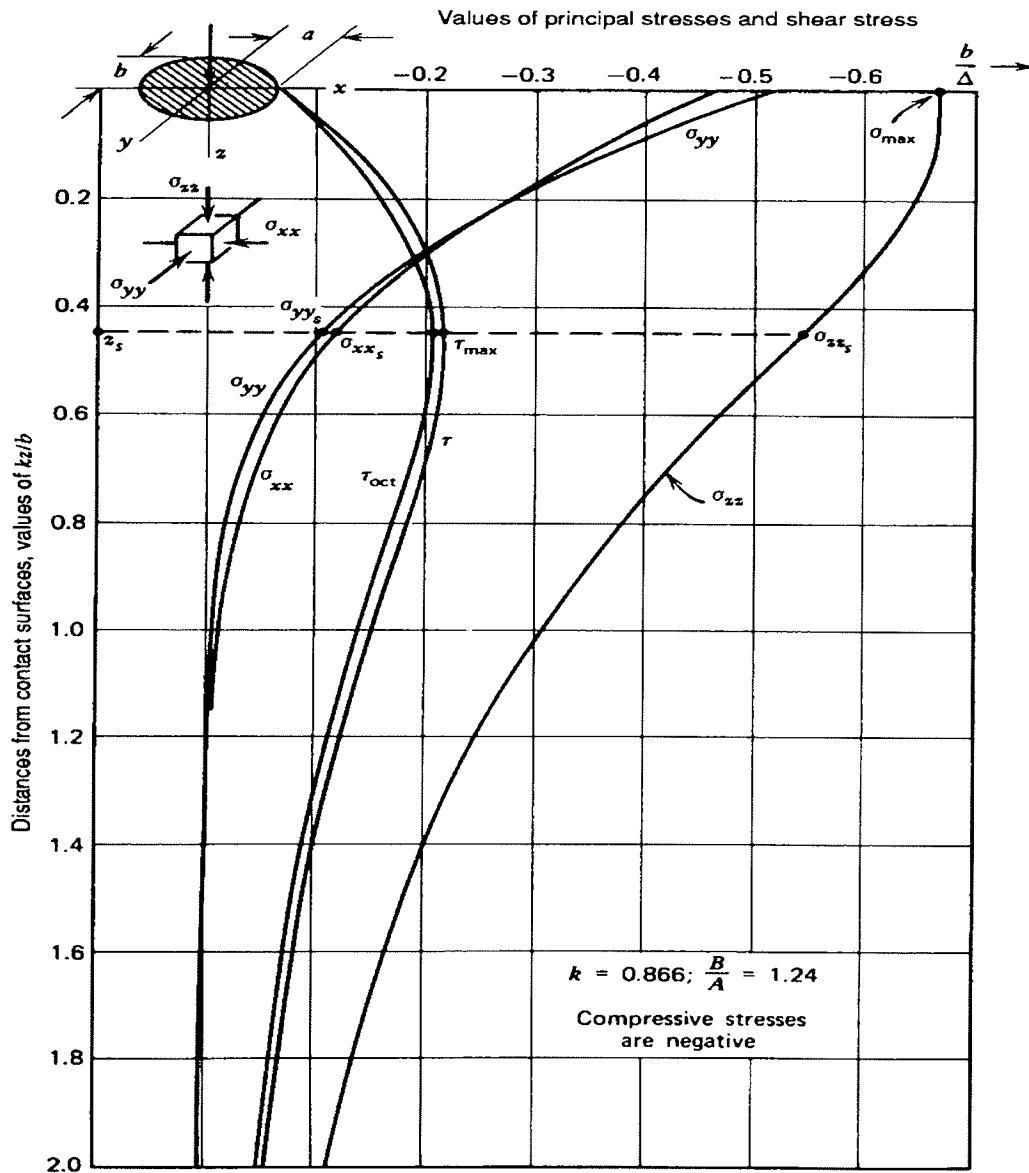


Fig. 2.1 Curves showing variation in principal stresses, maximum shear stress, and octahedral shear stress with variation in distance from the contact surface (Seely and Smith 1955).

The value of the maximum shear stress,  $\tau_{\max} = 0.22 \frac{b}{\Delta}$  and it occurs just beneath the surface of contact at a distance of  $\frac{kz_s}{b} = 0.44$ , as shown in Fig. 2.1. The maximum value

of the octahedral shear stress,  $\tau_{\text{oct}} = \frac{0.21b}{\Delta}$  and it occurs at the same distance,  $\frac{kz_s}{b} = 0.44$ , as the maximum shear stress (Seely and Smith 1955).

Fig. 2.2 shows a line contact of a circular cylinder resting on a plane subjected to radial (normal) load only, the line of contact being perpendicular to the paper. Principal stresses have their maximum values at the surface of contact of such bodies shown in Fig. 2.2 and their values are  $\sigma_{xx} = -\frac{b}{\Delta}$ ,  $\sigma_{yy} = -2\nu\frac{b}{\Delta}$ , and  $\sigma_{zz} = -\frac{b}{\Delta}$ . The greatest value of maximum shear stress,  $\tau_{\text{max}}$  is  $\frac{0.3b}{\Delta}$  and it occurs at a distance of  $\frac{z_s}{b} = 0.7861$ , for bodies shown in Fig. 2.2. The maximum octahedral shear stress  $\tau_{\text{oct(max)}} = \frac{0.27b}{\Delta}$  and it occurs at the same location as the maximum shear stress (Boresi et al. 1993).

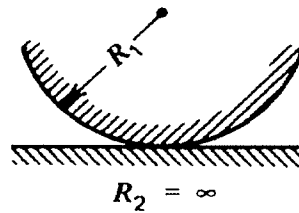


Fig. 2.2 Line contact between cylindrical bodies (Boresi et al. 1993)

Figs. 2.3a and b depict the cross section of a long roller of elastic material that rests on a flat surface of a thick solid elastic body. The roller is subjected to a distributed load  $w$ , which presses it against the body over a long narrow area of contact whose width is  $2b$ . A lateral distributed force load  $f$  causes the roller to slide on the body. If the coefficient of sliding friction is designated as  $\beta$ , then  $f = \beta w$ . In Fig. 2.3c, which is an enlarged view of the part near the contact area, the ordinates to the ellipse show the distribution of normal stresses over this area and the maximum stress is  $\sigma_{zz} = -\frac{b}{\Delta}$  (Boresi et al. 1993).

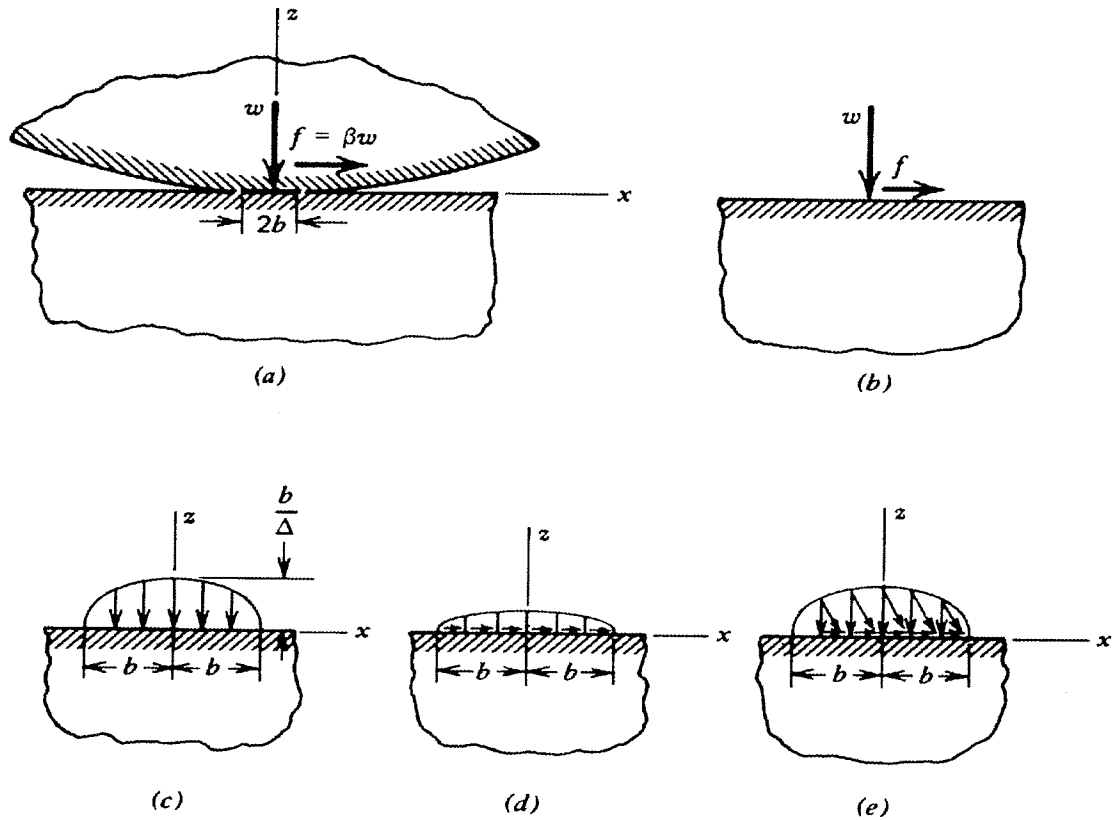


Fig. 2.3 Tangential and normal forces over the contact area (Boresi et al. 1993)

Mindlin (1949) has found that when sliding occurs, the shear stress on the contact area due to the frictional force  $f$  are distributed as ordinates to an ellipse as shown in Fig. 2.3d, and the maximum shear stress  $\sigma_{zx}$  at the centre is  $\sigma_{zx} = \beta \frac{b}{\Delta}$ . Fig. 2.3e shows the distribution of the combined normal and friction stresses on the contact surface. Smith and Liu (1953) have derived the equations for the stresses  $\sigma_{xx}$ ,  $\sigma_{yy}$ ,  $\sigma_{zz}$ , and  $\sigma_{zx}$  at any point in the body. Fig. 2.4 shows the principal stresses  $\sigma_1$ ,  $\sigma_2$ , and  $\sigma_3$  on the contact surface and at a distance  $z = \frac{b}{4}$  from the surface for a long roller resting on a flat surface shown in Fig. 2.3 under the influence of normal as well as tangential forces. The value of friction coefficient of  $\frac{1}{3}$  was employed while computing these principal stresses. Each

principal stress has its maximum value in the surface of the body at a distance of about  $0.3b$  from the center of the area of contact in the direction of the frictional force (Boresi et al. 1993). These maximum principal stresses are  $\sigma_1 = -\frac{1.4b}{\Delta}$ ,  $\sigma_2 = -\frac{0.72b}{\Delta}$ , and  $\sigma_3 = -\frac{0.53b}{\Delta}$ . These values may be compared with  $\sigma_1 = -\frac{b}{\Delta}$ ,  $\sigma_2 = -\frac{b}{\Delta}$ , and  $\sigma_3 = -\frac{0.5b}{\Delta}$  for the normal distributed load  $w$  only. This comparison clearly proves that the frictional force corresponding to a friction coefficient of  $\frac{1}{3}$  increases the maximum principal stress by 40%. In addition, the curves in Fig. 2.4 show that the principal stresses  $\sigma_2$  and  $\sigma_3$  are tensile stresses near the edge of the contact area opposite the direction of the tangential force. The largest magnitudes of these stresses are  $\frac{0.667b}{\Delta}$  and  $\frac{0.167b}{\Delta}$ , respectively. Nevertheless, these tensile principal stresses are sometimes quite large. The presence of the tensile principle stresses on the surfaces aids in understanding the occurrence of fatigue failure by pitting, etc., of bearing surfaces subjected to repeated loads. The value of maximum shear stress as computed from minimum and maximum principal stresses is  $\tau_{\max} = -0.43 \frac{b}{\Delta}$  (Boresi et al. 1993).

The principal shear stresses at points on the surface and from the surface a distance of  $z = \frac{b}{4}$  (where the maximum subsurface shear occurs) are shown in Figs. 2.5. There are three extreme values of shear stresses at each point. The ordinates to the curves representing  $\tau_1$  and  $\tau_3$  at distance  $z = \frac{b}{4}$  from the surface are everywhere smaller than at the surface as noted in Figs. 2.5a and c. This is true for all distances from the surface. However, in Fig. 2.5b, the curve for  $\tau_2$  at  $z = \frac{b}{4}$  rises above the curve representing values of  $\tau_2$  at the surface (Boresi et al. 1993).

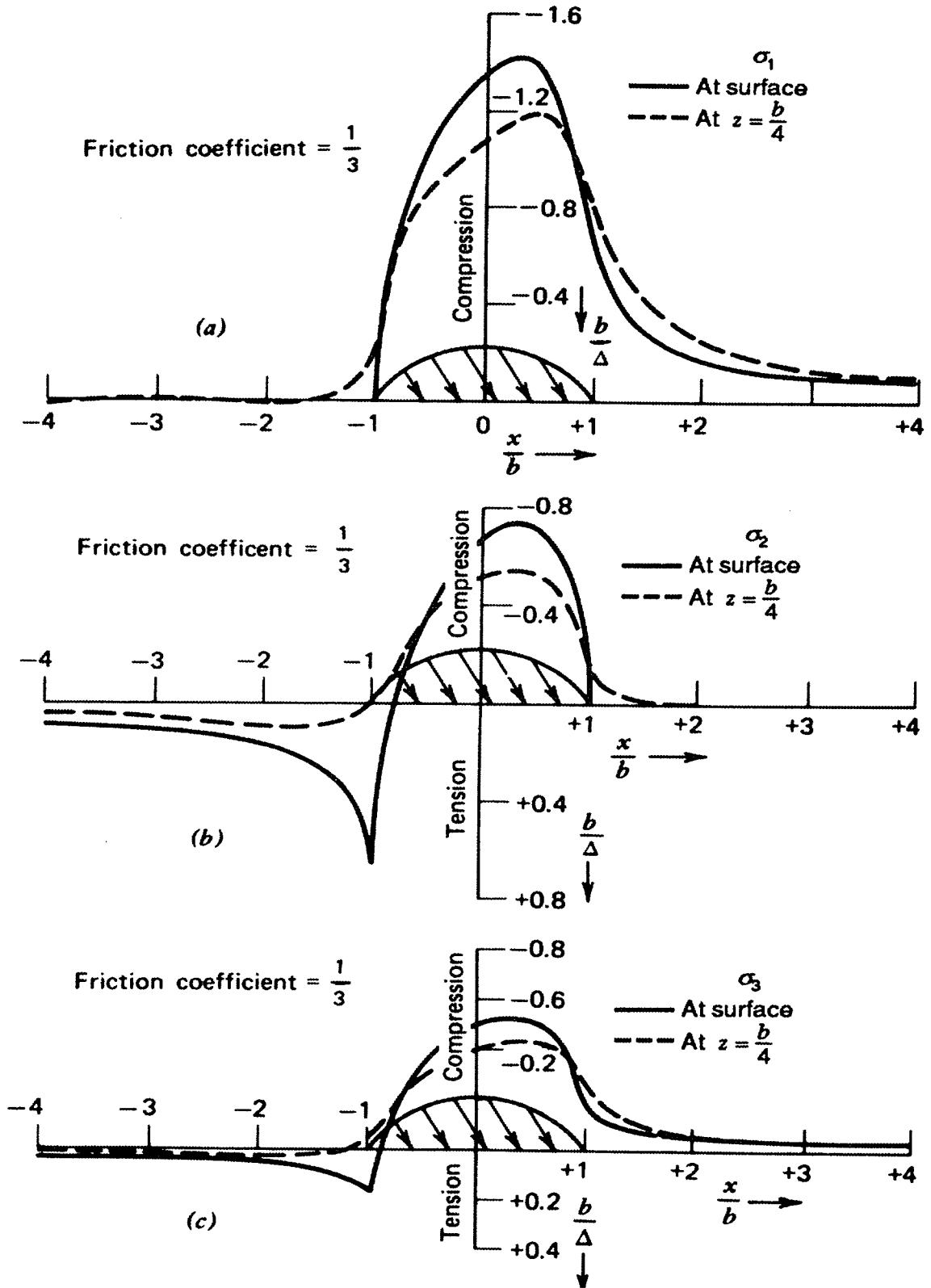


Fig. 2.4 Effect of tangential force on principal stresses (Boresi et al. 1993)

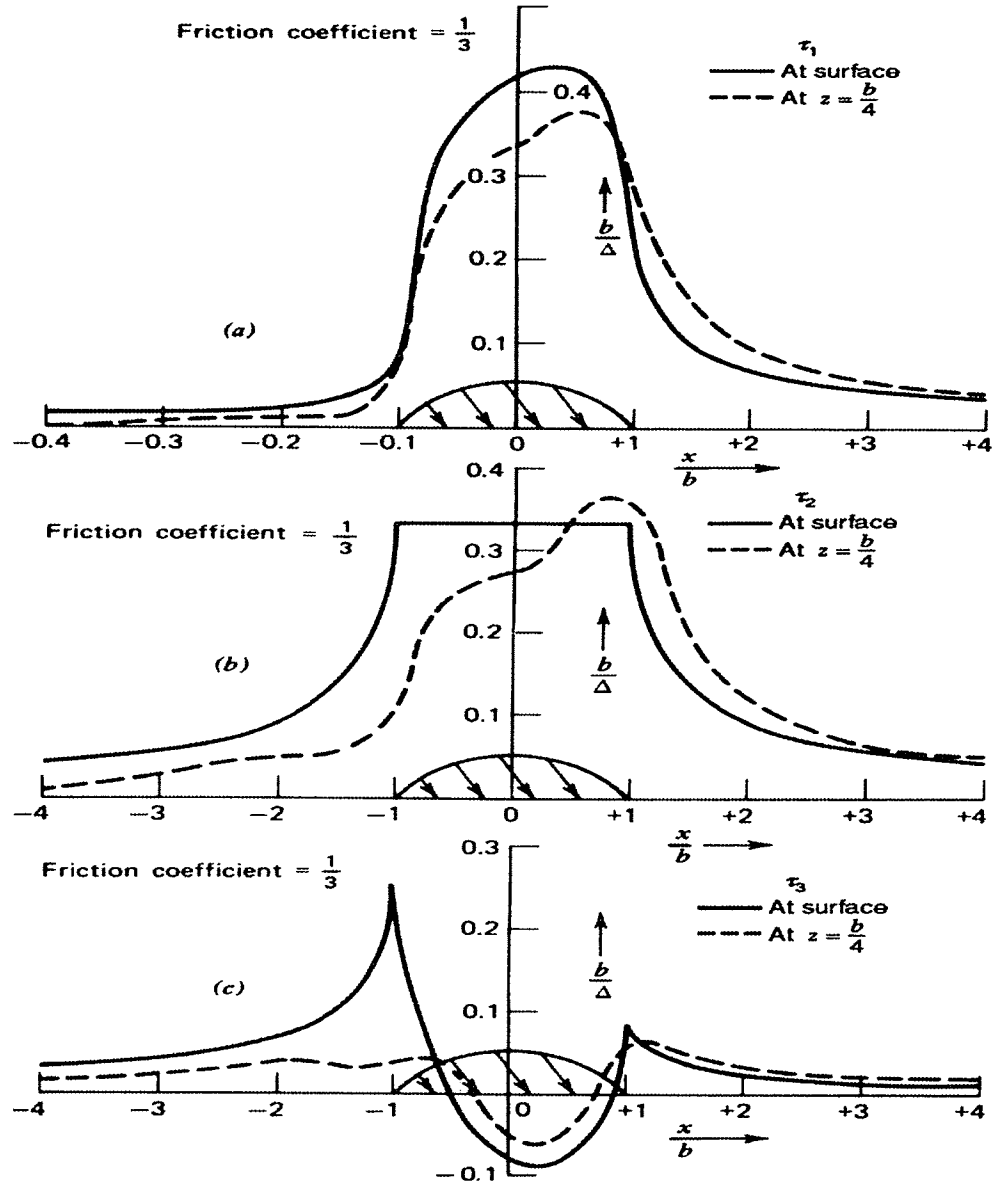


Fig. 2.5 Effect of tangential force on maximum shear stresses (Boresi et al. 1993)

Such curves for values of  $\tau_2$  have been plotted for several distances from the surface, and it is found that the largest value of  $\tau_2$  is  $\frac{0.36b}{\Delta}$ . This value occurs at a distance of about  $\frac{b}{4}$  from the surface. Therefore, the value  $\tau_1 = -\frac{0.43b}{\Delta}$  as mentioned above is the maximum shear stress, and it occurs at a point in the contact area about  $0.3b$  from the centre of the area. In Fig. 2.6 the ordinates to the curves represent the values of the octahedral shear

stresses  $\tau_{oct}$  that have been computed at each point using values of the principal stresses obtained from Fig. 2.4. The maximum value is  $\tau_{oct(max)} = \frac{0.37b}{\Delta}$ , and it occurs on the contact area at the same point that the maximum principal stress and maximum shear stresses occur (Figs. 2.4 and 2.5) (Boresi et al. 1993).

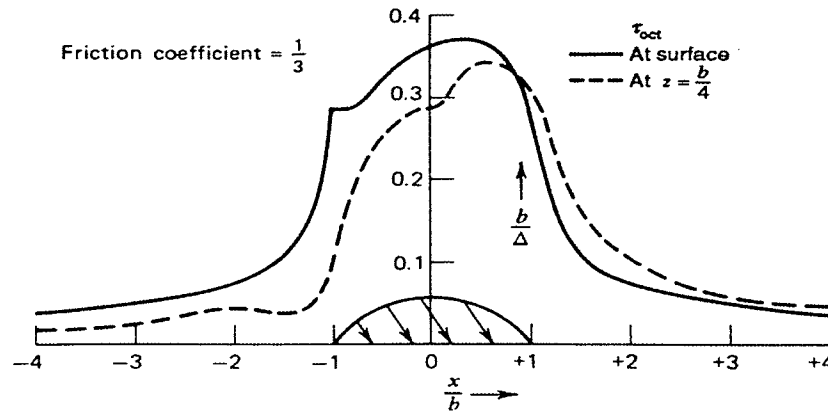


Fig. 2.6 Effect of tangential force on octahedral shear stress (Boresi et al. 1993)

Table 2.1 Values of contact stresses between two long cylindrical bodies sliding against each other while in line contact under normal and friction forces (Boresi et al. 1993)

Coefficient of Friction	0	$\frac{1}{12}$	$\frac{1}{9}$	$\frac{1}{6}$	$\frac{1}{3}$
Kind of Stress and Its Location	Values of Stress in Terms of $b/\Delta$ Corresponding to the Above Friction Coefficients				
Maximum tensile principal stress that occurs in surface at $x = -b$	0	$\frac{2b}{12\Delta}$	$\frac{2b}{9\Delta}$	$\frac{2b}{6\Delta}$	$\frac{2b}{3\Delta}$
Maximum compressive principal stress that occurs in the surface between $x = 0$ and $x = 0.3b$	$-\frac{b}{\Delta}$	$-1.09\frac{b}{\Delta}$	$-1.13\frac{b}{\Delta}$	$-1.19\frac{b}{\Delta}$	$-1.40\frac{b}{\Delta}$
Maximum shear stress <sup>a</sup>	$0.300\frac{b}{\Delta}$	$0.308\frac{b}{\Delta}$	$0.310\frac{b}{\Delta}$	$0.339\frac{b}{\Delta}$	$0.435\frac{b}{\Delta}$
Maximum octahedral shear stress <sup>a</sup>	$0.272\frac{b}{\Delta}$	$0.265\frac{b}{\Delta}$	$0.255\frac{b}{\Delta}$	$0.277\frac{b}{\Delta}$	$0.368\frac{b}{\Delta}$

<sup>a</sup> Note that these stresses occur at the surface when the friction coefficient is  $\frac{1}{10}$  or larger.

Principal stresses, maximum shear stresses, and maximum octahedral shear stresses depend on the value of the coefficient of friction. The changes in the maximum contact stresses with the coefficient of friction are given by Table 2.1. The increases in the maximum values of the tensile and compressive principal stresses caused by the frictional distributed load are very nearly proportional to the increases in the friction coefficient (Boresi et al. 1993).

## **2.4 Metal Fatigue**

All materials are anisotropic and inhomogeneous when viewed at a sufficiently small size scale. For example, engineering metals are composed of an aggregate of small crystal grains. Within each grain, the behavior is anisotropic due to the crystal planes, and if a grain boundary is crossed, the orientation of these planes changes. Inhomogeneities exist due to the grain structure and tiny voids or particles of a different chemical composition than the bulk of the material, such as hard silicate or alumina inclusions in steel. Multiple phases, involving grains or other regions of more than one chemical composition, are also common. As a result of such non-uniform microstructure, stresses are distributed in a non-uniform manner when viewed at the size scale of this microstructure. Regions where the stresses are severe are usually the points where fatigue damage starts. The details of the behavior at a micro-structural level vary widely for different materials due to their different bulk mechanical properties and their different microstructure (Dowling 2007). One of the most important physical observations is that the fatigue process can generally be broken into two distinct phases; initiation life and propagation life. The initiation life encompasses the development and early growth of a small crack. The propagation life is

the portion of the total life spent growing a crack to failure. Nevertheless, it is often very difficult, if not impossible, to define the transition from initiation to propagation. This distinction depends upon many variables, including component size, material, and the methods used to detect cracks, to name just a few (Bannantine et al. 1990).

Generally, fatigue cracks originate at a free surface, at a point of high stress concentration in the material. This may often be a preexisting flaw in the material, or perhaps a human-made discontinuity, such as the root of a thread, a rivet or bolt hole, or any point at which there is a sharp change in the size or shape of the material. It appears that, at least in metals, fatigue cracks nucleate due to the mechanism of slip. Slip occurs by the movement of dislocations, which produce fine slip bands. However, at a free surface, when slip takes place, the relative displacements of the atoms along the slip planes cause “steps” to occur, of the order of a nanometer ( $10^{-9}$  m) high. Under cyclic loading, reversed slip on adjacent slip planes may lead to the formation of extrusions and intrusions at the surface, as shown in Fig. 2.7 (Young et al. 1998). These may act as the nucleus of a surface crack, as additional slip continues to occur along only a few slip bands rather than across a much wider region. Thus, incipient fatigue cracks may form after only 5% to 10% of the specimen’s fatigue life. Subsequently, a crack will begin to grow. Initially, the crack will grow along the slip plane, but it will eventually change direction until it is growing in a plane perpendicular to the principal tensile stress, as show in Fig 2.7. Fatigue cracks will propagate under shear or tensile loading but not under compressive loading, since compression will close cracks rather than open them. On each tensile loading cycle, very high stresses occur at the crack tip (due to the stress

concentration effect of a sharp crack), causing the crack to propagate into the still undamaged material ahead of it. It is important to note that the crack propagates a finite distance in each loading cycle; this crack advance may be as much as 25  $\mu\text{m}/\text{cycle}$  (Young et al. 1998).

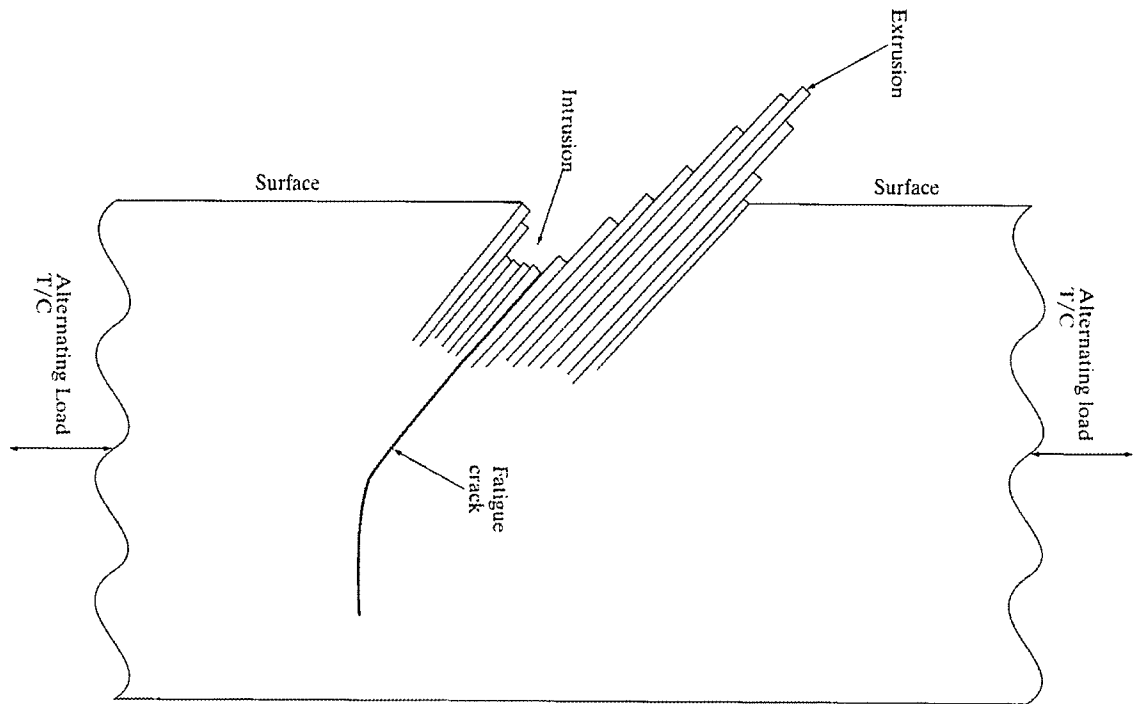


Fig. 2.7 Schematic diagram of crack initiation and subsequent crack growth, first along the slip line and then at right angles to the principal tensile stress (Young et al. 1998)

## 2.5 Basic Fracture Mechanic Concept

Fig. 2.8 shows the exaggerated view of the area around a crack tip in an infinitely wide plate in which the crack length,  $a$ , is very small as compared to the plate width. When a remote stress,  $\sigma$ , is applied, the crack opens a certain distance,  $d$ , and a high stress concentration is developed around the crack tip. Theoretically, this high stress concentration is infinite at the crack tip, but in real materials, plastic zones are created since the strain exceeds the ability of the material to act elastically. This process in which

an applied load causes a crack to open, crack opening relieves crack surfaces of stress, and the creation of crack tip plastic straining, is the fundamental mechanism that weakens components containing cracks or crack-like discontinuities. A description of the stress field in the vicinity of the crack tip can be obtained using special stress functions. The stress in the y-direction for the particular case of  $\theta = 0$ , is  $\sigma_{yy} = \frac{\sigma\sqrt{\pi a}}{\sqrt{2\pi r}}$  (Fisher et al. 1998). Under fatigue situation, if the crack length,  $a$ , and the plastic zone crack tip radius,  $r$ , is increased, the local stress,  $\sigma_{yy}$ , is decreased.

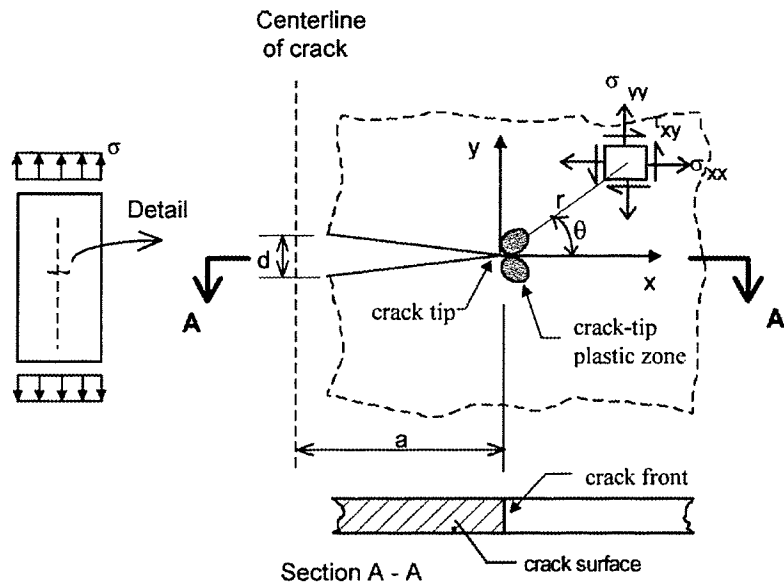


Fig. 2.8 A crack in an infinitely wide plate (Fisher et al. 1998)

## 2.6 Contact Fatigue

Contact fatigue is a surface-pitting-type failure commonly found in ball or roller bearings (Lampman 1996). This type of failure can also be found in gears, cams, valves, rails, and gear couplings. Contact fatigue has been identified in both ferrous and non-ferrous metals and in ceramics and cermets. Contact fatigue differs from classical structural bending or

torsional fatigue in that it results from a contact or Hertzian stress state. The contact geometry and the motion of the rolling elements produce an alternating subsurface shear stress. Subsurface plastic strain builds up with increasing cycles until a crack is generated. The crack then propagates until a pit is formed. Once surface pitting is initiated, the bearing becomes noisy and rough running. If allowed to continue, fracture of the rolling element and catastrophic failure occurs. Fractured races can result from fatigue spalling and high hoop stresses (Lampman 1996). Rolling contact components have a fatigue life (number of cycles to develop a noticeable fatigue spall). Nevertheless, unlike structural fatigue, contact fatigue has no endurance limit. If one compares the fatigue lives of cyclic torsion with rolling contact, the latter are seven orders of magnitude greater (Bhargava et al. 1989). Contact fatigue produces a surface damage that is unique and well recognized. Familiar examples are found in fatigue of ball and roller bearings. Even though, this spall is small, it would grow in size until roller fracture would occur, as bearing operation continues (Lampman 1996). One classic shape of fatigue spall in a ball bearing is a delta shape, as shown in Fig. 2.9 with a diagram of the pit. The apex of the pit is the initiation of point, usually the location of a surface defect like a dent. The pit grows in a fan shape, becoming wider and deeper as it grows in the direction of ball travel. Not all spalls in ball bearing races are of the shape shown in Fig. 2.9 (Harris 1964). Spalling type failures occur on track rails from wheel-track rolling contacts. An example of spalling type failure is shown in Fig. 2.10. The name comes from the morphology of the fracture surface in the bottom of the spall. Shelly failures are serious because they lead to rail fracture and derailments. Rail spalling has been reduced by the use of higher carbon steels for rails (Kilburn 1964).

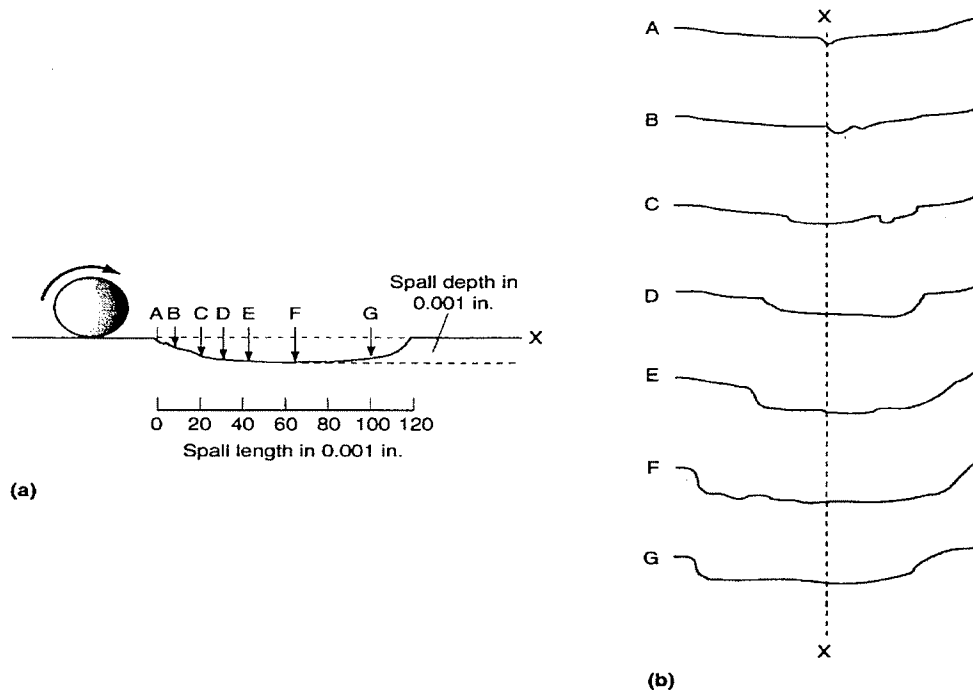


Fig. 2.9 Anatomy of a race spall in a ball bearing (a) Typical delta shape with the apex at the origin (b) Profiles of the spall (Harris 1964)

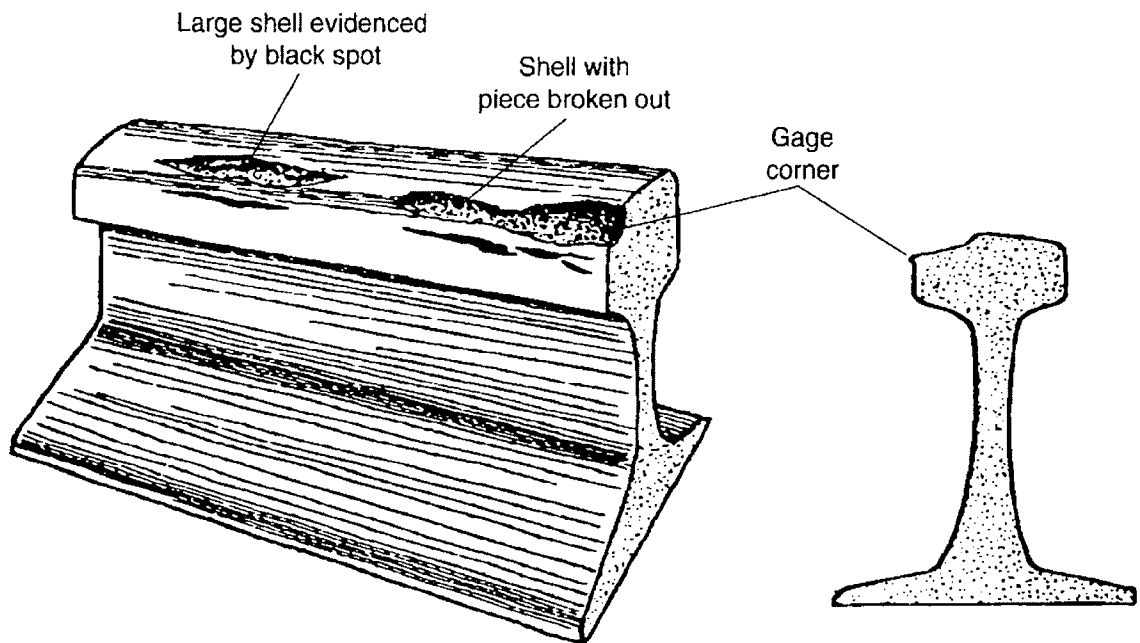


Fig. 2.10 "Shelly" rail spall from wheel-rail contact fatigue (Kilburn 1964)

The state of stress produced by rolling contact is concentrated in a small volume of material and produces intense plastic strain. The strain accumulates as the same volume is stressed with each rolling cycle until a crack is initiated and forms a spall. In the real world of contact fatigue, the mechanisms involved can be quite complex. Most models assume a condition of ideal geometric surfaces and little input by heat generation, environmental conditions, and in-homogeneities of material. Hertz stress analysis assumes a circular, elliptical, or line contact surface area between curved surfaces (depending on the geometry of the contacts) and a parabolic pressure distribution with the maximum pressure at the centre of the contact (Lampman 1996).

Because of the sensitivity of contact fatigue life to contact stress, reduction of contact stress can significantly improve bearing life. Of course, accurate estimation of the actual operating contact stress is important. Contact stress can be reduced by spreading out the area contact with a soft solid thin film applied to the surfaces. Nonetheless, hard coatings have been used to improve the fatigue life of bearing steels (Erdemir 1992).

### 3.1 General

The experimental program involved laboratory testing of three rollers and six roller path plates under cyclic loading. Rollers were 838 mm (33 in.) in diameter with an 89 mm ( $3\frac{1}{2}$  in.) flange thickness and a crown radius of 914 mm (36 in.). One of the rollers ( $R_1$ ) was made of gray cast iron. The material in Roller  $R_2$  was AISI 1060 high carbon steel without heat treatment, whereas the material in Roller  $R_3$  was AISI 1080 heat treated high carbon steel. Two of the rollers,  $R_1$  and  $R_2$ , were obtained from the Kelsey Hydro Generating Station located on Nelson River, Manitoba, and they were never placed in service. The 3<sup>rd</sup> Roller,  $R_3$ , was specially ordered, manufactured, and shipped from the United States specifically for this research project.

Figure 3.1 shows the nomenclature adopted for various parts of the roller. Rollers  $R_1$  and  $R_3$  are shown in Fig. 3.2. The 241 mm ( $9\frac{1}{2}$  in.) deep hub of the rollers was designed to accommodate a 152 mm (6 in.) diameter solid steel shaft. A *Gatke* circular fiber bushing was sandwiched at the interface between the shaft and the roller hub. Around the circumference of the cast iron Roller  $R_1$ , located in the roller web approximately 270 mm ( $10\frac{5}{8}$  in.) from the centre of the hub, there were three 63.5 mm ( $2\frac{1}{2}$  in.) diameter holes spaced at  $120^\circ$  apart, as shown in Figs. 3.1 and 3.2. These holes were cored through the original casting and were used to facilitate handling of the roller. The other two Rollers,  $R_2$  and  $R_3$ , used in this research study were without handling holes.

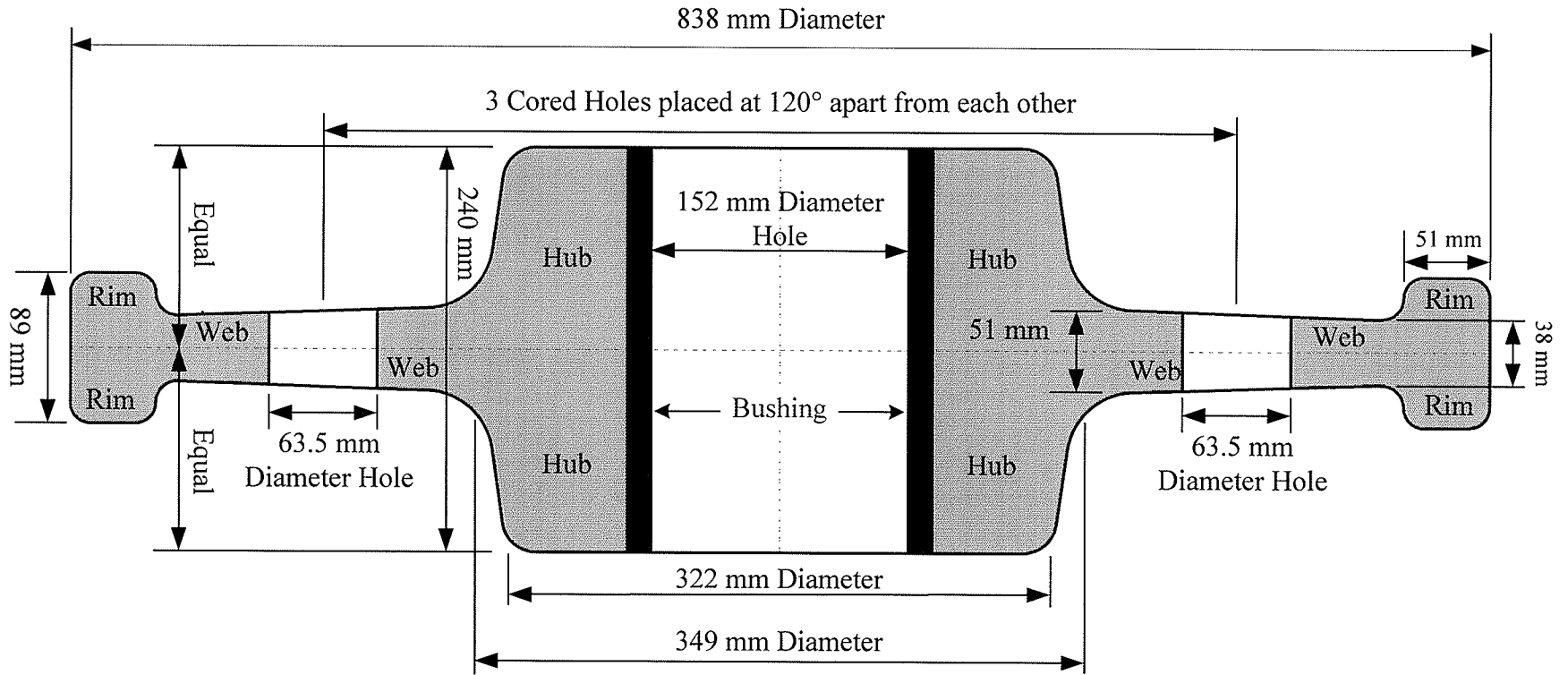


Fig. 3.1 A section through centre line of the Cast Iron Roller R<sub>1</sub> showing nomenclature and dimensions

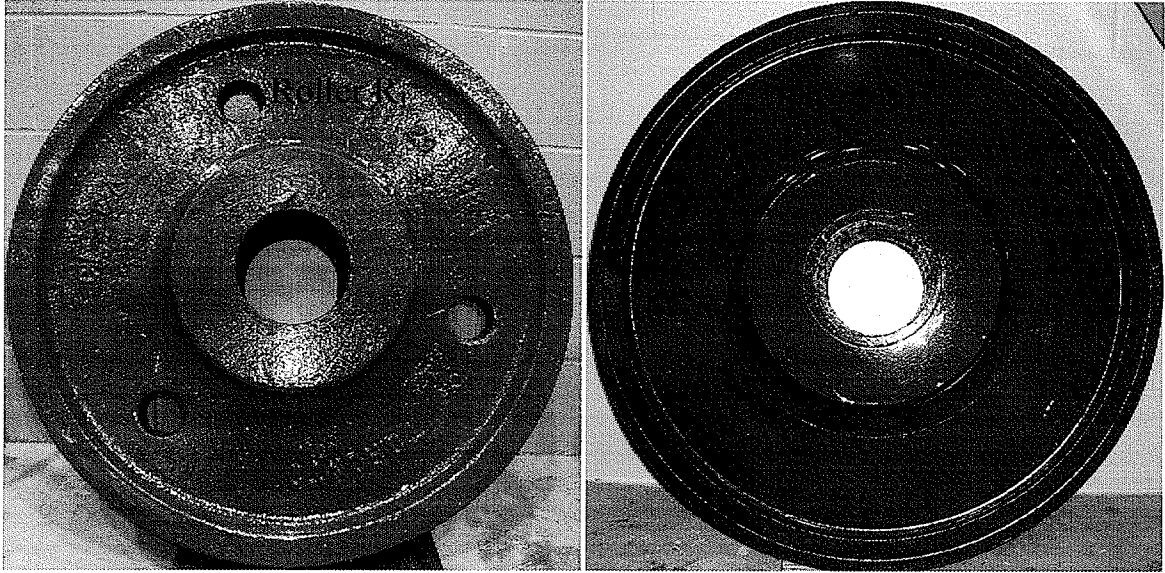


Fig. 3.2 Cast Iron Roller  $R_1$  and heat treated high carbon steel Roller  $R_3$



Fig. 3.3 A typical roller path plate

Cast iron Roller  $R_1$  had a flange width of 51 mm (2 in.), whereas, Rollers  $R_2$  and  $R_3$  had a flange (rim) width of 66.5 mm ( $2\frac{5}{8}$  in.). Web thickness of all rollers varied from 38 mm ( $1\frac{1}{2}$  in.) at the neck of rim to 51 mm (2 in.) at the neck of hub. Six rectangular steel Plates,  $P_1$  through  $P_6$ , measuring  $381 \times 178$  mm ( $15 \times 7$  in.) with a thickness of 51 mm (2

in.) were used as roller path plates in this research program as typically shown in Fig. 3.3. Plates P<sub>1</sub> and P<sub>2</sub> were AISI 1050 medium carbon steel without heat treatment, whereas, Plates P<sub>3</sub> through P<sub>6</sub> were SS 410 heat treated stainless steel.

### **3.2 Brinell Hardness Tests**

Prior to testing the rollers and the roller path plates under cyclic loading, a series of surface hardness measurements was performed using Proceq *EQUITOP* electronic hardness testing equipment. The surfaces of all specimens were cleaned and ground using a hand-grinder electric machine and sand paper. Readings were recorded in the L-scale and then converted into BHN using tables provided with the electronic equipment. Hardness measurements on the rollers were taken on the rolling surface, on the rim, on the web, and on the hub surfaces. Measurements on the rim surface were taken at 6.35 mm (¼ in.) intervals starting at the rolling surface of the roller and proceeding radially 51 to 76 mm (2 to 3 in.) toward the center of the roller. Twenty readings were taken on each roller path plate. The results are given in Table 3.3 and in Chapter 4.

### **3.3 Test Set-up**

A unique test set up was designed and constructed for this special fatigue type of testing. Figs. 3.4 through 3.8 show details of the test set-up along with the dimensions, whereas, Fig. 3.9 shows overall views of the test set-up from different angles. Detailed diagrams of various components of the test set-up are shown in Figs. 3.1 through 3.25. A brief description of the various components of the test setup is given in the following pages.

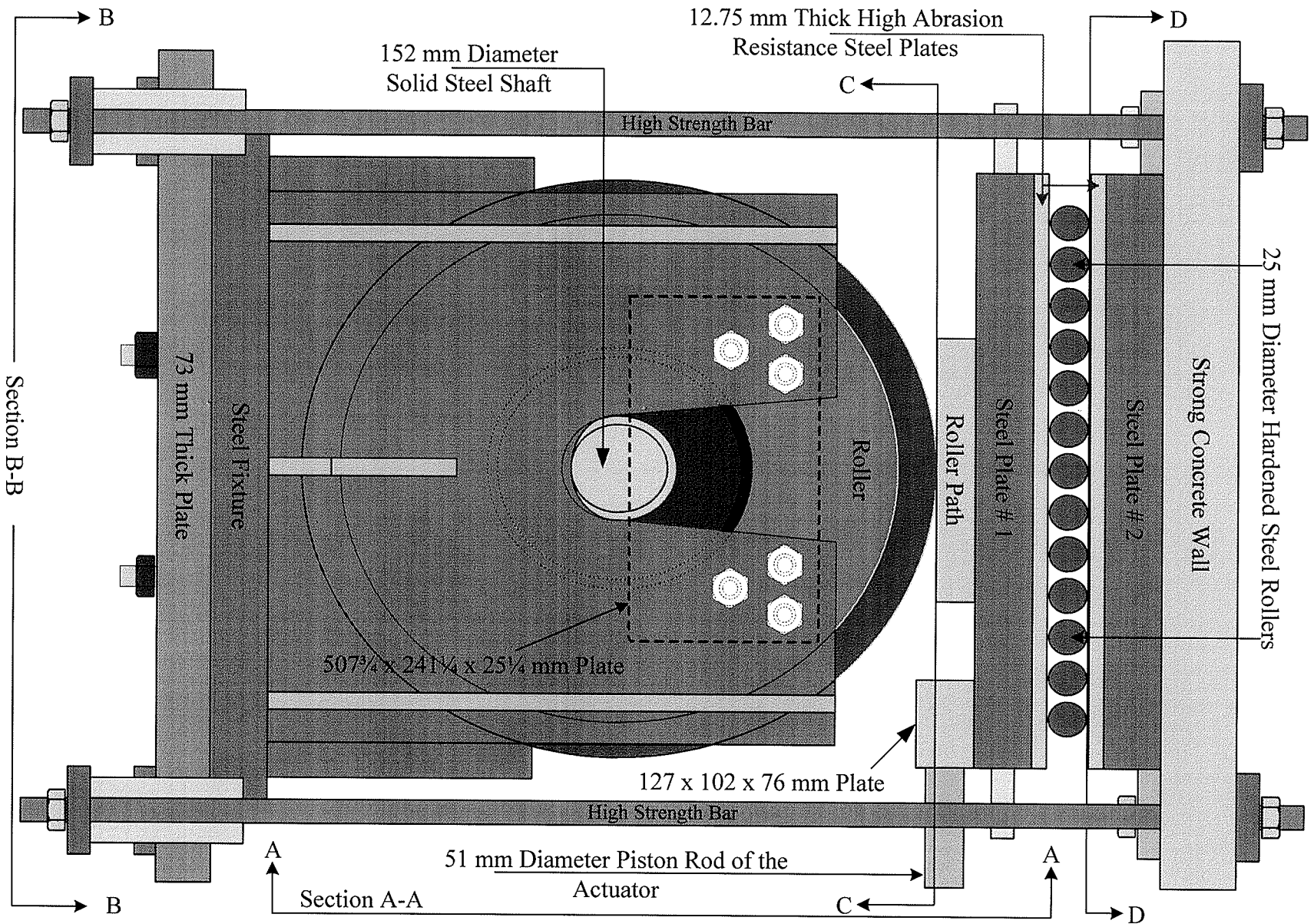


Fig. 3.4 Top view of the test set-up

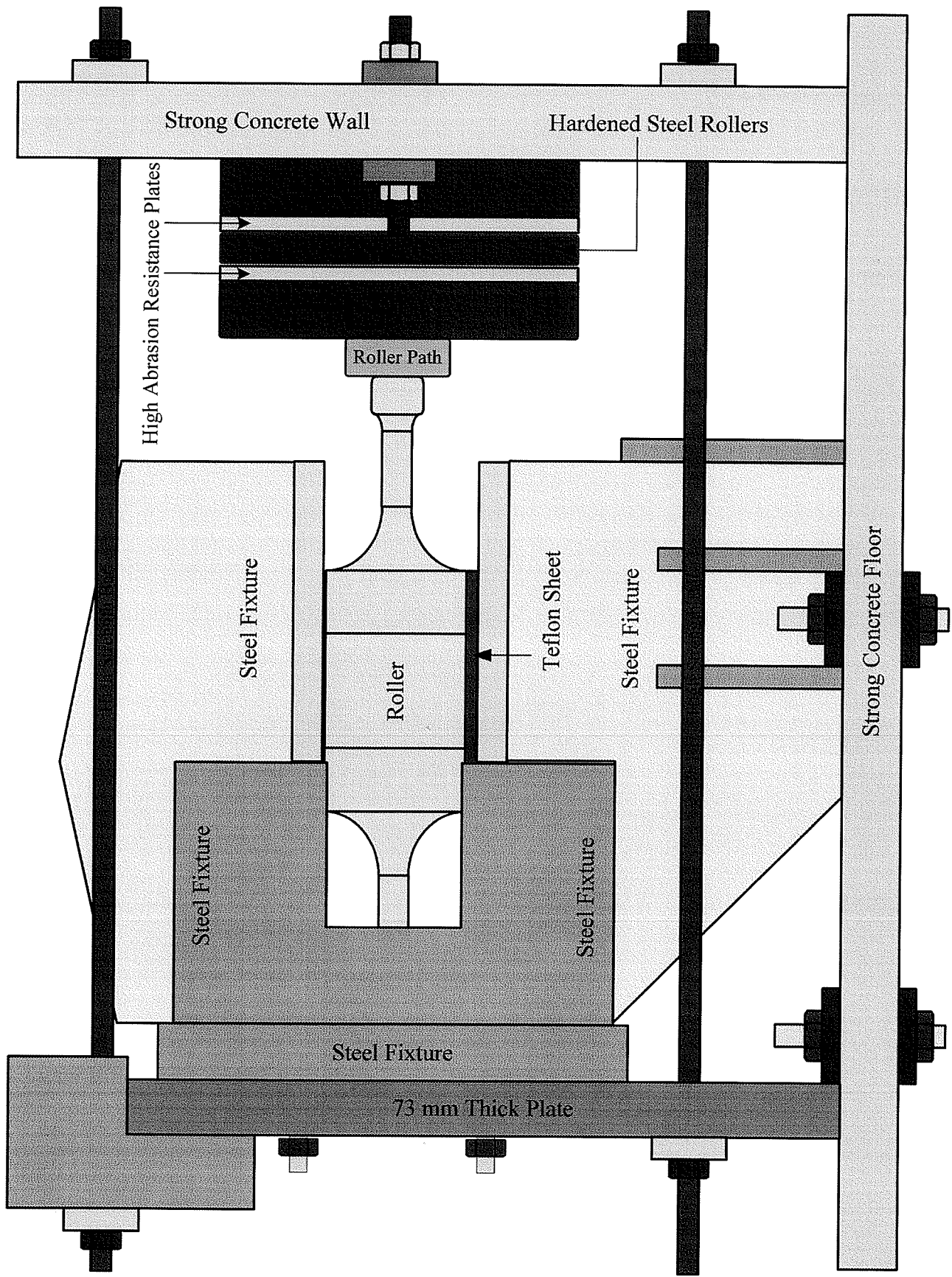


Fig. 3.5 Cross section of the test set-up (section A-A)

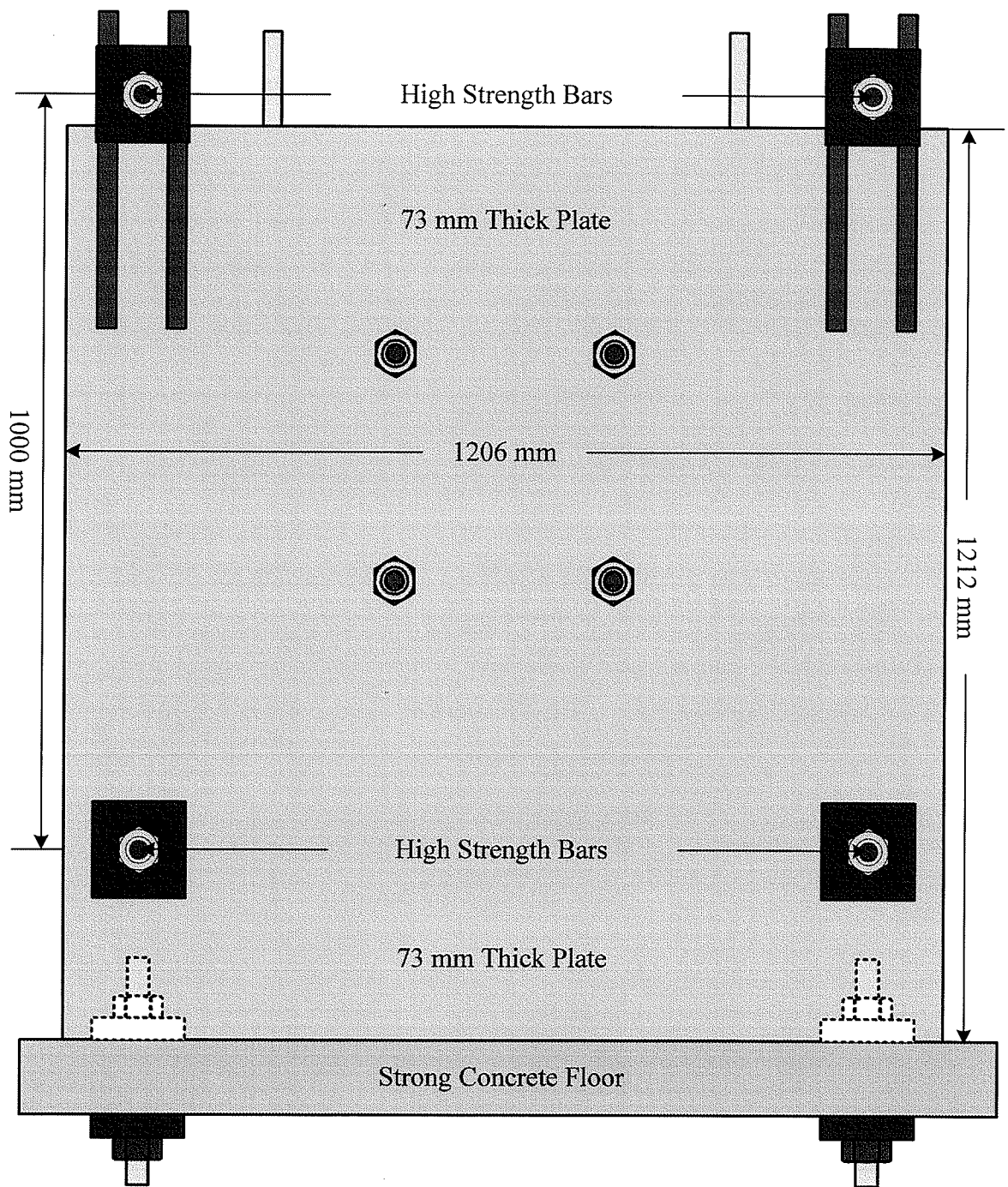


Fig. 3.6 Large base plate of steel fixture (section B-B)

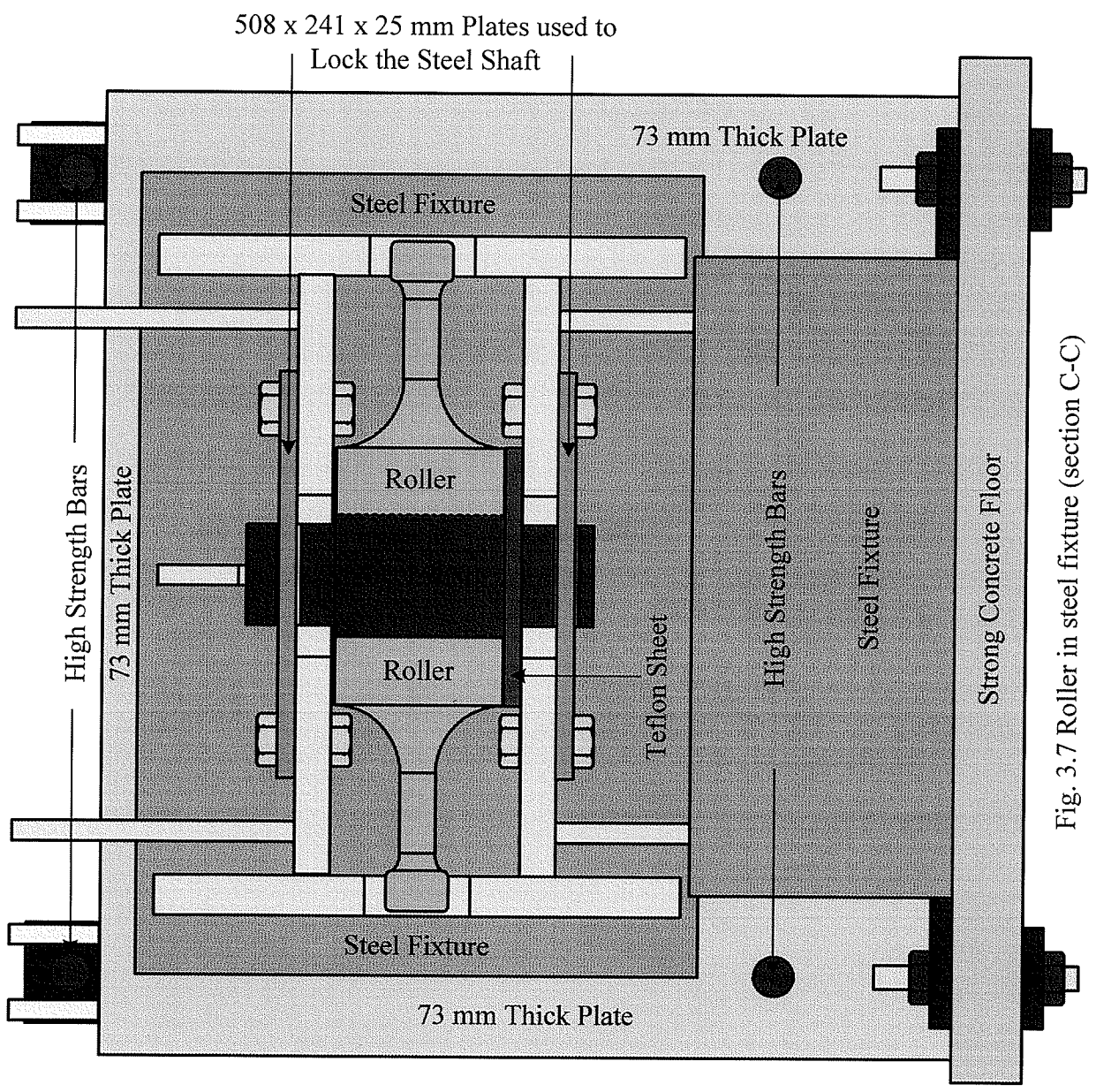
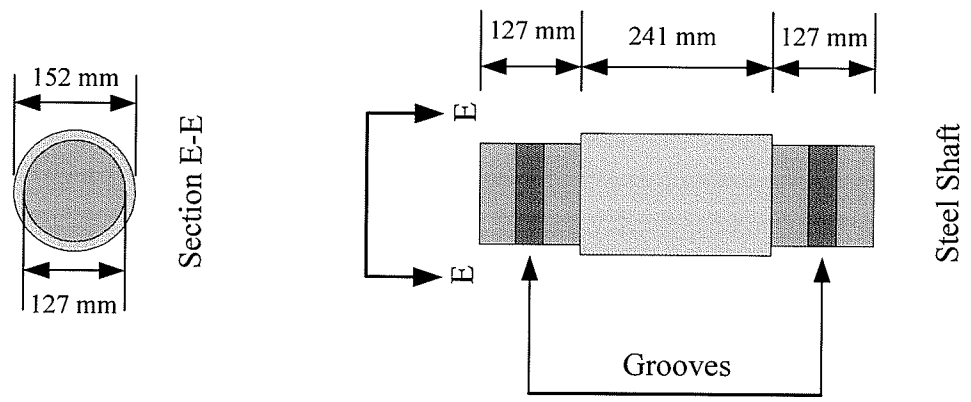


Fig. 3.7 Roller in steel fixture (section C-C)

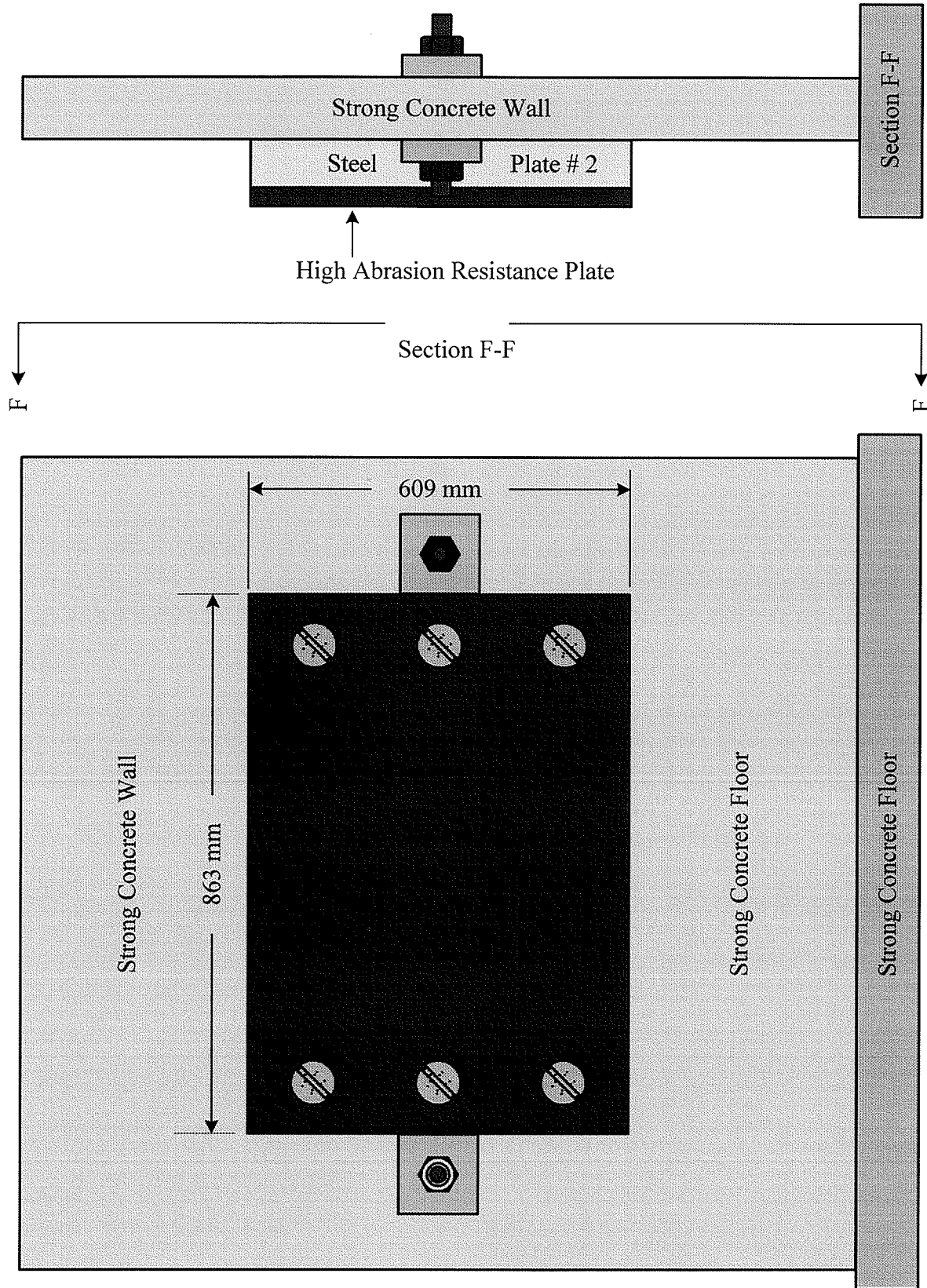


Fig. 3.8 Steel Plate 2 attached with the strong concrete wall (section D-D)

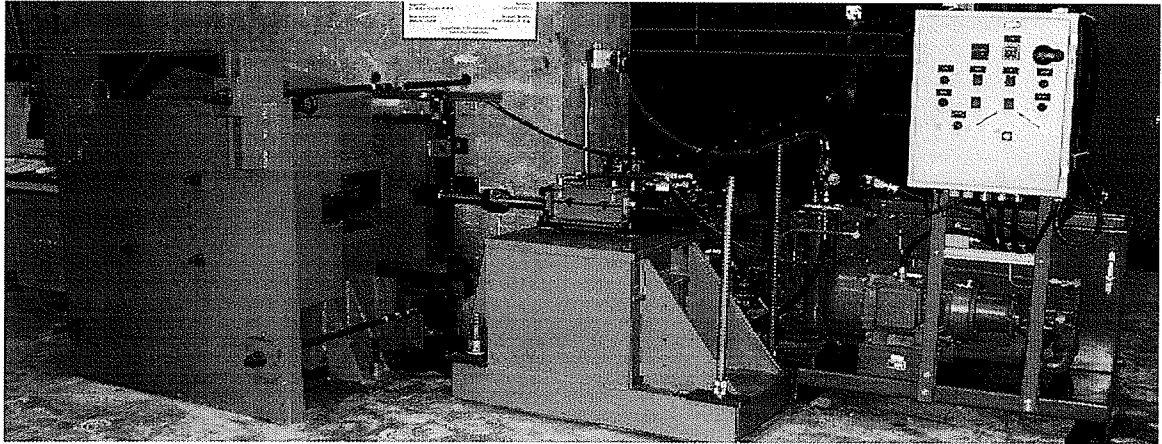


Fig. 3.9a Front view of the test set-up

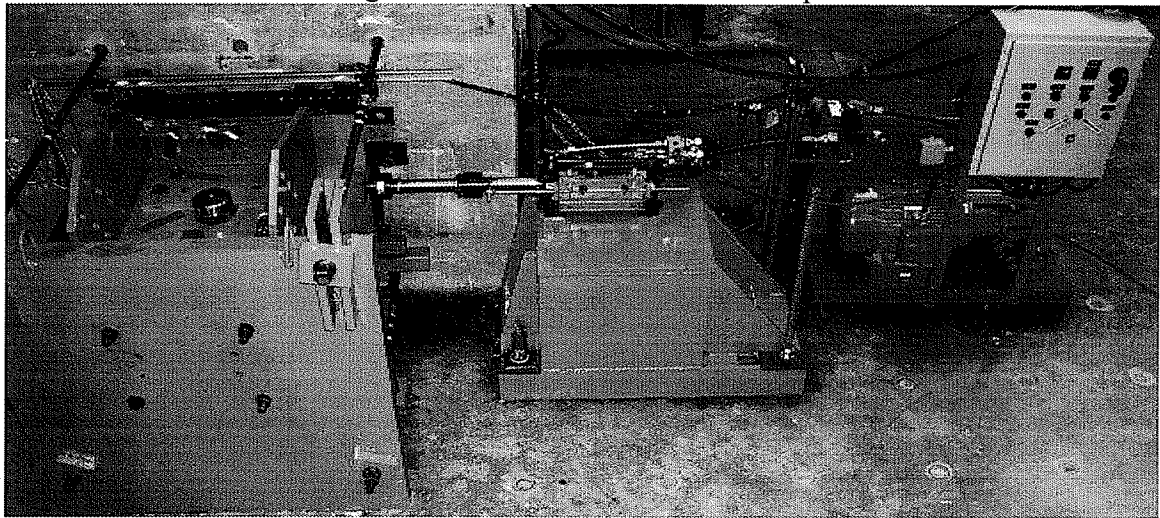


Fig. 3.9b Aerial view (front portion) of the test set-up

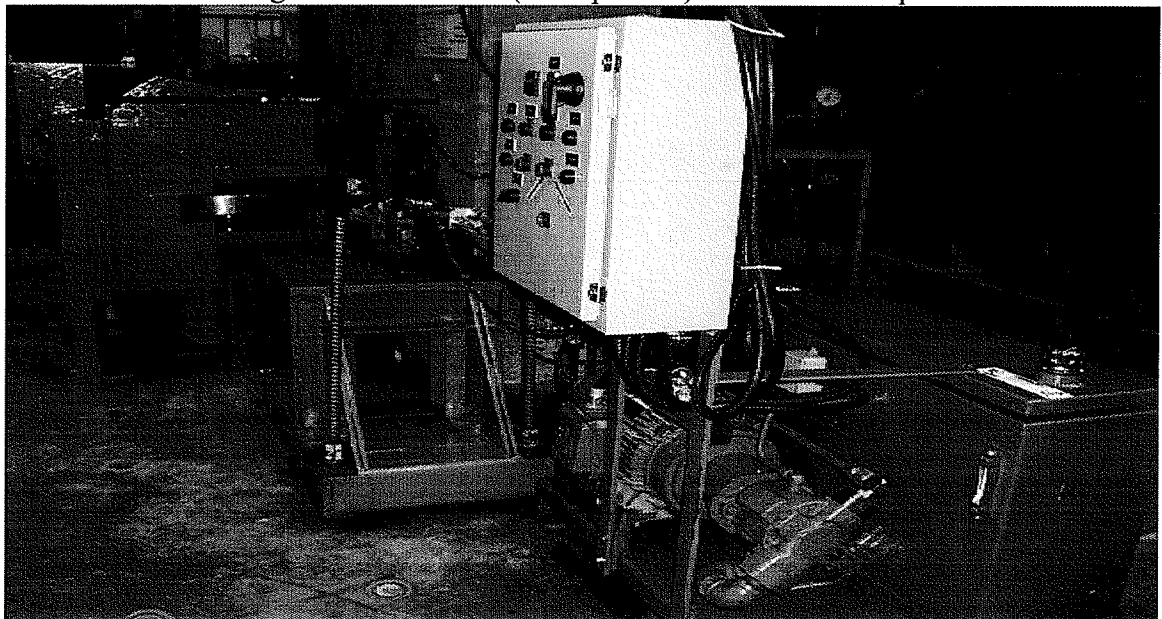


Fig. 3.9c Side view of the test set-up

### 3.3.1 Pump

A special pump was required for this test setup as shown in Fig. 3.9. The pump consisted of the following components: a motor, control shift valves, power panel switchboard, two hydraulic hoses, oil tank, oil filter, water hoses, oil cooling chamber, and a heavy-duty power cable. Two 4 m (13 ft.) long hydraulic hoses were connected to the control shift valve, which was wired to the control power-panel switchboard. The hydraulic pressure generated by the pump was transferred to a hydraulic actuator through two hydraulic hoses, one for forward motion of the actuator piston rod and other for backward motion of the actuator piston rod. The 15 kW (20 horsepower) motor of the pump was designed to generate a maximum pressure of 17 MPa (2½ ksi). This pressure value corresponded to a lateral load of 184.6 kN (41½ kips) on the hydraulic actuator. The pump was fully automatic with automatic shut-off switches and warning red lights whenever the temperature of the oil or the hydraulic oil level reached a critical level. An hour meter was also installed on the pump to monitor the running time on the motor. A digital meter was installed on the pump to monitor the number of cycles for the hydraulic actuator to deliver lateral load on the roller. A maximum of 100,000 cycles could be programmed in the digital meter. After it reached the desired number of cycles, the whole system automatically shut off. The oil in the 113.5 liter (30 US gallon) capacity tank was circulated through the motor, the control shift valve, the hydraulic hose (forward), the hydraulic hose (backward), the cooling chamber, the oil filter (enclosed in steel case), and back to the oil tank. The oil was continuously circulated in the hydraulic system and it was kept cool through the oil-cooling chamber, which was connected to two 12 m (39½ ft.) long water lines, one for cold water in and other for hot water out.

### 3.3.2 Hydraulic Actuator

A hydraulic actuator was designed and ordered for this special cyclic testing apparatus, as shown in Fig. 3.10. The purpose of the hydraulic actuator was to deliver a lateral cyclic load through a 51 mm (2 in.) diameter solid steel piston rod. Two hydraulic hoses, which were attached to the control shift valve of the pump, were connected to the hydraulic actuator, one at each far end of the actuator. The one, which was attached to the back of the actuator, was used for forward motion of the piston rod, and other one, which was attached to the front of the actuator, was used for backward motion of the piston rod. Two universal joints were used in the 51 mm (2 in.) diameter solid steel piston rod, one in the middle and other at the far end of the piston rod, as shown in Fig. 3.10. The purpose of these universal joints was to accommodate any kind of miss-alignment during cyclic loading. The overall length of the piston rod including the two universal joints was approximately 635 mm (25 in.).

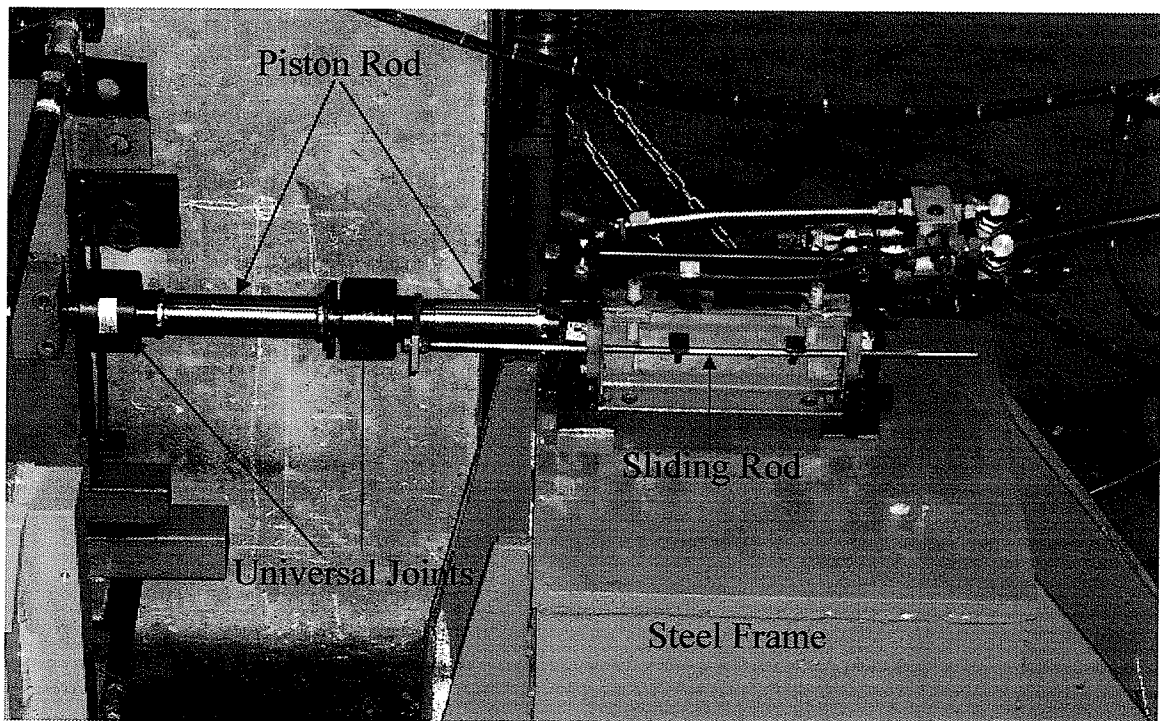


Fig. 3.10 Hydraulic actuator

The universal joint, which was attached at the far end of the 51 mm (2 in.) diameter solid steel piston rod of the actuator, was attached to  $127 \times 101.5 \times 76$  mm ( $5 \times 4 \times 3$  in.) solid steel plate through threads, as shown in Fig. 3.11. This solid plate was attached to  $863 \times 609 \times 76$  mm ( $34 \times 24 \times 3$  in.) solid steel plate (Plate 1) through welding and four countersunk steel bolts in order to avoid any kind of failure during cyclic loading. In order for the actuator to deliver the cyclic loading continuously and without interruptions, two small magnetic sensors, shown in Fig. 3.12, were used. These magnetic sensors were installed on a small steel frame mounted on the hydraulic actuator and wired to the power-panel switchboard of the pump.

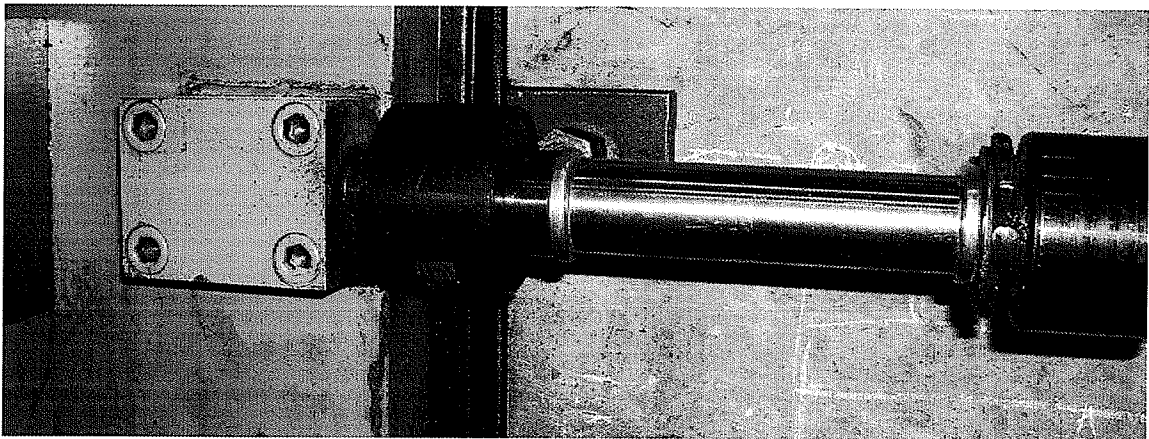


Fig. 3.11 Universal joints provided in the piston rod of the hydraulic actuator

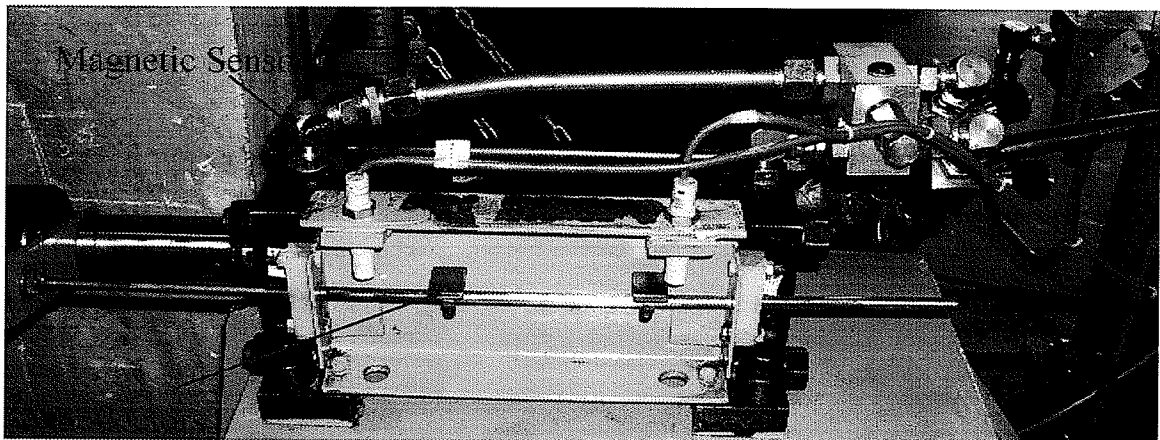


Fig. 3.12 Small steel frame attached with the hydraulic actuator

Two small reflectors, consisting of 25.4× 25.4 mm (1 × 1 in.) steel plate elements were attached to a long sliding rod (Fig. 3.12). The desired stroke length of the piston rod of the actuator was achieved by adjusting the spacing of these reflectors. As the piston rod moved back and forth, the sliding rod also moved back and forth. Electronic signals from the magnetic sensors were reflected from the small square steel plates and were sent to the power panel switchboard of the pump, which controlled the shift valve of the pump. The automatic cyclic movement of the hydraulic actuator piston rod was controlled by electronic relays through two magnetic sensors installed on the actuator. These electronic relays were installed in the power panel switchboard of the pump. The life expectancy of these electronic relays was approximately half a million cycles. Hence, it was necessary to install an automatic shut-off system, in case the electronic relays failed to work during cyclic loading. For this purpose, two mechanical limit switches were placed in the traveling path of the loading plate (Plate 1), as shown in Fig. 3.13.

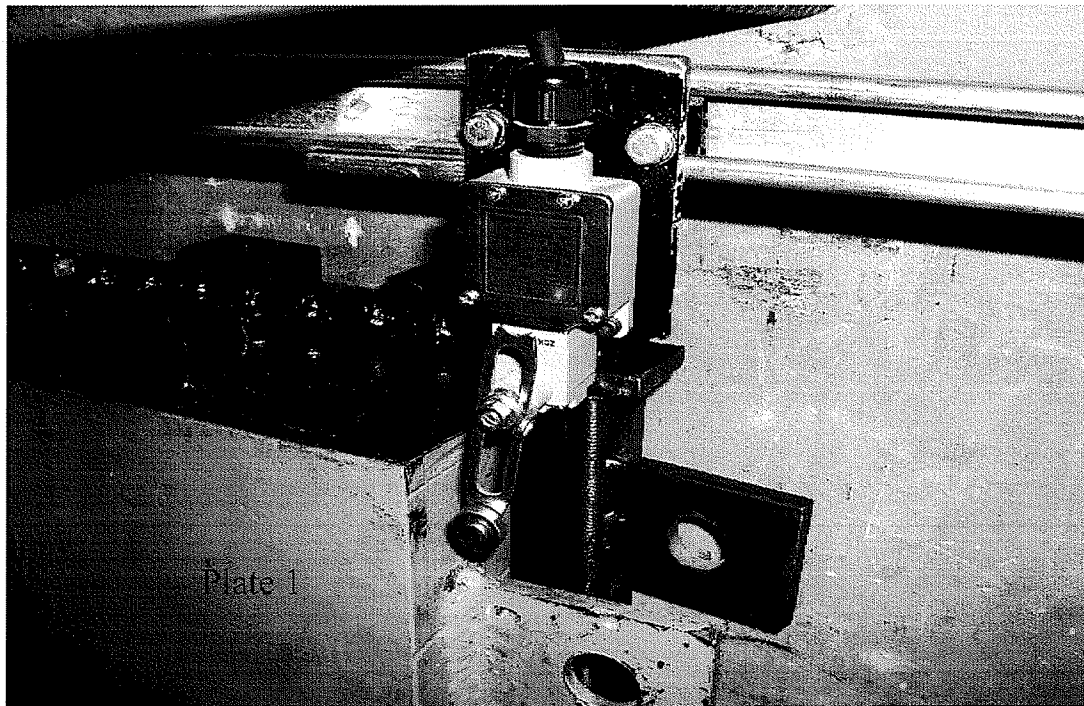


Fig. 3.13 Mechanical limit switch

These mechanical limit switches were wired with the power panel switchboard of the pump. Whenever the magnetic sensors or electronic relays failed to work and the piston rod of the hydraulic actuator tried to cross the prescribed stroke length, Plate 1 hit the lever arm of the mechanical limit switch and the whole system would be shut off. The hydraulic actuator was attached to a steel frame through four 19 mm ( $\frac{3}{4}$  in.) diameter steel bolts, as shown in Fig. 3.9. This steel frame (Figs. 3.9 and 3.10) was designed and fabricated to withstand dynamic cyclic reaction forces of the hydraulic actuator. The steel frame supporting the actuator was attached to the strong concrete floor of the Structural Engineering Laboratory using four 25.4 mm (1 in.) diameter steel bars (Figs. 3.9 and 3.14) which ran through the basement.



Fig. 3.14 Bars through the strong floor

### 3.3.3 Roller Path Plate

In order to support the roller path plate, two  $863 \times 609 \times 76$  mm ( $34 \times 24 \times 3$  in.) steel plates were used in this unique test set-up, as shown in Figs. 3.4, 3.5, 3.8 and 3.15. Plate 2 was permanently attached to the 609 mm (2 ft.) thick strong concrete wall of the

Structural Engineering Laboratory using two 25.4 mm (1 in.) diameter threaded steel rods. The other plate (Plate 1) was attached to the 51 mm (2 in.) diameter solid steel piston rod of the hydraulic actuator (Fig. 3.11). The roller path plates were attached to Plate 1 through four 19 mm ( $\frac{3}{4}$  in.) countersunk steel bolts, as shown in Fig. 3.15.

A series of high strength solid round bars (Fig. 3.16) was placed between steel Plates 1 and 2 to allow Plate 1 to roll freely back and forth. The bars were 25.4 mm (1 in.) in diameter and 609 mm (24 in.) long. They were heat-treated hardened steel bars with a BHN of 400. Twenty-four such bars were used in tandem. In order to avoid indentation of the rolling surfaces during cyclic loading, 12.7 mm ( $\frac{1}{2}$  in.) superior high abrasion resistance steel plates were attached to both steel Plate 1 and 2 using screws (Figs. 3.4, 3.5 and 3.8).

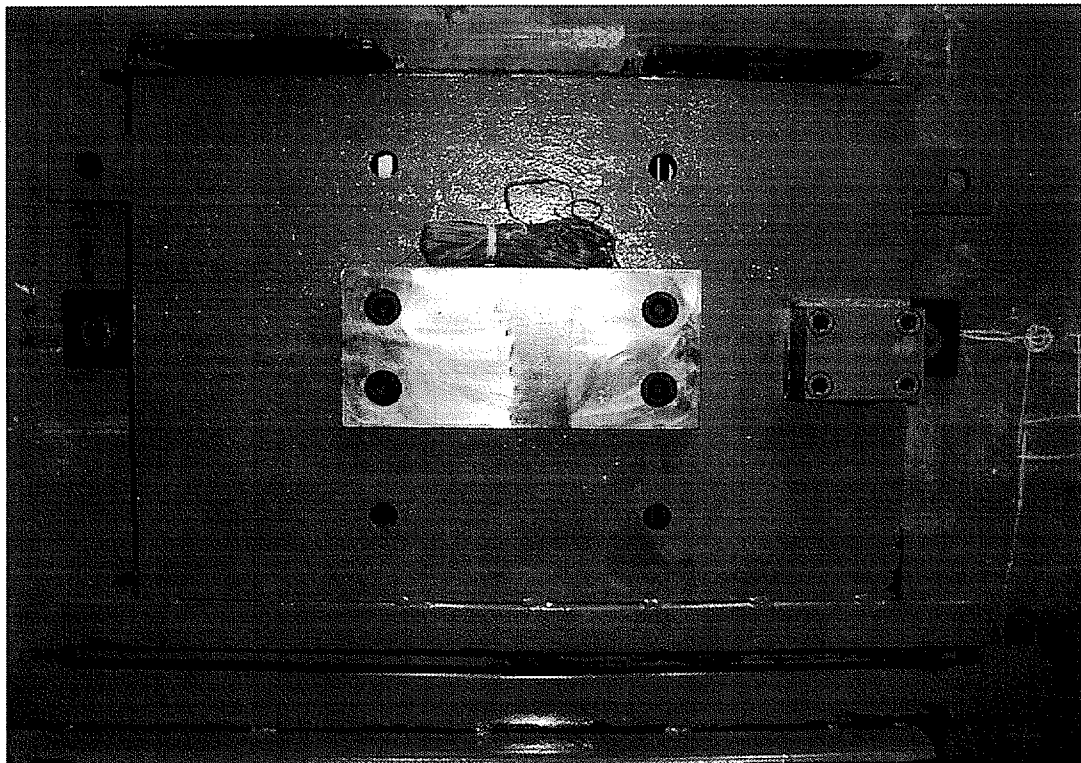


Fig. 3.15 Typical roller path plate attached with large supporting Plate 1

The yield and tensile strength of these high abrasion resistance steel plates were 1207 MPa (175 ksi) and 1310 MPa (190 ksi), respectively. The BHN was 400, which matched with the BHN number of hardened steel solid round bars.

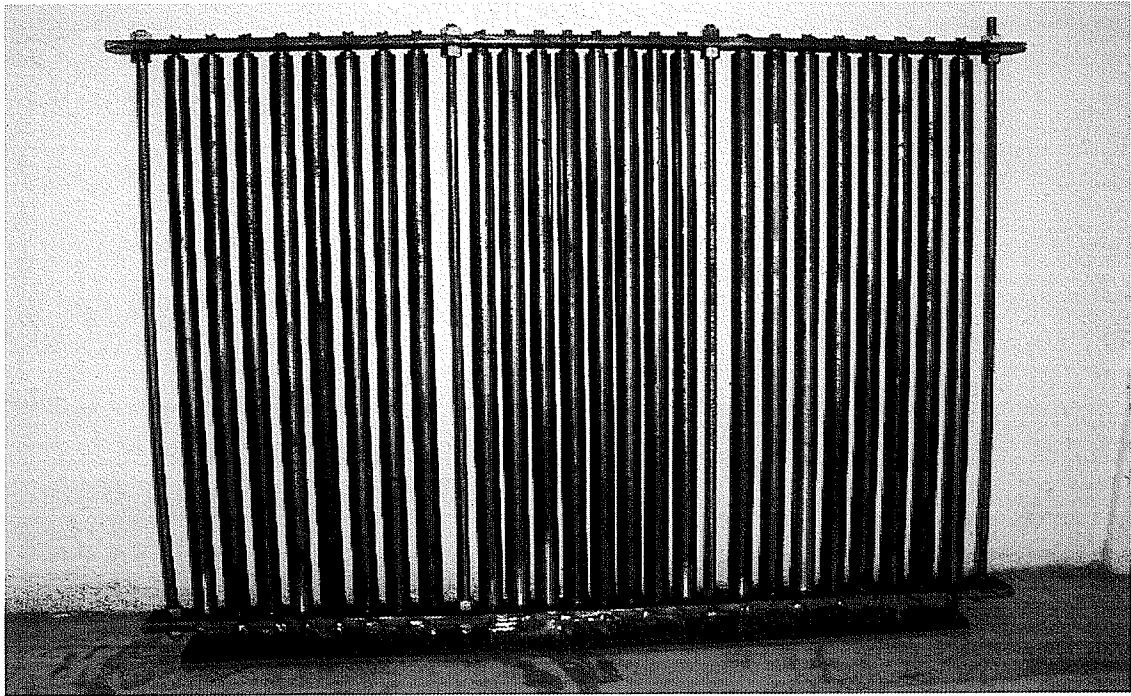


Fig. 3.16 High strength solid round bars

### 3.3.4 Rollers

The service radial compressive load on the rollers was applied through a unique steel fixture specially designed and constructed for this type of rollers. Details of the steel fixtures are shown in Figs. 3.4 through 3.7, and in Figs. 3.9 and 3.17. The steel fixture was built by welding together steel plates that varied in thickness from 25.4 mm to 76 mm (1 to 3 in.). The roller was placed in this steel fixture horizontally. A 12.7 mm ( $\frac{1}{2}$  in.) thick and 305 mm (12 in.) diameter circular Teflon sheet was placed beneath the roller in order to avoid friction between the roller and the steel fixture during cyclic testing, as shown in Figs. 3.5, 3.7, and 3.18.

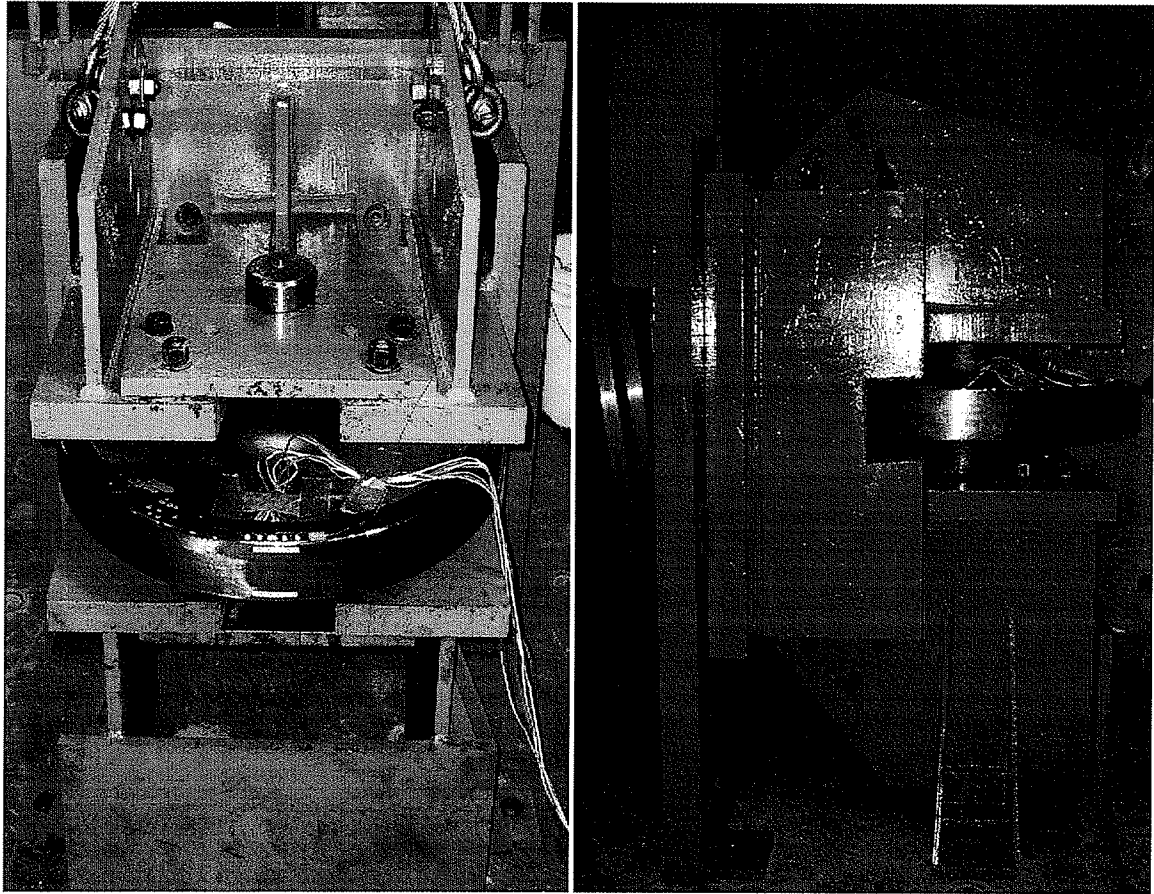


Fig. 3.17 Front and side view of the large steel fixture

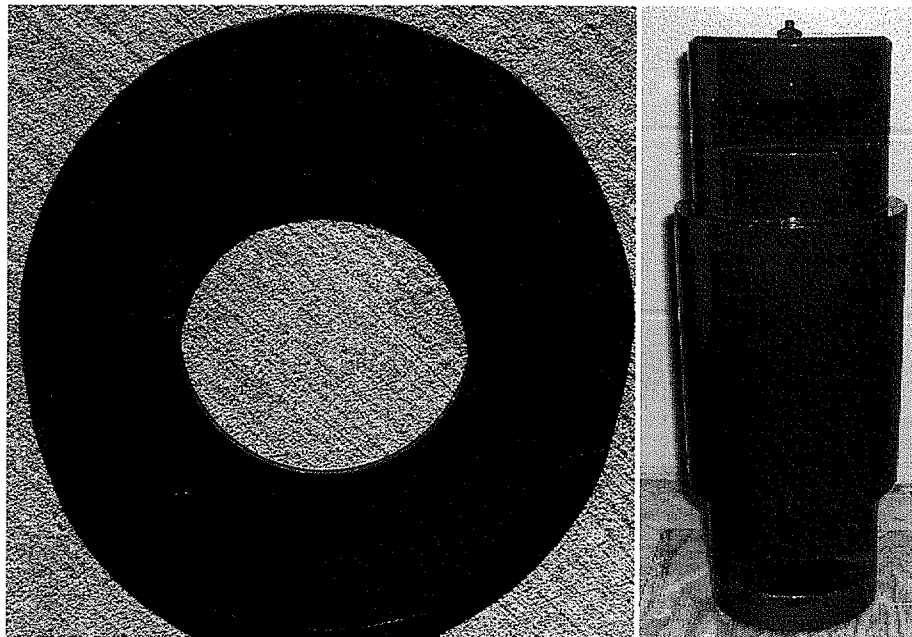


Fig. 3.18 Teflon plate and a solid steel shaft

A 152 mm (6 in.) diameter and 495 mm (19½ in.) long solid steel shaft was inserted through the steel fixture and the 152 mm (6 in.) diameter hole of the roller, as shown in Figs. 3.4, 3.7, 3.9, 3.17, and 3.18. A 25.4 mm (1 in.) wide groove was cut at the top and bottom of the shaft. The position of the shaft was fixed by inserting two 508 × 241 × 25.4 mm (20 × 9½ × 1 in.) steel plates into the shaft grooves and attaching these plates to the steel fixture through steel bolts, as shown in Figs. 3.4, 3.7, and 3.17. Hence, the shaft was completely locked into place and the roller could rotate freely. Before inserting the shaft into the roller, lubricating grease was applied to the inside roller hole and around the shaft in order to minimize the friction between the roller and the shaft during cyclic testing. After the roller was placed into the test fixture, the whole steel fixture was brought into contact with the roller path plate, as shown in Fig. 3.19. Arrangements were made to attach the steel fixture to the strong concrete floor at four places, one on each corner of the steel fixture, using four 25.4 mm (1 in.) diameter, 2 m (6½ ft.) long steel rods.

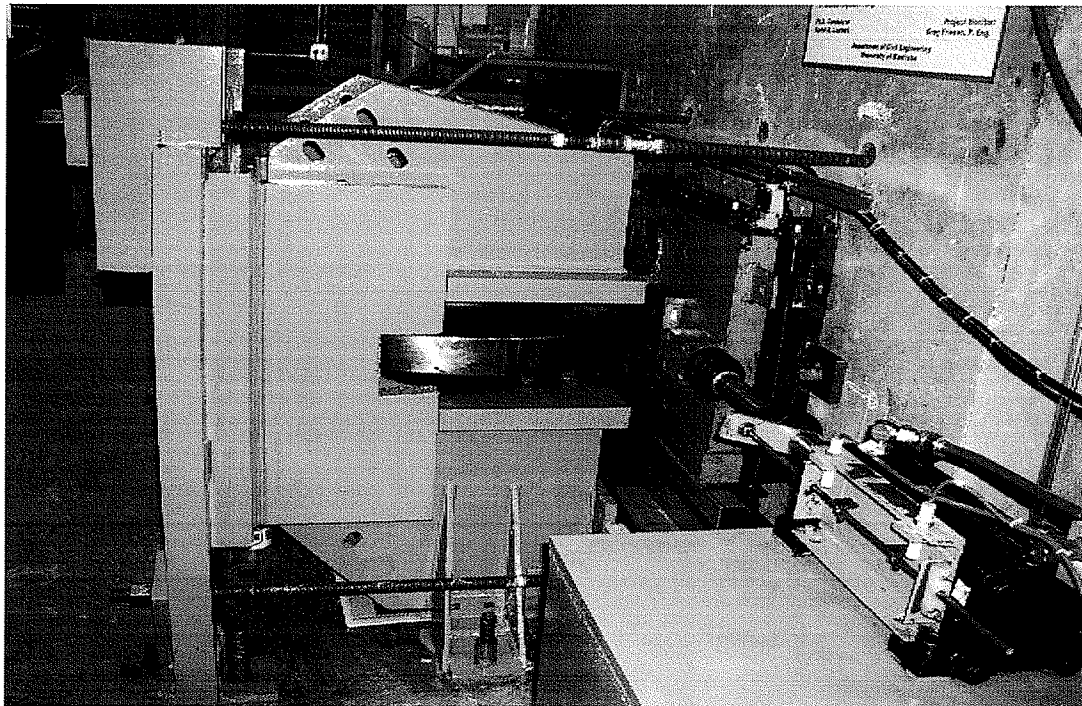


Fig. 3.19 Roller in contact with roller path plate

The service compressive radial load on the roller was applied by compressing the whole steel fixture against the roller path plate by pushing the test fixture through four high strength rods, which ran through the strong concrete wall and steel fixture. The high strength rods were already calibrated in order to monitor the strain values during cyclic testing. Four hydraulic jacks, as shown in Fig. 3.20, were used to pull the test fixture.

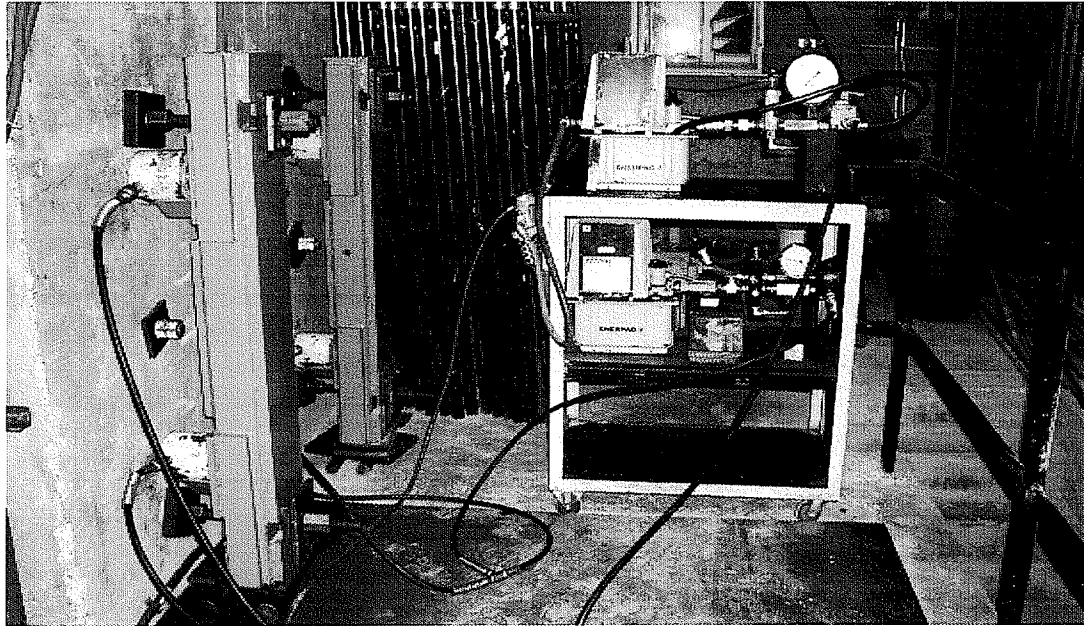


Fig. 3.20 Spreader steel beams and hydraulic jacking system

To ensure that all four rods were equally stressed, two spreader steel beams, shown in Fig. 3.20, were used. All jacks were pumped simultaneously and a uniform and constant static tensile load was induced in each high strength bar. The test fixture was fixed to the concrete floor after applying the required service radial load on the roller.

### 3.4 Instrumentation

Four 2.5 m (8¼ ft.) long high strength bars were used to apply the service compressive radial load on the rollers. The nominal thread diameter of these bars was 25.4 mm (1 in.)

and their ultimate strength was 567 kN (127½ kips). Each bar was instrumented at its mid length with a single-element unidirectional strain gauge (gauge 1 through 4) and was calibrated using a 267 kN (60 kips) capacity testing machine in order to monitor the radial load applied on the rollers. Strain gauges were installed on all rollers and roller path plates in order to monitor and record the strain values during cyclic loading. The strain gauges were installed as per the instructions of the manufacturer. Two configurations of strain gauges were used: single-element (unidirectional) and 3-element rosette stacked types. Three element rosette strain gauges consist of three single element (unidirectional) strain gauges placed at 0°, 45°, and 90°. The purpose of using rosette strain gauges was to determine the principal strain values at a particular point of interest. Seven single element unidirectional strain gauges were installed on each roller path Plate P<sub>1</sub> and P<sub>2</sub>, whereas, five single element unidirectional strain gauges were installed on each of roller path Plate P<sub>3</sub> through P<sub>6</sub>, as shown in Figs. 3.21 along with their nomenclature. Each roller was tested with two different roller path plates utilizing two opposite sides of the roller. A total of 20 strain gauges were installed on Roller R<sub>1</sub>, ten on each test side of the roller (Fig. 3.21), whereas, a total of 14 strain gauges were installed on each of Rollers R<sub>2</sub> and R<sub>3</sub>, seven on each test side of the roller, as shown in Fig. 3.21.

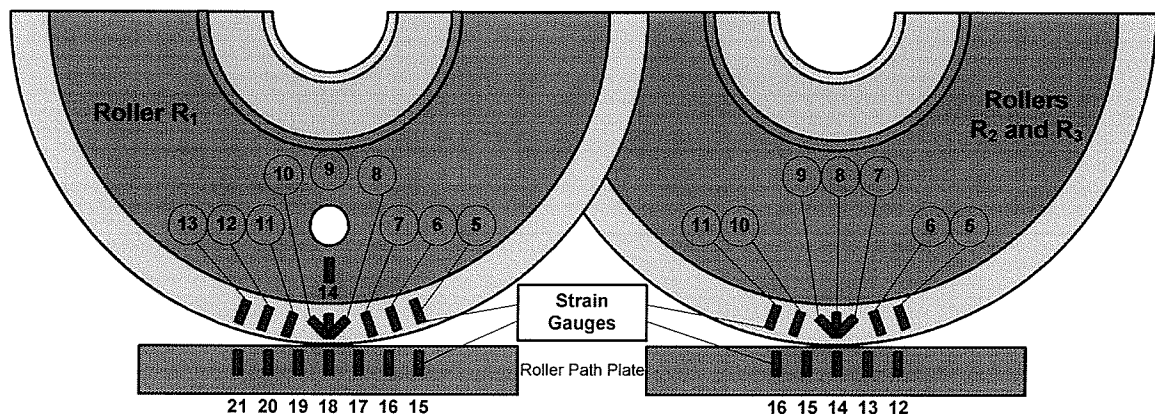


Fig. 3.21 Typical strain gauge layout and nomenclature

A rosette three-element strain gauge was installed on each test side of all rollers. All strain gauge wires were connected to a data acquisition system and a Pentium III computer in order to record the strain values during cyclic testing, as shown in Fig. 3.22.

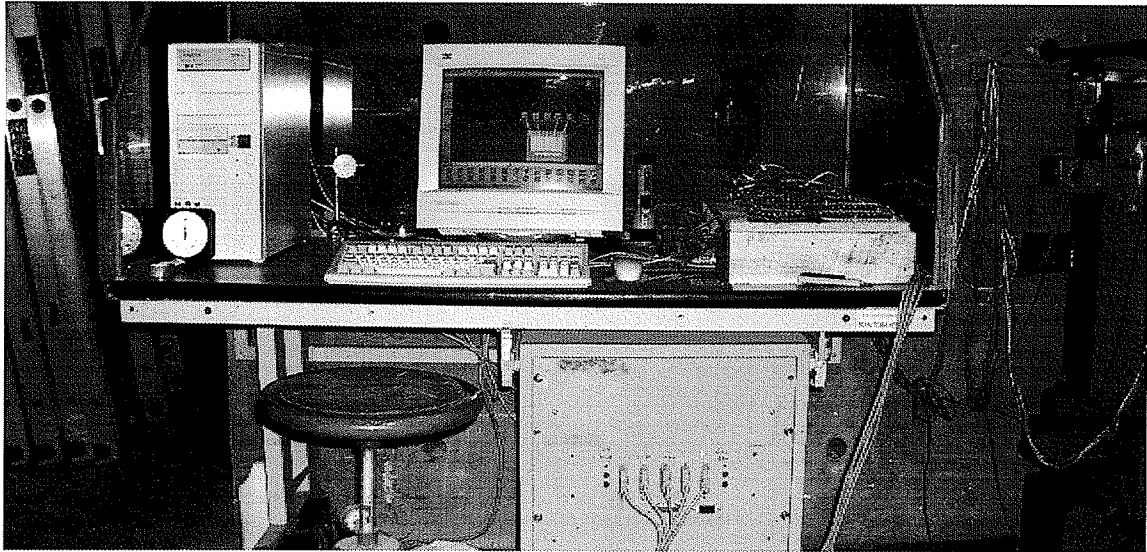


Fig. 3.22 Data acquisition system and a Pentium III computer

Due to friction between the roller and the shaft during a cyclic testing, heat was generated at the interface of the roller bushing and the shaft and this heat was transmitted throughout the roller. In order to monitor the temperature of the roller surface, which could affect the strain gauges, a thermocouple, as shown in Fig. 3.23, was installed at the rim surface of the roller where strain gauges were installed. The thermocouple was wired to a digital thermometer, Fig. 3.24, and daily temperature readings were recorded and corrections were applied to the strain gauge values, according to the manufacturer's recommendations. A cooling fan was also installed to lower surface temperature.

### 3.5 Testing Procedure

The rollers were tested at two opposite locations labeled as side "A" and side "B". For each cyclic test, a roller was in contact with the roller path plate on one side only. Roller

R<sub>1</sub> was tested to a million cycles on side A (Test R<sub>1A</sub>) and 818,726 cycles on side B (Test R<sub>1B</sub>) with roller path Plates P<sub>1</sub> and P<sub>2</sub>, respectively. The test was continuous and uninterrupted during this trend.

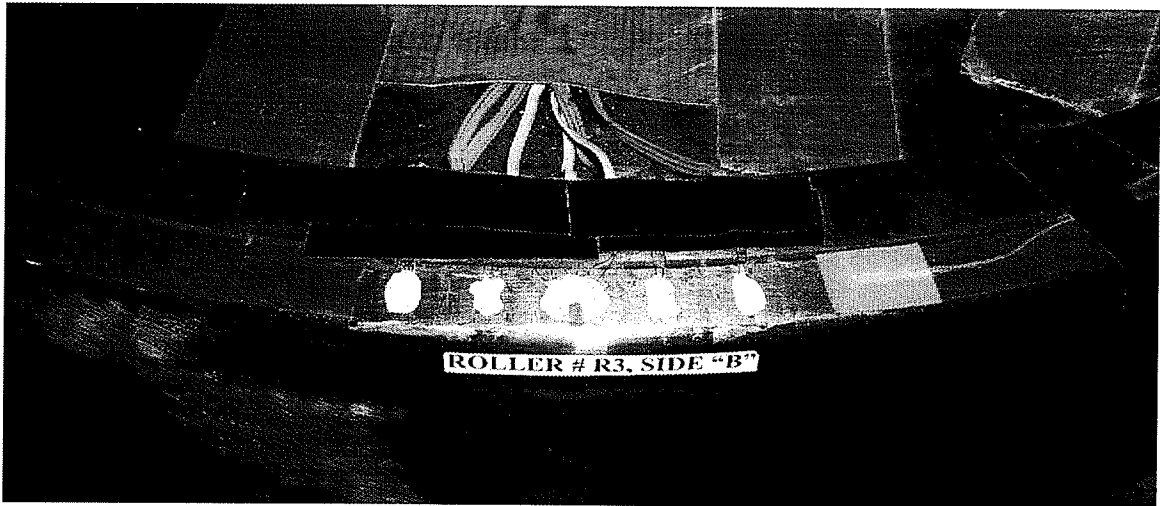


Fig. 3.23 Thermocouple on rim surface where strain gauges were installed

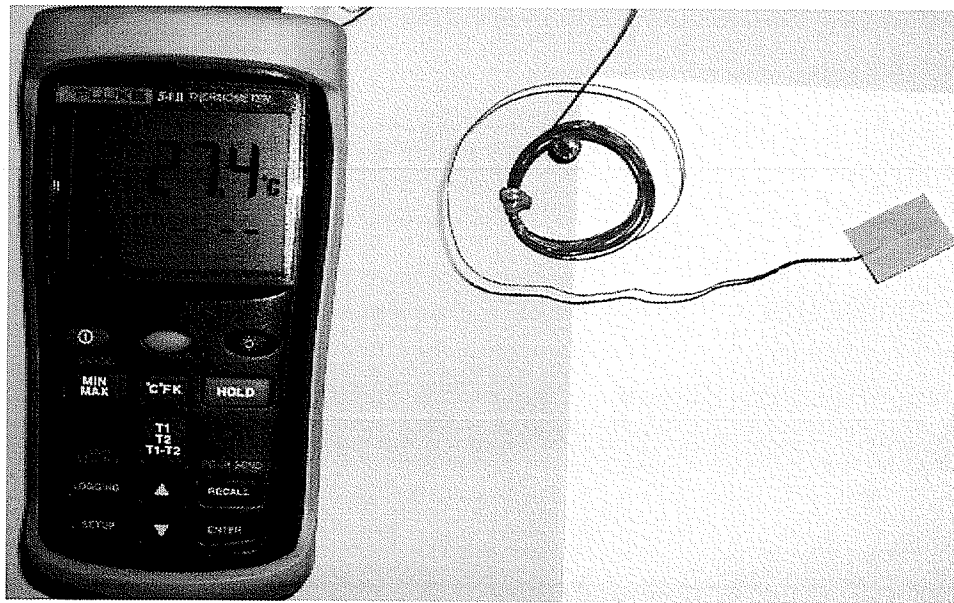


Fig. 3.24 Digital thermometer and a thermocouple

After completing each test, the test setup was dismantled and indentation profiles in the roller path plates were measured. Photographs were taken for all specimens before and after testing. Roller R<sub>2</sub> was tested continuously to 220,000 cycles on side A (Test R<sub>2A</sub>)

and 200,000 cycles on side B (Test R<sub>2B</sub>) with roller path Plates P<sub>3</sub> and P<sub>4</sub>, respectively. Roller R<sub>3</sub> was tested for 200,000 cycles at side A with roller path Plate P<sub>5</sub> (Test R<sub>3A1</sub>). After completing 200,000 cycles, the test setup was dismantled and indentation profiles in the roller path Plate P<sub>5</sub> were measured. After this test, Roller R<sub>3</sub> was re-loaded at the same location side A along with same roller path Plate P<sub>5</sub> and was re-tested for an additional 200,000 cycles (Test R<sub>3A2</sub>). A similar procedure was used to test Side B of the same Roller R<sub>3</sub> with roller path Plate P<sub>6</sub> up to 200,000 cycles (Test R<sub>3B1</sub>) and up to an additional 200,000 cycles (Test R<sub>3B2</sub>).

### **3.6 Frequency of the Cyclic Testing**

Roller R<sub>1</sub> was rolled back and forth on roller path Plates P<sub>1</sub> and P<sub>2</sub> for a total circumferential distance of 75 mm, or 37.5 mm from either side of the central strain gauge 9 on Roller R<sub>1</sub> and central strain gauge 18 on roller path Plates P<sub>1</sub> and P<sub>2</sub> shown in Fig. 3.21. The frequency of the cyclic testing for Roller R<sub>1</sub> was set as 3 sec. per cycle (0.33 Hz) for side A and 2.2 sec. per cycle (0.45 Hz) for side B. Thus, one cycle consisted of a total travel of 150 mm with a speed of 50 mm/sec on side A and 68.2 mm/sec on side B. The Rollers R<sub>2</sub> and R<sub>3</sub> were rolled back and forth on roller path plates for a total circumferential distance of 50 mm or 25 mm from either side of the central strain gauge 8 on Rollers R<sub>2</sub> and R<sub>3</sub> and central strain gauge 14 on the roller path plates. The frequency of the cyclic testing and the speed for all rollers are listed in Table 3.1.

### **3.7 Indentation Measurement**

At the end of each cyclic test, the test-setup was dismantled and indentation measurements were taken for each roller path plate using the set-up shown in Fig. 3.25. A

dial gauge was used to measure the indentations and map the profile of the contact area. The set-up used consisted of a steel base that could be moved in two orthogonal horizontal directions. The roller path plate was placed securely on top of the steel base plate. The complete testing area of the roller path plate was traversed by moving the base plate in the two orthogonal horizontal directions and the maximum deflection/indentation was recorded for each roller path plate.

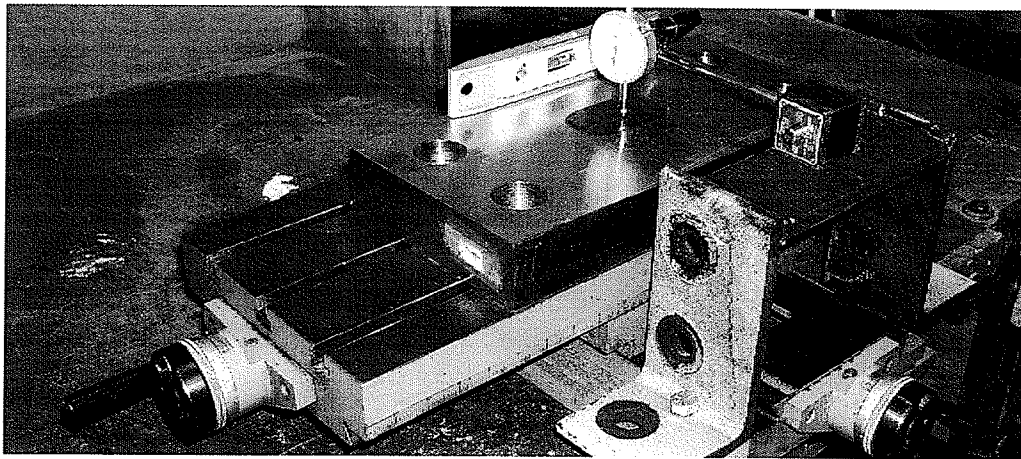


Fig. 3.25 Indentation depth test set-up

Table 3.1 Stroke length, frequency and speed for rollers

Test	Plate	Stroke mm	Cycle Time sec/cycle	Frequency Hz	Roller Speed mm/sec
R <sub>1A</sub>	P <sub>1</sub>	75	3.0	0.33	50.00
R <sub>1B</sub>	P <sub>2</sub>	75	2.2	0.45	68.20
R <sub>2A</sub>	P <sub>3</sub>	50	2.1	0.48	47.62
R <sub>2B</sub>	P <sub>4</sub>	50	2.4	0.42	41.67
R <sub>3A1</sub>	P <sub>5</sub>	50	2.4	0.42	41.67
R <sub>3A2</sub>	P <sub>5</sub>	50	2.9	0.34	34.48
R <sub>3B1</sub>	P <sub>6</sub>	50	2.4	0.42	41.67
R <sub>3B2</sub>	P <sub>6</sub>	50	2.5	0.40	40.00

### 3.8 Scanning Electron Microscope

In order to observe the extent of damage under cyclic testing, all tested contact areas of rollers and roller path plates were examined using the electron microscope (SEM) at the Materials Testing Laboratory in Mechanical Engineering Department, University of Manitoba shown in Fig.3.26.

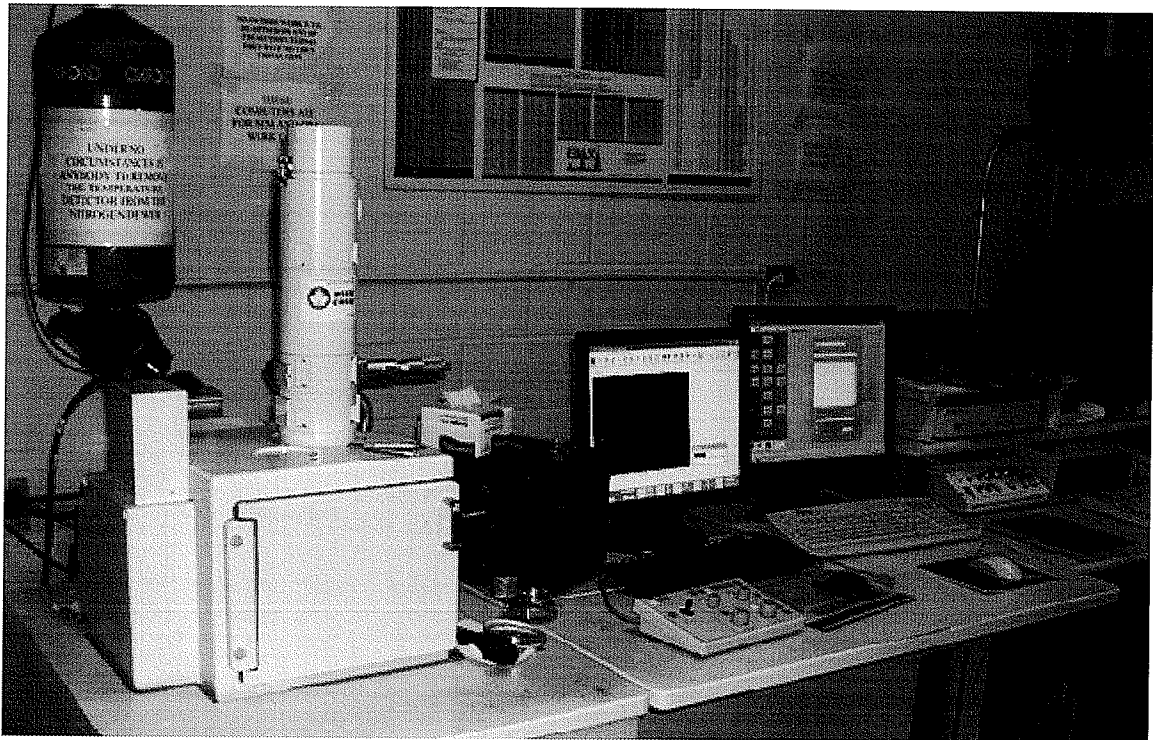


Fig. 3.26 Scanning Electron Microscope

Samples were extracted from both tested and non-tested areas of all rollers and roller path plates. Initially large pieces of chunk were cut from the rollers and roller path plates using abrasive water-jet cutting technology at the MGI Canada Inc., Selkirk, Manitoba, as shown in Fig. 3.27. After that, small samples in exact dimensions were cut using a lathe machine at the Selkirk Machine Works (1982) Ltd., Selkirk, Manitoba. Abrasive water-jet cutting is a method that utilizes high-pressure water and abrasive to cut large steel parts. Water is pressurized to 379 MPa (55 ksi) using hydraulic intensification, and then

forced through a small orifice in the cutting head. At the head, abrasive (garnet) is added to the water, creating a cutting stream, which exits the 1-mm diameter nozzle at 1.5 times the speed of sound (344 m/sec), as depicted in Fig. 3.28. Through a combination of micro-erosion grinding and shearing action of the pressure, a narrow cross section of material is removed all the way through the thickness. The process is then controlled via computer. Any two-dimensional shape from nearly any material is possible. The resulting surface finish on the cut surfaces is far superior when compared to laser cut, torch cut or sawed surfaces.

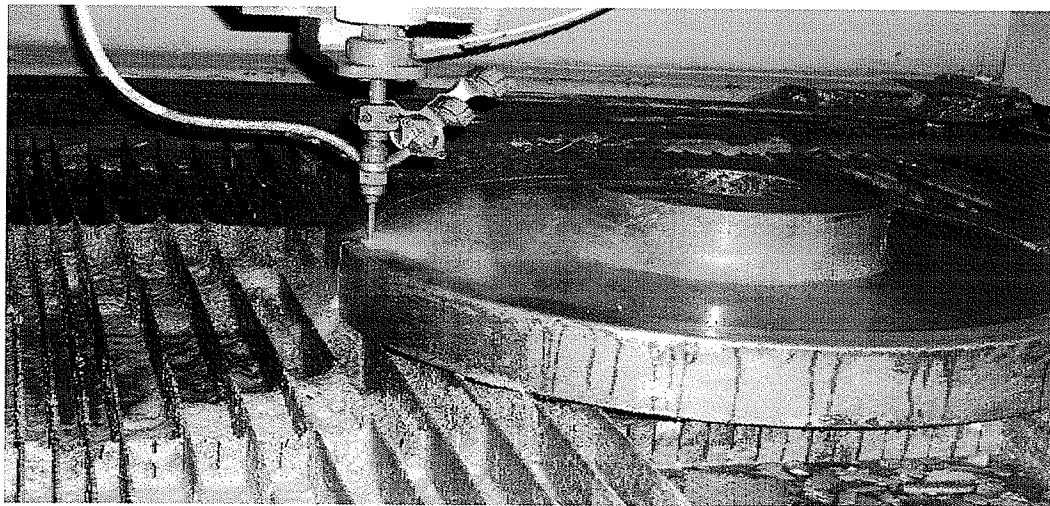


Fig. 3.27 Roller R<sub>3</sub> being cut using abrasive water-jet technology

Two samples were extracted from each tested contact area of all rollers and roller path plates; one for scanning the contact-surface and the other for scanning the inside surface perpendicular to the contact surface in order to observe the extent and depth of damage. All samples were 20 mm ( $\frac{3}{4}$  in.) in depth. Control samples extracted from the non-tested areas of rollers and roller path plates were 20 × 15 mm ( $\frac{3}{4}$  ×  $\frac{1}{2}$  in.) in dimension, as typically shown in Fig. 3.29.

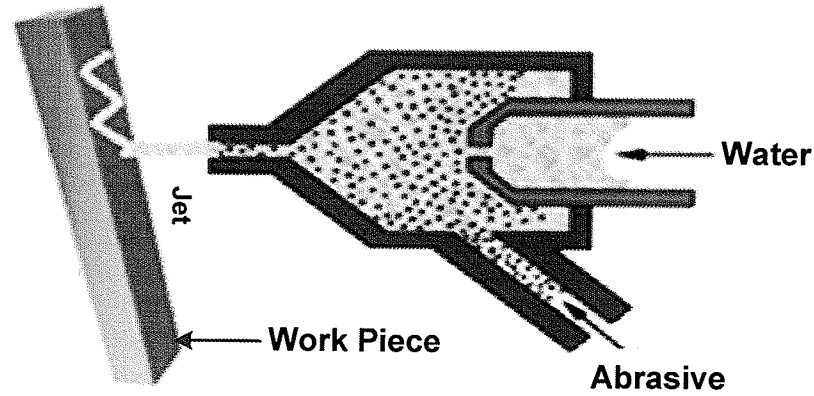


Fig. 3.28 Water-jet cutting

Those samples that were extracted from the tested contact areas of the specimens were  $20 \times 15 \text{ mm}$  ( $\frac{3}{4} \times \frac{1}{2} \text{ in.}$ ) and  $30 \times 10 \text{ mm}$  ( $1.2 \times 0.4 \text{ in.}$ ) in dimension. The different configuration of sample dimensions was selected to accommodate three samples at a time (one control sample and two other samples from tested area) in the sample holder of the electron microscope. Hence, three samples were scanned at a time in order to save time and reduce per hour cost of using electron microscope. Table 3.2 shows number of samples and nomenclature adopted for scanning electron microscope testing program. The results of SEM are given in Chapter 4.

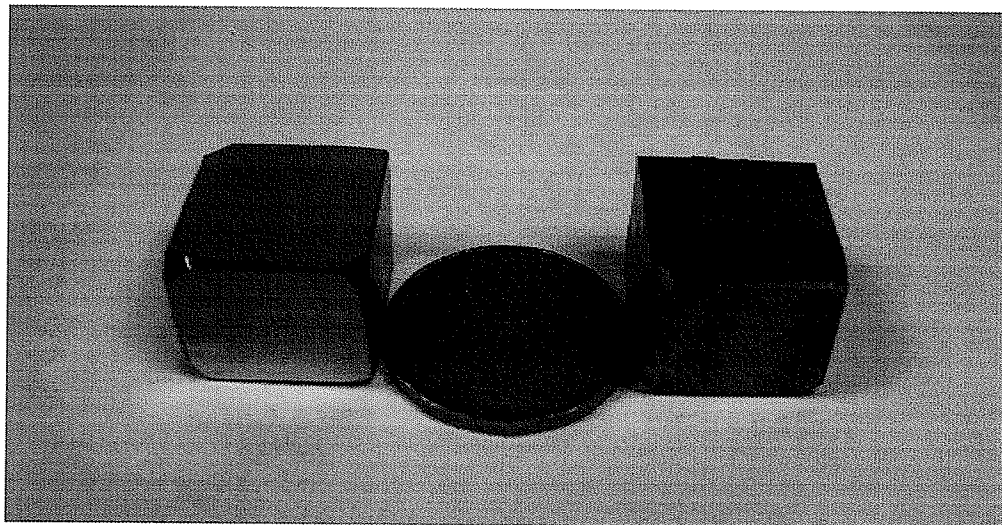


Fig. 3.29 Typical control samples for SEM

Table 3.2 Number of samples and nomenclature for SEM testing

Specimen	Number of Samples	Nomenclature	
		Control Sample	Tested Samples
R <sub>1</sub>	5	R <sub>1C</sub>	R <sub>1AS</sub> , R <sub>1AT</sub> , R <sub>1BS</sub> , R <sub>1BT</sub>
R <sub>2</sub>	5	R <sub>2C</sub>	R <sub>2AS</sub> , R <sub>2AT</sub> , R <sub>2BS</sub> , R <sub>2BT</sub>
R <sub>3</sub>	5	R <sub>3C</sub>	R <sub>3AS</sub> , R <sub>3AT</sub> , R <sub>3BS</sub> , R <sub>3BT</sub>
P <sub>1</sub>	3	P <sub>1C</sub>	P <sub>1S</sub> , P <sub>1T</sub>
P <sub>2</sub>	3	P <sub>2C</sub>	P <sub>2S</sub> , P <sub>2T</sub>
P <sub>3</sub>	3	P <sub>3C</sub>	P <sub>3S</sub> , P <sub>3T</sub>
P <sub>4</sub>	3	P <sub>4C</sub>	P <sub>4S</sub> , P <sub>4T</sub>
P <sub>5</sub>	3	P <sub>5C</sub>	P <sub>5S</sub> , P <sub>5T</sub>
P <sub>6</sub>	3	P <sub>6C</sub>	P <sub>6S</sub> , P <sub>6T</sub>

### 3.9 Material Properties

Five different types of materials were used in this research study; three kinds of rollers and two types of roller path plates. In order to identify and specify exact material properties, all control specimens were studied under the eye of microscope for surface pore structure. To expose surface pore structure, all specimens were properly ground and polished using different scales of grinding papers and polishing grades and at the end surfaces were properly etched using appropriate chemicals. Pore surface structure of cast iron Roller R<sub>1</sub> is revealed in Fig. 3.30, which is a typical of gray cast iron. Fig. 3.31 depicts pore surface structure of Roller R<sub>3</sub>, which is a typical of heat treated high carbon steel. Pore surface structure of roller path Plate P<sub>1</sub> is shown in Fig. 3.32. Fig. 3.33 shows the surface pore structure of Plate P<sub>3</sub>, which is typical of a heat-treated stainless steel.



Fig. 3.30 Pore surface structure of cast iron Roller R<sub>1</sub> (X200)



Fig. 3.31 Pore structure of heat treated high carbon steel Roller R<sub>3</sub> (X200)

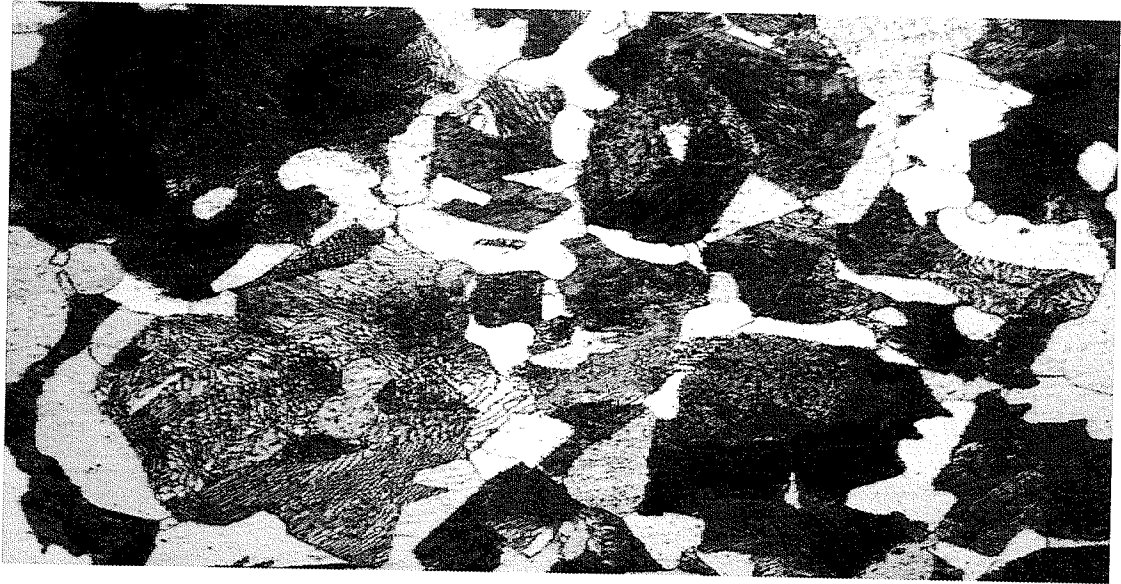


Fig. 3.32 Pore structure of roller path Plate P<sub>1</sub> (X200)

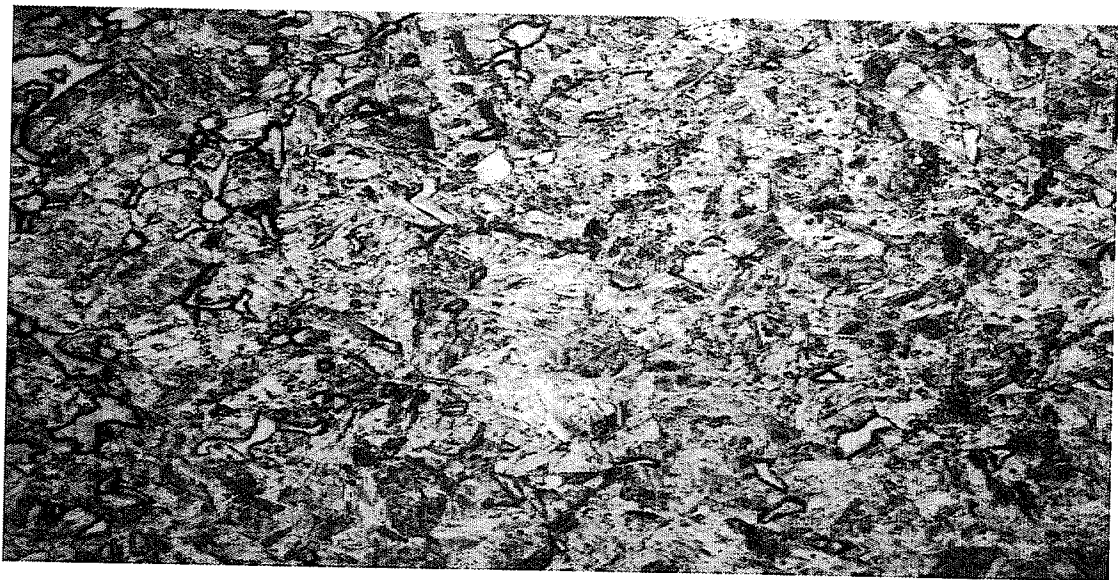


Fig. 3.33 Surface pore structure of stainless steel Plate P<sub>3</sub>, (X200)

After the completion of SEM testing, all control samples were sent to Arrow Laboratory, Inc. in Wichita, Kansas, US, for the determination of carbon content (Table 3.3). Based on available information of surface pore structure, BHN, and carbon contents, specimens were identified and material properties were specified through literature search. Mechanical properties for all five different types of materials are listed in Table 3.3.

Table 3.3 Material properties of rollers and roller path plates

Specimen	Specification	Carbon Content, %	Hardness (BHN)	Elastic Modulus GPa (ksi)	Poisson's Ratio	Yield Strength MPa (ksi)	Ultimate Strength MPa (ksi)
R <sub>1</sub>	Gray Cast Iron ASTM A48 Class 20A	3.69	219-391	103.4 <sup>1</sup> (15000)	0.27 <sup>1</sup>	196 <sup>1</sup> (28.4)	236.5 <sup>1</sup> (34.3)
R <sub>2</sub>	AISI 1060 High Carbon Steel (No Heat Treatment)	0.66	326-373	207 <sup>2</sup> (30,000)	0.29 <sup>2</sup>	482.6 <sup>2</sup> (70)	814 <sup>2</sup> (118)
R <sub>3</sub>	AISI 1080 Heat Treated High Carbon Steel	0.74	428-473	207 <sup>2</sup> (30,000)	0.29 <sup>2</sup>	980 <sup>2</sup> (142.2)	1325 <sup>2</sup> (192.2)
P <sub>1</sub>	AISI 1050 Medium Carbon Steel (No Heat Treatment)	0.49	291	207 <sup>2</sup> (30,000)	0.28 <sup>2</sup>	413.7 <sup>2</sup> (60)	724 <sup>2</sup> (105)
P <sub>3</sub>	Heat Treated Stainless Steel SS 410	0.15	364	200 <sup>3</sup> (29,000)	0.29 <sup>3</sup>	1000 <sup>3</sup> (145)	1310 <sup>3</sup> (190)

<sup>1</sup>(Muzyczka 1992), (Angus 1976), (Baucio 1993), and (Smith 1993)

<sup>2</sup>(Davis 1996), (Davis 1999) (Gale and Totemeier 2004), (Harvey 1982), (Shackelford and Alexander 2000), (Smith 1993), and (Steiner 1996)

<sup>3</sup>(Beddoes and Parr 1999), (Harvey 1982), and (Lamb and Bringas 2002)

### 4.1 General

The experimental investigation involved laboratory testing of three rollers and six roller path plates under cyclic loading in this research study. The details of the experimental program along with the testing parameters are discussed at length in Chapter 3. In this chapter, results from the laboratory investigation are presented and discussed in detail.

### 4.2 Brinell Hardness Tests

Twenty-one readings were taken on each roller path Plate  $P_1$  through  $P_6$ . The average BHN for the AISI 1050 medium carbon steel Plates  $P_1$  and  $P_2$ , which were not heat treated, was 291 along with a range of 2, whereas, for the heat-treated stainless steel SS 410 Plates,  $P_3$  through  $P_6$ , the average BHN was 364 along with a range of 2.

The hardness measurements indicated that the roller hardness profile for gray cast iron Roller  $R_1$  varied from 391 BHN at the rolling surface to 219 BHN at 38 mm ( $1\frac{1}{2}$  in.) below the rolling surface. The variation in hardness as a function of the distance below the rolling surface for the three rollers tested in this research program is presented in Fig. 4.1. The average BHN at the web surface was found to be 225 with a range of 2. The average BHN at the hub surface was found to be 231 along with a range of 2.

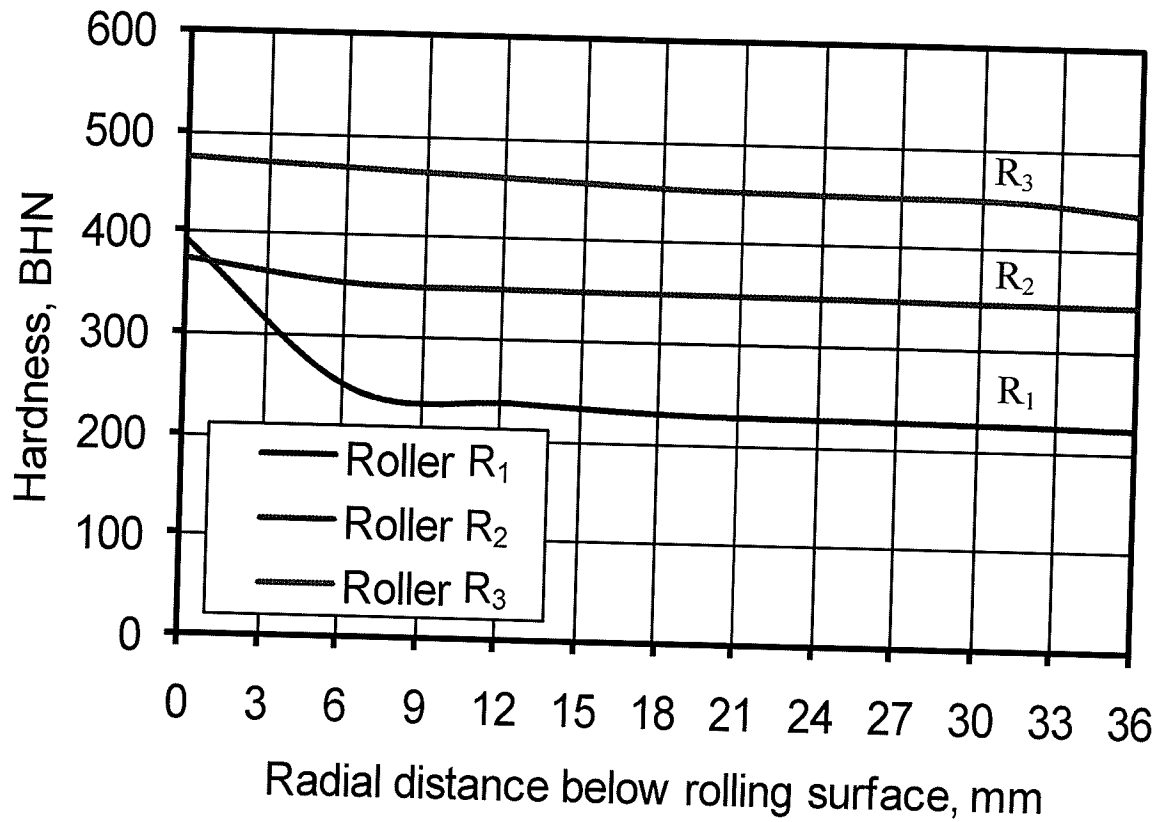


Fig. 4.1 BHN vs. radial distance below rolling surface

The hardness for the AISI 1060 high carbon (with no heat treatment) steel Roller R<sub>2</sub> varied from 373 BHN at the rolling surface to 326 BHN at 63.5 mm (2½ in.) below the rolling surface. The average BHN at the web surface was found to be 300 with a range of 2. The average BHN at the hub surface was found to be 362 with a range of 2.

The hardness for the AISI 1080 heat-treated high carbon steel Roller R<sub>3</sub> varied from 473 BHN at the rolling surface to 428 BHN at 38 mm (1½ in.) below the rolling surface, as shown in Fig. 4.1. The average BHN at the web surface was found to be 364 with a range of 2. The average BHN at the hub surface was found to be 330 with a range of 2.

### 4.3 Radial Compressive Load

The radial compressive load on all rollers was applied by tensioning the four high strength rods using hydraulic jacks. These four rods were calibrated in order to monitor the strain values during cyclic testing. The total radial compressive load on the roller was calculated as the sum of the individual tensile loads in the high strength rods. After releasing the jack pressure on the four rods, there was some relaxation of the applied load. This varied from 4.6% to 8.3%. The values of the radial compressive load, after releasing jack pressure and just prior to cyclic testing, were used in the finite element (FE) analysis discussed in Chapter 5. The steel fixture carrying the roller was held against the strong concrete wall through four high strength rods. As the roller moved back and forth under high radial and lateral loads, the strains in the four high strength rods varied with the movement of the roller. An example of the strain variation on one of these rods is shown in Fig. 4.2. Thus, the total radial load (calculated as the sum of forces in the four rods) also varied during each cycle of loading, as shown in Fig. 4.3.

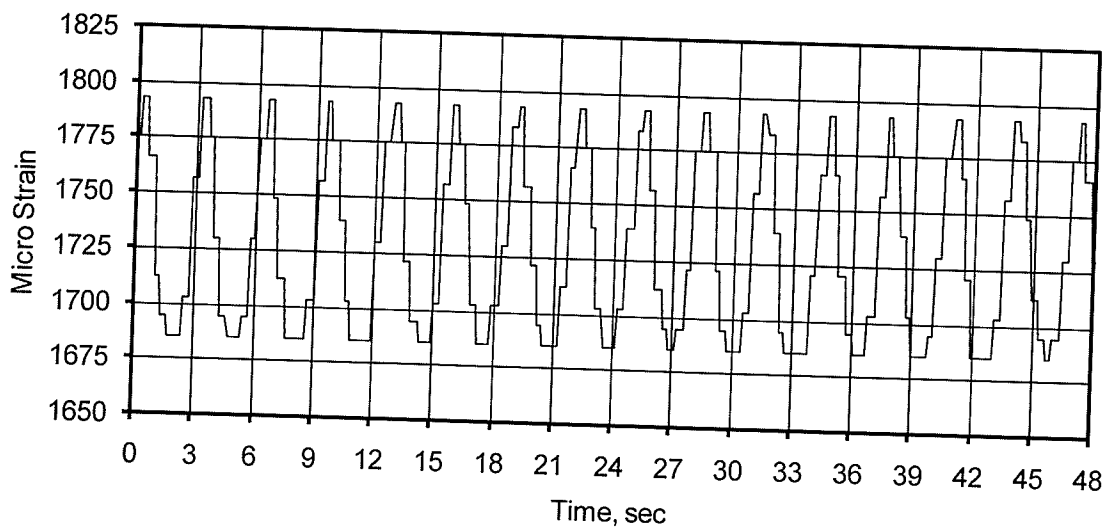


Fig. 4.2 Strain versus time for high strength Bar 1, Test R<sub>1A</sub>, after 1<sup>st</sup> cycle

The minimum and maximum radial loads, along with the average radial load during cyclic loading, are listed in Table 4.1. These values remained almost constant during cyclic testing, as shown, for one of the rollers, in Fig. 4.4.

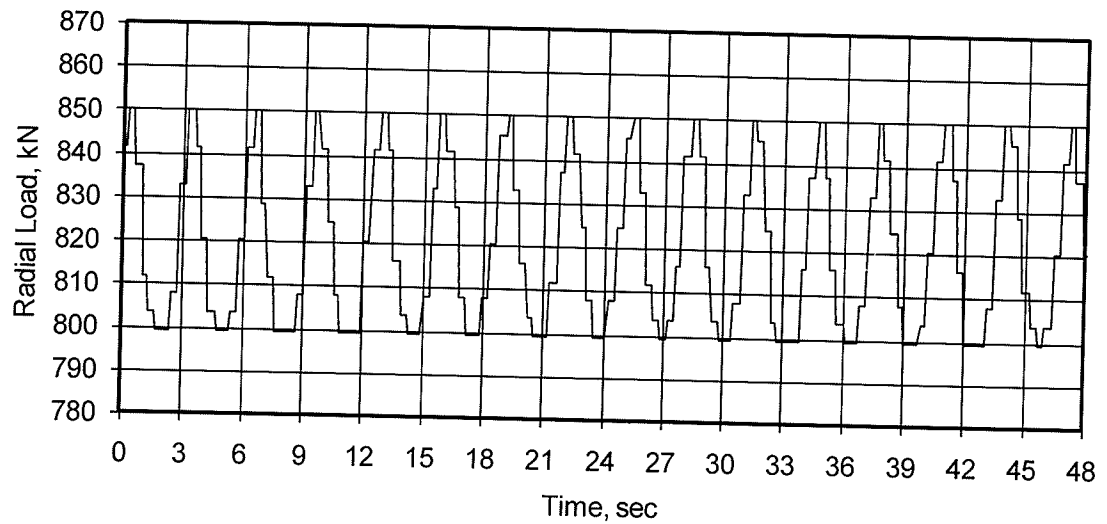


Fig. 4.3 Radial compressive load vs. time in Roller  $R_{1A}$ , after 1<sup>st</sup> cycle

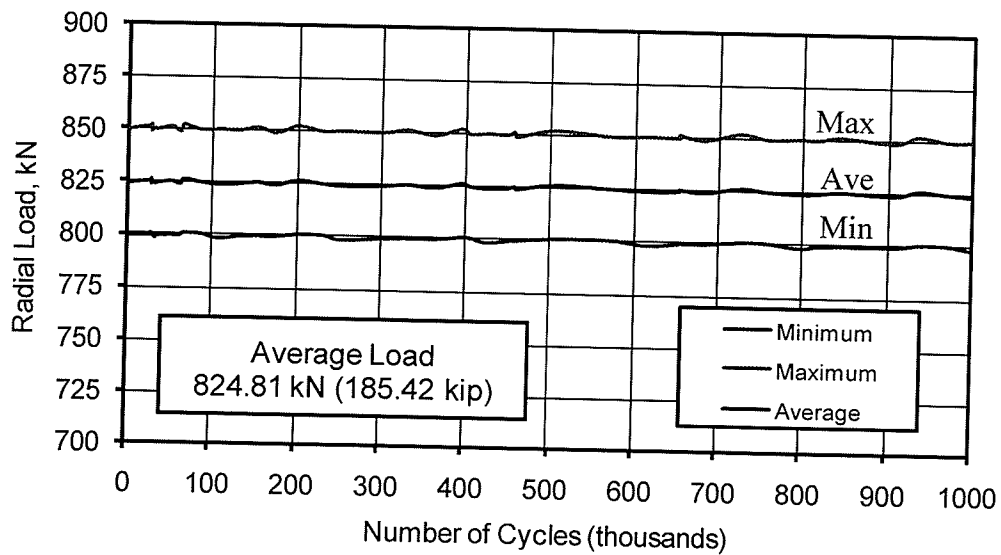


Fig. 4.4 Radial compressive load vs. number of cycles in Roller  $R_{1A}$

#### 4.4 Strains in Roller R<sub>1A</sub>

As the roller moved back and forth, all micro strains varied significantly. Maximum tensile strains were observed in all gauges installed on the rim surface of the roller when these gauges were farthest away from the contact point, which is obvious, and minimum tensile strains were recorded when the gauges were either in contact with the roller path plate or very close to the contact point. The reason for minimum tensile strains, when the gauges were either in contact or very close to the contact point, was that the rolling rim surface which had a depth of 88.85 mm (3½ in.) and a crown radius of 914 mm (36 in.) along with a 6.35 mm (¼ in.) long chamfer, inclined at 45° in between the rolling surface and rim surface, as shown in Fig. 4.5, deformed under the application of the radial load, placing the strain gauges in tension. Gauges 5 through 13 were installed on the rim surface of Roller R<sub>1</sub>.

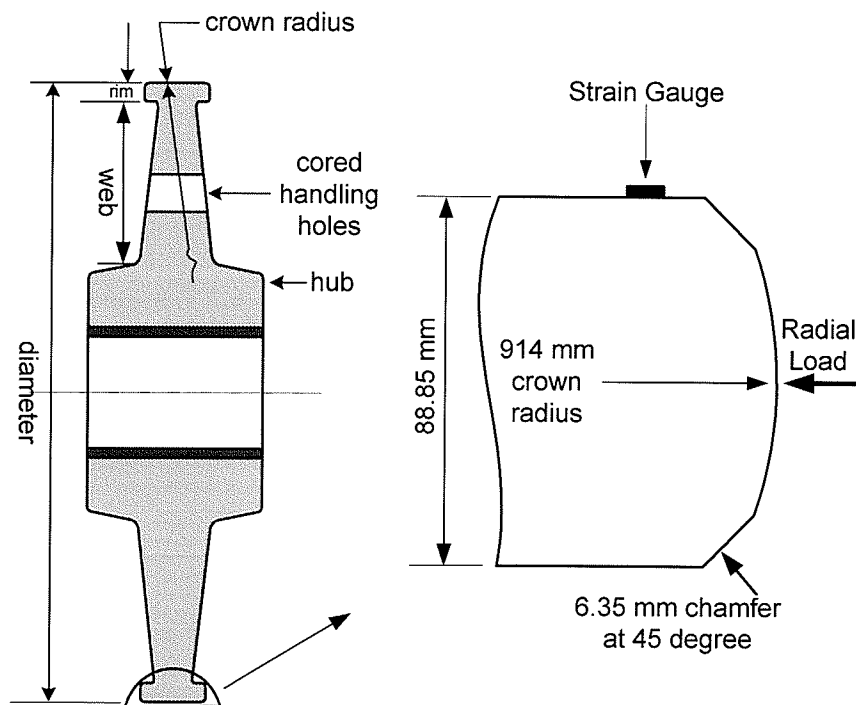


Fig. 4.5 Enlarged view of the rim where strain gauges were installed

The magnitude of the strain on a particular point on a roller varied, depending on the relative position of the point with respect to the point in direct contact with the roller path plate. As shown in Fig. 4.6, the strain recorded by gauge 9 in Roller R<sub>1A</sub>, varied from 842  $\mu\epsilon$  (in tension), when the gauge was in direct alignment with the point in contact with the roller path, to 1340  $\mu\epsilon$  (in tension), when the gauge was the farthest away from the contact point.

Table 4.1 Radial compressive load applied on all rollers

Test	Load Applied kN (kips)	Load Just Prior to Testing kN (kips)	Relaxation, %	Load During Cyclic Testing		
				Minimum kN (kip)	Average kN (kip)	Maximum kN (kip)
R <sub>1A</sub>	881.43 (198.16)	838.08 (188.42)	4.9	799.29 (179.68)	824.81 (185.42)	850.32 (191.15)
R <sub>1B</sub>	887.72 (199.58)	834.72 (187.66)	6.0	800.03 (179.85)	829.48 (186.47)	858.94 (193.09)
R <sub>2A</sub>	887.87 (199.61)	814.23 (183.06)	8.3	797.22 (179.22)	806.46 (181.29)	815.71 (183.37)
R <sub>2B</sub>	943.29 (212.07)	888.42 (199.73)	5.8	885.64 (199.09)	903.21 (203.04)	920.78 (207.01)
R <sub>3A1</sub>	887.87 (199.61)	814.23 (183.06)	8.3	802.09 (180.31)	821.27 (184.62)	840.45 (188.93)
R <sub>3A2</sub>	893.08 (200.78)	851.52 (191.44)	4.6	845.07 (189.97)	859.02 (193.11)	872.97 (196.24)
R <sub>3B1</sub>	854.55 (192.12)	807.77 (181.59)	5.4	799.30 (179.68)	815.08 (183.23)	830.86 (186.78)
R <sub>3B2</sub>	793.44 (178.36)	740.37 (166.45)	6.7	732.63 (164.69)	753.17 (169.31)	773.73 (173.93)

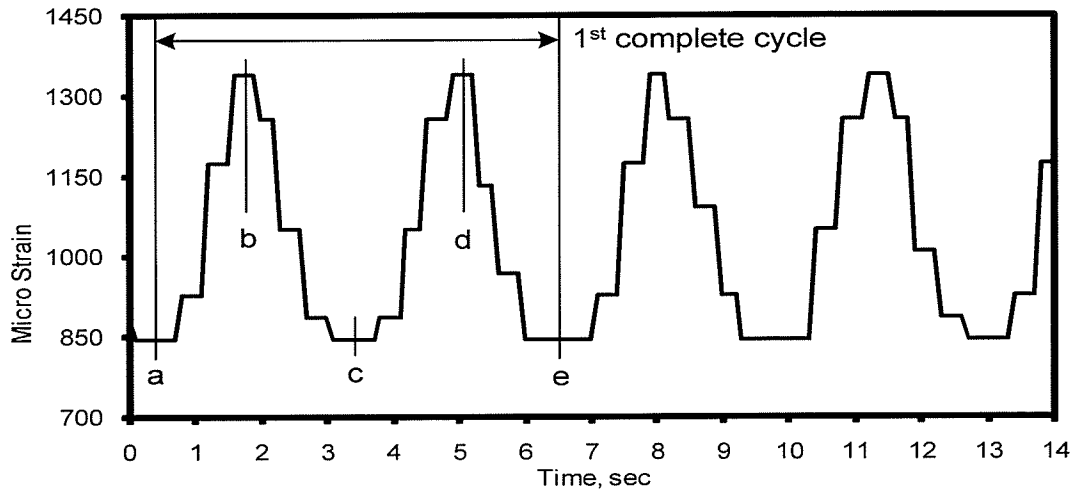


Fig. 4.6 Strain vs. time for gauge 9 in Roller  $R_{1A}$  after 1<sup>st</sup> cycle

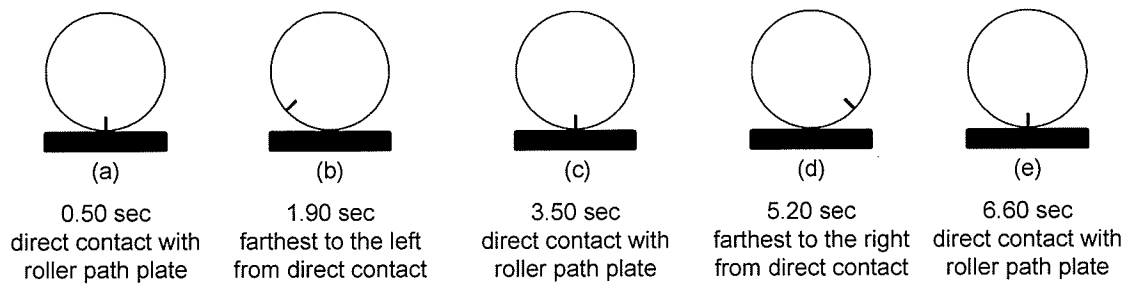


Fig. 4.7 Location of gauge 9 in Roller  $R_{1A}$ , during 1<sup>st</sup> complete cycle

The location of gauge 9 during the 1<sup>st</sup> complete cycle is illustrated by five points a, b, c, d, and e in Figs. 4.6 and 4.7. Gauge 14 was installed in the web area of the Roller  $R_1$ , 88.85 mm (3½ in.) away from the contact area of the rolling rim surface. A compressive strain in the range of 1363-1658  $\mu\epsilon$  was recorded at that location.

Before testing each roller under cyclic loading, the roller and roller path were aligned so that the central gauge of each roller coincided exactly with the centre of the rolling surface of roller path plate. However, during cyclic testing of Roller  $R_{1A}$ , it was noticed that the roller had started slipping gradually with respect to roller path Plate  $P_1$  after about

300,000 cycles and it was not rolling symmetrically, as was set to do in the beginning of the test. At the end of a million cycles, the roller slipped a maximum distance of 44.5 mm (1¾ in.). This is the reason that gauges 5 and 6 were in contact with the roller path plate, whereas gauges 12 and 13 were far away from the contact area during each cyclic movement. For this reason, there was significant change in the strain curves for gauges 5, 6 and 7 as compared to that of gauges 12 and 13, as shown in Figs. 4.8 through 4.10. The strain differences between the maximum and the minimum at each gauge location at the first and last cycle of loading for Roller R<sub>1</sub> are listed in Table 4.2.

In the majority of the gauges installed on the rim surface of the Roller R<sub>1A</sub>, it was found that with the increase in the number of cycles, the strain dropped from a higher tensile strain to a lower tensile strain or even to compressive strain. This may be attributed to the formation of micro cracks after repeated cyclic loading and the material might have lost its stiffness in the vicinity of these micro cracks. The literature review reveals that with the increase in the size of micro crack, the local stress within the vicinity of micro crack decreases, as discussed in Section 2.5. After 457,727 cycles, there was a sudden drop of 900 µε in the minimum and maximum strain curves in gauge 5. This may also be attributed to the formation of micro cracks that might have developed in that area where the gauge was situated. A continuous drop in the micro strain was observed in gauge 6 up to 500,000 cycles. After that, the strain remained constant until the test was stopped at one million cycles. The strains recorded by gauge 7 show a continuous drop from their original high value until the end of a million cycles. Gauge 9 showed a similar trend to that of gauge 7, a continuous drop in the strain values.

Table 4.2 Micro strains in Roller R<sub>1</sub>

Gauge Location	Test R <sub>1A</sub> <sup>(1)</sup>				Test R <sub>1B</sub> <sup>(2)</sup>			
	1 <sup>st</sup> Cycle		Million Cycle		1 <sup>st</sup> Cycle		818,726 Cycle	
	Minimum Maximum	Difference	Minimum Maximum	Difference	Minimum Maximum	Difference	Minimum Maximum	Difference
5	1414 1520	106	384 514	130	1482 1559	74	1377 1507	130
6	1498 1605	107	-471 -228	244	1531 1661	130	1353 1619	266
7	236 824	588	-43 103	146	-339 893	1232	-472 -296	176
8	153 1293	1140	1004 1573	569	-231 1917	2148	497 1270	773
9	842 1340	498	562 716	154	747 2009	1262	1258 1407	149
10	383 1554	1171	754 1220	466	-129 2057	2186	203 927	724
11	616 833	217	-343 -196	147	218 900	682	0 283	283
12	1544 1751	207	1513 1693	180	1554 1668	114	1502 1641	139
13	1542 1664	122	1497 1609	112	1498 1605	107	1414 1563	149
14	-1658 -1363	295	-1813 -1465	348	-1624 -1324	300	-1698 -1542	156

<sup>1</sup>Roller Path Plate was P<sub>1</sub>, <sup>2</sup>Roller Path Plate was P<sub>2</sub>

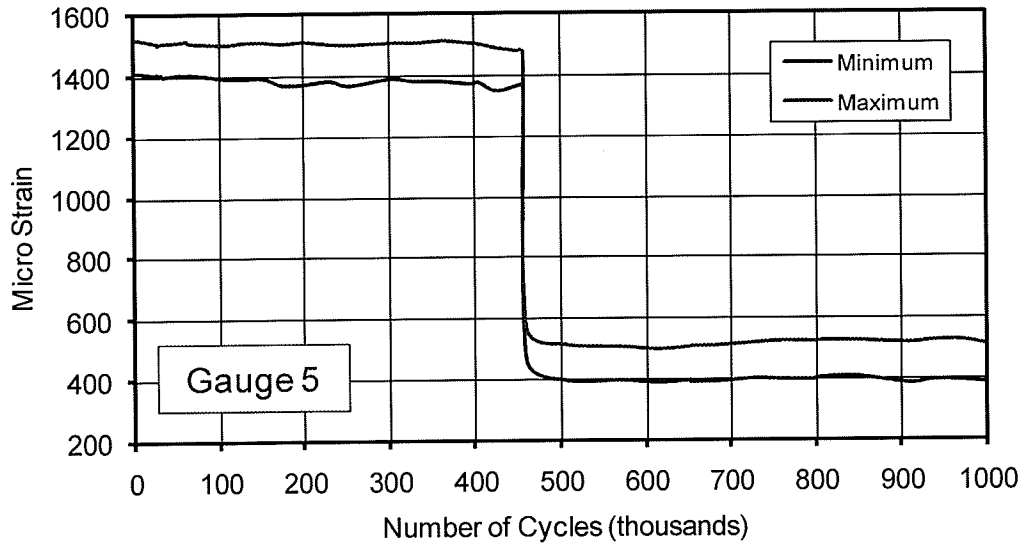


Fig. 4.8a Strain vs. number of cycles for gauge 5 in Roller R<sub>1A</sub>

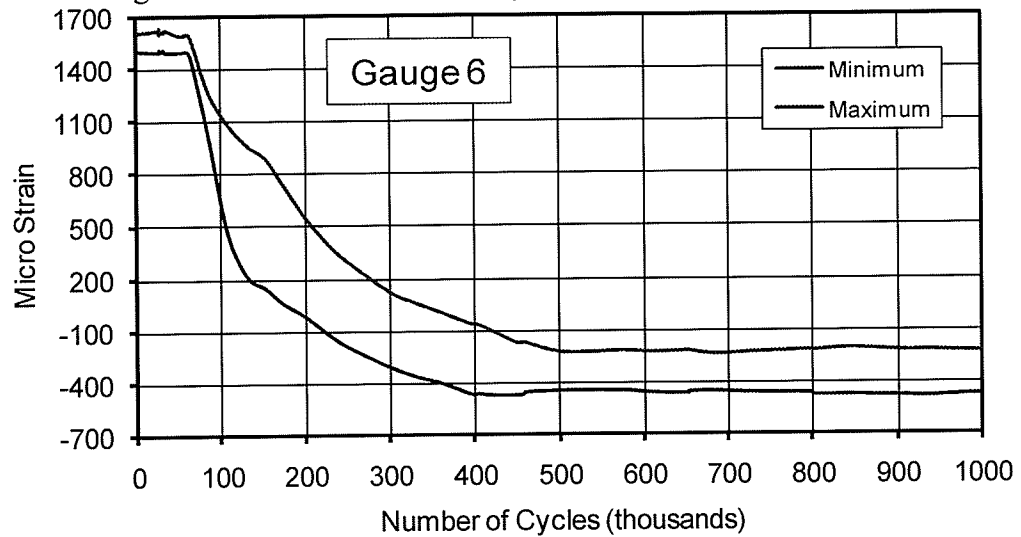


Fig. 4.8b Strain vs. number of cycles for gauge 6 in Roller R<sub>1A</sub>

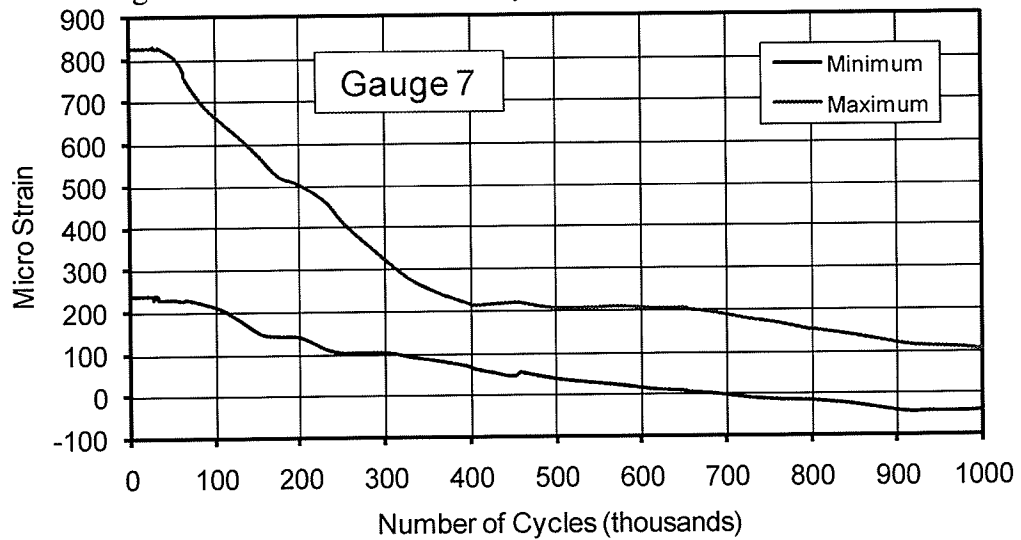


Fig. 4.8c Strain vs. number of cycles for gauge 7 in Roller R<sub>1A</sub>

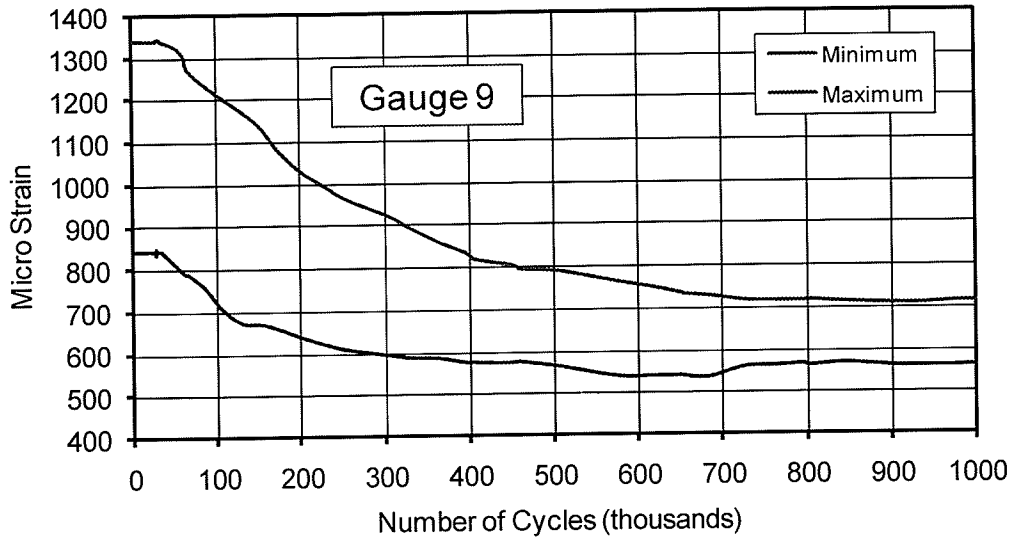


Fig. 4.9a Strain vs. number of cycles for gauge 9 in Roller R<sub>1A</sub>

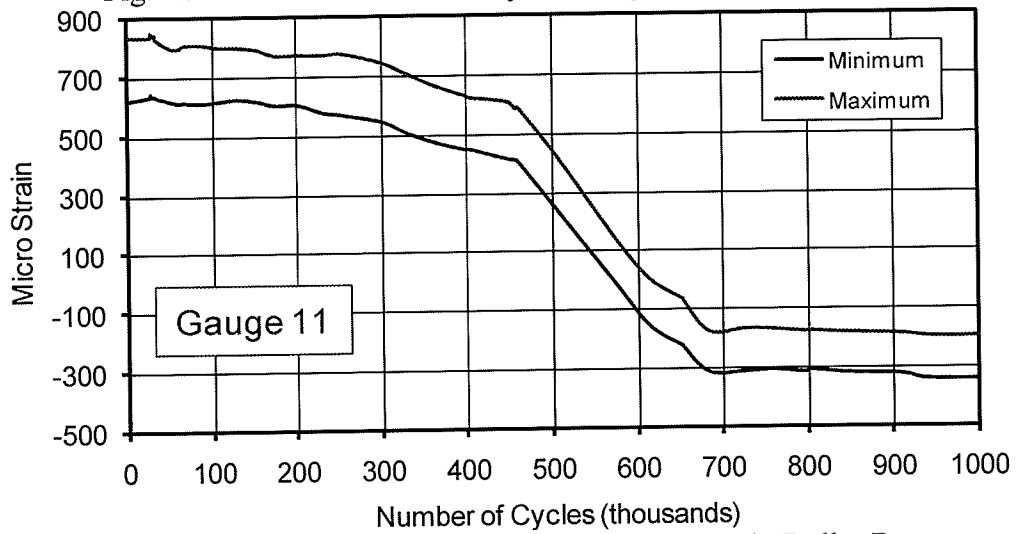


Fig. 4.9b Strain vs. number of cycles for gauge 11 in Roller R<sub>1A</sub>

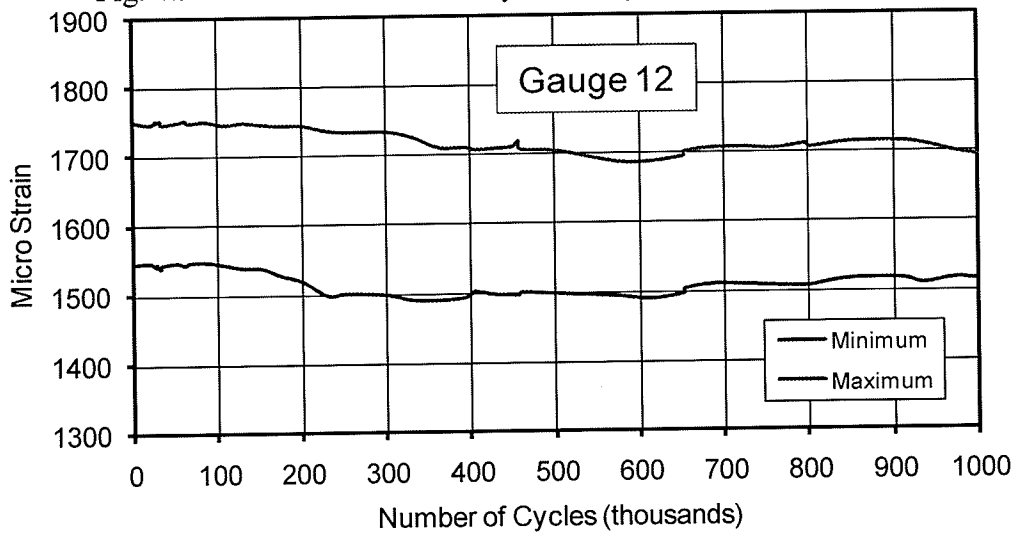


Fig. 4.9c Strain vs. number of cycles for gauge 12 in Roller R<sub>1A</sub>

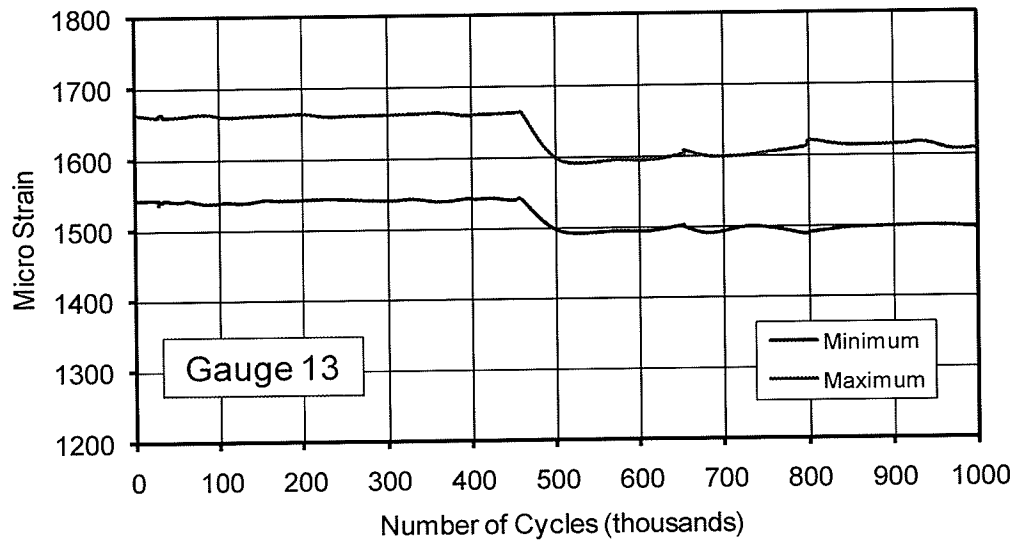


Fig. 4.10 Strain vs. number of cycles for gauge 13 in Roller R<sub>1A</sub>

Strain values recorded by gauge 11 also went through downward trend until 683,718 cycles. Since gauge 12 was not in contact with the roller path plate, due to the slipping of the roller, there was no change in the strain values. Gauge 13 also behaved in a similar manner as that of gauge 12 but with a higher micro strain range. There are two interesting observations that are of importance to note:

- (a) The strain difference between the minimum and the maximum strain values became smaller as the number of cycles of loading increased reaching a constant value after a certain number of cycles, as shown for gauge 7 and 9 in Figs. 4.8, and 4.9; and,
- (b) Both the maximum and the minimum strain values decreased as the number of cycles increased, reaching a constant value after a certain number of cycles, for all strain gauges installed on the rim surface except strain gauges 8 and 10, which were part of rosette strain gauge and were placed at 45° to a plane perpendicular to the rolling surface of roller path plate.

Since gauge 14 was installed in the web area of Roller R<sub>1A</sub>, 88.85 mm (3½ in.) away from the contact area of the rolling rim surface, it showed no significant change in the strain values during cyclic testing. This is the reason why, in subsequent tests, no strain gauges were installed in the web areas of Rollers R<sub>2</sub> and R<sub>3</sub>. With the exception of gauge 14, the maximum strain recorded during 1<sup>st</sup> cycle was 1751 µε (tensile) for the cyclic test conducted on Roller R<sub>1A</sub>.

Using three-element rosette strain gauges (gauge 8, 9, and 10), principal strains and maximum shearing strains were calculated. The plots of principal strains and maximum shearing strains as a function of the number of cycles for Roller R<sub>1A</sub>, up to one million cycles are presented in Fig. 4.11. There was a continuous increase in the minimum and maximum micro strain in the maximum principal direction up until 662,000 cycles. After that, the strain values decreased to the end of the test. In the maximum principal direction, the strain ranged from 1015 µε (tension) to 1821 µε (tension) during the first cycle, whereas, at the end of a million cycles, it ranged from 1542 µε (tension) to 2098 µε (tension). In the minimum principal direction, the maximum difference between the maximum and minimum micro strains occurred right after first cycle but became smaller after 460,425 cycles. After that, this difference remained almost constant up to the end of test. The maximum principal strain recorded during the 1<sup>st</sup> cycle was 1821 µε (tensile) for the cyclic test conducted on Roller R<sub>1A</sub>. The modulus of elasticity of cast iron Roller R<sub>1</sub> was 103.4 GPa (15000 ksi). By multiplying maximum principal strain (1821 µε) and the modulus of elasticity of Roller R<sub>1</sub>, a corresponding stress level of 188 MPa (27.3 ksi) is achieved.

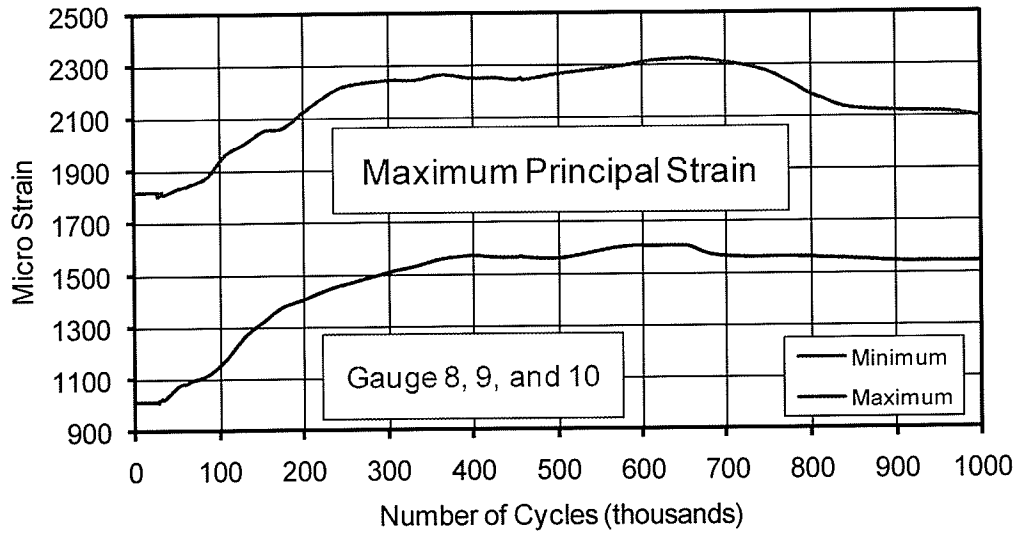


Fig. 4.11a Maximum principal strain in Roller R<sub>1A</sub>

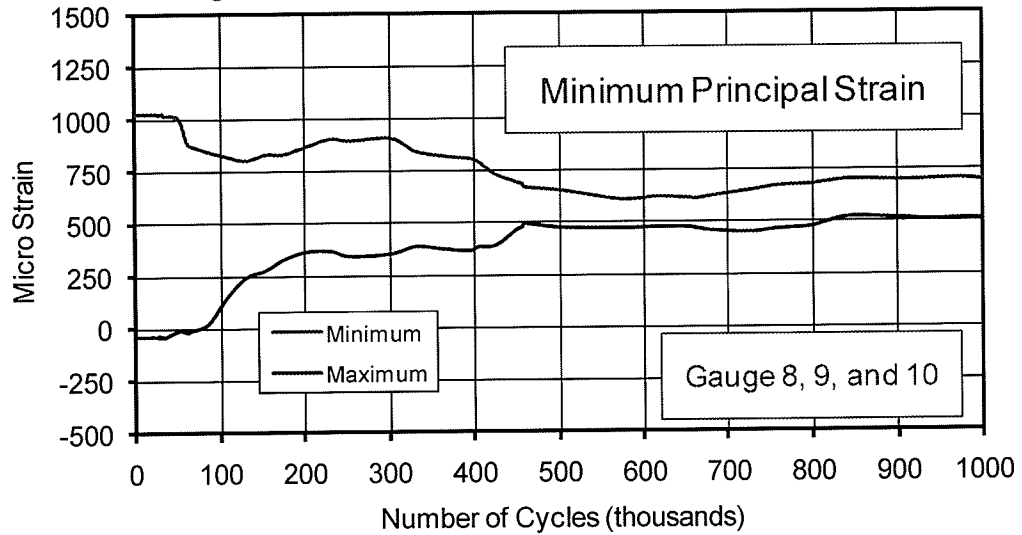


Fig. 4.11b Minimum principal strain in Roller R<sub>1A</sub>

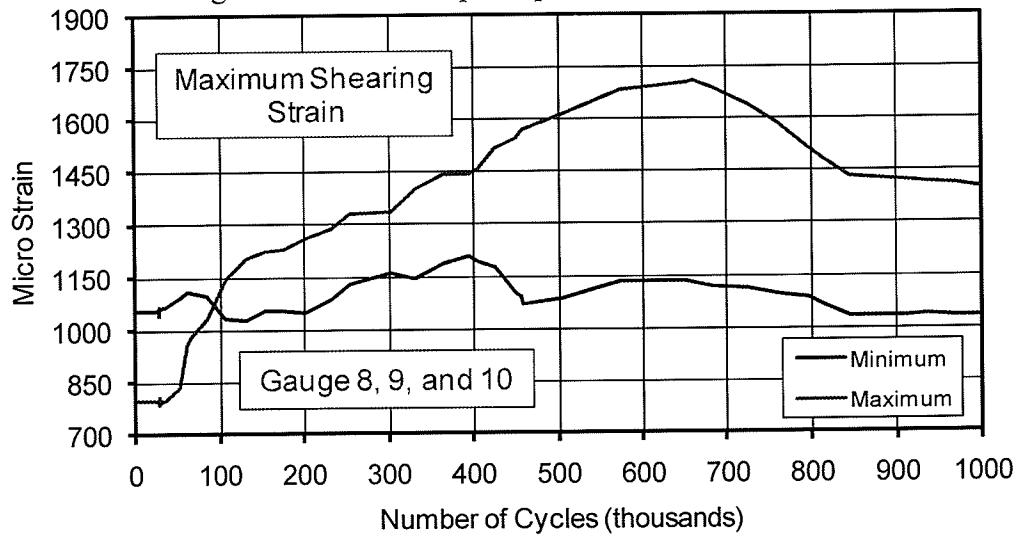


Fig. 4.11c Maximum shearing strain in Roller R<sub>1A</sub>

Table 4.3 summarizes the strain differences between the maximum and minimum in the principal directions and the difference in the maximum shearing strains for the rosette strain gauge installed on both sides of all rollers, after the first and last cycle of loading.

#### 4.5 Strains in Roller R<sub>1B</sub>

Tensile strains were observed in almost all the gauges installed on the rim surface of Roller R<sub>1B</sub>. The reason for tensile strain is explained in Section 4.4. The phenomena observed in the testing of Roller R<sub>1B</sub>, were very much similar to those of Roller R<sub>1A</sub>, as discussed in Section 4.4.

Table 4.2 summarizes the differences between the maximum and the minimum strains at each strain gauge location after the first and last cycles of loading for Roller R<sub>1</sub>. Because gauges 5, 6, 12 and 13 were not in contact with the roller path Plate P<sub>2</sub> in each cyclic movement, there was no significant change observed in the micro strain curves of these gauges. The micro strain is plotted in Fig. 4.12 as a function of the number of cycles for gauges 7 and 9 installed on Roller R<sub>1B</sub>. In gauge 7, there was a continuous drop in the maximum strain recorded from 893  $\mu\epsilon$  tensile to 296  $\mu\epsilon$  compressive. In the central gauge 9, there was a drop of 610  $\mu\epsilon$  in the maximum tensile strain curve, whereas, there was an increase of 534  $\mu\epsilon$  in the minimum tensile strain curve. This increase and decrease in the micro strain curves continued up to 370,434 cycles, after which they remained almost constant till the end of the test. Gauge 11 was the mirror image of gauge 7 and showed similar trend as that of gauge 7. With the exception of gauge 14, the maximum strain recorded during 1<sup>st</sup> cycle was 2057  $\mu\epsilon$  (tensile) for the cyclic test conducted on Roller R<sub>1B</sub>.

Table 4.3 Principal and maximum shearing micro strains in rollers

Roller	Maximum Principal Strain				Minimum Principal Strain				Maximum Shearing Strain			
	At 1 <sup>st</sup> Cycle		At Last Cycle		At 1 <sup>st</sup> Cycle		At Last Cycle		At 1 <sup>st</sup> Cycle		At Last Cycle	
	Minimum Maximum	Difference	Minimum Maximum	Difference	Minimum Maximum	Difference	Minimum Maximum	Difference	Minimum Maximum	Difference	Minimum Maximum	Difference
R <sub>1A</sub>	1015 1821	806	1542 2098	556	-42 1024	1066	506 697	191	797 1057	260	1036 1401	365
R <sub>1B</sub>	879 2557	1678	1320 1564	244	-779 1496	2275	-57 696	753	1061 1658	597	868 1377	509
R <sub>2A</sub>	244 350	106	194 327	133	-168 -75	93	-488 -336	152	412 425	13	663 682	19
R <sub>2B</sub>	365 517	152	539 653	114	-243 -121	122	-454 -356	98	608 638	30	993 1009	16
R <sub>3A1</sub>	84 169	85	18 132	114	-176 -85	91	-155 -46	109	254 260	6	173 178	5
R <sub>3A2</sub>	74 178	104	47 152	105	-155 -63	92	-113 -45	68	229 241	12	160 197	37
R <sub>3B1</sub>	88 190	102	34 195	161	-154 23	177	-111 26	137	167 242	75	145 169	24
R <sub>3B2</sub>	114 220	106	52 162	110	-212 -28	184	-197 8	205	248 326	78	154 249	95

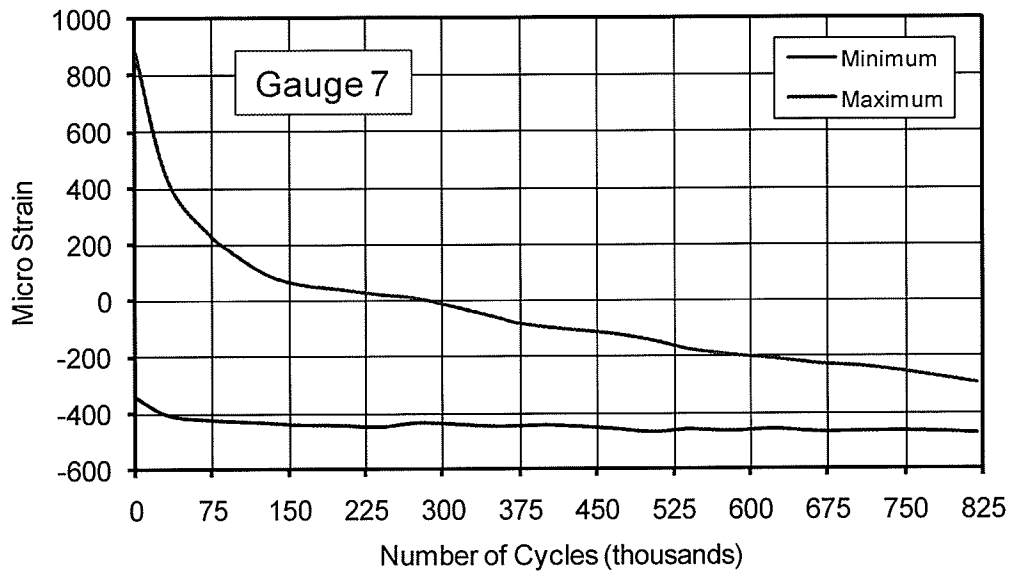


Fig. 4.12a Strain vs. number of cycles for gauge 7 in Roller R<sub>1B</sub>

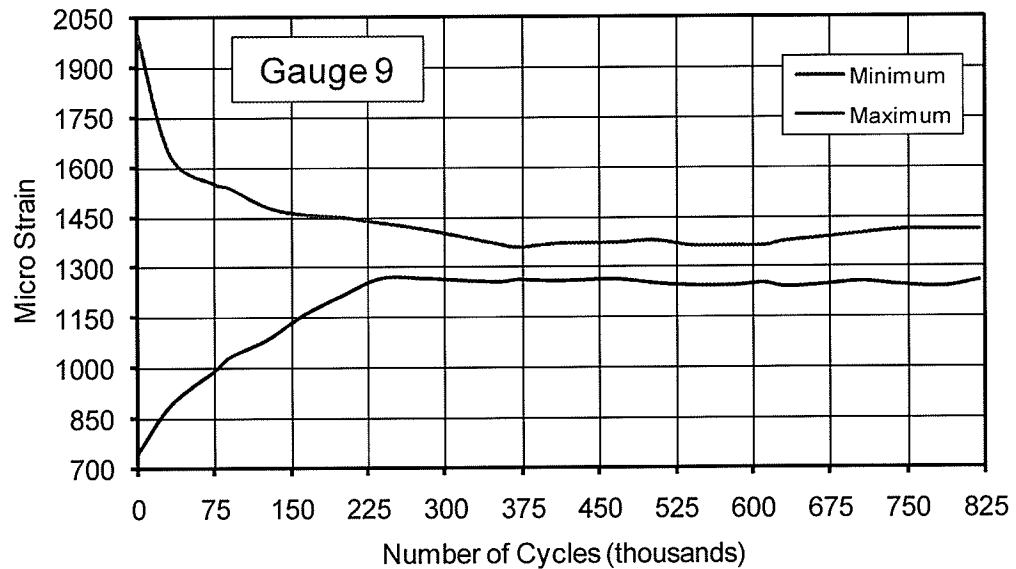


Fig. 4.12b Strain vs. number of cycles for gauge 9 in Roller R<sub>1B</sub>

Figure 4.13 shows the principal strains and maximum shearing strains versus number of cycles for the rosette strain gauge installed on Roller R<sub>1B</sub>. There was a continuous change in the minimum and maximum strains recorded in the maximum principal direction up to 370,434 cycles. After that, the strain values remained almost constant up to the end of the test.

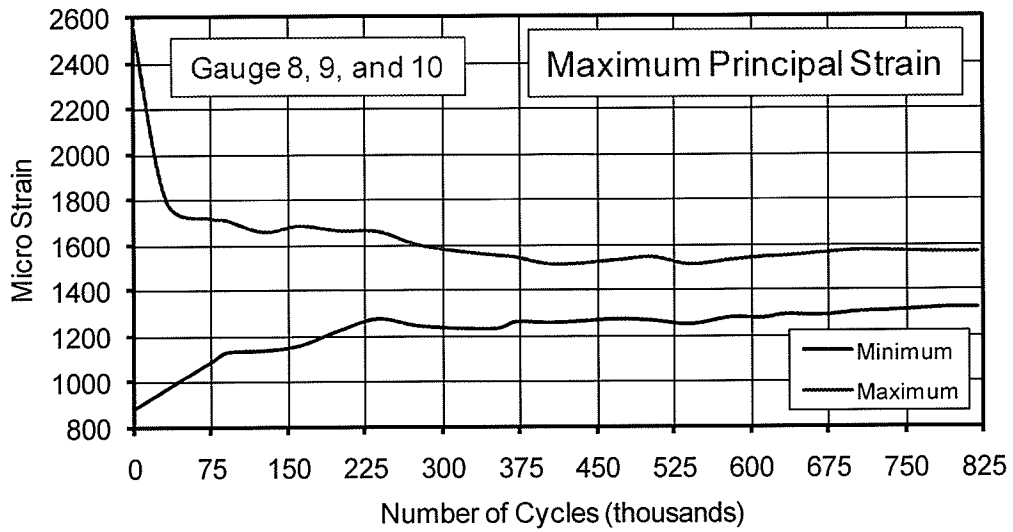


Fig. 4.13a Maximum principal strain in Roller R<sub>1B</sub>

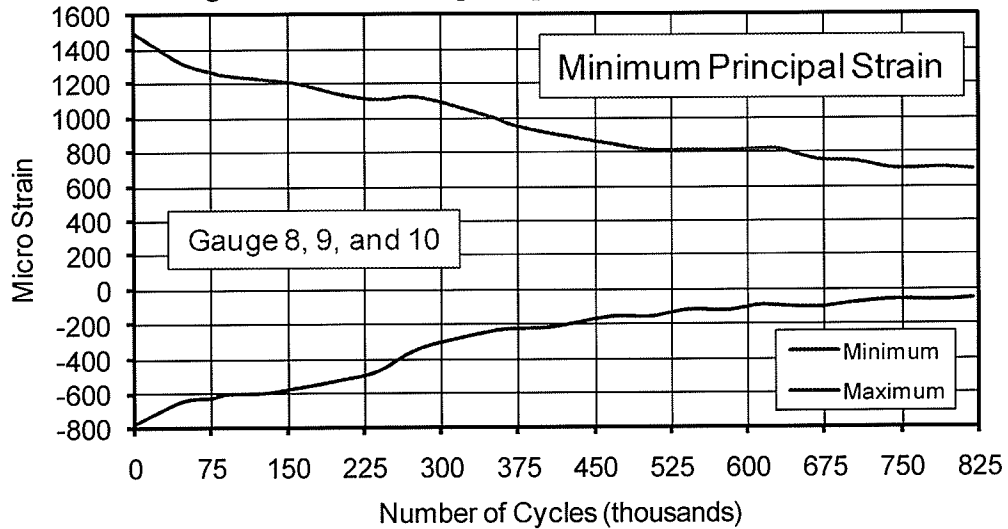


Fig. 4.13b Minimum principal strain in Roller R<sub>1B</sub>

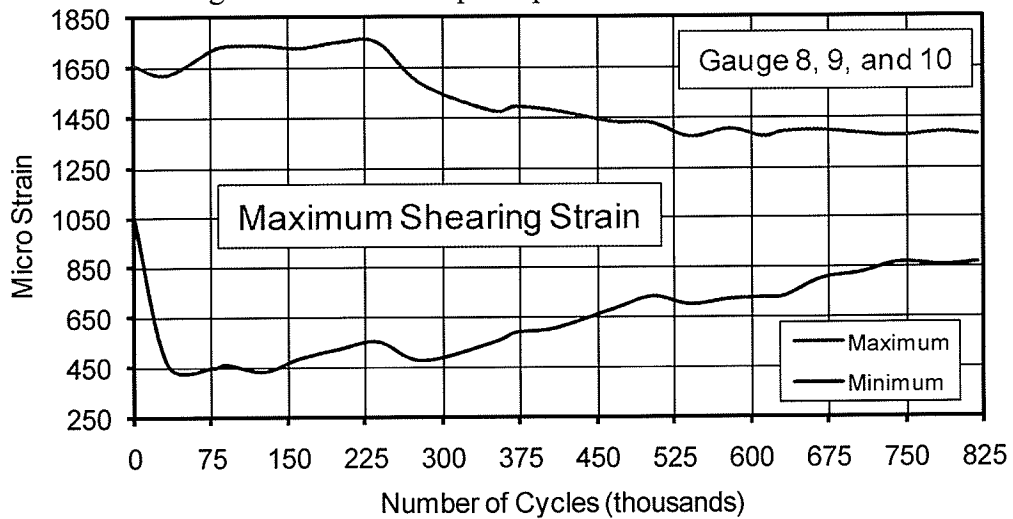


Fig. 4.13c Maximum shearing strain in Roller R<sub>1B</sub>

The maximum difference between the maximum and minimum strains in the maximum principal direction was right after the 1<sup>st</sup> cycle but became smaller at each subsequent cycle up until 370,434 cycles. After that, this difference remained constant. Almost a similar trend was found in the strain range in the minimum principal direction. More or less, a similar trend was observed in the maximum shearing strain. The maximum principal strain recorded during the 1<sup>st</sup> cycle was 2557  $\mu\epsilon$  (tensile) for the cyclic test conducted on Roller R<sub>1B</sub>. Multiplying this strain (2557  $\mu\epsilon$ ) by the modulus of elasticity (103.4 GPa), a corresponding stress level of 264 MPa (38.3 ksi) at a location where rosette strain gauge was installed, is achieved.

#### **4.6 Strains in Roller R<sub>2</sub>**

Table 4.4 summarizes the strain differences between the maximum and the minimum at each strain gauge location in Roller R<sub>2</sub> after the first and last cycle of loading. Gauges 5 and 6 were symmetrically placed across gauges 10 and 11, as shown in Fig. 3.21. During cyclic testing, gauges 6 and 10 came into contact with the roller path plate, whereas, gauges 5 and 11 were never in contact with the roller path plate. As the roller moved back and forth, the strains in the roller varied between a maximum and a minimum. A maximum compressive strain or a minimum tensile strain was recorded when the gauge was either in contact or very close to the contact point of the roller path plate and a minimum compressive strain or a maximum tensile strain was observed when the gauge was farthest away from the contact point during each cyclic movement. The reason for the maximum compressive strain or a minimum tensile strain when the gauge was either in contact or very close to the contact point, was that the rolling rim surface (of Rollers R<sub>2</sub> and R<sub>3</sub>) had a depth of 88.85 mm (3½ in.) and a crown radius of 914 mm (36 in.) along

with a chamfer of 3.2 mm ( $\frac{1}{8}$  in.) long, inclined at 45° in between the rolling surface and rim surface. The strain gauges 5 through 11 were installed on the rim surface of Rollers R<sub>2</sub> and R<sub>3</sub>.

Table 4.4 Micro strains in Roller R<sub>2</sub>

Gauge Location	Test R <sub>2A</sub> <sup>(1)</sup>				Test R <sub>2B</sub> <sup>(2)</sup>			
	At 1 <sup>st</sup> Cycle		At Last Cycle		At 1 <sup>st</sup> Cycle		At Last Cycle	
	Minimum Maximum	Difference	Minimum Maximum	Difference	Minimum Maximum	Difference	Minimum Maximum	Difference
5	17 102	85	-280 -225	55	61 160	99	-24 81	105
6	-80 42	122	-394 -310	84	-54 84	138	-215 -77	138
7	-23 62	85	-15 62	77	-31 99	130	-116 7	109
8	-153 -69	84	-474 -329	145	-223 -115	108	-429 -337	92
9	107 184	77	-214 -92	122	168 267	99	250 350	100
10	-129 -22	107	-400 -297	103	-207 -69	138	-423 -280	143
11	-23 77	100	-278 -221	57	-32 114	146	-171 -23	148

<sup>1</sup>Roller Path Plate was P<sub>3</sub>, <sup>2</sup>Roller Path Plate was P<sub>4</sub>

Almost a similar trend was observed in the strain gauges of Side B as those observed on Side A when Roller  $R_2$  was tested. A compressive strain was recorded in strain gauges 8 and 10, on both sides of Roller  $R_2$ . The rest of all strain gauges installed on both sides of Roller  $R_2$  recorded both tensile and compressive strain during each cyclic loading. With the exception of the strain gauge at the location of gauge 7, there was an increase in the compressive strain or a change from tensile to compressive strain in all other locations, as typically shown in Fig. 4.14. Strain gauge 7 was part of three-element rosette strain gauge and was installed at an angle of  $45^\circ$  to a plane perpendicular to the roller path plate.

The maximum strains recorded during 1<sup>st</sup> cycle were  $184 \mu\epsilon$  (tensile) and  $267 \mu\epsilon$  (tensile) for the two cyclic tests conducted on Roller  $R_2$ , Side A and Side B, respectively. Lower strains were recorded in Roller  $R_{2A}$  as compared to those observed in  $R_{2B}$ . The reason for this is that the average radial cyclic load on Side B was 12% higher than that in Side A. Average radial cyclic load recorded on Roller  $R_{2B}$  was 9.5% more than that in Roller  $R_{1A}$ . In spite of this reason, much lower strains were recorded in Roller  $R_2$  as compared to those observed in Roller  $R_1$ . The reason for this is that the material in Roller  $R_2$  was AISI 1060 high carbon steel with no heat treatment, whereas the material in Roller  $R_1$  was cast iron.

Table 4.3 summarizes the strain differences between the maximum and the minimum in principal directions and in the maximum shearing strains for the rosette strain gauge installed on both sides of all three rollers, at the first and last cycles of loading. The modulus of elasticity of Roller  $R_2$  was 207 GPa (30,000 ksi). Maximum principal strains

recorded during the 1<sup>st</sup> cycle were 425  $\mu\epsilon$  (tensile) and 638  $\mu\epsilon$  (tensile) for the two cyclic tests conducted on Roller R<sub>2</sub>, Side A and Side B, respectively. Multiplication of these two principal strains and the modulus of elasticity of Roller R<sub>2</sub> results in 88 MPa (12.8 ksi) and 132 MPa (19.2 ksi) respectively.

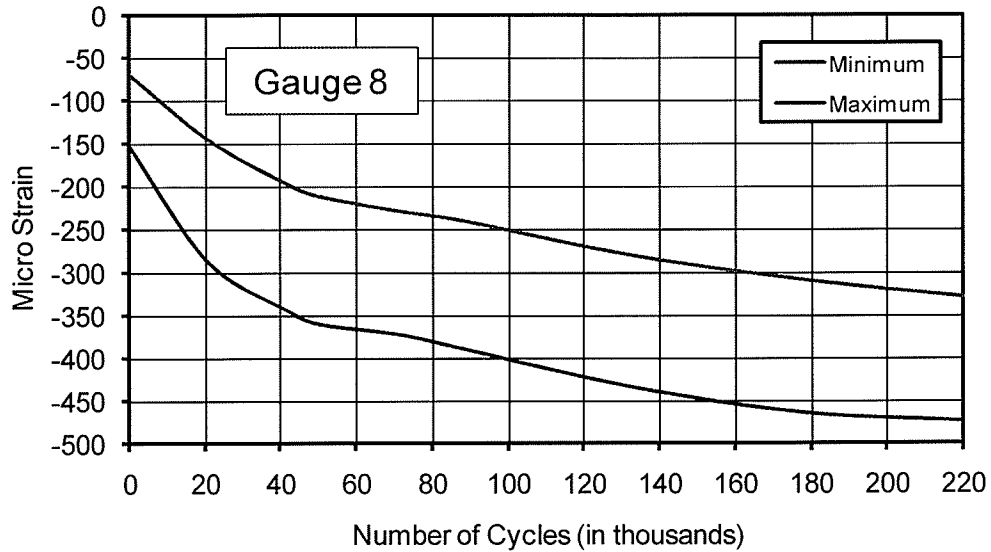


Fig. 4.14a Strain vs. number of cycles for gauge 8 in Roller R<sub>2A</sub>

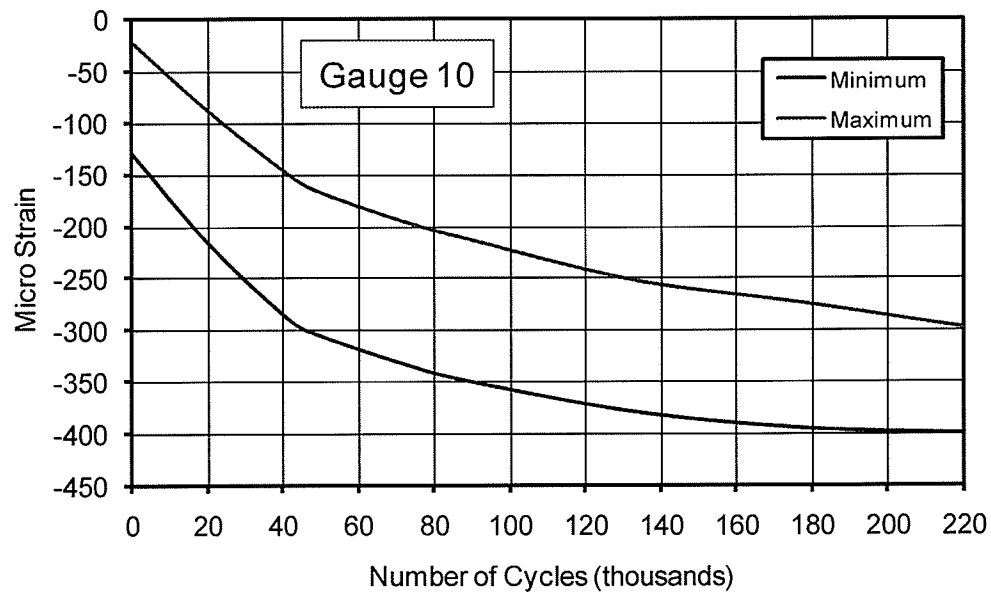


Fig. 4.14b Strain vs. number of cycles for gauge 10 in Roller R<sub>2A</sub>

#### 4.7. Strains in Roller R<sub>3</sub>

The differences between the maximum and minimum strains at each strain gauge location, during the first and last cycles of loading for the four tests conducted on Roller R<sub>3</sub>, are summarized in Tables 4.5 and 4.6, respectively. A similar trend was seen in the micro strains of all gauges installed on both sides of Roller R<sub>3</sub>. The majority of the strain gauges recorded a decrease in the tensile strain or a change from tensile strain to compressive strain.

Table 4.5 Micro strains in Roller R<sub>3A</sub> on Roller Path Plate P<sub>5</sub>

Gauge Location	Test R <sub>3A1</sub>				Test R <sub>3A2</sub>			
	At 1 <sup>st</sup> Cycle		At Last Cycle		At 1 <sup>st</sup> Cycle		At Last Cycle	
	Minimum Maximum	Difference	Minimum Maximum	Difference	Minimum Maximum	Difference	Minimum Maximum	Difference
5	22 106	84	-47 60	107	22 175	153	-24 114	138
6	23 153	130	-32 130	162	38 168	130	-8 130	138
7	-38 46	84	-53 31	84	-23 69	92	-8 84	92
8	84 168	84	4 125	121	69 176	107	38 139	101
9	-31 23	54	-69 16	85	-53 23	76	-53 23	76
10	38 167	129	-24 106	130	15 152	137	-27 106	133
11	-1 152	153	-47 99	146	-8 130	138	-50 106	156

Table 4.6 Micro strains in Roller R<sub>3B</sub> on Roller Path Plate P<sub>6</sub>

Gauge Location	Test R <sub>3B1</sub>				Test R <sub>3B2</sub>			
	At 1 <sup>st</sup> Cycle		At Last Cycle		At 1 <sup>st</sup> Cycle		At Last Cycle	
	Minimum Maximum	Difference	Minimum Maximum	Difference	Minimum Maximum	Difference	Minimum Maximum	Difference
5	0 169	169	-93 70	163	8 200	192	-53 106	159
6	31 199	168	-138 33	171	38 206	168	-24 125	149
7	-54 122	176	-104 91	195	-54 130	184	-110 98	208
8	57 187	130	-143 0	143	74 197	123	6 144	138
9	-85 83	168	-70 114	184	-122 54	176	-153 38	191
10	7 191	184	-157 46	203	30 206	176	-38 158	196
11	-6 186	192	-125 77	202	-13 155	168	-83 94	177

Only three strain gauges 7, 9, and 11 partially exhibited an increase in the compressive strain. Strain gauges 7 and 9 were part of three-element rosette strain gauge and were placed at 45° to a plane perpendicular to the rolling surface of roller path plate. The four cyclic tests conducted on both sides of Roller R<sub>3</sub> revealed exactly similar phenomena. Roller R<sub>3</sub> did not exhibit any significant change in the strain curves as compared to those in Roller R<sub>1</sub>. The maximum strains recorded during the 1<sup>st</sup> cycle were 168  $\mu\epsilon$  (tensile)

and  $176 \mu\epsilon$  (tensile) for the two cyclic Tests  $R_{3A1}$  and  $R_{3A2}$  conducted on Roller  $R_3$ , Side A, respectively. Similarly, the maximum strains recorded during the 1<sup>st</sup> cycle were  $199 \mu\epsilon$  (tensile) and  $206 \mu\epsilon$  (tensile) for the two cyclic Tests  $R_{3B1}$  and  $R_{3B2}$  conducted on Roller  $R_3$ , Side B, respectively. The average radial cyclic load recorded on Roller  $R_{3A2}$  was 4.15% higher than that in Roller  $R_{1A}$ . In spite of this, much lower strains were recorded in Roller  $R_3$  as compared to those observed in Roller  $R_1$ . The micro strains recorded in Roller  $R_3$  were even less than those found in Roller  $R_2$ , despite the fact that the average radial cyclic load recorded on Roller  $R_{2B}$  was 19.9% higher than that in Roller  $R_{3B2}$ . The reason for this is that the material in Roller  $R_3$  was AISI 1080 heat treated high carbon steel, whereas, the material in Roller  $R_2$  was high carbon steel without heat treatment.

#### **4.8 Strains in Plates $P_1$ and $P_2$**

Table 4.7 summarizes the differences between the maximum and minimum strains at each strain gauge location for roller path Plates  $P_1$  and  $P_2$ , during the first and last cycles of loading. Tensile strains were observed in almost all the strain gauges installed on all roller path plates. The reason for this is that during each cyclic test, a roller was in contact with the roller path plate at its centre and the gauges were installed on a surface perpendicular to the rolling surface, and 88.85 mm ( $3\frac{1}{2}$  in.) far from the centre of contact area. As the roller rolled on the roller path plate back and forth, the strains varied accordingly. Higher strains were seen in the central strain gauges 17, 18, and 19 as compared to gauges 15, 16, 20, and 21 in Plate  $P_1$ . Almost all of the strain gauges installed on both plates, exhibited both a decrease and an increase in the tensile strains or a change from tensile strain to compressive strain. Higher strains were observed in Plate

P<sub>2</sub> as compared to those in Plate P<sub>1</sub>; the reason was that the Plate P<sub>2</sub> had 4.67 kN (1.05 kips) more average compressive load than that on Plate P<sub>1</sub>. Plates P<sub>1</sub> and P<sub>2</sub> did not exhibit any significant change in the strain curves as compared to those in Roller R<sub>1</sub>. Plates P<sub>1</sub> and P<sub>2</sub> recorded maximum strains of 264  $\mu\epsilon$  and 422  $\mu\epsilon$  during the 1<sup>st</sup> cycle, respectively.

Table 4.7 Micro strains in roller path Plates P<sub>1</sub> and P<sub>2</sub>

Gauge Location	Plate P <sub>1</sub>				Plate P <sub>2</sub>			
	Test R <sub>1A</sub>				Test R <sub>1B</sub>			
	At 1 <sup>st</sup> Cycle		At Last Cycle		At 1 <sup>st</sup> Cycle		At Last Cycle	
	Minimum Maximum	Difference	Minimum Maximum	Difference	Minimum Maximum	Difference	Minimum Maximum	Difference
15	69 100	31	39 73	34	199 223	24	252 274	22
16	7 55	48	-14 28	42	184 214	30	276 305	29
17	152 214	62	111 183	72	212 243	31	297 335	38
18	193 264	71	171 241	70	377 422	45	471 519	48
19	64 128	64	50 112	62	269 314	45	315 361	46
20	7 55	48	-119 -80	39	185 208	23	162 208	46
21	8 68	60	-26 71	97	192 207	15	170 219	49

#### 4.9 Strains in Plates P<sub>3</sub> and P<sub>4</sub>

The differences between the maximum and the minimum strains at each strain gauge location for roller path Plates P<sub>3</sub> and P<sub>4</sub> are summarized in Table 4.8, during the first and last cycles of loading.

Table 4.8 Micro strains in roller path Plates P<sub>3</sub> and P<sub>4</sub>

Gauge Location	Plate P <sub>3</sub>				Plate P <sub>4</sub>			
	Test R <sub>2A</sub>				Test R <sub>2B</sub>			
	At 1 <sup>st</sup> Cycle		At Last Cycle		At 1 <sup>st</sup> Cycle		At Last Cycle	
	Minimum Maximum	Difference	Minimum Maximum	Difference	Minimum Maximum	Difference	Minimum Maximum	Difference
12	23 70	47	-8 46	54	60 122	62	14 90	76
13	31 70	39	-45 24	69	45 107	62	37 100	63
14	18 49	31	-35 18	53	68 107	39	39 84	45
15	15 53	38	-8 30	38	54 99	45	-3 54	57
16	0 46	46	-23 24	47	22 68	46	-1 59	60

All of the strain gauges installed on both plates, exhibited a decrease in tensile strain or a change from tensile strain to compressive strain. Higher tensile strains were observed in all the gauges installed on Plate P<sub>4</sub> as compared to those in Plate P<sub>3</sub>. The reason for this is that the average radial cyclic load on Plate P<sub>4</sub> was 12% higher than that in Plate P<sub>3</sub>. A

similar trend was seen in the strain curves of Plate P<sub>3</sub> to those of Plate P<sub>4</sub>. Much lower strains were recorded in Plates P<sub>3</sub> and P<sub>4</sub> as compared to those in Plates P<sub>1</sub> and P<sub>2</sub>. The reason was that the material in Plates P<sub>3</sub> through P<sub>6</sub>, was heat treated stainless steel SS 410, whereas, the material in Plates P<sub>1</sub> and P<sub>2</sub> was AISI 1050 medium carbon steel with no heat treatment. Plates P<sub>3</sub> and P<sub>4</sub> recorded maximum strains of 70  $\mu\epsilon$  and 122  $\mu\epsilon$  during the 1<sup>st</sup> cycle, respectively.

#### 4.10 Strains in Plates P<sub>5</sub> and P<sub>6</sub>

Tables 4.9 and 4.10 summarize the differences between the maximum and minimum strains at each strain gauge location for Plates P<sub>5</sub> and P<sub>6</sub>, respectively.

Table 4.9 Micro strains in roller path Plate P<sub>5</sub>

Gauge Location	Test R <sub>3A1</sub>				Test R <sub>3A2</sub>			
	At 1 <sup>st</sup> Cycle		At Last Cycle		At 1 <sup>st</sup> Cycle		At Last Cycle	
	Minimum Maximum	Difference	Minimum Maximum	Difference	Minimum Maximum	Difference	Minimum Maximum	Difference
12	15 76	61	-2 67	69	38 91	53	22 79	57
13	38 92	54	15 84	99	53 107	54	18 82	64
14	46 92	46	23 76	99	61 99	38	38 84	46
15	38 92	54	7 69	76	38 92	54	21 80	59
16	15 69	54	-7 53	60	23 76	53	-6 45	51

Table 4.10 Micro strains in roller path Plate P<sub>6</sub>

Gauge Location	Test R <sub>3B1</sub>				Test R <sub>3B2</sub>			
	At 1 <sup>st</sup> Cycle		At Last Cycle		At 1 <sup>st</sup> Cycle		At Last Cycle	
	Minimum Maximum	Difference	Minimum Maximum	Difference	Minimum Maximum	Difference	Minimum Maximum	Difference
12	8 84	76	-24 50	74	39 100	61	8 81	73
13	29 106	77	-36 25	61	29 91	62	-32 52	84
14	38 91	53	-2 46	48	53 99	46	1 68	67
15	31 84	53	-25 41	66	23 100	77	-20 60	80
16	7 61	54	-46 16	62	-8 68	76	-49 29	78

All of the strain gauges installed on both plates exhibited a decrease in tensile strain or a change from tensile strain to compressive strain. Higher strains were recorded in Test R<sub>3A2</sub> as compared to those of Test R<sub>3A1</sub>. The reason was that the average compressive load recorded in Test R<sub>3A2</sub> was 4.6% higher than that in Test R<sub>3A1</sub>. Plates P<sub>5</sub> and P<sub>6</sub> did not exhibit any significant change in the strain curves over the number of cycles. Plate P<sub>5</sub> recorded maximum tensile strains of 92  $\mu\epsilon$  and 107  $\mu\epsilon$  during the 1<sup>st</sup> cycle for the two cyclic Tests R<sub>3A1</sub> and R<sub>3A2</sub>, respectively. Similarly, Plate P<sub>6</sub> recorded maximum tensile strains of 106  $\mu\epsilon$  and 100  $\mu\epsilon$  during the 1<sup>st</sup> cycle for the two cyclic Tests R<sub>3B1</sub> and R<sub>3B2</sub>, respectively.

#### **4.11 Indentation Measurements**

At the end of each cyclic test, the test-setup was dismantled and indentation measurements were taken for each roller path plate using the set-up shown in Fig. 3.25. Plate P<sub>1</sub> exhibited a maximum indentation of 1.48 mm (0.0583 in.) after one million cycles of repeated loading, whereas, Plate P<sub>2</sub> exhibited a maximum indentation of 1.21 mm (0.0476 in.). The difference in the indentation depths for the two plates was due to the fact that Plate P<sub>1</sub> was subjected to 181,274 (22%) more number cycles of repeated loading than that in Plate P<sub>2</sub>.

Plates P<sub>3</sub> and P<sub>4</sub> were subjected to 220,000 and 200,000 number of cycles of repeated loading, respectively, but they recorded a very low indentation of 0.03 mm (0.0012 in.) and 0.11 mm (0.0043 in.), respectively. This shows that these plates performed very well in the cyclic testing as compared to Plates P<sub>1</sub> and P<sub>2</sub>. The reason was that these plates were heat-treated stainless steel as compared to Plates P<sub>1</sub> and P<sub>2</sub>. The maximum indentation in Plate P<sub>5</sub> after 200,000 and 400,000 cycles of repeated loading was 0.05 mm (0.00197 in.) and 0.12 mm (0.0047 in.), respectively. After 200,000 and 400,000 cycles of repeated loading, Plate P<sub>6</sub> went through a maximum indentation of 0.02 mm (0.00079 in.) and 0.09 mm (0.00354 in.), respectively. These two plates, P<sub>5</sub> and P<sub>6</sub>, also performed very well with respect to the indentation depth.

#### **4.12 Inspection of Specimens**

Before and after each cyclic test, pictures were taken for all specimens. At the end of each cyclic test, the rolling contact surface of all specimens was examined by visual

inspection. Tested contact areas of both sides of Roller R<sub>1</sub> are shown in Fig. 4.15. Despite a very small distance of travel 75 mm (2.95 in.), traveled by Roller R<sub>1</sub> in each cycle, the contact areas of Roller R<sub>1</sub> went through severe deformation and distortion. Two sets of major and minor visual cracks were observed. Cracks were vertical, horizontal, diagonal as well as longitudinal. Almost a similar trend and behavior was observed in the crack pattern of Roller R<sub>1B</sub>, which was subjected to 818,726 cycles of repeated loading. There were more cracks on Side A as compared to those of Side B.

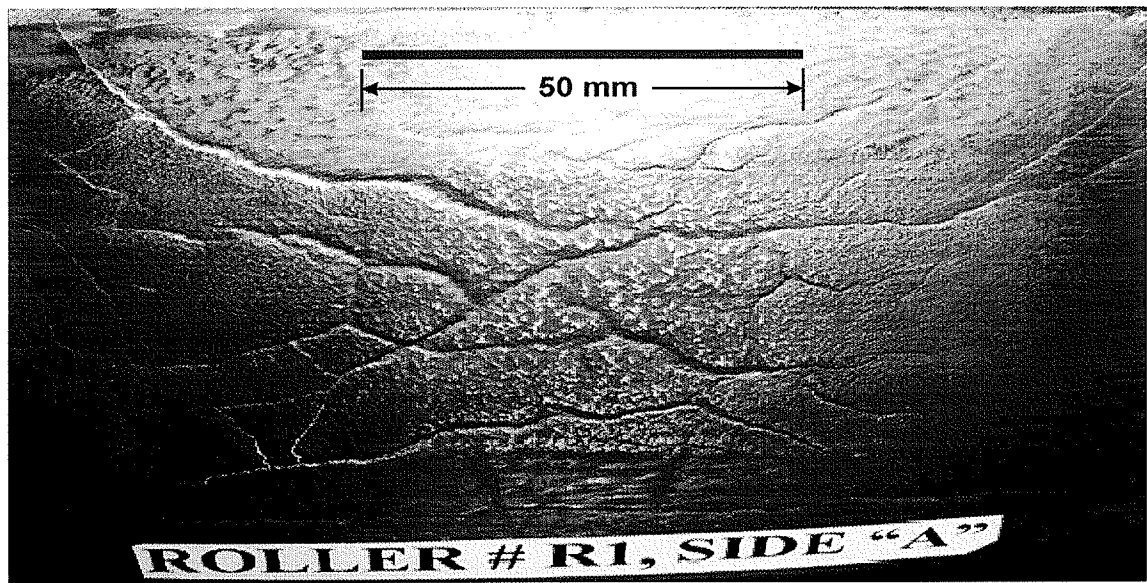


Fig. 4.15a Roller R<sub>1</sub> Side A after cyclic loading

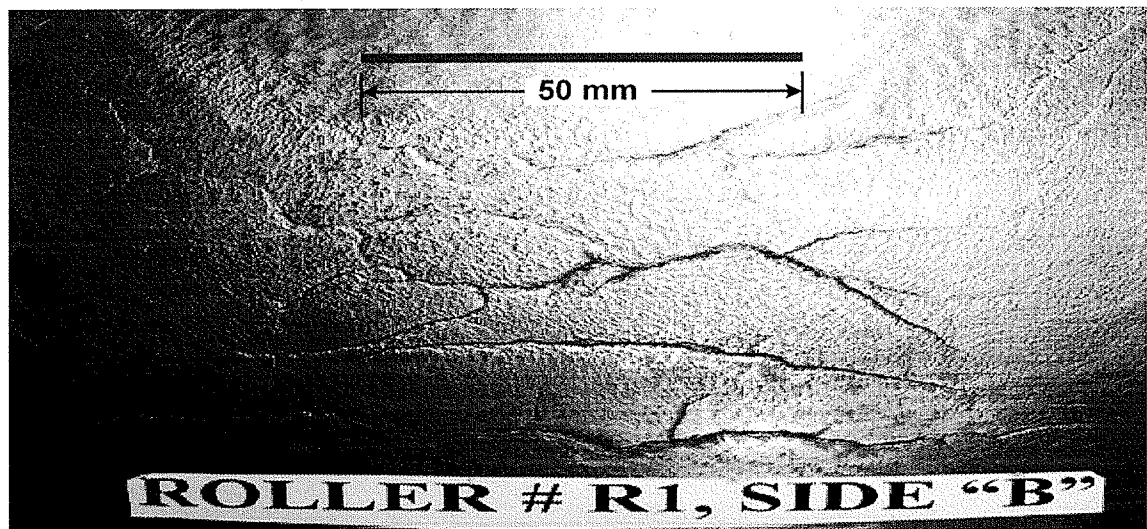


Fig. 4.15b Roller R<sub>1</sub> Side B after cyclic loading

Figure 4.16 shows the tested contact area of Roller  $R_{2A}$  subjected to 220,000 cycles of repeated loading. This roller performed very well as it is evident from this figure. There was no sign of any kind of crack or deformation in the tested contact areas of both sides of Roller  $R_2$ . There was no sign of any kind of crack or deformation in the tested contact areas of either side of Roller  $R_3$ . There was only discoloration of the surface areas. By visual inspection, Roller  $R_3$  also performed very well.

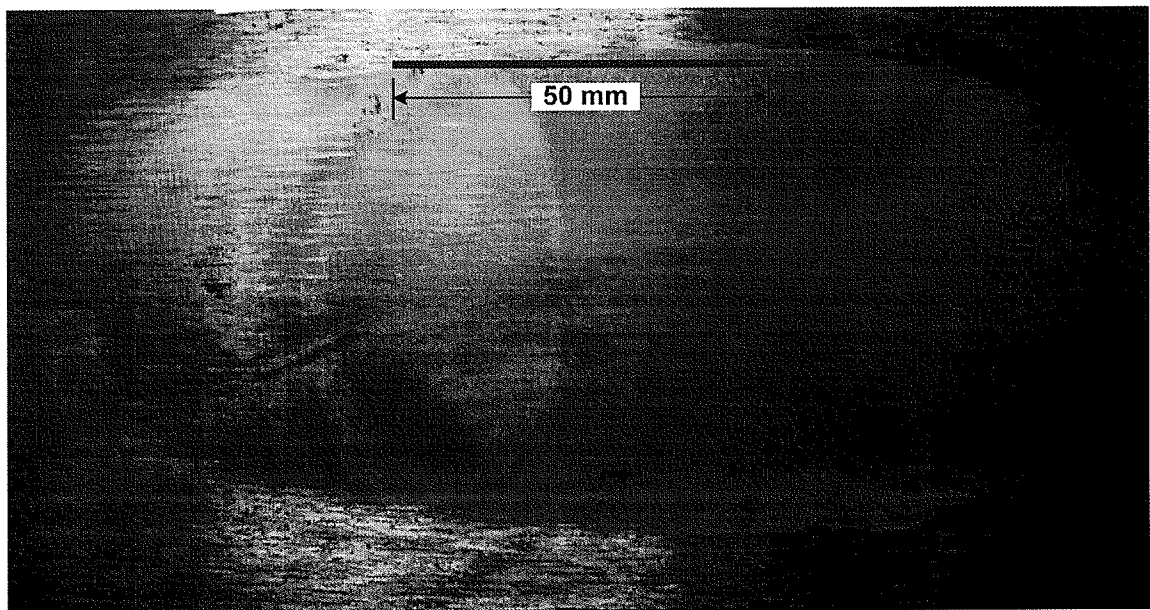


Fig. 4.16 Roller  $R_{2A}$  after 220,000 cycles of repeated loading

Figure 4.17 shows a typical plate before cyclic testing and the tested contact areas of Plates  $P_1$  and  $P_2$  after cyclic testing. As evident from the figures, many cracks along with severe deformation and distortion were seen in these two plates. Careful review of the contact areas revealed that the two contact surfaces of roller and plate in Tests  $R_{1A}$  and  $R_{1B}$  had similar crack pattern and deformation style. The material in these two plates was AISI 1050 medium carbon steel with no heat treatment.



Fig. 4.17a A typical roller plate before cyclic testing

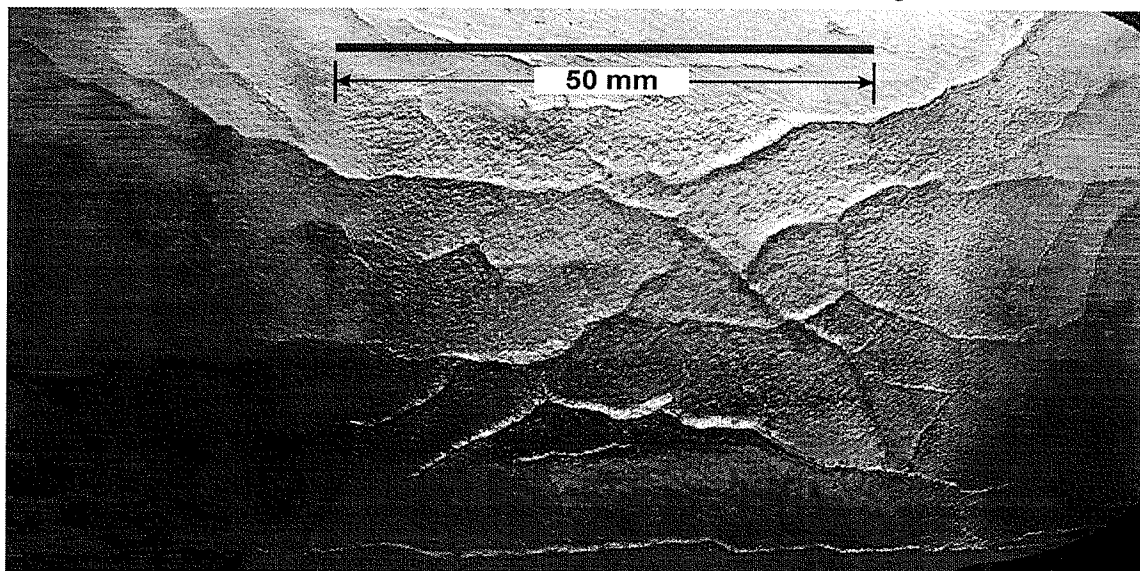


Fig. 4.17b Roller path Plate P<sub>1</sub> after cyclic testing

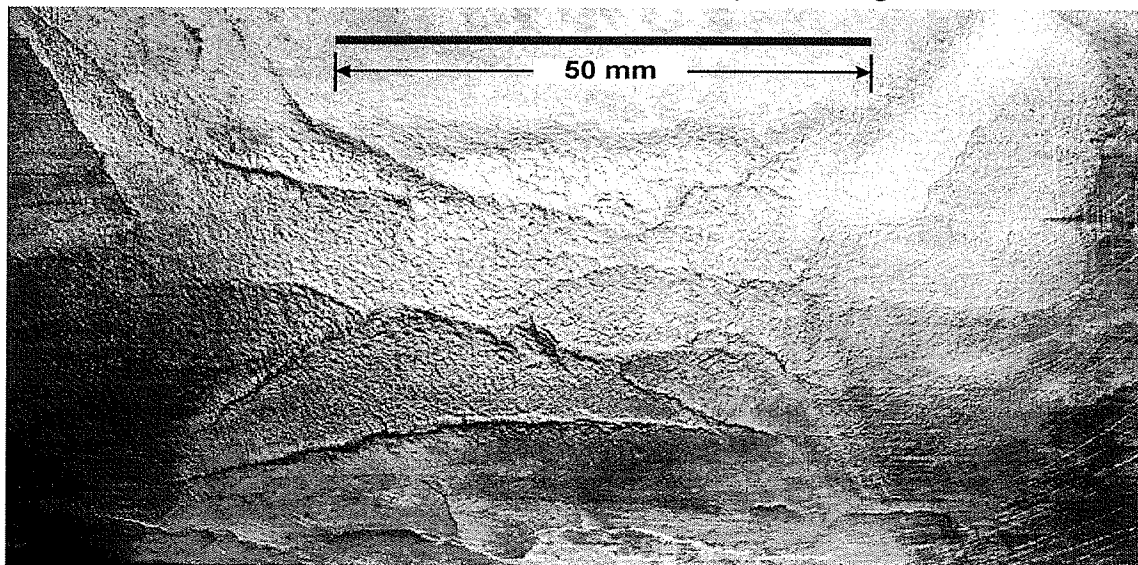


Fig. 4.17c Roller path Plate P<sub>2</sub> after cyclic testing

There was no sign of any kind of crack in the tested contact areas of Plates P<sub>3</sub> through P<sub>6</sub>. The performance of these plates was much superior to that of Plates P<sub>1</sub> and P<sub>2</sub>.

#### 4.13 Scanning Electron Microscope Images

In order to observe the extent of damage that took place under cyclic testing, tested contact areas of all specimens were scanned using a scanning electron microscope, shown in Fig.3.26, and computer-controlled optical microscope. Two samples were extracted from each tested contact area of all rollers and roller path plates; one for scanning the contact surface and the other for scanning the inside surface perpendicular to the contact surface in order to observe the extent and depth of damage. Figs. 4.18 through 4.21 show the tested and non-tested surface areas of Roller R<sub>1</sub> using both SEM and computer-controlled optical microscope. Large cracks are very clearly seen in these figures.

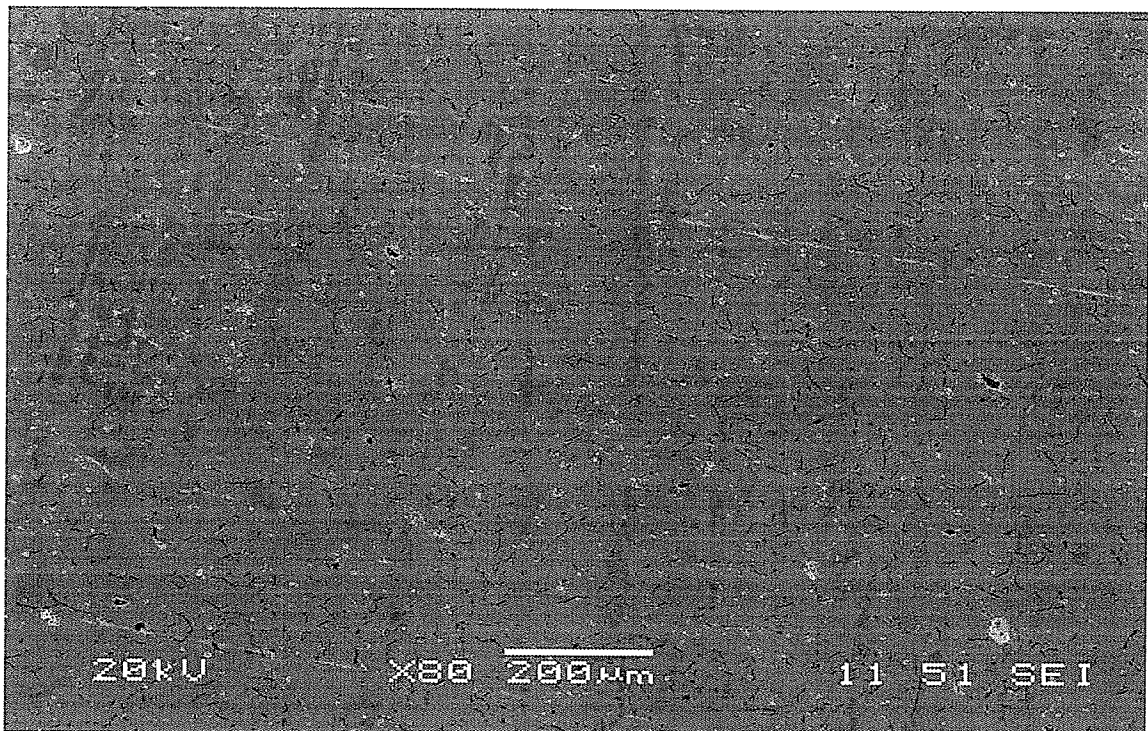


Fig. 4.18 Roller R<sub>1</sub>, control specimen, using SEM

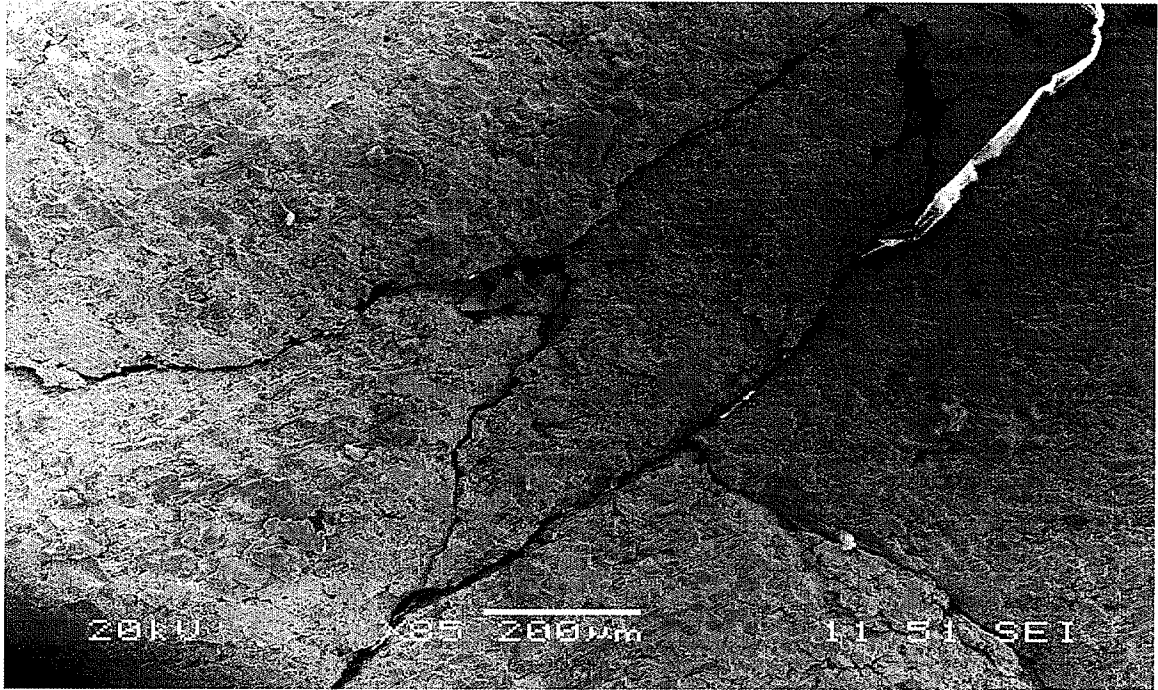


Fig. 4.19 Roller R<sub>1A</sub>, inside surface perpendicular to the tested contact surface showing depth of damage, using scanning electron microscope

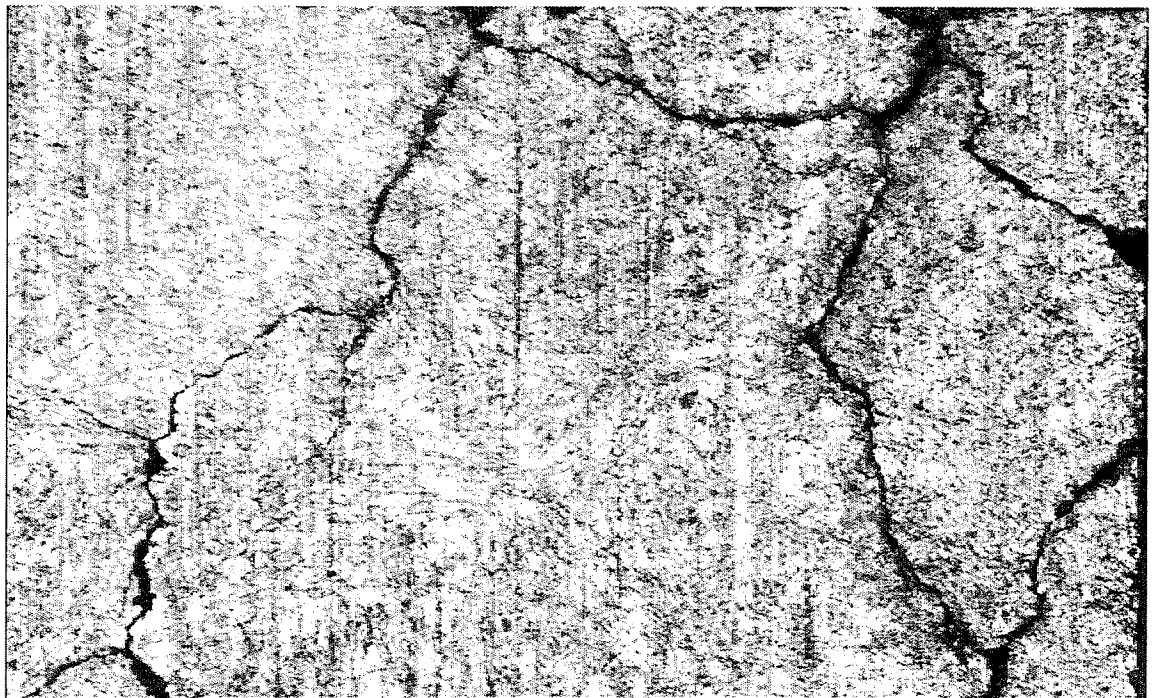


Fig. 4.20 Roller R<sub>1A</sub>, inside surface perpendicular to the tested contact surface showing depth of damage, using an optical microscope, (X200)



Fig. 4.21 Roller R<sub>1B</sub>, inside surface perpendicular to the tested contact surface showing depth of damage, using an optical microscope, (X200)

Control and tested contact surface areas of Rollers R<sub>2</sub> and R<sub>3</sub> are shown in Figs. 4.22 through 4.25. No sign of any kind of crack was observed in these two rollers.

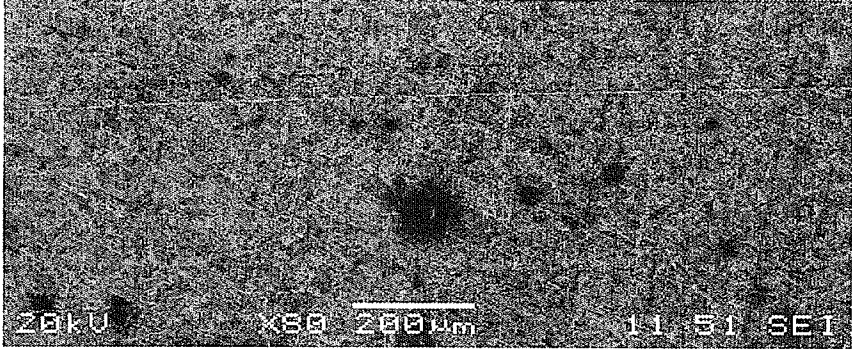


Fig. 4.22 Roller R<sub>2</sub>, control specimen, using SEM

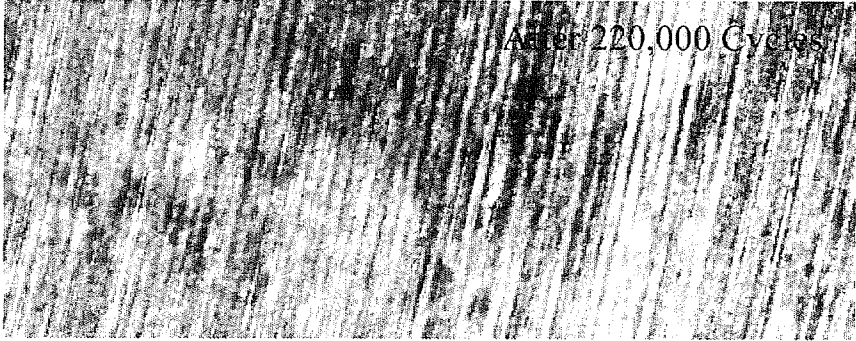


Fig. 4.23 Tested surface area of Roller R<sub>2A</sub> using an optical microscope, (X200)

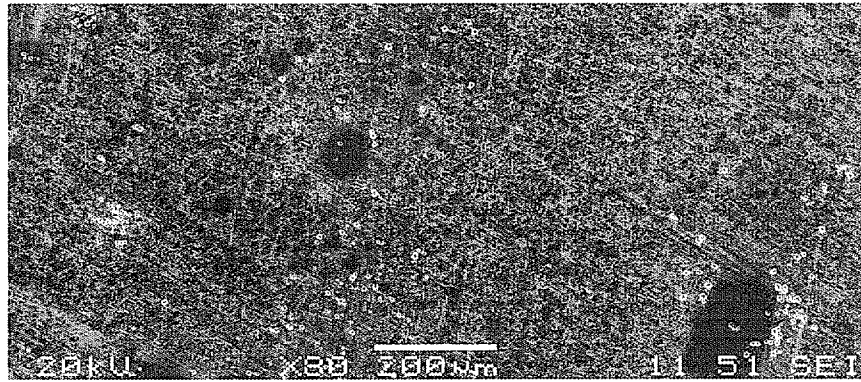


Fig. 4.24 Roller R<sub>3</sub>, control specimen, using SEM

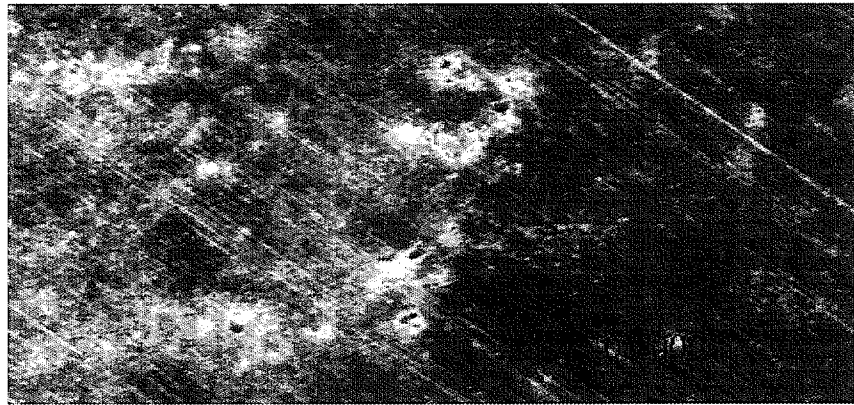


Fig. 4.25 Tested surface area of Roller R<sub>3</sub>, using an optical microscope, (X200)

Figures 4.26 through 4.28 show the control and tested surface areas of specimens extracted from Plates P<sub>1</sub> and P<sub>2</sub>. Several large cracks are evident in these plates.

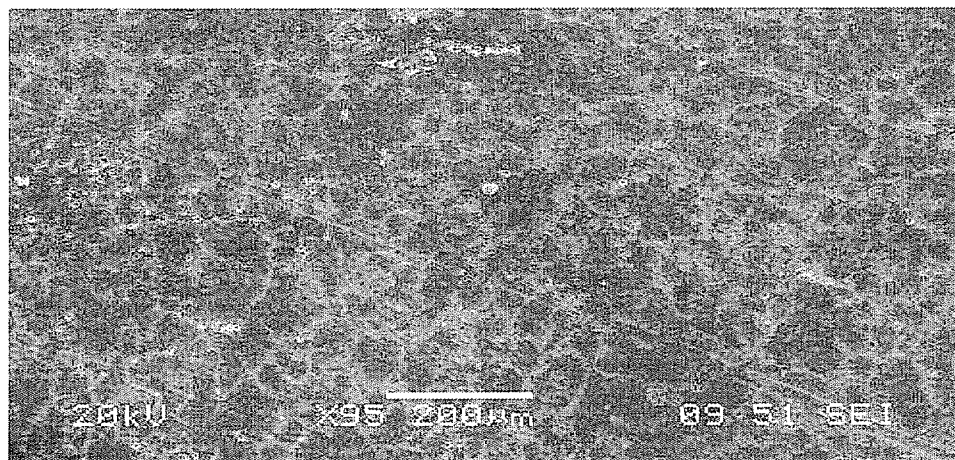


Fig. 4.26 Control specimen, Plate P<sub>1</sub>, using SEM



Fig. 4.27 Tested contact surface area of Plate P<sub>1</sub>, using SEM

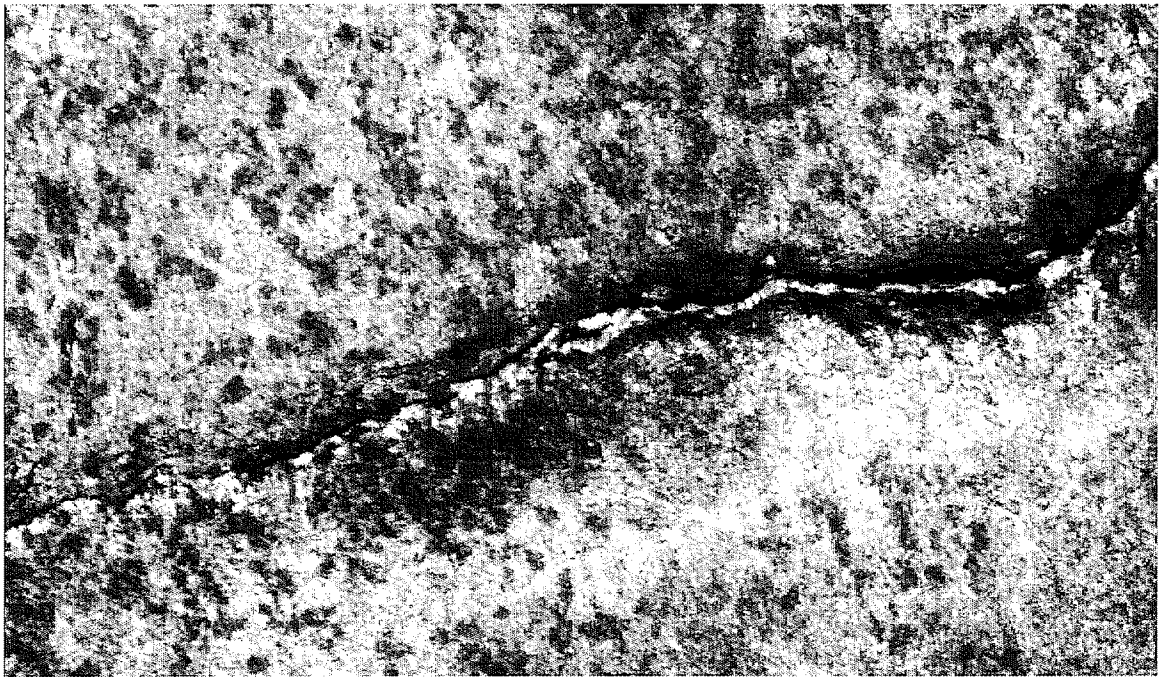


Fig. 4.28 Plate P<sub>2</sub>, inside surface perpendicular to the tested contact surface showing depth of damage, using an optical microscope (X200)

A typical control specimen of heat-treated stainless steel plate (P<sub>3</sub> through P<sub>6</sub>) is shown in Fig. 4.29. The tested contact surface area of Plate P<sub>5</sub> after 400,000 cycles of repeated loading is shown in Fig. 4.30. The performance of these four plates was much superior to that of Plates P<sub>1</sub> and P<sub>2</sub>.

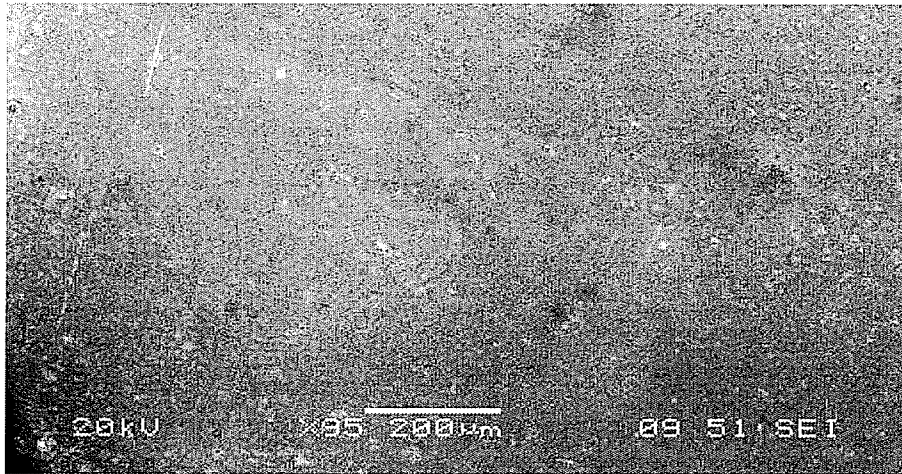


Fig. 4.29 Plate P<sub>3</sub>, control specimen, using SEM

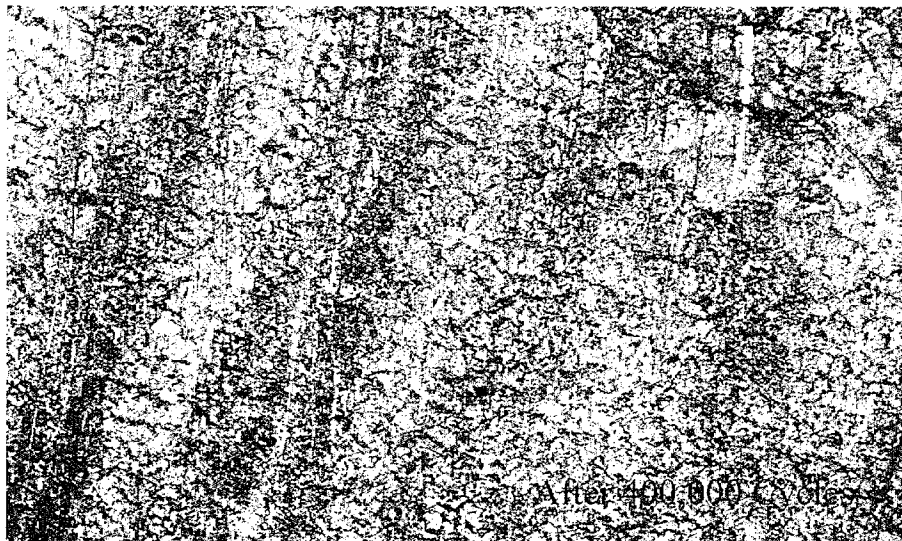


Fig. 4.30 Tested contact surface area of Plate P<sub>5</sub>, using an optical microscope, (X200)

#### 4.14 Summary

Table 4.11 summarizes the results obtained through experimental investigation that involved laboratory testing of three rollers and six roller path plates under cyclic loading. The maximum strains recorded during the 1<sup>st</sup> cycle were +2057  $\mu\epsilon$ , +267  $\mu\epsilon$ , and +176  $\mu\epsilon$  for the Rollers R<sub>1B</sub>, R<sub>2B</sub>, and R<sub>3A2</sub>, respectively. The average radial cyclic load on these rollers was 829.5 kN (186½ kips), 903 kN (203 kips), and 859 kN (193 kips),

respectively. Although, the average radial cyclic load on Roller  $R_{3A2}$  was 3.6% higher than that in Roller  $R_{1B}$ , the maximum strain recorded during the 1<sup>st</sup> cycle on Roller  $R_{1B}$  was 11.7 times more than the maximum strain recorded during the 1<sup>st</sup> cycle on Roller  $R_{3A2}$ . Likewise, despite the average radial cyclic load on Roller  $R_{2B}$  was 8.9% higher than that in Roller  $R_{1B}$ , the maximum strain recorded during the 1<sup>st</sup> cycle on Roller  $R_{1B}$  was 7.7 times more than the maximum strain recorded during the 1<sup>st</sup> cycle on Roller  $R_{2B}$ .

The maximum principal strains recorded during the 1<sup>st</sup> cycle were +2557  $\mu\epsilon$ , +638  $\mu\epsilon$ , and +241  $\mu\epsilon$  for the Rollers  $R_{1B}$ ,  $R_{2B}$ , and  $R_{3A2}$ , respectively. Although, the average radial cyclic load on Roller  $R_{3A2}$  was 3.6% higher than that in Roller  $R_{1B}$ , the maximum principal strain recorded during the 1<sup>st</sup> cycle on Roller  $R_{1B}$  was 10.6 times more than the maximum strain recorded during the 1<sup>st</sup> cycle on Roller  $R_{3A2}$ . Likewise, despite the average radial cyclic load on Roller  $R_{2B}$  was 8.9% higher than that in Roller  $R_{1B}$ , the maximum principal strain recorded during the 1<sup>st</sup> cycle on Roller  $R_{1B}$  was 4 times more than the maximum principal strain recorded during the 1<sup>st</sup> cycle on Roller  $R_{2B}$ .

It is clear from the above comparisons that the material in Roller  $R_1$  was less stiff as compared to those of Rollers  $R_2$  and  $R_3$ . The high values of strains found in Roller  $R_1$  are most likely due to micro cracking on the roller contact surface. In addition, the material in Roller  $R_3$  is more rigid than that of Roller  $R_2$ . This hypothesis is also confirmed by BHN, SEM examination, and physical inspection of the rollers after cyclic testing.

The maximum strains recorded during the 1<sup>st</sup> cycle were +422  $\mu\epsilon$  and +107  $\mu\epsilon$  in roller path Plates P<sub>2</sub> and P<sub>5</sub> in Tests R<sub>1B</sub> and R<sub>3A2</sub>, respectively. The average radial load on these two roller path plates was 829.5 kN and 859 kN, respectively. Although, the average cyclic load on roller path Plate P<sub>5</sub> in Test R<sub>3A2</sub> was 3.6% higher than that in roller path Plate P<sub>2</sub> in Test R<sub>1B</sub>, the maximum strain recorded during the 1<sup>st</sup> cycle on roller path Plate P<sub>2</sub> was 4 times more than the maximum strain recorded during the 1<sup>st</sup> cycle on roller path Plate P<sub>5</sub> in Test R<sub>3A2</sub>. This clearly indicates that the material in roller path Plates P<sub>3</sub> through P<sub>6</sub> is far superior to that in roller path Plates P<sub>1</sub> and P<sub>2</sub>. This premise is also confirmed by the BHN, SEM testing, and physical examination of the plates after cyclic testing.

The average radial compressive load applied on rollers in laboratory testing during cyclic movement varied from 753.17 kN (169.31 kips) to 903.21 kN (203.04 kips). The maximum service load limit for 838 mm (33 in.) diameter rollers is 734 kN (165 kips) and 1050 kN (236 kips) for serviceability and strength criteria, respectively. The objective of applying radial load during cyclic testing was to check the serviceability criteria and not strength. The static ultimate strength of these rollers is quite high. The indentation profile of roller path Plates P<sub>1</sub> and P<sub>2</sub> after cyclic testing failed serviceability criteria, whereas, roller path Plates P<sub>3</sub> through P<sub>6</sub> passed serviceability criteria. Roller path plate deformation increases frictional forces that lead to higher principal tensile stresses as predicted in the literature discussed in Section 2.3. Lubricating the roller path plate surface could help in reducing the frictional forces but not if the indentation is very high.

The rim surface, where strain gauges were installed on rollers, was perpendicular to the rim-rolling surface and its location was 44.5 mm far from the contact point on the roller. The major visible cracks were found on the contact surfaces of Roller  $R_1$  and roller path Plates  $P_1$  and  $P_2$  only. No visible cracks were found on the location where strain gauges were installed on rollers and roller path plates. The maximum principal stresses calculated at the 1<sup>st</sup> cycle were 264 MPa, 131 MPa, and 67.6 MPa for Roller  $R_{1B}$ ,  $R_{2B}$ , and  $R_{3B2}$ , respectively. These principal stresses are lower than the yield strength of the respective rollers. There was a need to carry out a finite element analysis of the rollers and roller path plates in order to find out the type and magnitude of stresses developed in the contact zone. Based on the finite element results, fatigue analysis of the rollers and roller path plates could be carried out. This would eventually lead to the calculation of fatigue life of rollers and roller path plates. At the end of the day, one would be able to answer the question related to the main cause of fatigue failure of rollers and roller path plates.

Table 4.11 Summary of laboratory test results

Specimen	Test	Hardness BHN	Modulus of Elasticity (GPa)	Average Cyclic Load (kN)	Number of Cycles (thousand)	Maximum Strain at 1 <sup>st</sup> Cycle, $\mu\epsilon$	Maximum Principal Strain at 1 <sup>st</sup> Cycle, $\mu\epsilon$	<sup>1</sup> Maximum Principal Stress at 1 <sup>st</sup> Cycle, MPa	Indentation Depth, mm	Physical Damage
R <sub>1</sub>	R <sub>1A</sub>	219	103	824.8	1000	+1751	+1821	188.3	NA	Visible Cracks
	R <sub>1B</sub>			829.5	818.7	+2057	+2557	264.4	NA	
R <sub>2</sub>	R <sub>2A</sub>	373	207	806.5	220	+184	+425	88.0	NA	No Cracks
	R <sub>2B</sub>			903.2	200	+267	+638	132.0	NA	
R <sub>3</sub>	R <sub>3A1</sub>	473		821.3	200	+168	+260	53.8	NA	No Cracks
	R <sub>3A2</sub>			859.0	400	+176	+241	49.9	NA	
	R <sub>3B1</sub>			815.1	200	+199	+242	50.1	NA	
	R <sub>3B2</sub>			753.2	400	+206	+326	67.5	NA	
P <sub>1</sub>	R <sub>1A</sub>	291		824.8	1000	+264	NA	NA	1.48	Visible Cracks
P <sub>2</sub>	R <sub>1B</sub>			829.5	818.7	+422	NA	NA	1.21	
P <sub>3</sub>	R <sub>2A</sub>	364		806.5	220	+70	NA	NA	0.03	No Cracks
P <sub>4</sub>	R <sub>2B</sub>			903.2	200	+122	NA	NA	0.11	
P <sub>5</sub>	R <sub>3A1</sub>		821.3	200	+92	NA	NA	0.05		
P <sub>5</sub>	R <sub>3A2</sub>		859.0	400	+107	NA	NA	0.12		
P <sub>6</sub>	R <sub>3B1</sub>		815.1	200	+106	NA	NA	0.02		
P <sub>6</sub>	R <sub>3B2</sub>		753.2	400	+100	NA	NA	0.09		

<sup>1</sup>Maximum Principal Stress = Maximum Principal Strain  $\times$  Modulus of Elasticity

### 5.1 Introduction

Although an experimental investigation of structural members and components is an excellent source of information regarding their performance characteristics, this may not always be feasible due to the high cost associated with physical testing. An alternative source of information is the use of finite element programs. If properly evaluated, and professionally administered, such programs can be very valuable tools at relatively low cost (Muzyczka 1992). A finite element (FE) analysis was conducted on a three dimensional model of a roller and a plate using the ANSYS<sup>®</sup> general-purpose finite element program, version 10 (Swanson 2005). The roller and plate were modeled together as a contact stress problem. The university “research version” of the ANSYS<sup>®</sup> is capable of solving maximum of 512,000 degrees of freedom (DOF). Contact stress problems are highly nonlinear and require significant computer resources to solve. It is important to understand the physics of the problem and take time to set up the model to run as efficiently as possible.

### 5.2 Finite Element Model

The geometry of roller and roller path plate was created in millimeters and the values of modulus of elasticity and external load in terms of pressure were entered in the ANSYS<sup>®</sup> program as  $\text{N/mm}^2$ . Consequently, all resulting stress values are in Mega-Pascal (MPa). Material and geometric non-linearities were not considered in the analysis. The Gatke circular fiber bushing was also not modeled and the roller was considered as one single material.

The computer run time was reduced by taking advantage of the symmetric geometry of the roller and roller path plate. As a result, initially one-quarter of the roller was modeled along with one-quarter of roller path plate as a contact stress problem. Because of the limited DOF (512,000) in the university ANSYS<sup>®</sup> version and in order to achieve more accurate results, the roller geometry was further reduced to one-eighth of the original size, as shown in Fig. 5.1. One quarter of roller path plate was used, as shown in Fig. 5.1.

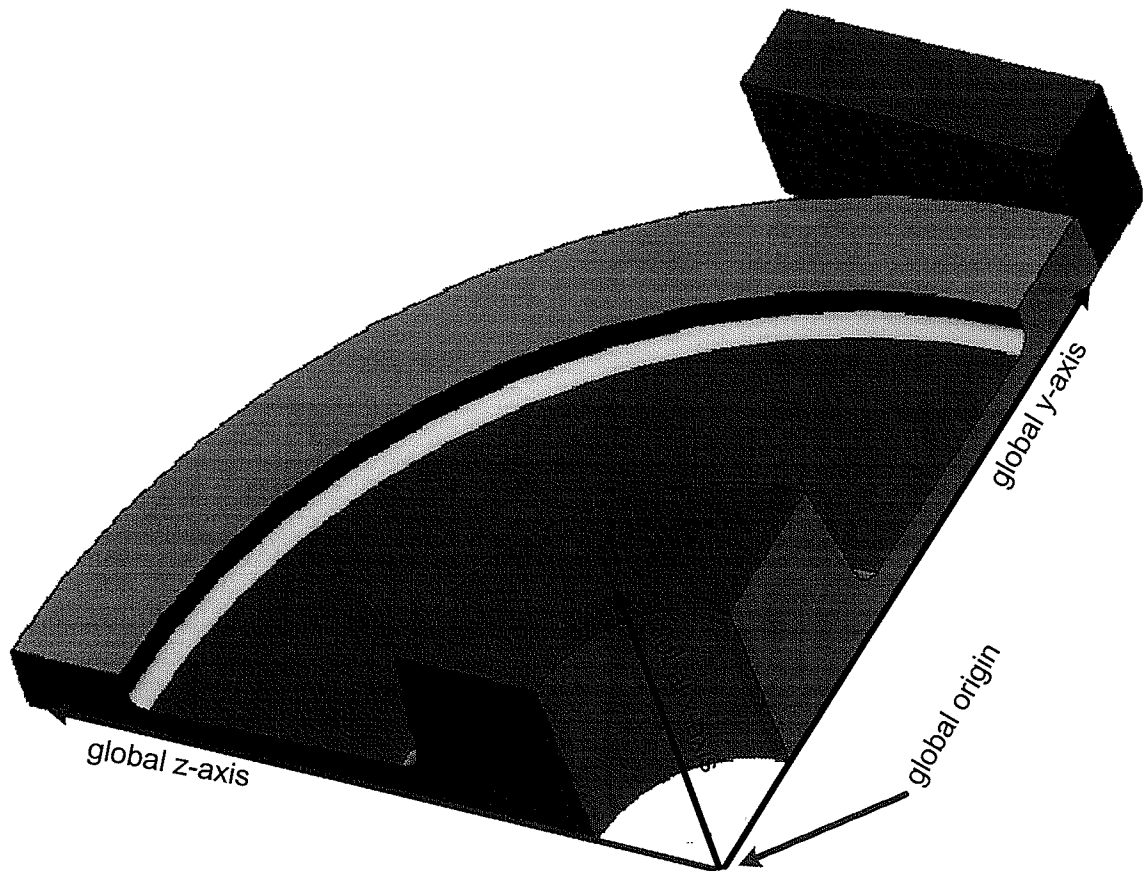


Fig. 5.1 One-eighth of a roller along with one quarter of a roller path plate

The solution of the FE model was obtained by writing ANSYS<sup>®</sup> executable commands in a file and the file was run in ANSYS<sup>®</sup> batch mode. The material properties used in FE model were taken from Table 3.3 and were kept constant for all ANSYS<sup>®</sup> runs. The cast iron Roller  $R_1$  was tested on roller path Plates  $P_1$  and  $P_2$ . Thus, one program  $R_1P_1$  was

developed in ANSYS® to analyze Roller R<sub>1</sub> and Plates P<sub>1</sub> and P<sub>2</sub>. The listing of this program is given in Appendix B. Because of the three 63.5 mm (2½ in.) diameter handling holes spaced at 120° in the cast iron Roller R<sub>1</sub>, there were two options to model the same roller; one option was to apply the external load between the handling holes and the other option was to apply the external load through one of the handling holes. Since the later is more critical, it was adopted in the program R<sub>1</sub>P<sub>1</sub>. The program R<sub>1</sub>P<sub>1</sub> was run two times, once with an external load of 838 kN (188½ kips) to simulate laboratory testing of Roller R<sub>1A</sub> with Plate P<sub>1</sub> and a second time with an external load of 734 kN (165 kips) to simulate service load conditions.

The geometries of Rollers R<sub>2</sub> and R<sub>3</sub> were exactly the same, whereas, the geometry of cast iron Roller R<sub>1</sub> was slightly different from that of Rollers R<sub>2</sub> and R<sub>3</sub>. The modulus of elasticity and the Poisson's ratio of Rollers R<sub>2</sub> and R<sub>3</sub> were also the same and these two rollers were tested on heat treated stainless steel Plates P<sub>3</sub> through P<sub>6</sub>. Therefore, one program R<sub>3</sub>P<sub>3</sub> was developed in ANSYS® to analyze Rollers R<sub>2</sub> and R<sub>3</sub> and Plate P<sub>3</sub> through P<sub>6</sub>. The program R<sub>3</sub>P<sub>3</sub> was also run two times, once with an external load of 814 kN (183 kips) to simulate laboratory testing of R<sub>2A</sub> and R<sub>3A1</sub> and a second time with an external load of 734 kN (165 kips) to simulate service load conditions.

The roller and plate volume was divided into several small segments and two types of solid structural brick elements were used in the FE model. A 3-D 20-noded SOLID95 structural brick element was incorporated in the small contact zone volumes of roller and plate, whereas, 3-D 8-noded SOLID45 brick element was used in the rest of all volume

segments of roller and plate. Both elements have three degrees of freedom at each node; namely, translation in the x, y, and z directions. A hexahedral shape for both elements was adopted in roller and in roller path plate as typically shown in Fig. 5.2. The degree of fineness of mesh was achieved near the contact zones of both roller and plate.

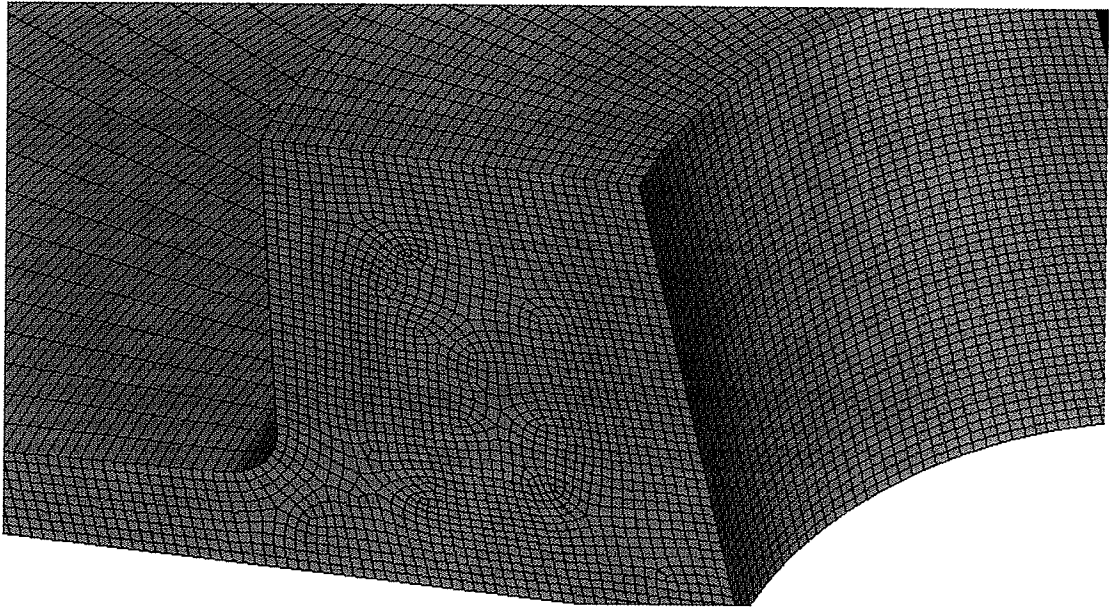


Fig. 5.2 Hexahedral shape of elements in roller

Two types of contact structural surface elements were used in the FE model. A TARGE170 element was used in the small contact area of roller on top of the SOLID95 elements, whereas, a CONTA175 element was used in the small contact area of plate on top of the SOLID95 elements. The model  $R_1P_1$  consisted of a total of 511,763 nodes, whereas, model  $R_3P_3$  had 511,913 nodes. The CPU run time, using specially built personal computer with 2.93 GHz Intel® Dual Core™ 2 Extreme Processor, 4 GB of RAM, 64-bit version of both Windows XP operating system and ANSYS®, was 29½ days.

### **5.3 Boundary Conditions**

The global rectangular xyz coordinate system is shown in Fig. 5.1, with the origin being at the centre of the roller hole. The symmetrical boundary conditions (zero out-of-plane translation) were applied on two surfaces of roller and two surfaces of roller path plate: on global xy-plane and on global yz-plane, as shown in Fig. 5.3. The area of the back of the plate was fixed (zero translation) in global y-direction only. The external load was applied in terms of pressure on an inside roller-hole area. The pressure was calculated by dividing the external load by a rectangular area obtained by the product of roller-hole diameter and roller hub height. Because of the crown radius in all rollers, the roller and roller path plate in both models were in contact at a single point only before the application of external pressure, as typically shown in Fig. 5.3. The fixed boundary condition (zero translation in y-direction only) applied to the back of the plate and the application of external load in terms of pressure on an inside roller-hole area represents exactly the same situation as that of laboratory testing.

### **5.4 Finite Element Results**

Typical results obtained from the ANSYS® FE analysis included colored stress contour plots indicating high stress concentrations and plots showing the variation of stresses along the selected paths in roller and in roller path plate.

#### **5.4.1 Program R<sub>1</sub>P<sub>1</sub> with External Load of 838 kN**

In this section, results of model R<sub>1</sub>P<sub>1</sub> run with the external load of 838 kN (188½ kips) are presented. The external load of 838 kN applied in laboratory testing in R<sub>1A</sub> and in FE analysis was 12.41% higher than the actual maximum service load of 734 kN (165 kips).

#### 5.4.1.1 Cast Iron Roller R<sub>1</sub>

The yield strength of cast iron Roller R<sub>1</sub> was 196 MPa (28.4 ksi). The contact area between roller and plate after the application of external load was found to be approximately equal to 161 mm<sup>2</sup> (¼ in<sup>2</sup>). This contact area was one-quarter of an elliptic-shape with major axis of 20.5 mm (0.81 in.) in x-axis and minor axis of 10 mm (0.39 in.) in z-axis.

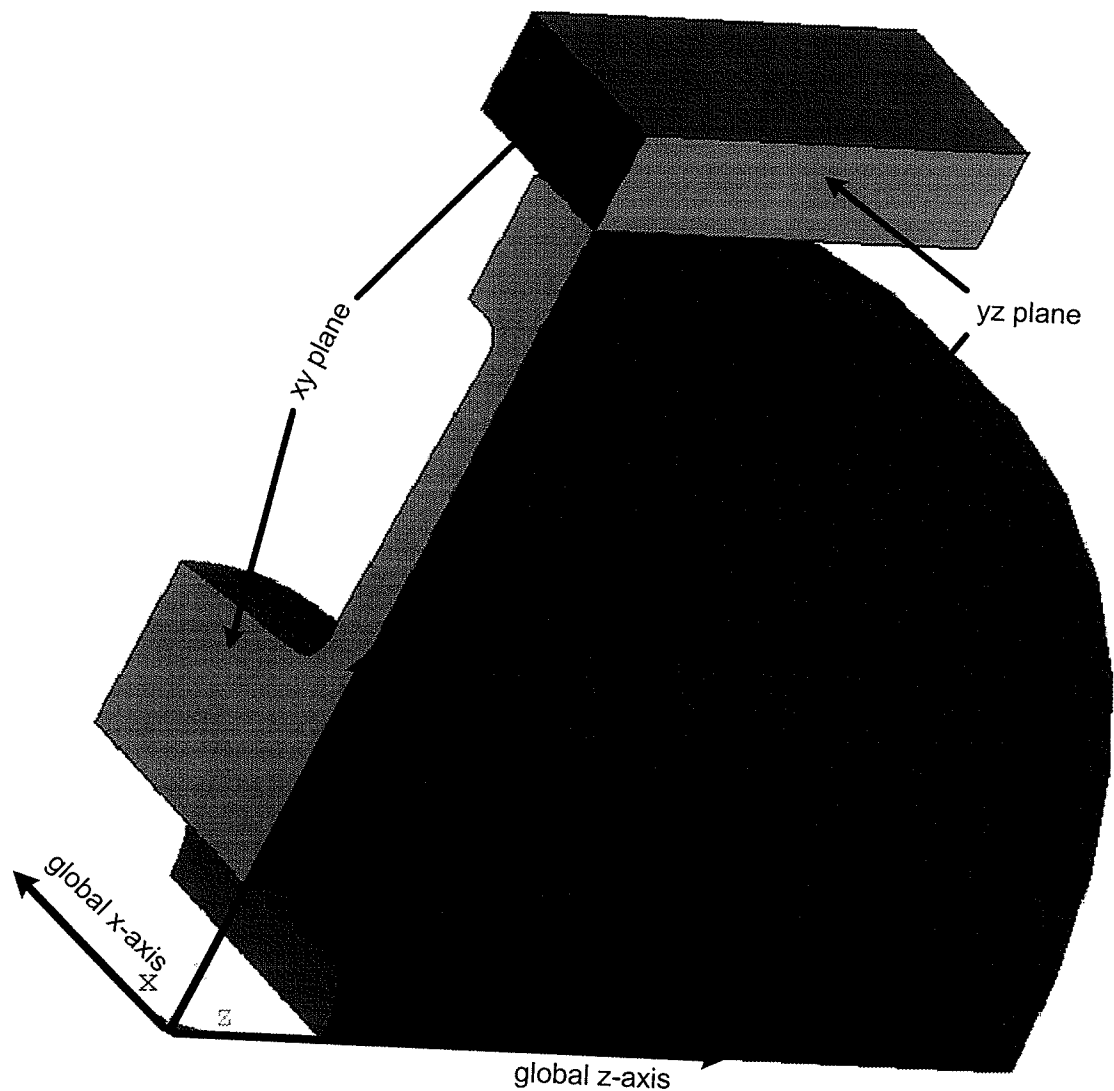


Fig. 5.3 Boundary conditions

High stress concentration values were found in an extremely small area in the contact zones of both rollers and roller path plates. This stress concentration occurred in a location in rollers at the edge of contact between rollers and roller path plates. Whereas, the same stress concentration occurred in roller path plates at two locations. These infinite-like stress concentration values were discarded and were not used in the results analysis. Figure 5.4 shows stress contour plot of principal stress  $\sigma_1$  in cast iron Roller R<sub>1</sub>. It is evident from the FE results that the high values of compressive and tensile stresses were local in nature and were observed only in the very small contact zone of the roller. During the post processing phase of ANSYS<sup>®</sup> result analysis, it was found that the stresses in the rest of the roller were below 55 MPa. A maximum compressive principal stress  $\sigma_1$  of 988 MPa was observed in the roller very close to the edge of the contact area between the roller and the roller path plate, as shown in Fig. 5.4, 19.8 mm (0.78 in.) far from the initial contact point in roller in the x-axis, whereas, a maximum tensile  $\sigma_1$  of 579 MPa was observed at the edge of the contact area, 20.5 mm (0.81 in.) away from the initial contact point in roller in the x-axis. The contour plot of principal stress  $\sigma_2$  in Roller R<sub>1</sub> is shown in Fig. 5.5. The principal stress  $\sigma_2$  varied from maximum compressive stress of 1501 MPa within the contact area to a maximum tensile stress of 365 MPa at the edge of contact area. The maximum compressive stress of 1501 MPa was recorded at the same location where the maximum compressive  $\sigma_1$  was found. A maximum tensile stress of 365 MPa was recorded at the same location as the maximum tensile  $\sigma_1$  was recorded. Figure 5.6 shows the stress contour plot of  $\sigma_3$  in Roller R<sub>1</sub>. Maximum compressive principal stress  $\sigma_3$  of 1991 MPa occurred at the same location as that of maximum compressive  $\sigma_1$ .

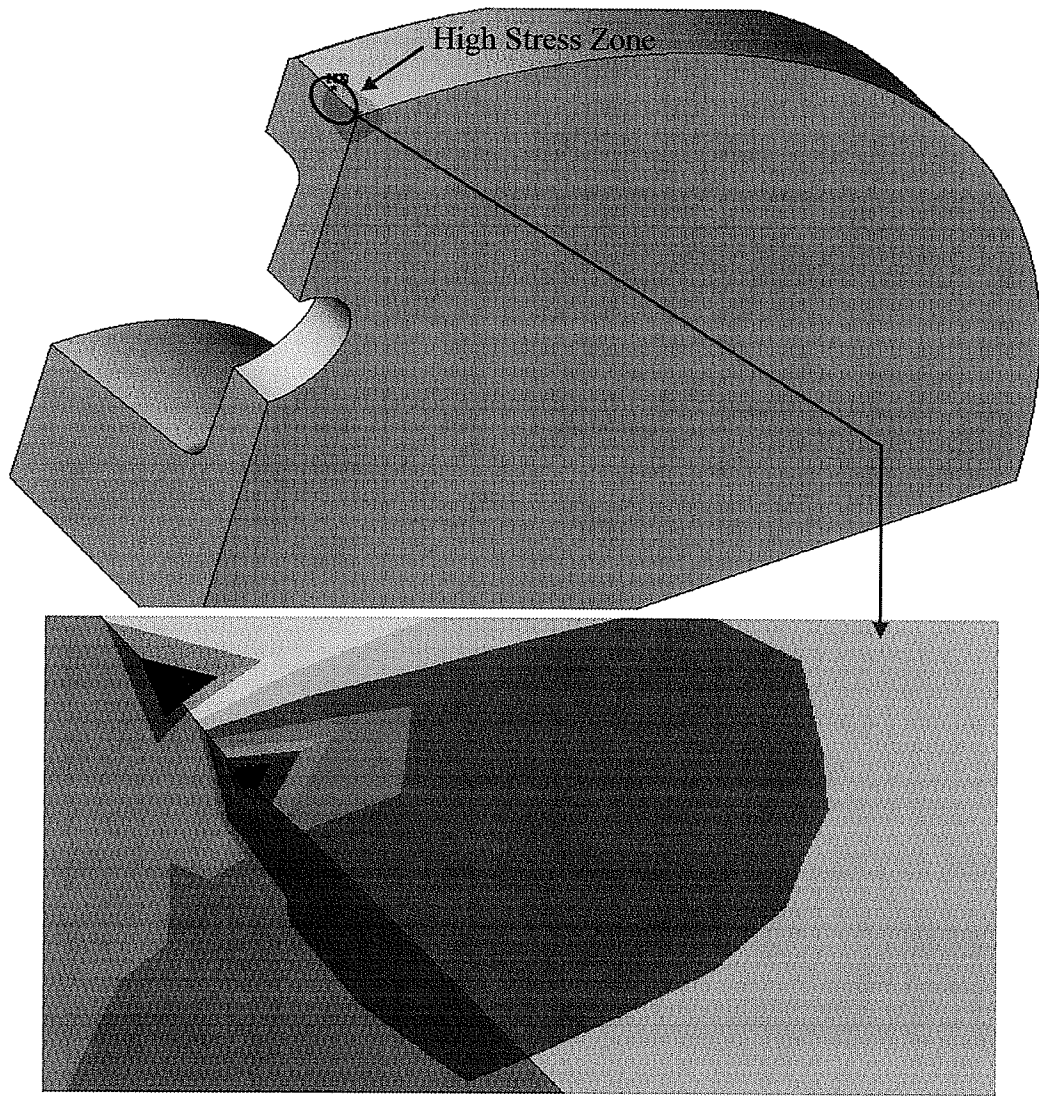


Fig. 5.4 Contour plot of principal stress  $\sigma_1$  in Roller  $R_1$

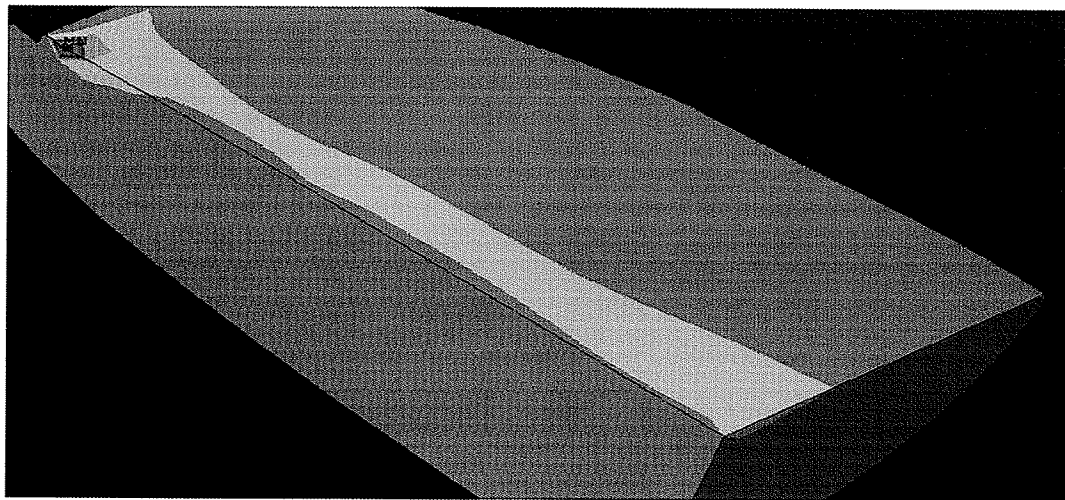


Fig. 5.5 Contour plot of principal stress  $\sigma_2$  in Roller  $R_1$

A maximum value of stress intensity<sup>1</sup>  $\sigma_i$  of 1618 MPa was found at the same location as the maximum compressive  $\sigma_1$  was found. Also, the maximum value of 1504 MPa of von Misses<sup>2</sup> or equivalent stress  $\sigma_e$  was observed at the same location as the stress intensity was observed. Three paths were created in the roller and in the roller path plate to demonstrate the variation of different kinds of stresses. These paths originated from the initial contact point in the roller and in the plate in global x, y, and z directions, as typically shown in Fig 5.7.



Fig. 5.6 Contour plot of principal stress  $\sigma_3$  in Roller  $R_1$

The variation of principal stresses in Roller  $R_1$  is shown on a path along the x-axis in Fig. 5.8. Principal stresses  $\sigma_1$ ,  $\sigma_2$ , and  $\sigma_3$  at the initial contact point were compressive 755, 1256, and 1989 MPa, respectively, and they remained almost constant until a distance of 16 mm (0.63 in.). After that they increased to a maximum compressive stress of 988,

<sup>1</sup>The stress intensity  $\sigma_i$  is the largest of the absolute values of  $\sigma_1 - \sigma_2$ ,  $\sigma_2 - \sigma_3$ , or  $\sigma_3 - \sigma_1$ .

<sup>2</sup> $\sigma_e = \frac{1}{\sqrt{2}} \sqrt{(\sigma_1 - \sigma_2)^2 + (\sigma_2 - \sigma_3)^2 + (\sigma_3 - \sigma_1)^2}$

1501, and 1991 MPa, respectively, at a location of 19.8 mm (0.78 in.) far from the initial contact point in roller. After that, principal stresses  $\sigma_1$  and  $\sigma_2$  became tensile 579 and 365 MPa, respectively, at the edge of contact area, at a location of 20.5 mm (0.81 in.) far from the initial contact point. After that, all three principal stresses decreased gradually until they vanished to almost zero.

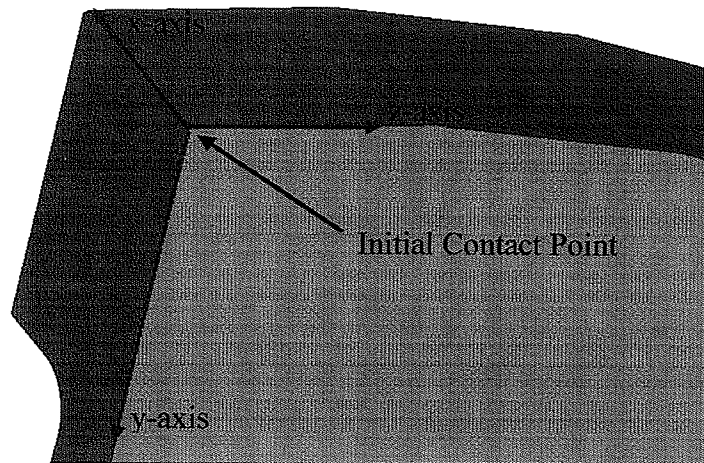


Fig. 5.7 Three paths created in Roller  $R_1$

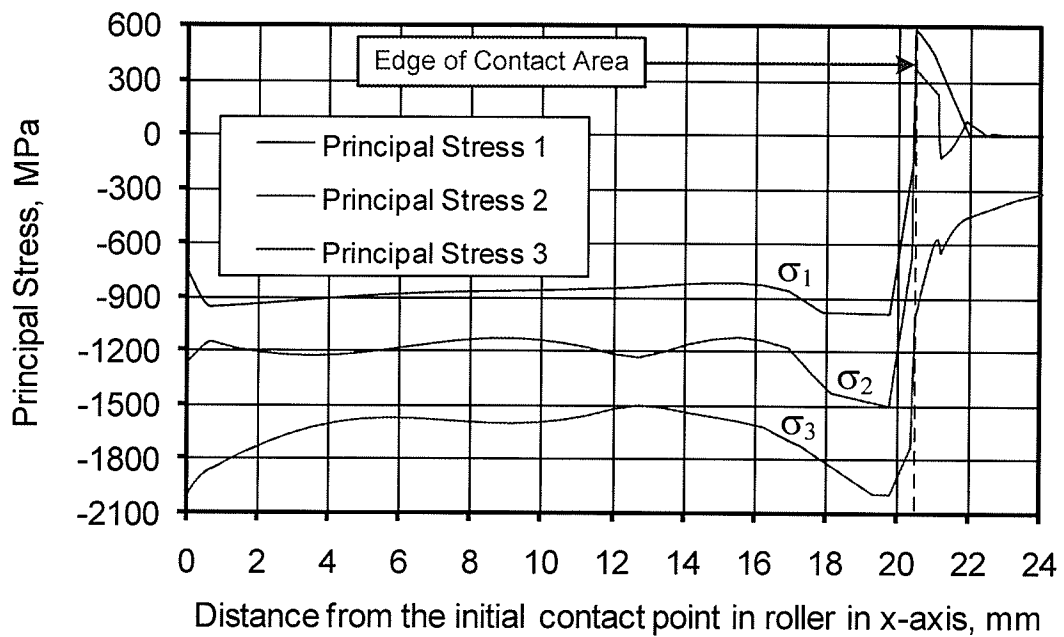


Fig. 5.8 Principal stresses on a path along the x-axis in Roller  $R_1$

The location of the highest compressive principal stresses was very close to the edge of an elliptic contact area between roller and roller path plate. The position of this point was 19.8 mm (0.78 in.) far from the initial contact point in roller in the x-axis. The highest maximum values of all of the principal compressive stresses, maximum principal shear stress  $\tau_{\max}$ , stress intensity  $\sigma_i$ , von Misses or equivalent stress  $\sigma_e$ , octahedral normal stress  $\sigma_o$ , and octahedral shear<sup>3</sup> stress  $\tau_o$  were observed at this location in Roller R<sub>1</sub> and are summarized in Table 5.1.

Fig. 5.9 depicts the principal stresses, maximum principal shear stress and octahedral shear stress on a path in y-axis in Roller R<sub>1</sub>. The curves shown in Fig. 2.1 are for principal stresses, maximum principal shear stress, and octahedral shear stresses for two semi-circular solid elastic disks initially in contact at a single point; each having double principal radius of curvature. The Poisson's ratio and the B/A ratio employed for developing these curves was ¼ and 1.24, respectively. The constants A and B depend on the principal radii of curvature of the two elastic bodies in contact. The curves shown in Fig. 5.9 are for Roller R<sub>1</sub> (on roller path Plate P<sub>1</sub>). The Roller R<sub>1</sub> had principal radii of curvature of 419 mm (16½ in.) and 914 mm (36 in.). The principal radii of curvature of roller path Plate P<sub>1</sub> were infinitely large; therefore the B/A ratio for Roller R<sub>1</sub> and roller path Plate P<sub>1</sub> came out to be 2.18. The Poisson's ratio of Roller R<sub>1</sub> and roller path Plate P<sub>1</sub> was 0.27 and 0.28, respectively. It is clear that the format, trend and style of two set of curves in Figs. 2.1 and 5.9 matches with each other. The maximum principal stress  $\sigma_3$  in

---


$${}^3\tau_o = \frac{\sqrt{2}}{3}\sigma_e$$

Fig. 5.9 is similar in trend to maximum principal stress  $\sigma_{zz}$  in Fig. 2.1. Also, the principal stresses  $\sigma_1$  and  $\sigma_2$  in Fig. 5.9 are similar in fashion to principal stresses  $\sigma_{xx}$  and  $\sigma_{yy}$  in Fig. 2.1. All three principal stresses in both cases have maximum values at the contact surface. The only difference is that the maximum principal shear and octahedral shear stresses have maximum values at the contact surface in Fig. 5.9; whereas, in Fig. 2.1 they have maximum values just beneath the subsurface.

Table 5.1 Maximum stresses in MPa in rollers and in roller path plates

FEA	R <sub>1</sub> P <sub>1</sub>				R <sub>3</sub> P <sub>3</sub>			
	838 kN (188½ kips)		734 kN (165 kips)		814 kN (183 kips)		734 kN (165 kips)	
Type of Stress	R <sub>1</sub>	P <sub>1</sub>	R <sub>1</sub>	P <sub>1</sub>	R <sub>2</sub> -R <sub>3</sub>	P <sub>3</sub>	R <sub>2</sub> -R <sub>3</sub>	P <sub>3</sub>
$\sigma_1$	-988	-1138	-820	-999	-266	-1063	-263	-963
$\sigma_2$	-1501	-1654	-1299	-1447	-1332	-1738	-1217	-1569
$\sigma_3$	-1991	-2399	-1697	-2098	-1551	-2379	-1443	-1708
$\tau_{max}$	501.5	630.5	438.5	549.5	642.5	658	590	372.5
$\sigma_i$	1003	1261	877	1099	1285	1316	1180	745
$\sigma_e$	868.7	1098	760.6	957	1191	1140	1085	686
$\sigma_o$	-1493	-1730	-1272	-1514.7	-1050	-1727	-974	-1413
$\tau_o$	409.5	517.6	358.5	451	561	537	511	323

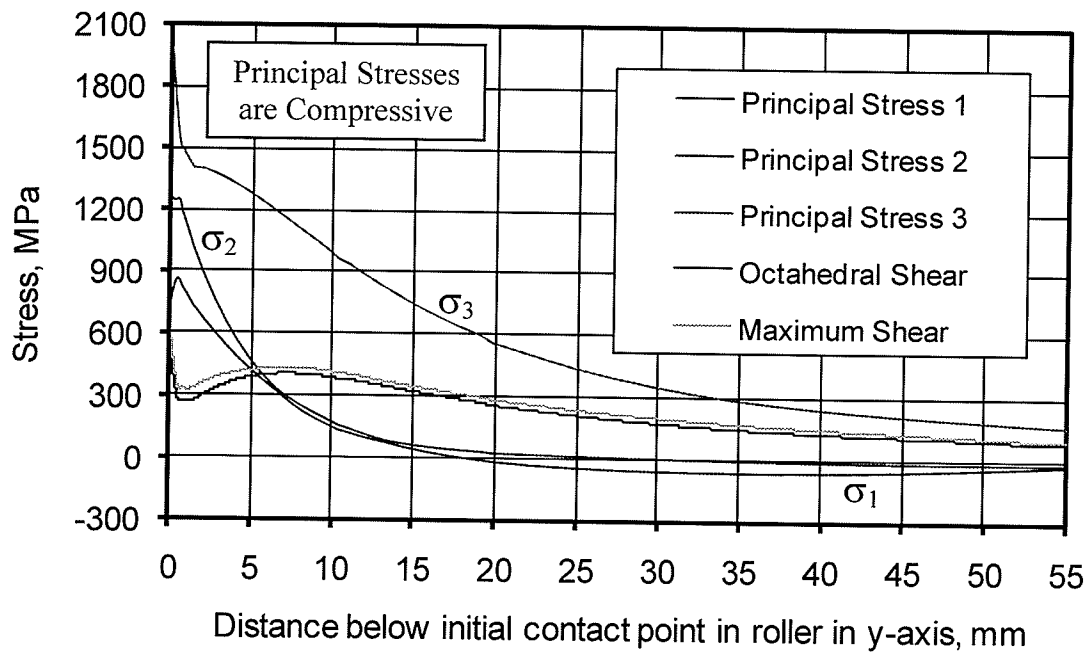


Fig. 5.9 Path plots of principal and octahedral shear stresses in the y-axis in Roller  $R_1$

Path plots of Equivalent or von Misses stress  $\sigma_e$ , stress intensity  $\sigma_i$ , and octahedral normal stresses  $\sigma_o$  along the y-axis, below the contact point, in Roller  $R_1$  are shown in Fig. 5.10. Again, all of these stresses have maximum values at the contact surface and they decrease at locations further away along the y-axis. Principal stresses on a path along the z-axis (rolling direction) in Roller  $R_1$  are presented in Fig. 5.11.

The curves shown in Fig. 2.4 are for principal stresses for a roller on a plane under the influence of both normal and tangential (frictional) forces. The coefficient of friction and the B/A ratio used in developing these curves was  $\frac{1}{3}$  and  $\infty$ , respectively. The curves shown in Fig. 5.11 are for a Roller  $R_1$  (on roller path Plate  $P_1$ ) under the effect of radial compressive load only and no tangential (frictional) forces were employed in the FE analysis. The B/A ratio for Roller  $R_1$  and roller path Plate  $P_1$  was 2.18. Thus, the two set of curves shown in Figs. 2.4 and 5.11 cannot be compared. Nevertheless, it is important

to note that principal stresses  $\sigma_1$  and  $\sigma_2$  in Figs. 2.4 and 5.11 changes from compressive to tensile stresses in rolling direction. The principal stresses  $\sigma_1$  and  $\sigma_2$  in Fig. 5.11 change from compressive to tensile stresses of 133 and 8 MPa, at a location of 10.25 mm (0.40 in.) and 12 mm (0.47 in.) far from the initial contact point, respectively. The two set of curves shown in Figs 2.4 and 5.11 have maximum values at the contact surface.

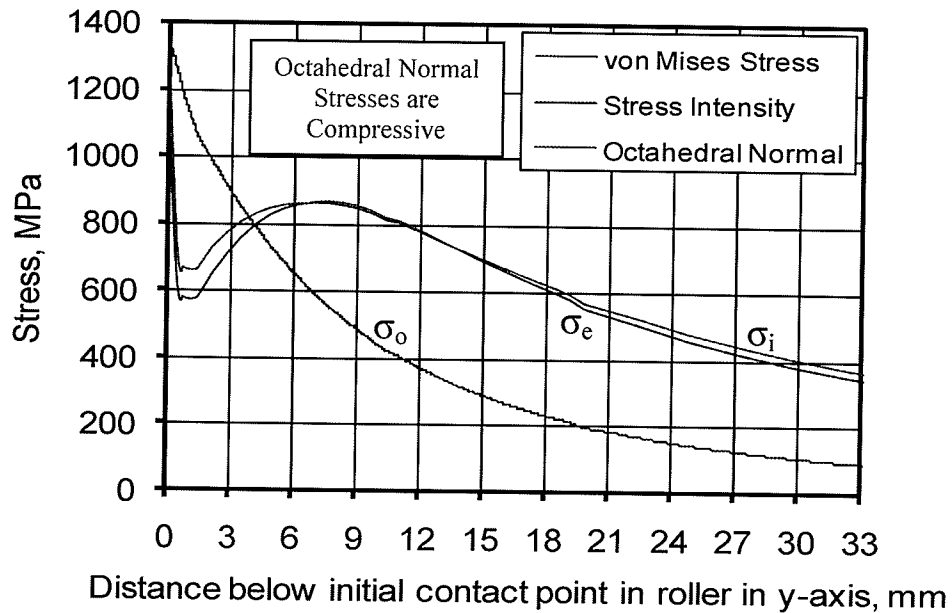


Fig. 5.10 Path plots of  $\sigma_e$ ,  $\sigma_i$ , and  $\sigma_o$  in the y-axis in Roller R<sub>1</sub>

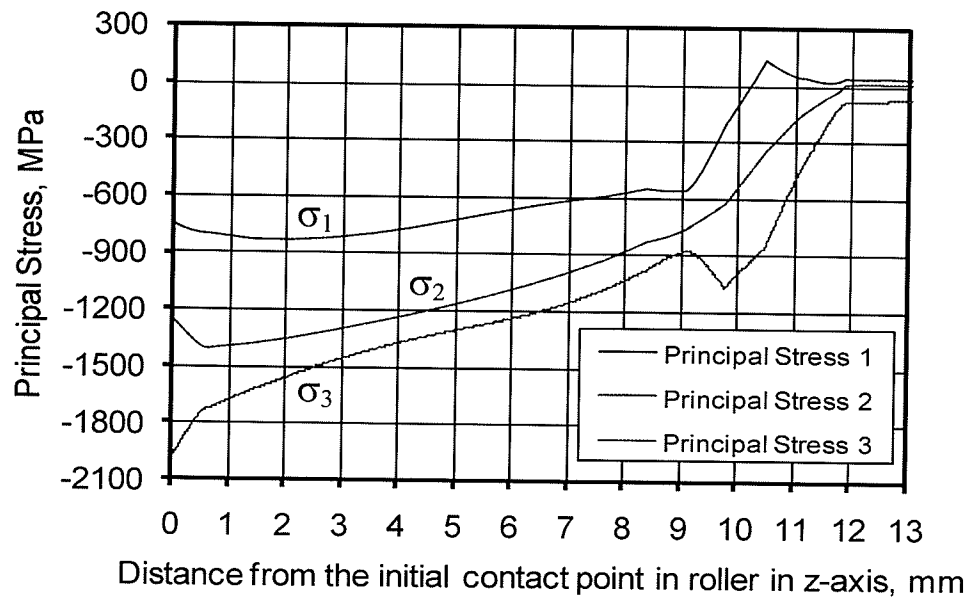


Fig. 5.11 Principal stresses on a path along the z-axis (rolling direction) in Roller R<sub>1</sub>

Equivalent or von Mises stress  $\sigma_e$ , stress intensity  $\sigma_i$ , maximum principal shear stress  $\tau_{max}$ , and octahedral (normal and shear) stresses along the z-axis are shown in Fig. 5.12. The curves shown in Figs. 2.5 and 2.6 are for maximum principal shear and octahedral shear stresses, respectively, for a roller on a plane under the influence of normal and tangential forces. The coefficient of friction and the B/A ratio used in developing these curves was  $\frac{1}{3}$  and  $\infty$ , respectively. The B/A ratio for Roller  $R_1$  and roller path Plate  $P_1$  was 2.18. Thus, the set of curves shown in Figs. 2.5, 2.6 and 5.12 cannot be compared. However, it is important to note that the set of curves shown in Figs. 2.5, 2.6, and 5.12 have similar trend and their maximum values occur at the contact surface.

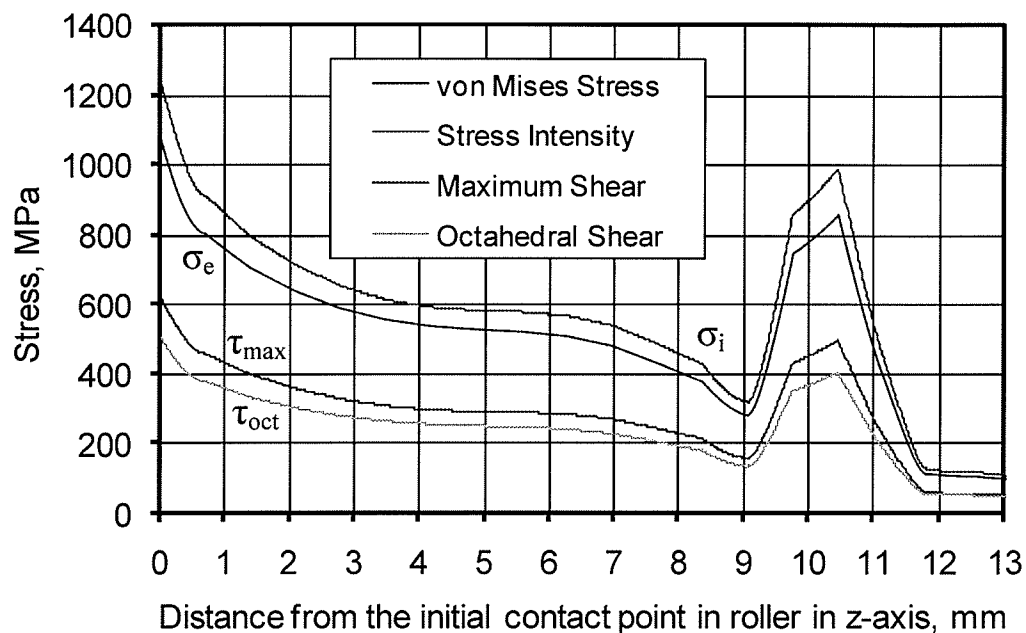


Fig. 5.12 Path plots of  $\sigma_e$ ,  $\sigma_i$ ,  $\tau_{max}$ , and octahedral stresses along the z-axis in Roller  $R_1$

#### 5.4.1.2 Plates $P_1$ and $P_2$

In this section, results of Plates  $P_1$  and  $P_2$  from the FE program  $R_1P_1$ , using an external load of 838 kN (188½ kips) are presented. The yield strength of Plates  $P_1$  and  $P_2$  was

determined to be 413.7 MPa. The location of the highest compressive principal  $\sigma_1$ , as shown in Fig. 5.13, was at a depth of 15.4 mm (0.61 in.) below the initial contact point in Plate  $P_1$  in the global y-axis. The variation of principal stresses on the path along the y-axis versus the distance in mm below the initial contact point in Plate  $P_1$  is shown in Fig. 5.14. A high values of stresses occurred at this location where maximum values of all of the principal compressive stresses, maximum principal shear stress  $\tau_{max}$ , stress intensity  $\sigma_i$ , von Misses or equivalent stress  $\sigma_e$ , and octahedral stresses were observed. These are summarized in Table 5.1. The maximum compressive principal stress  $\sigma_1$  was 1138 MPa, as shown in Figs. 5.13 and 5.14, and was observed at the same location. However, the maximum tensile stress of 1299 MPa was observed at location (20, 10.5, 0.0) mm (0.79, 0.41, 0.0 in.) (in xyz coordinate system), away from the initial contact point in Plate  $P_1$ . The location of maximum tensile principal stress  $\sigma_1$  and  $\sigma_2$  in Roller  $R_1$  was at the edge of contact between roller and plate, at a distance of 20.5 mm far from the initial contact point, along x-axis, as discussed in Section 5.4.1.1. The location of maximum tensile principal stress  $\sigma_1$  in Plate  $P_1$  coincides with the location of  $\sigma_1$  in Roller  $R_1$ .

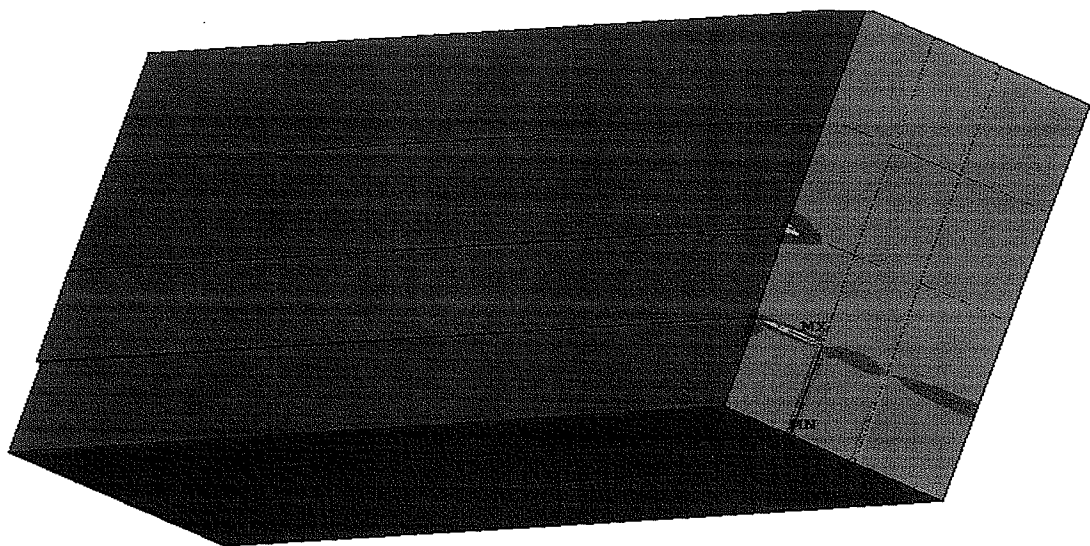


Fig. 5.13 Contour plot of principal stress  $\sigma_1$  in Plate  $P_1$

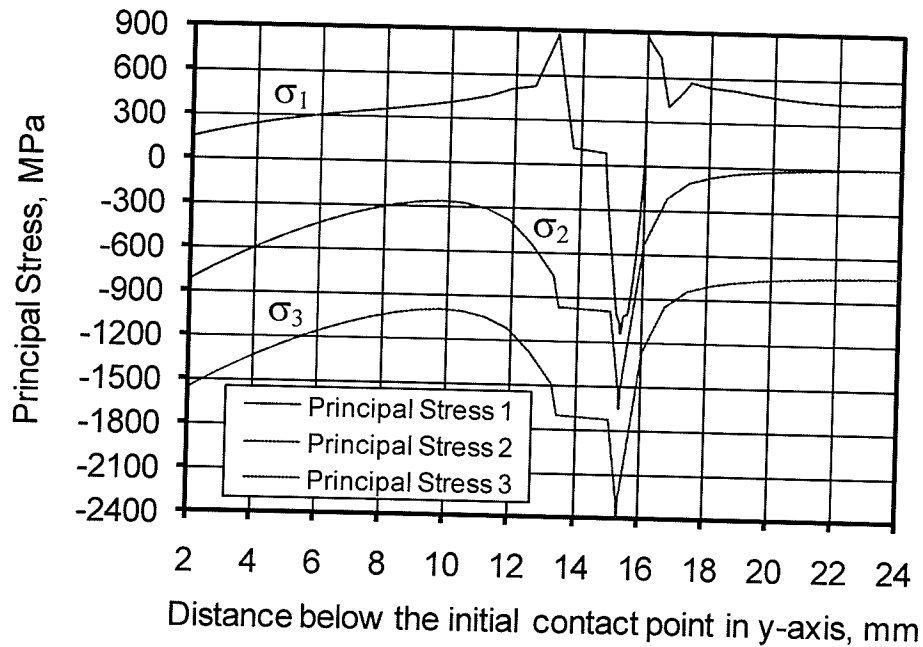


Fig. 5.14 Principal stresses on a path along the y-axis in Plate P<sub>1</sub>

All three principal stresses are maximum compressive at a depth of 15.4 mm (0.61 in.) below the initial contact point of the plate, and their values are -1138, -1654, and -2399 MPa, respectively, as shown in Fig. 5.14.

Figure 5.15 depicts path plots of principal stresses on a path along the z-axis (rolling direction) in Plate P<sub>1</sub>. All three principal stresses are maximum compressive at the initial contact point and they decrease at locations further away from the initial contact point along the z-axis. It is important to note that principal stress  $\sigma_1$  changes to a maximum tensile stress of 318.5 MPa at a distance of 12 mm (0.47 in.) from the initial contact point of the Plate P<sub>1</sub>. Equivalent stress  $\sigma_e$ , stress intensity  $\sigma_i$ , maximum principal shear stress  $\tau_{max}$ , and octahedral shear stresses on a path along the z-axis in Plate P<sub>1</sub> are shown in Fig. 5.16. These stresses have maximum values at the initial contact point in plate and they decrease further away from the initial contact point in z-axis.

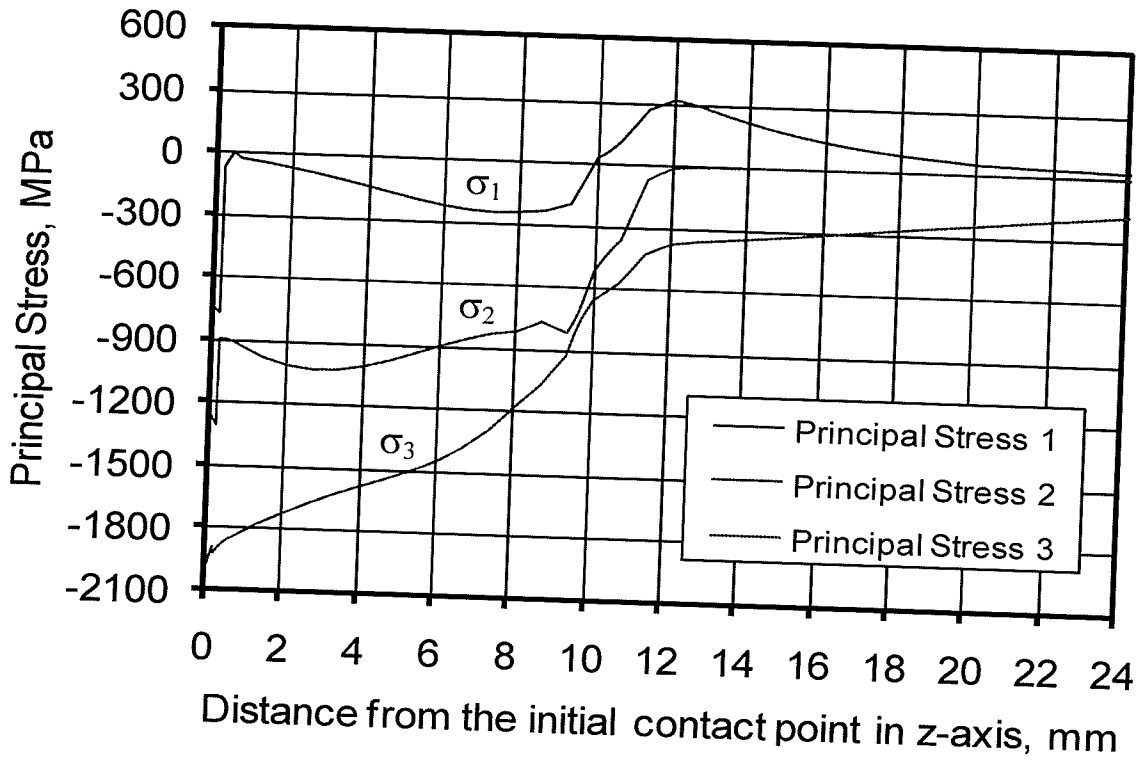


Fig. 5.15 Principal stresses on a path along the z-axis (rolling direction) in Plate P<sub>1</sub>

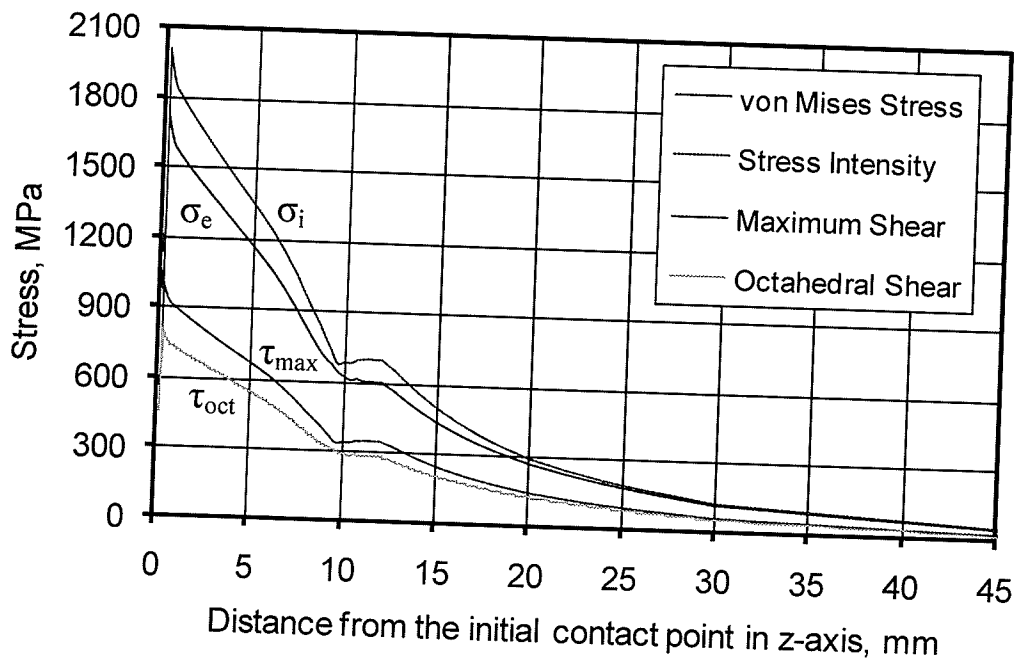


Fig. 5.16 Path plots of  $\sigma_e$ ,  $\sigma_i$ ,  $\tau_{max}$ , and octahedral stresses along the z-axis in Plate P<sub>1</sub>

#### 5.4.2 Program R<sub>1</sub>P<sub>1</sub> with External Load of 734 kN

The external load of 734 kN (165 kips) applied only in the FE analysis, represents the actual maximum service load in real life situation. The contact area between roller and plate after the application of the external load was found approximately equal to 152.4 mm<sup>2</sup> (0.24 in<sup>2</sup>). This contact area was one-quarter of an elliptic-shape with major axis of 19.8 mm (0.78 in.) in x-axis and minor axis of 9.8 mm (0.38 in.) in z-axis. The behavior, pattern, and format of resulting contour and path plots of all types of stresses in Roller R<sub>1</sub> and in roller path Plate P<sub>1</sub> retrieved from program R<sub>1</sub>P<sub>1</sub> run with the external load of 734 kN (165 kips) were identical in all respects to those of program R<sub>1</sub>P<sub>1</sub> run with the external load of 838 kN (188½ kips) discussed in Section 5.4.1. The only difference was in the values of contact areas and stresses. Table 5.1 summarizes the maximum values of principal stresses, stress intensity  $\sigma_i$ , von Misses or equivalent stresses  $\sigma_e$ , and octahedral stresses in rollers and in roller path plates retrieved from program R<sub>1</sub>P<sub>1</sub> and R<sub>3</sub>P<sub>3</sub>.

#### 5.4.3 FEA of Rollers R<sub>2</sub> and R<sub>3</sub>

Rollers R<sub>2</sub> and R<sub>3</sub> and roller path Plates P<sub>3</sub> were analyzed using FE program R<sub>3</sub>P<sub>3</sub>. This program was run twice, once with an external load of 814 kN (183 kips) to simulate laboratory testing of R<sub>2A</sub> and R<sub>3A1</sub> and a second time with an external load of 734 kN (165 kips) to simulate service load conditions. The external load of 814 kN (183 kips) applied during testing of R<sub>2A</sub> and R<sub>3A1</sub> and used in the FE analysis was 9.86% higher than the actual maximum service load of 734 kN (165 kips). Rollers R<sub>2</sub> and R<sub>3</sub> were identical but different than the cast iron Roller R<sub>1</sub>. The modulus of elasticity and the Poisson's ratio of Rollers R<sub>2</sub> and R<sub>3</sub> were also identical between the two rollers. Cast iron Roller R<sub>1</sub>

had three handling holes along with a flange width of 51 mm (2 in.), whereas, Rollers  $R_2$  and  $R_3$  were without handling holes and had a flange (rim) width of 66.5 mm ( $2\frac{5}{8}$  in.). This was the only difference between Roller  $R_1$  and Rollers  $R_2$  and  $R_3$ . As a result, the stresses in Roller  $R_2$  (and in Roller  $R_3$ ), as well as the stresses in roller path Plates  $P_3$  through  $P_6$  retrieved from program  $R_3P_3$  (using two different load cases) were identical to the stresses obtained in program  $R_1P_1$  as discussed in Sections 5.4.1 and 5.4.2. The only difference was in the magnitude of the contact areas and stresses. Table 5.1 summarizes the maximum values of all types of stresses in rollers and in roller path plates retrieved from program  $R_1P_1$  and  $R_3P_3$ .

### **5.5 Comparison between FE Results and Laboratory Test Results**

A static compressive radial load only was applied to roller and roller path plate in FE ANSYS<sup>®</sup> model. In laboratory testing program, constant radial compressive load along with the lateral (frictional) load was applied to roller and roller path plate during cyclic operation of the roller. Hence, results from the FE program and the results from the laboratory cyclic tests cannot be compared because of the main reason that the roller and roller path plate were in the state of dynamic motion and they were continuously moving back and forth and therefore all strain values were fluctuating and changing with every one tenth of a second. The only way to compare the results is to consider the strain data from laboratory testing program when the roller and roller path plate were not moving. Before initiating each cyclic test, the radial compressive load was applied gradually and slowly by tensioning the four high strength rods using hydraulic jacks as discussed in Section 4.3. The values of the radial compressive load, after releasing jack pressure and just prior to starting the cyclic testing, were used in the FE analysis. The strain values just

prior to starting of the cyclic testing were retrieved to compare with the FE results. The Strain gauges 9 and 14 were installed on Roller  $R_1$  both sides, and strain gauge 18 was installed on roller path Plates  $P_1$  and  $P_2$ . These three gauges were aligned in the same line in the global y-axis and their location is shown in Fig. 5.17.

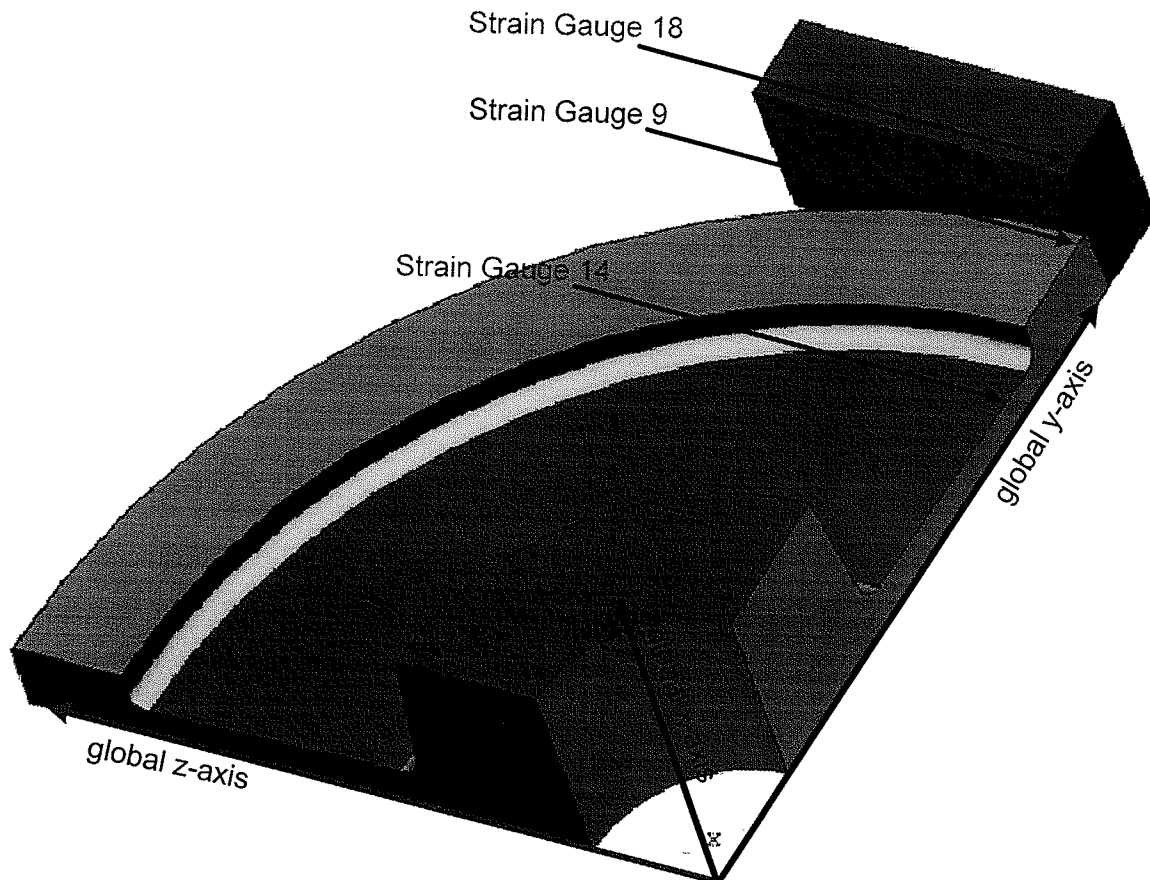


Fig. 5.17 Location of strain gauges 9, 14, and 18 on Roller  $R_1$  and Plates  $P_1$  and  $P_2$

A micro strain of +999.6 was recorded in strain gauge 9 under the static radial compressive load of 838 kN (188½ kips) after the release of jack pressure and just prior to cyclic testing. The same radial compressive load of 838 kN (188½ kips) was applied in FE program  $R_1P_1$ . Fig. 5.18 shows a path plot of micro strain along a line on the rim surface in global y-axis (retrieved from FE model) where strain gauge 9 (10 mm far from the left hand) was installed on Roller  $R_1$  (program  $R_1P_1$ ) under the radial compressive

load of 838 kN (188½ kips). A micro strain of +947.6 was recorded at a location where gauge 9 was installed. The difference between the laboratory test result and FE result is 52 micro strains (5.2%).

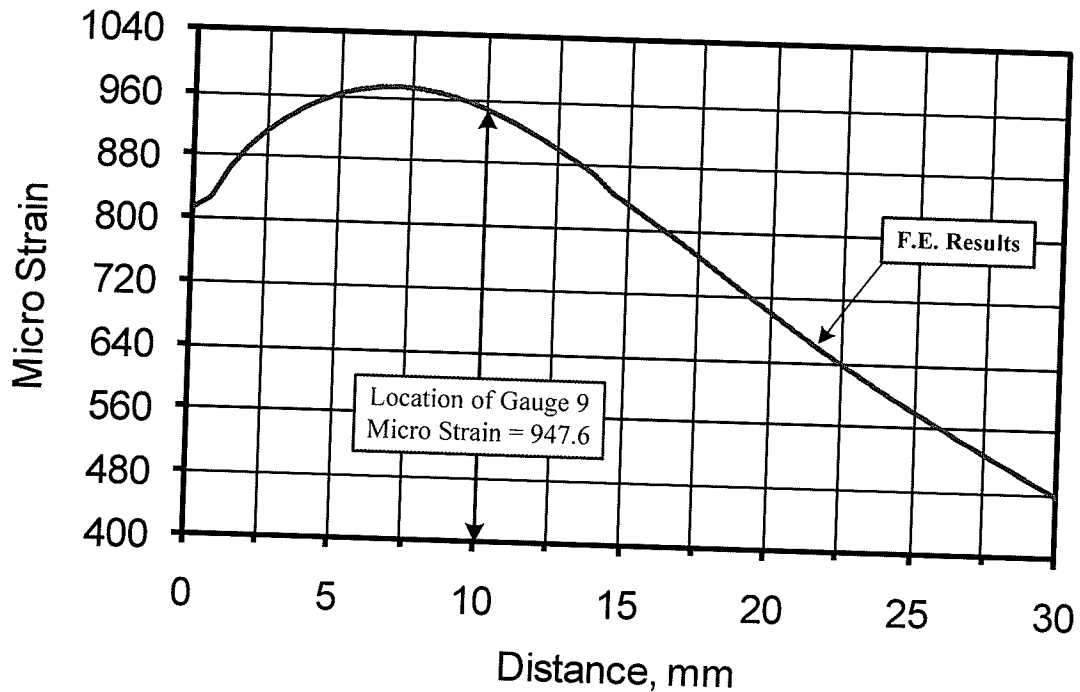


Fig. 5.18 F.E. Strain along a line in global y-axis passing through the location of gauge 9

A micro strain of -1500.3 was recorded in strain gauge 14 under the static radial compressive load of 838 kN (188½ kips) after the release of jack pressure and just prior to cyclic testing. The same radial compressive load of 838 kN (188½ kips) was applied in FE program R<sub>1</sub>P<sub>1</sub>. Fig. 5.19 shows a path plot of micro strain along a line in the web area in global y-axis (retrieved from FE model) where strain gauge 14 (26.9 mm far from the left hand) was installed on Roller R<sub>1</sub> (program R<sub>1</sub>P<sub>1</sub>) under the radial compressive load of 838 kN (188½ kips). A micro strain of -1440.2 was recorded at a location where gauge 14 was installed. The difference between the laboratory test result and FE result is 60.1 micro strains (4.0%).

A micro strain of +199.7 was recorded in strain gauge 18 in Plate P<sub>1</sub> under the static radial compressive load of 838 kN (188½ kips) after the release of jack pressure and just prior to cyclic testing. The same radial compressive load of 838 kN (188½ kips) was applied in FE program R<sub>1</sub>P<sub>1</sub>. Fig. 5.20 shows a path plot of micro strain along a line in global y-axis (retrieved from FE model) where strain gauge 18 (10 mm far from the left hand) was installed on Plate P<sub>1</sub> (program R<sub>1</sub>P<sub>1</sub>) under the radial compressive load of 838 kN (188½ kips). A micro strain of +182.4 was recorded at a location where gauge 18 was installed. The difference between the laboratory test result and FE result is 17.3 micro strains (8.7%). Table 5.2 summarizes the comparison between laboratory test results and FE analysis results for some of the selected strain gauges.

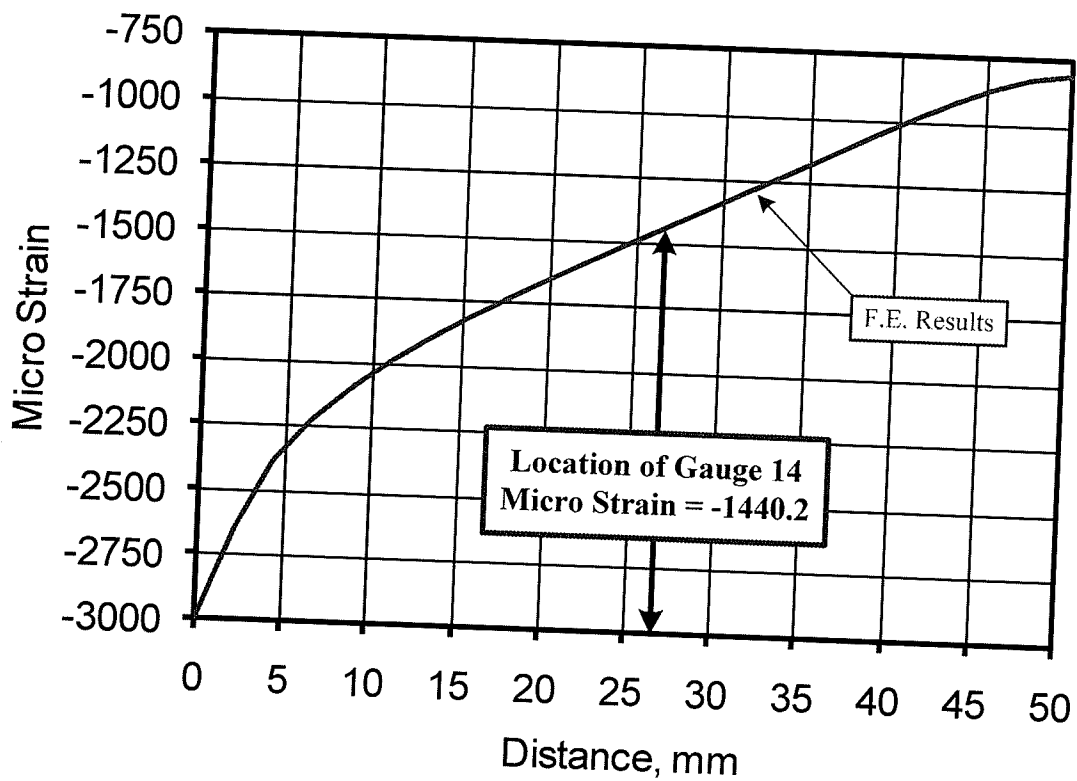


Fig. 5.19 Path plot along a line in global y-axis where gauge 14 was installed

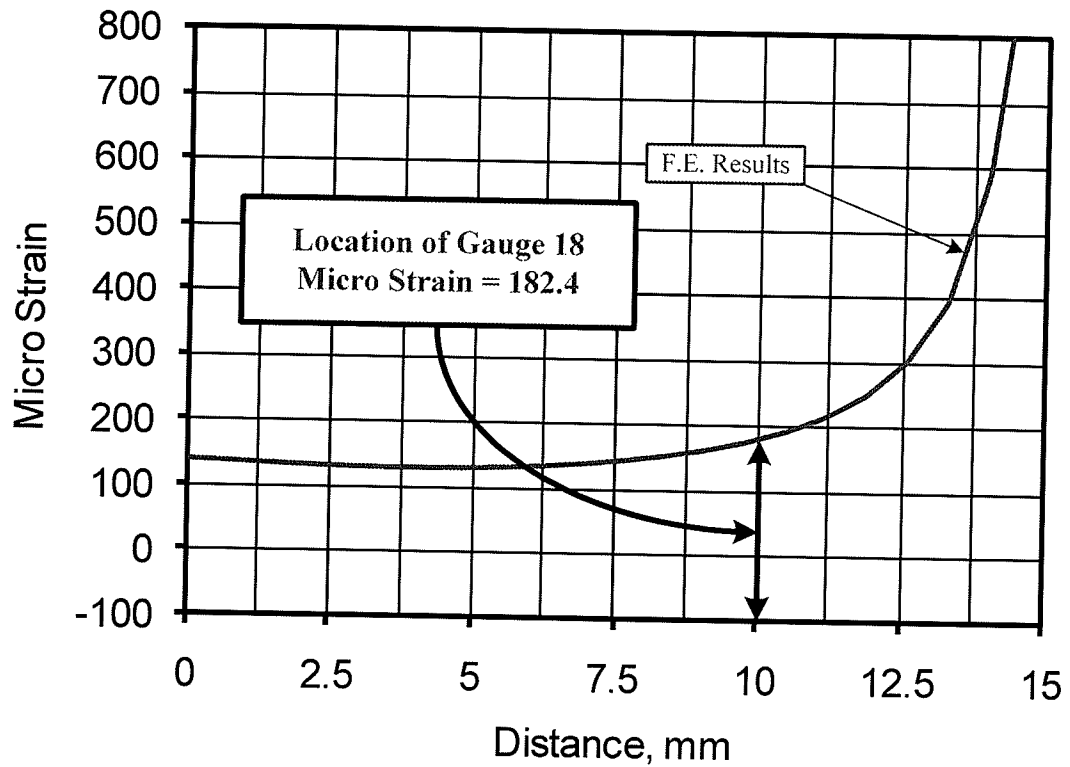


Fig. 5.20 Path plot along a line in global y-axis where gauge 18 was installed

Table 5.2 Comparison between FE results and laboratory test results

Test	Gauge Number	Location	Micro Strain in Laboratory Tests	Micro Strain in FE Analysis	Difference %
R <sub>1A</sub>	9	R <sub>1</sub>	+999.6	+947.6	5.2
	14	R <sub>1</sub>	-1500.3	-1440.2	4.0
	18	P <sub>1</sub>	+199.7	+182.4	8.7
R <sub>2A</sub>	8	R <sub>2</sub>	-100.9	-90.1	10.7
	14	P <sub>3</sub>	+30.3	+28.2	6.9

## 5.6 Summary

High values of contact stresses were recorded in the contact zones of rollers and roller path plates as shown in Table 5.1. These contact stresses are somewhat close to the ultimate strength of rollers and roller path plates. Using hand calculations and formulae given in (Roark 2002), contact stresses and contact areas for rollers and roller path plates were computed and are shown in Appendix C. The FE results indicated that high stresses in contact areas in both in roller and in roller path plate were critical. The maximum values of all types of stresses were found in these zones in roller and in roller path plate. The trend and style of stresses found in the contact area of roller and roller path plate exactly matched with those found in the literature. The results obtained from FE analysis and those from using hand calculations and formulae given in (Roark 2002) proved that the contact stresses were higher than the yield strength of roller and roller path plate.

### 6.1 General

The National Institute of Standards and Technology (formerly the National Bureau of Standards), a division of the U.S. Department of Commerce, completed a study in 1983 of the economic effects of fracture of materials in the United States (Milne 1994). The total cost of the economic effects of fracture of materials in the United States was estimated to be \$119 billion dollars per year. This was 4% of the gross national product (GNP) and therefore, represented a significant use of resources and work force. The definition of fracture used in that study was quite broad, including not only fracture in the sense of cracking, but also deformation and a host of related problems such as delamination. Wear and corrosion were not included in that study. Separate studies indicated that adding these to obtain the total cost for materials durability would increase the total to roughly 10% of the GNP. A study of fracture costs in Europe reported in 1991 also yielded an overall cost of 4% of the GNP, and similar value is likely to apply to all industrial nations (Milne 1994).

At least half of the mechanical failures are structural failures due to fatigue loading (Dowling 2007). No exact numbers are available, but many references have suggested that 90 percent of all mechanical failures are fatigue related (Stephens et al. 2001). Fatigue failures continue to be a major concern in engineering design. Mechanical failures due to fatigue have been the subject of engineering efforts for more than 150 years. The term fatigue was used quite early, as in an 1839 book on Mechanics by J. V. Poncelet of France (Dowling 2007).

## 6.2 What is Fatigue?

Components of structures are frequently subjected to repeated loads and the resulting cyclic stresses can lead to microscopic physical damage to the materials involved. Even at stresses well below a given material's ultimate strength, this microscopic damage can accumulate with continued cycling until it develops into a crack or other macroscopic damage that leads to failure of the component. This process of damage and failure due to cyclic loading is termed as fatigue (Dowling 2007). "Fatigue is the initiation and propagation of microscopic cracks into macro cracks by the repeated application of stresses (Fisher et al. 1998)." "Fatigue may be defined as the process of progressive localized permanent structural change occurring in a material subjected to conditions that produce fluctuating stresses and strains at some point or points and that may culminate in cracks or complete fracture after a sufficient number of fluctuations (ASTM 1987)."

Most structural components are subjected to variation in applied loads, causing variation in stresses in the parts. If the fluctuating stresses are large enough, even though the maximum applied stress may be considerably less than the static strength of the material, failure may occur when the stress is repeated often enough. This kind of failure is called a fatigue failure (Davis et al. 1982). "Metal fatigue is a process that causes failure or damage of a component subjected to repeated stresses. It is a complicated metallurgical process, which is difficult to describe accurately and model precisely on a microscopic level. Despite these complexities, fatigue damage assessment for design of components and structures must be performed" (Hassan et al. 1998).

Metals are composed of aggregations of small crystals with haphazard orientations. The crystals themselves are frequently non-isotropic. Experiments indicate that some crystals in a stressed piece of metal reach their limit of elastic action sooner than others, which permits slip to occur. In addition, the distribution of stress from crystal to crystal within a piece of stressed metal is most likely non-uniform, and when a piece is subjected to cyclic stress fluctuation; the constituent particles tend to move slightly with respect to one another. This movement finally weakens some minute element to such an extent that it ruptures. In the zone of failure, a stress concentration develops and with successive recurrence of stress, the fracture spreads from this nucleus across the entire section. This is the reason; fatigue failures are frequently termed to as progressive fractures (Davis et al. 1982).

The comparative movement of the elements of minute steel crystals was first observed in 1899. The movement became evident as parallel lines, called slip lines, across the face of individual crystal grains as they were viewed under the microscope when illuminated by oblique lighting. It was observed that the slip lines developed in steel by subjecting it to repeated cycles of stress would grow into microscopic cracks that in turn spread and cause failure of the piece (Gough 1933).

### **6.3 Stress-Based Approach**

The traditional stress-based (stress-life) approach was developed to its present form by 1955. The analysis is based on the nominal stresses in the affected region of the structural engineering component. The nominal stresses that can be resisted under fatigue loading

are determined by considering mean stresses and by adjusting for the effect of stress raisers, such as grooves, holes, fillets, and keyways (Dowling and Thangjitham 2000).

The stress-life technique was the first method used in an attempt to understand and quantify metal fatigue damage and it was the standard fatigue design approach for almost 100 years. The S-N method is still widely used in design applications where the applied stress is primarily within the elastic range of the material and the resultant lives (cycles to failure) are long, such as power transmission shafts. The stress-life method does not work well in low-cycle applications, where the practical strains have a significant plastic component. In this choice, a strain-based technique is more appropriate. The dividing line between low and high cycle fatigue depends on the material being considered, but usually falls between  $10^4$  and  $10^5$  cycles. One of the major disadvantages of the stress-life technique is that it ignores true stress-strain behavior and treats all strains as elastic. This may be significant since the initiation of fatigue cracks is caused by plastic deformation. The assumptions of the S-N approach are valid only if the plastic strains are small. At long lives, most steels have only a small component of cyclic strain, which is plastic, and in some cases, it is effectively too small to measure and hence the S-N approach is valid (Bannantine et al. 1990).

If a test specimen of a material is subjected to a sufficiently severe fluctuating stress, a fatigue crack or damage will develop, leading to complete failure of the specimen. If the test is repeated at a higher stress level, the number of cycles to failure will be smaller. The results of such tests from a number of different stress levels may be plotted to obtain

a stress-life curve. The amplitude of stress  $\sigma_a$  or  $S_a$ , is commonly plotted versus the number of cycles to failure,  $N_f$  (McGregor and Grossman 1952). If S-N data are found to approximate a straight line on a log-log plot, the following equation can be fitted to obtain a mathematical representation of the curve (Graham et al. 1968):

$$\sigma_a = \sigma'_f (2N_f)^b \quad 6.1$$

Where  $\sigma'_f$  fatigue strength coefficient and  $b$  is fatigue strength exponent. Constants for the above equation are available in literature for several metals. These constants are based on fitting test data for un-notched uniaxial specimens tested under completely reversed (mean stress,  $\sigma_m = 0$ ) loading (Graham et al. 1968). In plain carbon and low alloy steels there is a distinct stress level below which fatigue failure does not occur under ordinary conditions and the S-N curve appears to become flat. Such lower limiting stress amplitudes are called fatigue limits or endurance limits,  $S_e$  (Brockenbrough and Johnston 1981).

#### 6.4 Mean Stress

One of the methods used for developing data on mean stress effects is to choose several values of mean stresses, running tests at various stress amplitudes for each of these and the results can be plotted as a family of S-N curves. Another way of presenting the same information is a constant-life diagram (Dowling 2007). This is done by using points from the S-N curves at various values of life in cycles, and then plotting combinations of stress amplitude and mean stress that produce each of these lives. The stress amplitude for zero mean stress can be designated as  $\sigma_{ar}$ . On a constant-life diagram,  $\sigma_{ar}$  is, therefore, intercept at  $\sigma_m = 0$  of the curve for any particular life. The graph can then be normalized

in a meaningful way by plotting values of the ratio  $\frac{\sigma_a}{\sigma_{ar}}$  versus the mean stress, as shown in Fig. 6.1. Such a normalized amplitude-mean diagram forces agreement at  $\sigma_m = 0$ , where  $\frac{\sigma_a}{\sigma_{ar}} = 1$ , and tends to consolidate the data at various mean stresses and lives into a single curve. This provides an opportunity to fit a single curve that gives an equation representing the data. For values of stress amplitude approaching zero, the mean stress should approach the ultimate strength of the material, so that a line or curve representing such data should also pass through the point  $(\sigma_m, \frac{\sigma_a}{\sigma_{ar}}) = (\sigma_u, 0)$ . A straight line is often used, as shown by the solid line in Fig. 6.1, and this is justified by the observation that for tensile mean stresses, most data for ductile materials tend to lie near or beyond such a line, as is the case in Fig. 6.1. Thus, the straight line is generally conservative and the error is such that it causes extra safety in life estimates. The equation of this line is given by (Dowling 2007):

$$\frac{\sigma_a}{\sigma_{ar}} + \frac{\sigma_m}{\sigma_u} = 1 \quad 6.2$$

Equation 6.2 and the corresponding straight line on the normalized plot (Fig. 6.1) were developed by Smith (1942) from an early proposal by Goodman and they are called the modified Goodman equation and line, respectively. A variety of other equations have been developed and proposed to fit the central tendency of data of this type. One of the earliest to be employed was the Gerber parabola (shown in Fig. 6.1), and gives the following equation (Dowling 2007):

$$\frac{\sigma_a}{\sigma_{ar}} + \left(\frac{\sigma_m}{\sigma_u}\right)^2 = 1 \quad 6.3$$

Better agreement for ductile metals is often achieved by replacing  $\sigma_u$  in Eq. 6.2 with either (i) the corrected true fracture strength  $\tilde{\sigma}_{fB}$  from a tension test, or (ii) the constant  $\sigma'_f$

from the un-notched uniaxial S-N curve for  $\sigma_m = 0$ , in the form of Eq. 6.1 (Dowling 2007):

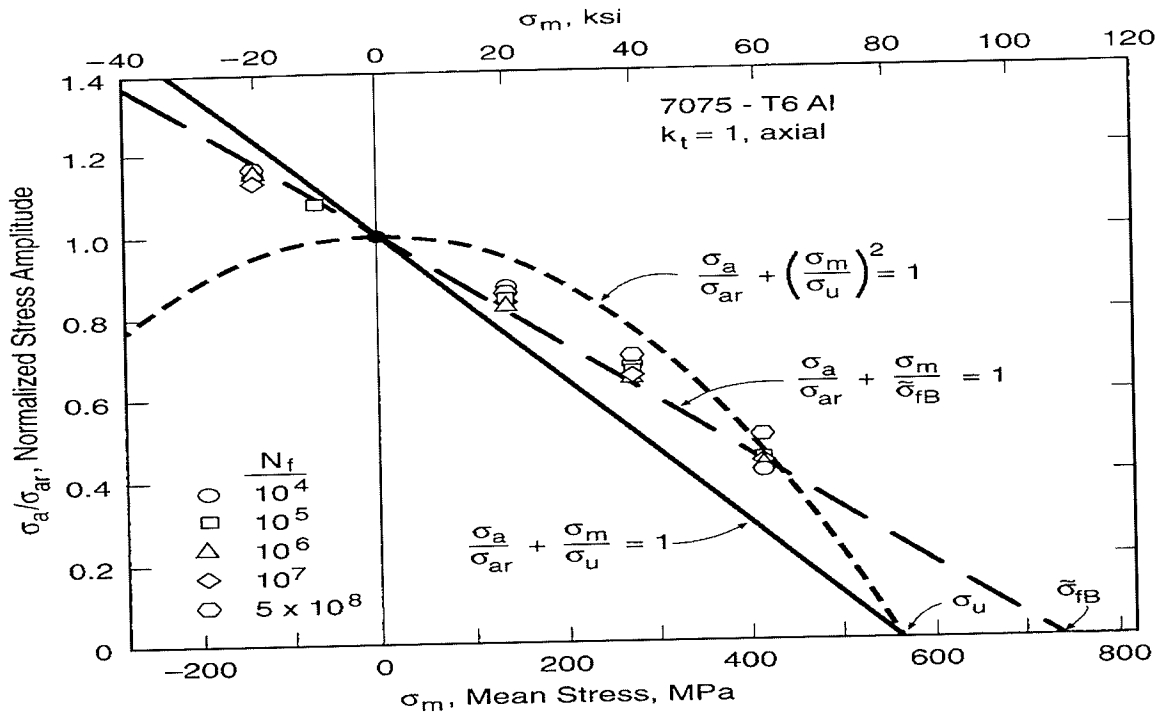


Fig. 6.1 Normalized amplitude-mean diagram (Dowling 2007)

$$\frac{\sigma_a}{\sigma_{ar}} + \frac{\sigma_m}{\tilde{\sigma}'_{fB}} = 1, \quad \frac{\sigma_a}{\sigma_{ar}} + \frac{\sigma_m}{\sigma'_f} = 1 \quad (a, b) \quad 6.4$$

Such a modification of the Goodman line was proposed by J. Morrow in the first edition of the Society of Automotive Engineers' Fatigue Design Handbook (Graham et al. 1968). The constant  $\sigma'_f$  is often approximately equal to  $\tilde{\sigma}'_{fB}$ , and both of these values are somewhat higher than  $\sigma_u$  for ductile metals. Equation 6.4 with  $\sigma'_f$  generally gives reasonable results for steels. Substituting values of stress amplitude  $\sigma_a$  and mean stress  $\sigma_m$  in Eq. 6.4 gives stress amplitude  $\sigma_{ar}$  that is expected to produce the same life at zero mean stress as the  $(\sigma_a, \sigma_m)$  combination. Therefore,  $\sigma_{ar}$  can be thought of as an equivalent completely reversed stress amplitude. Substituting  $\sigma_{ar}$  into a stress-life curve

for zero mean stress thus provides a life estimate for the  $(\sigma_a, \sigma_m)$  combination. For example, assume that the S-N curve for completely reversed loading is known and has an equation of the form of Eq. 6.1. Because tests at  $\sigma_m = 0$  are employed to obtain the constants  $\sigma'_f$  and  $b$ , the stress amplitude  $\sigma_a$  corresponds to the special case denoted by  $\sigma_{ar}$ , therefore, the equation needs to be written as (Dowling 2007):

$$\sigma_{ar} = \sigma_f(2N_f)^b \quad 6.5$$

Combining Eq. 6.5 with Eq. 6.4 yields a more general stress-life equation that applies for non-zero mean stress (Dowling 2007):

$$\sigma_{ar} = (\sigma_f - \sigma_m)(2N_f)^b \quad 6.6$$

### 6.5 Multi-Axial Fatigue

Engineering components of structures are often subjected to complicated states of stress and strain. Parts such as crankshafts, propeller shafts, and rear axles are often subjected to combined bending and torsion with complex stress states in which the three principal stresses are non-proportional and/or whose directions change during a loading cycle. Fatigue under these circumstances is termed as multi-axial fatigue and it is an important design consideration for reliable operation and optimization of many engineering components (Bannantine et al. 1990). Fatigue due to multi-axial loading where plastic deformations take place is currently an area of active research. For ductile engineering metals, it is reasonable to assume that the fatigue life is controlled by the cyclic amplitude of the octahedral shear stress. The amplitudes of the principal stresses,  $\sigma_{1a}$ ,  $\sigma_{2a}$ , and  $\sigma_{3a}$  can then be employed to compute effective stress amplitude,  $\bar{\sigma}_a$ , using a relationship similar to that employed for the octahedral shear yield criterion (Lampman 1996):

$$\bar{\sigma}_a = \frac{1}{\sqrt{2}} \sqrt{(\sigma_{1a} - \sigma_{2a})^2 + (\sigma_{2a} - \sigma_{3a})^2 + (\sigma_{3a} - \sigma_{1a})^2} \quad 6.7$$

An effective mean stress,  $\bar{\sigma}_m$ , can be calculated from the mean stresses in the three principal directions (Dowling 2007):

$$\bar{\sigma}_m = \sigma_{1m} + \sigma_{2m} + \sigma_{3m} \quad 6.8$$

The quantities  $\bar{\sigma}_a$  and  $\bar{\sigma}_m$  can be combined into an equivalent completely reversed uniaxial stress,  $\sigma_{ar}$ , by generalizing Eq. 6.4 for the amplitude-mean diagram (Dowling 2007):

$$\sigma_{ar} = \frac{\bar{\sigma}_a}{1 - \frac{\bar{\sigma}_m}{\sigma_f}} \quad 6.9$$

## 6.6 Fatigue Life of Specimens

Many references suggest that the fatigue strength coefficient,  $\sigma_f' = (\sigma_u + 345)$  MPa, for  $BHN < 500$ , where  $\sigma_u$  is the ultimate strength of the material (Bannantine et al. 1990). This formula is conservative and was used to calculate  $\sigma_f'$  for rollers and roller path plates in this study. The fatigue strength exponent,  $b$ , of the tested rollers and roller path plates was obtained from related literature and is listed in Table 6.1.

Table 6.1 Fatigue properties of rollers and roller path plates

Specimen	Fatigue Strength Coefficient $\sigma_f'$ (MPa)	Fatigue Strength Exponent $b$	Reference
R <sub>1</sub>	581.5	-0.123	(Tucker and Olberts 1969)
R <sub>2</sub>	1159	-0.1055	(Park and Stone 1981)
R <sub>3</sub>	1670	-0.090	(Boller and Seeger 1987) (Davis 1999) (Lampman 1996) (Shiozawa and Sakai 1996)
P <sub>1</sub>	1069	-0.127	
P <sub>3</sub>	1655	-0.083	

A point P, where high local contact stresses were found in the rolling contact surface area of Roller R<sub>1</sub> under a radial compressive load, F, of 734 kN (165 kips), as discussed in Sections 5.4.2, was considered. The three principal stresses,  $\sigma_1$ ,  $\sigma_2$ , and  $\sigma_3$  as given in Table 5.1 at this point P are -820, -1299, and -1697 MPa, respectively. Assuming the roller travels (rolls) a distance of 220 mm (a 30° rotation), as depicted in Fig. 6.2, the new position of point P is designated as P'. The stresses in all three principal directions at point P' will be zero. The fatigue life of Roller R<sub>1</sub> due to movement of point P was computed according to Sections 6.4 and 6.5 as follows:

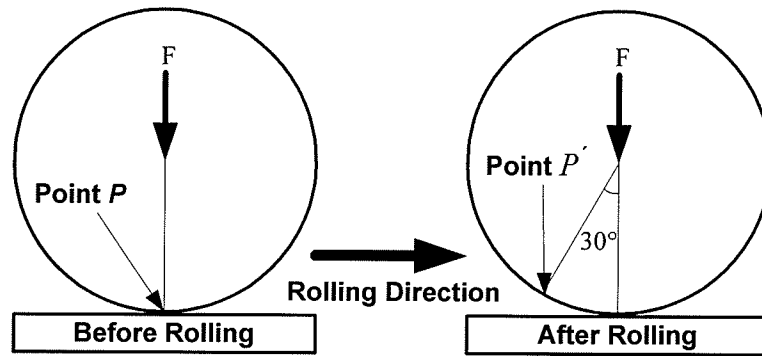


Fig. 6.2 Movement of point P in roller

$$\sigma_{a1} = \frac{\sigma_{\max} - \sigma_{\min}}{2} = \frac{0 - (-820)}{2} = 410 \text{ MPa}, \quad \sigma_{a2} = 649.5 \text{ MPa}, \quad \sigma_{a3} = 848.5 \text{ MPa}$$

$$\sigma_{m1} = \frac{\sigma_{\max} + \sigma_{\min}}{2} = -410 \text{ MPa}, \quad \sigma_{m2} = -649.5 \text{ MPa}, \quad \sigma_{m3} = -848.5 \text{ MPa}$$

These stresses were then used to form “equivalent” alternating and mean stresses. They are equivalent because their joint effect gives the same life in uniaxial tests as that expected from the multi-axial situations. The equivalent alternating stress is calculated from Eq. 6.7 as follows:

$$\bar{\sigma}_a = \frac{1}{\sqrt{2}} \sqrt{(410 - 649.5)^2 + (649.5 - 848.5)^2 + (848.5 - 410)^2} = 380.3 \text{ MPa}$$

The equivalent mean stress,  $\bar{\sigma}_m$ , from Eq. 6.8 is simply the sum of the mean normal stresses in three mutually perpendicular principal directions:

$$\bar{\sigma}_m = -410 - 649.5 - 848.5 = -1908 \text{ MPa}$$

With the values for  $\bar{\sigma}_a$  and  $\bar{\sigma}_m$  known, the J. Morrow Eq. 6.9 can be used to obtain the uniaxial fully reversed fatigue strength,  $\sigma_{ar}$ . From Table 6.1 for Roller R<sub>1</sub>,  $\sigma'_f = 581.5$  MPa. Thus,

$$\sigma_{ar} = \frac{380.3}{1 - \frac{-1908}{581.5}} = 88.83 \text{ MPa}$$

Thus, the fatigue life for Roller R<sub>1</sub> can be calculated using the S-N Equation 6.5 with fatigue strength exponent b taken from Table 6.1 as -0.123, as follows:

$$N_f = \frac{1}{2} \left( \frac{88.83}{581.5} \right)^{\frac{1}{-0.123}} = 2.15 \text{ million cycles}$$

This means that the 1<sup>st</sup> macro crack will initiate or appear after 2.15 millions of cycles of repeated loading. Since rollers and roller path plates were analyzed in ANSYS<sup>®</sup> FE program with the normal (radial) force only and no tangential or frictional forces were incorporated, the principal stresses used in above example do not reflect the real life situation. As discussed in Section 2.3, the maximum compressive principal stress,  $\sigma_1$ , is always accompanied by tensile principal stress  $\sigma_2$  and  $\sigma_3$ , for a roller on plane under the influence of both normal and tangential (frictional) forces. By maximizing the effective

stress amplitude,  $\bar{\sigma}_a$ , and minimizing the equivalent mean stress,  $\bar{\sigma}_m$ , and considering that the compressive principal stress  $\sigma_1$  is accompanied by tensile principal stresses  $\sigma_2$  and  $\sigma_3$  will constitute the worst-case scenario. In this case, the maximum compressive principal stress,  $\sigma_1$ , in Roller  $R_1$  is set equal to the ultimate strength of Roller  $R_1$ , which is 236.5 MPa. The tensile principal stresses,  $\sigma_2$  and  $\sigma_3$ , are chosen in such a manner as to get the maximum effective stress amplitude,  $\bar{\sigma}_a$ , and minimum equivalent mean stress,  $\bar{\sigma}_m$ . In this option, a stress value equal to half of the principal stress,  $\sigma_1$  ( $\therefore \sigma_2 = \sigma_3 = 118.25$  MPa) is required. Repeating calculations in the above example with the principal stress  $\sigma_1$ ,  $\sigma_2$ , and  $\sigma_3$  as -236.5, 118.25, and 118.25 MPa, respectively yield the following:

$$\sigma_{a1} = 118.25 \text{ MPa}, \quad \sigma_{a2} = 59.125 \text{ MPa}, \quad \sigma_{a3} = 59.125 \text{ MPa}$$

$$\sigma_{m1} = -118.25 \text{ MPa}, \quad \sigma_{m2} = 59.125 \text{ MPa}, \quad \sigma_{m3} = 59.125 \text{ MPa}$$

$$\bar{\sigma}_a = 59.125 \text{ MPa}, \quad \bar{\sigma}_m = -118.25 + 59.125 + 59.125 = 0.0 \text{ MPa}$$

$$N_f = 58.9 \text{ million cycles}$$

This means that the fatigue life of Roller  $R_1$  under the influence of both radial and tangential (frictional) forces leading to worst-case scenario principal stresses is 58.9 million cycles. This high value of fatigue life of Roller  $R_1$  is due to the very low values of principal stresses employed in above example. It is evident from the FE analysis that very high contact stresses are present in the contact area of roller and roller path plate. One of the three coupon test results on cast iron roller conducted by Muzykza (1992) revealed

that the ultimate compressive strength of cast iron roller was 979 MPa. Repeating calculations in the above example with the principal stress  $\sigma_1$ ,  $\sigma_2$ , and  $\sigma_3$  as -979, 489.5, and 489.5 MPa, respectively yield the fatigue life of Roller R<sub>1</sub> as ½ million cycles, which makes sense and matches with the laboratory test results. Following a similar procedure, the fatigue life of the rollers and the roller path plates examined in this study under the influence of radial and tangential forces leading to worst-case scenario maximum principal stresses, was computed and is listed in Table 6.2.

Table 6.2 Fatigue life of specimens under worst-case scenario

Specimen	Principal Stress, MPa			Effective Stress Amplitude, $\bar{\sigma}_a$ MPa	Equivalent Mean Stress, $\bar{\sigma}_m$ MPa	Life, $N_f$ million
	$\sigma_1$	$\sigma_2$	$\sigma_3$			
R <sub>1</sub>	-979	+489.5	+489.5	244.75	0.0	½
R <sub>2</sub>	-814	+407	+407	203.5	0.0	7¼
R <sub>3</sub>	-1325	+662.5	+662.5	331.25	0.0	32
P <sub>1</sub>	-724	+362	+362	181	0.0	½
P <sub>3</sub>	-1310	+655	+655	327.5	0.0	150

In all cases, the principal compressive stress  $\sigma_1$  was chosen to be equal to the ultimate strength of the specimen. If the three principal stresses at point P in Fig. 6.2 in Roller R<sub>1</sub> before rolling are set equal to -880, +440, and +440 MPa (principal stress,  $\sigma_1$  of 979 MPa is reduced by 10%) and the above calculations are repeated, the fatigue life of Roller R<sub>1</sub>

is one million cycles. This means if the contact principal stresses are reduced by 10%, the life is increased by 100%. This proves that the high contact stresses are fatal to the fatigue life of rollers and roller path plates.

## **6.7 Discussion of the Results**

In laboratory tests, Roller  $R_1$  was rolled back and forth on roller path Plates  $P_1$  and  $P_2$  for a total circumferential distance of 75 mm or 37.5 mm from either side of the central strain gauge. Rollers  $R_2$  and  $R_3$  were rolled back and forth on roller path plates  $P_3$  through  $P_6$  for a total circumferential distance of 50 mm or 25 mm from either side of the central strain gauge. Thus, the variation of strains took place over a short distance of 37.5 mm or 25 mm. The strain gauges were installed on the top rim surface perpendicular to the rim-rolling surface and they were 44.5 mm (1¾ in.) far from the critical contact stress zone. In laboratory testing, the rollers and roller path plates were subjected to both radial and tangential (frictional) forces; however, it was not possible to record the magnitude of the lateral force. The fatigue life of the rollers and the roller path plates was computed on the basis of the variation of worst-case scenario principal stresses over a distance of 220 mm (8½ in.). The principal stresses used in fatigue analysis included the effect of both radial and tangential forces. Stress amplitude in the laboratory testing is much smaller than that in fatigue analysis.

During cyclic testing, it was not possible to record when the first crack appeared on the rollers or roller path plates due to inaccessibility. Therefore, the strain variation results obtained from laboratory tests cannot be directly compared to the results obtained from

fatigue analysis. However, the final visual inspection and scanning electron microscope results of the rollers and the roller path plates can be compared to the results of fatigue analysis.

Theoretical analyses showed that the fatigue life of Roller  $R_1$  and roller path Plates  $P_1$  and  $P_2$  under the influence of both radial (normal) and tangential (frictional) forces is  $\frac{1}{2}$  a million cycles. Roller  $R_1$  and Plates  $P_1$  and  $P_2$  were subjected to a million and 0.82 million cycles, respectively. Visual inspection and SEM results showed complete failure of Roller  $R_1$  and Plates  $P_1$  and  $P_2$ . There is an indication of a clear drop in strain values in the strain gauge results. For example in strain gauge 5 in Roller  $R_1$ , Side A, there was a sudden drop of  $900 \mu\epsilon$  in the minimum and maximum strain curves after 457,727 cycles, as discussed in Section 4.4. This supports the assumption that there is an agreement between laboratory results and fatigue analysis results.

The fatigue life of Rollers  $R_2$  and  $R_3$  and roller path Plate  $P_3$  is very high, as compared to that of Roller  $R_1$  and roller path Plate  $P_1$ . Laboratory test results, visual inspection and SEM results of Rollers  $R_2$  and  $R_3$  and roller path Plate  $P_3$  support the fatigue analysis results. High principal compressive and tensile contact stresses under the influence of both radial (normal) and tangential (frictional) forces, evidenced by both FE results and literature review, are the main cause of fatigue failure of rollers and roller path plates.

### 7.1 Summary

The main objectives of this doctoral thesis were to review current design standards of rollers used by Manitoba Hydro, to test rollers and roller path plates under fatigue loading, to perform finite element analysis of rollers and roller path plates, to assess fatigue life of rollers and roller path plates, and, to make recommendations for the design of rollers and roller path plates.

The design of gate rollers involves the use of an empirical formula, based on BHN, to obtain the initial roller diameter and the tread width (Noonan and Strange 1934). Currently, Tread surface Hertzian contact stresses and subsurface shear stresses are computed using methods developed by Thomas and Hoersch (1930). Although the Noonan and Strange (1934) formula was based on tests involving small diameter cylindrical forged steel rollers, it has been subsequently adopted for the design of large diameter crowned wrought-steel wheels, some in excess of 760 mm in diameter. The applicability of this formula to crowned wheels is questionable. Furthermore, this formula provides no information on the fatigue life of rollers or the relationship between the safe working loads and ultimate load capacity of the wheels, thereby making the safe wheel capacity unknown.

To meet the objectives of this study, both experimental and theoretical work were carried out. The experimental program involved laboratory testing of three rollers and six roller path plates under cyclic loading. A unique testing station was developed to test rollers

and roller path plates under cyclic loading. Rollers were 838 mm (33 in.) in diameter with an 89 mm (3½ in.) flange thickness and a crown radius of 914 mm (36 in.). One of the rollers ( $R_1$ ) was made of gray cast iron. The material in Roller  $R_2$  was AISI 1060 high carbon steel without heat treatment, whereas the material in Roller  $R_3$  was AISI 1080 heat treated high carbon steel. Two of the rollers ( $R_1$  and  $R_2$ ) were obtained from the Kelsey Hydro Generating Station in Manitoba. The third Roller,  $R_3$  was specially ordered, manufactured, and shipped from the United States specifically for this research project. Six rectangular steel Plates ( $P_1$  through  $P_6$ ), measuring  $381 \times 178$  mm ( $15 \times 7$  in.) with a thickness of 51 mm (2 in.) were used as roller path plates in this research program. Plates  $P_1$  and  $P_2$  were AISI 1050 medium carbon steel without heat treatment, whereas, Plates  $P_3$  through  $P_6$  were SS 410 heat-treated stainless steel. Strain gauges were installed on all rollers and roller path plates in order to monitor and record the strain values during cyclic loading.

The rollers were tested at two opposite locations labeled as side A and side B. For each cyclic test, a roller was in contact with the roller path plate on one side only. Roller  $R_1$  was tested to a million cycles on side A (Test  $R_{1A}$ ) and 818,726 cycles on side B (Test  $R_{1B}$ ) with roller path Plates  $P_1$  and  $P_2$ , respectively. The test was continuous and uninterrupted during this trend. Roller  $R_2$  was tested continuously to 220,000 cycles on side A (Test  $R_{2A}$ ) and 200,000 cycles on side B (Test  $R_{2B}$ ) with roller path Plates  $P_3$  and  $P_4$ , respectively. Roller  $R_3$  was tested for 200,000 cycles at side A with roller path Plate  $P_5$  (Test  $R_{3A1}$ ). After completing 200,000 cycles, the test setup was dismantled and indentation profiles in the roller path Plate  $P_5$  were measured. After this test, Roller  $R_3$

was re-loaded at the same location side A along with same roller path Plate P<sub>5</sub> and was re-tested for an additional 200,000 cycles (Test R<sub>3A2</sub>). A similar procedure was used to test Side B of the same Roller R<sub>3</sub> with roller path Plate P<sub>6</sub> up to 200,000 cycles (Test R<sub>3B1</sub>) and up to an additional 200,000 cycles (Test R<sub>3B2</sub>). Prior to testing the rollers and the roller path plates under cyclic loading, a series of surface hardness measurements was performed using Proceq EQUITOP electronic hardness testing equipment. Roller R<sub>1</sub> was rolled back and forth on roller path Plates P<sub>1</sub> and P<sub>2</sub> for a total circumferential distance of 75 mm (3 in.). The Rollers R<sub>2</sub> and R<sub>3</sub> were rolled back and forth on roller path plates for a total circumferential distance of 50 mm (2 in.). Before and after each cyclic test, photographs were taken for all specimens. At the end of each cyclic test, the test-setup was dismantled and the rolling contact surface of all specimens was examined by visual inspection. Indentation measurements were taken for each roller path plate using a special set-up.

In order to observe the extent of damage under cyclic testing, all tested contact areas of rollers and roller path plates were scanned using an electron microscope and computer-controlled optical microscope. Samples were extracted from both tested and non-tested areas of all rollers and roller path plates. Initially, large pieces of chunk were cut from the rollers and roller path plates using abrasive water-jet cutting technology. After that, small samples in exact dimensions were cut using a lathe machine.

A finite element (FE) analysis was conducted on a three dimensional contact stress model of a roller and a plate using the ANSYS<sup>®</sup> general-purpose finite element program, version

10.0 (Swanson 2005). Contact stress problems are highly nonlinear and require significant computer resources to solve. The computer run time was reduced by taking advantage of the symmetric geometry of the roller and roller path plate. As a result, one-eighth of the roller was modeled along with one-quarter of roller path plate as a contact stress problem. Two programs R<sub>1</sub>P<sub>1</sub> and R<sub>3</sub>P<sub>3</sub> were developed in ANSYS® to analyze rollers and roller plates. The program R<sub>1</sub>P<sub>1</sub> was developed to analyze Roller R<sub>1</sub> and Plates P<sub>1</sub> and P<sub>2</sub>, whereas, the program R<sub>3</sub>P<sub>3</sub> was developed to analyze Rollers R<sub>2</sub> and R<sub>3</sub> and roller path Plates P<sub>3</sub> through P<sub>6</sub>. The program R<sub>1</sub>P<sub>1</sub> was run two times, once with an external load of 838 kN (188½ kips) to simulate laboratory testing of Roller R<sub>1A</sub> and a second time with an external load of 734 kN (165 kips) to simulate service load conditions. The program R<sub>3</sub>P<sub>3</sub> was also run two times, once with an external load of 814 kN (183 kips) to simulate laboratory testing of Rollers R<sub>2A</sub> and R<sub>3A1</sub> and a second time with an external load of 734 kN (165 kips) to simulate service load conditions. The fixed boundary condition applied to the back of the plate and the application of external load in terms of pressure on an inside roller-hole area represented exactly the same situation as that of laboratory testing. The CPU run time, using specially built personal computer with 2.93 GHz Intel® Dual Core™ 2 Extreme Processor, 4 GB of RAM, 64-bit version of both Windows XP operating system and ANSYS®, was 29½ days. Based on FE stress results, fatigue life of rollers and roller path plates was assessed using the multi-axial stress-life method.

The BHN of Rollers R<sub>1</sub>, R<sub>2</sub>, and R<sub>3</sub> and roller path Plates P<sub>1</sub> and P<sub>3</sub> was 219, 373, 473, 291, and 364, respectively. Very high strains were observed for the two cyclic tests

conducted on Roller R<sub>1</sub>, whereas, much lower strains were found in Rollers R<sub>2</sub> and R<sub>3</sub> as compared to those in Roller R<sub>1</sub>. Although, the average radial cyclic load on Roller R<sub>3A2</sub> was 3.6% higher than that in Roller R<sub>1B</sub>, the maximum strain recorded during the 1<sup>st</sup> cycle in Roller R<sub>1B</sub> was 11.7 times more than the maximum strain recorded during the 1<sup>st</sup> cycle in Roller R<sub>3A2</sub>. Likewise, despite the average radial cyclic load on Roller R<sub>2B</sub> was 8.9% higher than that in Roller R<sub>1B</sub>, the maximum strain recorded during the 1<sup>st</sup> cycle in Roller R<sub>1B</sub> was 7.7 times more than the maximum strain recorded during the 1<sup>st</sup> cycle in Roller R<sub>2B</sub>. Although, the average radial cyclic load on Roller R<sub>3A2</sub> was 3.6% higher than that in Roller R<sub>1B</sub>, the maximum principal strain recorded during the 1<sup>st</sup> cycle in Roller R<sub>1B</sub> was 10.6 times more than the maximum strain recorded during the 1<sup>st</sup> cycle in Roller R<sub>3A2</sub>. Likewise, despite the average radial cyclic load on Roller R<sub>2B</sub> was 8.9% higher than that in Roller R<sub>1B</sub>, the maximum principal strain recorded during the 1<sup>st</sup> cycle in Roller R<sub>1B</sub> was 4 times more than the maximum principal strain recorded during the 1<sup>st</sup> cycle in Roller R<sub>2B</sub>. It is clear from the above comparisons that the material in Roller R<sub>1</sub> was less stiff as compared to those of Rollers R<sub>2</sub> and R<sub>3</sub>. The high values of strains found in Roller R<sub>1</sub> are most likely due to micro cracking on the roller contact surface. In addition, the material in Roller R<sub>3</sub> is more rigid than that of Roller R<sub>2</sub>. This hypothesis is also confirmed by BHN, SEM examination, and physical inspection of the rollers after cyclic testing.

Higher strains were observed in roller path Plates P<sub>1</sub> and P<sub>2</sub>, whereas, lower strains were found in roller path Plates P<sub>3</sub> through P<sub>6</sub>. Although, the average radial cyclic load in Plate P<sub>5</sub> in Test R<sub>3A2</sub> was 3.6% higher than that in Plate P<sub>2</sub>, the maximum strain recorded

during the 1<sup>st</sup> cycle in Plate P<sub>2</sub> was 4 times more than the maximum strain recorded during the 1<sup>st</sup> cycle in Plate P<sub>5</sub> in Test R<sub>3A2</sub>. This showed that the material in Plate P<sub>3</sub> through P<sub>6</sub> was far superior to that in Plates P<sub>1</sub> and P<sub>2</sub>. This premise was also confirmed by the BHN, indentation depths, SEM testing, and physical examination of the plates after cyclic testing. Plates P<sub>1</sub> and P<sub>2</sub> exhibited higher indentation depths as compared to roller path Plates P<sub>3</sub> through P<sub>6</sub>. Two sets of major and minor visual cracks were observed in Roller R<sub>1</sub> and in roller path Plates P<sub>1</sub> and P<sub>2</sub>. Cracks were vertical, horizontal, diagonal as well as longitudinal. There was no sign of any kind of crack or deformation in the tested contact areas of both sides of Rollers R<sub>2</sub> and R<sub>3</sub> and in roller path Plates P<sub>3</sub> through P<sub>6</sub>.

A comparison between laboratory test results and FE analysis results indicated that the two results were in good agreement with each other. The FE results indicated that a high stress concentration zone in contact areas in both in roller and in roller path plate was critical. The maximum values of all types of stresses were found in these zones in roller and in roller path plate. The trend and style of stresses found in the contact area of roller and roller path plate exactly matched with those found in the literature. The results obtained from FE analysis and those from using hand calculations and formulae given by Roark (2002) proved that the contact stresses were higher than the yield strength of roller and roller path plate.

The average radial compressive load applied on rollers in laboratory testing during cyclic movement varied from 753.17 kN (169.31 kips) to 903.21 kN (203.04 kips). The

maximum service load limit for 838 mm (33 in.) diameter rollers is 734 kN (165 kips) and 1050 kN (236 kips) for serviceability and strength criteria, respectively. The objective of applying radial load during cyclic testing was to check the serviceability criteria and not strength. The static ultimate strength of these rollers is quite high. The indentation profile of roller path Plates P<sub>1</sub> and P<sub>2</sub> after cyclic testing failed serviceability criteria, whereas, roller path Plates P<sub>3</sub> through P<sub>6</sub> passed serviceability criteria. Roller path plate deformation increases frictional forces that lead to higher principal tensile stresses as predicted in the literature discussed in Section 2.3. Lubricating the roller path plate surface could help in reducing the frictional forces but not if the indentation is very high.

In laboratory tests, Roller R<sub>1</sub> was rolled back and forth on roller path Plates P<sub>1</sub> and P<sub>2</sub> for a total circumferential distance of 75 mm (3 in.). Rollers R<sub>2</sub> and R<sub>3</sub> were rolled back and forth on roller path plates P<sub>3</sub> through P<sub>6</sub> for a total circumferential distance of 50 mm (2 in.). Thus, the variation of strains took place over a short distance of 37.5 mm (1½ in.) or 25 mm (1 in.). The strain gauges were installed on the top rim surface perpendicular to the rim-rolling surface and they were 44.5 mm (1¾ in.) far from the critical contact stress zone. In laboratory testing, the rollers and roller path plates were subjected to both radial and tangential forces; however, it was not possible to record the magnitude of the lateral force. The fatigue life of the rollers and the roller path plates was computed on the basis of the variation of worst-case scenario principal stresses over a distance of 220 mm (8½ in.). The principal stresses used in fatigue analysis included the effect of both radial and tangential forces. Stress amplitude in the laboratory testing is much smaller than that in fatigue analysis.

During cyclic testing, it was not possible to record when the first crack appeared on the rollers or roller path plates due to inaccessibility. Therefore, the strain variation results obtained from laboratory tests cannot be directly compared to the results obtained from fatigue analysis. However, the final visual inspection and scanning electron microscope results of the rollers and the roller path plates can be compared to the results of the fatigue analysis.

Theoretical analyses showed that the fatigue life of Roller  $R_1$  and roller path Plates  $P_1$  and  $P_2$  under the influence of both normal and frictional forces, leading to worst-case scenario principal stresses, was one half of a million cycles. Roller  $R_1$  and Plates  $P_1$  and  $P_2$  were subjected to a million and 0.82 million cycles, respectively. Visual inspection and SEM results showed complete failure of Roller  $R_1$  and Plates  $P_1$  and  $P_2$ . There is an indication of a clear drop in strain values in the strain gauge results. For example in strain gauge 5 in Roller  $R_1$ , Side A, there was a sudden drop of  $900 \mu\epsilon$  in the minimum and maximum strain curves after 457,727 cycles. This supports the assumption that there is an agreement between laboratory results and fatigue analysis results. The fatigue life of Rollers  $R_2$  and  $R_3$  and roller path Plates  $P_3$  through  $P_6$  was very high as compared to those of Roller  $R_1$  and roller path Plates  $P_1$  and  $P_2$ . Laboratory test results, visual inspection and SEM results of Rollers  $R_2$  and  $R_3$  and roller path Plates  $P_3$  through  $P_6$  support the fatigue analysis results.

A reduction of 10% in the worst-case scenario principal stresses, under the influence of both radial and tangential forces, resulted in an increase of 100% in fatigue life of Roller

R<sub>1</sub>. High principal contact stresses under the influence of both radial and tangential forces, evidenced by FE, fatigue analyses, and literature review, are the main cause of fatigue failure of rollers and roller path plates.

In his laboratory testing, Muzyczka (1992) found that the ultimate load capacity of a 685.5 mm (27 in.) diameter cast iron roller under radial load only was 2197 kN (494 kips). This was based on an average value and the load was applied through handling holes. Based on Muzyczka's (1992) experimental results, the author believes that the ultimate load capacity of an 838 mm (33 in.) diameter Roller R<sub>1</sub> would be at least 2669 kN (600 kips). The ultimate load capacity of Rollers R<sub>2</sub> and R<sub>3</sub> would be even higher, because they were without handling holes. The maximum service load limit for 838 mm (33 in.) diameter rollers is 734 kN (165 kips) and 1050 kN (236 kips) for serviceability and strength criteria, respectively. This clearly shows that the static ultimate load capacity of these rollers is quite good. The main problem is the contact stresses and fatigue life of the rollers.

## **7.2 Conclusions**

Based on the results obtained from laboratory cyclic tests, visual inspection, scanning electron microscope, finite element analyses, and fatigue analysis, the following important conclusions are drawn from this research study:

1. The BHN of Rollers R<sub>1</sub> recorded as 219 was 1.7 and 2.16 times less than that of Rollers R<sub>2</sub> and R<sub>3</sub>, respectively. Very high strains were observed for the two

cyclic tests conducted on Roller R<sub>1</sub>, whereas, much lower strains were found in Rollers R<sub>2</sub> and R<sub>3</sub> as compared to those in Roller R<sub>1</sub>. Although, the average radial cyclic loads on Rollers R<sub>2B</sub> and R<sub>3A2</sub> were 8.9% and 3.6% respectively, higher than those of Roller R<sub>1B</sub>, the maximum strain recorded during the 1<sup>st</sup> cycle in Roller R<sub>1B</sub> was 7.7 and 11.7 times more than the maximum strain recorded during the 1<sup>st</sup> cycle in Rollers R<sub>2B</sub> and R<sub>3A2</sub>, respectively. Likewise, although, the average radial cyclic loads on Rollers R<sub>2B</sub> and R<sub>3A2</sub> were 8.9% and 3.6% respectively, higher than those of Roller R<sub>1B</sub>, the maximum principal strain recorded during the 1<sup>st</sup> cycle in Roller R<sub>1B</sub> was 4 and 10.6 times more than the maximum principal strain recorded during the 1<sup>st</sup> cycle in Rollers R<sub>2B</sub> and R<sub>3A2</sub>, respectively. It is clear from the above comparisons that the material in Roller R<sub>1</sub> was less stiff as compared to those of Rollers R<sub>2</sub> and R<sub>3</sub>. Roller R<sub>1</sub> was subjected to a million and 0.82 million cycles. Visual inspection and SEM results showed complete failure of Roller R<sub>1</sub>. The fatigue life of Roller R<sub>1</sub> under the influence of worst-case scenario principal stresses was ½ a million cycles. Based on these results, it is concluded that the cast iron Roller R<sub>1</sub> performed very poorly, as compared to Rollers R<sub>2</sub> and R<sub>3</sub>. The high values of strains found in Roller R<sub>1</sub> are most likely due to micro cracking on the roller contact surface.

2. The BHN of roller path Plates P<sub>1</sub> and P<sub>2</sub> recorded as 291 was 1.25 times less than that of roller path Plates P<sub>3</sub>-P<sub>6</sub>. Higher strains were observed in roller path Plates P<sub>1</sub> and P<sub>2</sub>, whereas, lower strains were found in roller path Plates P<sub>3</sub> through P<sub>6</sub>. Although, the average radial cyclic load in Plate P<sub>5</sub> was 3.6% higher than that in

Plate P<sub>2</sub>, the maximum strain recorded during the 1<sup>st</sup> cycle in Plate P<sub>2</sub> was 4 times more than the maximum strain recorded during the 1<sup>st</sup> cycle in Plate P<sub>5</sub>. Roller path Plates P<sub>1</sub> and P<sub>2</sub> were subjected to a million and 0.82 million cycles, respectively. Plates P<sub>1</sub> and P<sub>2</sub> exhibited higher indentation depths as compared to roller path Plates P<sub>3</sub> through P<sub>6</sub>. Visual inspection and SEM results showed complete failure of these plates. The fatigue life of Plates P<sub>1</sub> and P<sub>2</sub> under the influence of worst-case scenario principal stresses was one-half of a million cycles. Based on above, it is concluded that the material in medium carbon steel Plates P<sub>1</sub> and P<sub>2</sub> (without heat treatment) was less stiff as compared to those in Plates P<sub>3</sub> through P<sub>6</sub>, and thus, these plates performed very poorly.

3. Roller R<sub>2</sub> was subjected to 0.20 to 0.22 million cycles. Visual inspection and SEM results showed no sign of any kind of crack or damage in Roller R<sub>2</sub>. The fatigue life of Roller R<sub>2</sub> under the influence of worst-case scenario principal stresses was 7¼ million cycles. Therefore, this roller performed much better than Roller R<sub>1</sub> and roller path Plates P<sub>1</sub> and P<sub>2</sub>.
4. Strains in Roller R<sub>3</sub> were even lower than those found in Roller R<sub>2</sub>. Roller R<sub>3</sub> was subjected to 0.20 to 0.40 million cycles. Visual inspection and SEM results showed no sign of any kind of crack or damage in Roller R<sub>3</sub>. The fatigue life of Roller R<sub>3</sub> under the influence of worst-case scenario principal stresses was 32 million cycles. Thus, Roller R<sub>3</sub> performed far superior to that of Roller R<sub>1</sub>. The reason was that it was heat treated high carbon steel.

5. The BHN of roller path Plates P<sub>3</sub>-P<sub>6</sub> recorded as 364 was 1.25 times more than that of roller path Plates P<sub>1</sub>-P<sub>2</sub>. Although, the average radial cyclic load on roller path Plate P<sub>5</sub> was 3.6% higher than that in Plate P<sub>2</sub>, the maximum strain recorded during the 1<sup>st</sup> cycle on Plate P<sub>5</sub> was 4 times less than the maximum strain recorded during the 1<sup>st</sup> cycle on Plate P<sub>2</sub>. Thus, strains in roller path Plates P<sub>3</sub>-P<sub>6</sub> were much lower than that in roller path Plates P<sub>1</sub>-P<sub>2</sub>. Plates P<sub>3</sub> through P<sub>6</sub> exhibited much lower indentation depths as compared to those of roller path Plates P<sub>1</sub>-P<sub>2</sub>. Visual inspection and SEM results showed no sign of any kind of crack or damage in roller path Plates P<sub>3</sub>-P<sub>6</sub>. The fatigue life of Plates P<sub>3</sub>-P<sub>6</sub> under the influence of worst-case scenario principal stresses was 150 million cycles. Based on above, it is concluded that the material in Plates P<sub>3</sub>-P<sub>6</sub> was far superior to those of Plates P<sub>1</sub>-P<sub>2</sub>. Therefore, heat-treated stainless steel roller path Plates P<sub>3</sub> through P<sub>6</sub> performed extremely well.

6. The average radial compressive load applied on rollers in laboratory testing during cyclic movement varied from 753.17 kN (169.31 kips) to 903.21 kN (203.04 kips). The maximum service load limit for 838 mm (33 in.) diameter rollers is 734 kN (165 kips) and 1050 kN (236 kips) for serviceability and strength criteria, respectively. The objective of applying radial load during cyclic testing was to check the serviceability criteria and not strength. The static ultimate strength of these rollers is quite high. The indentation profile of roller path Plates P<sub>1</sub> and P<sub>2</sub> after cyclic testing failed serviceability criteria, whereas, roller path Plates P<sub>3</sub> through P<sub>6</sub> passed serviceability criteria. Plate deformation increases frictional forces that lead to higher principal tensile stresses as predicted in the

literature discussed in Section 2.3. Lubricating the roller path plate surface could help in reducing the frictional forces but not if the indentation is very high.

7. A reduction of 10% in the worst-case scenario principal stresses, under the influence of both radial and tangential forces, resulted in an increase of 100% in fatigue life of Roller  $R_1$ . Thus, the high principal contact stresses under the influence of both radial and tangential forces, evidenced by finite element analyses, fatigue analyses, and literature review, are the main cause of fatigue failure of rollers and roller path plates.

### **7.3 Recommendations**

Based on the findings of this doctoral research, the following recommendations are proposed:

1. Cast iron rollers should not be used as rollers.
2. Although high carbon steel Roller  $R_2$  performed very well, it is recommended that the material be heat-treated in order to increase its fatigue life.
3. Medium carbon steel (without heat-treatment) plates must not be used as roller path plates. Instead, heat-treated stainless steel or high carbon steel roller path plates with heat-treatment must be used.
4. In order to reduce contact stresses, which are detrimental to the fatigue life of rollers and roller path plates, the contact surfaces of rollers and roller path plates must be covered with a very thick film of hard steel coatings (Erdemir 1992).

## References

1. Angus, H. T., 1976, *Cast Iron: Physical and Engineering Properties*, 2<sup>nd</sup> Ed., Butterworth, London, England
2. ASTM E 1150-1987, Standard Definitions of Fatigue, *1995 Annual Book of Standards*, ASTM, 1995, pp. 753-762
3. Bannantine, J., Comer, J., and Handrock, J., 1990, *Fundamentals of Metal Fatigue Analysis*, New Jersey, Prentice Hall
4. Baucio, M., Editor, 1993, *ASM Metals Reference Book*, ASM International, American Society for Metals, Materials Park, Ohio
5. Beddoes, J. and Parr, J. G., 1999, *Introduction to Stainless Steels*, 3<sup>rd</sup> ed., ASM International, Materials Park, OH, USA
6. Bhargava, V., Hahn, G. T., and Rubin, C. A., 1989, Rolling Contact Deformation and Microstructural Changes in High Strength Bearing Steel, *Wear*, Vol. 133, 1989, p 69
7. Boller, C. and Seeger, T., 1987, *Materials Data for Cyclic Loading*, Elsevier Science Publications, Amsterdam
8. Boresi, A. P., Schmidt, R. J., and Sidebottom, O. M., 1993, *Advanced Mechanics of Materials*, 5<sup>th</sup> ed., John Wiley & Sons, Inc., New York
9. Brockenbrough, R. L. and Johnston, B. G., 1981, *USS Steel Design Manual*, ADUSS 27-3400-04, United States Steel Corp., Monroeville, PA
10. Davis, H. E., Troxell, G. E., and Hauck, G. F. W., 1982, *The Testing of Engineering Materials*, 4/e, McGraw-Hill, New York, 1982

11. Davis, J. R., Editor, 1996, ASM Specialty Handbook: Carbon and Alloy Steels, *ASM International Handbook Committee*, Materials Park, OH, USA
12. Davis, J. R., Editor, 1999, Metals Handbook, 2<sup>nd</sup> ed., *ASM International Handbook Committee*, Materials Park, OH, USA
13. Doucet, M. R., 2000, An Evaluation of the Design Standards of Rollers and Roller Paths for Hydro Gates, *An under-graduate student final year report*, Civil Engineering Department, University of Manitoba, MB, Canada
14. Dowling N. E. and Thangjitham, S. 2000, An Overview and Discussion of Basic Methodology for fatigue, *Fatigue and Fracture Mechanics: 31<sup>st</sup> Volume, ASTM STP 1389*, G. R. Halford and J. P. Gallagher, Eds., American Society for Testing and Materials, West Conshohocken, PA, pp. 3-36
15. Dowling, N. E., 2007, *Mechanical Behavior of Materials*, 3<sup>rd</sup> Ed., Pearson Prentice Hall, NJ, USA
16. Erdemir, A., 1992, Rolling Contact Fatigue and Wear Resistance of Hard Coatings on Bearing Steel Substrates, *Surface Coating Technology*, Vol. 54-55, No. 1-3, 1992, p 482-489
17. Fisher, J. W., Kulak, G. L., and Smith, I. F. C., 1998, A Fatigue Primer for Structural Engineers, *National Steel Bridge Alliance, American Institute of Steel Construction*, Chicago, Illinois
18. Gale, W. F. and Totemeier, T. C., Editors, 2004, *Smithells Metals Reference Book*, 8<sup>th</sup> ed., Elsevier Butterworth-Heinemann, Burlington, MA, USA
19. Gough, H. J., 1933, *Crystalline Structure in Relation to Failure of Metals-Especially by Fatigue*, Proceedings, ASTM, vol. 33, part II, pp. 3-114

20. Graham, J. A., Millan, J. F., and Appl, F. J., Eds., 1968, *Fatigue Design Handbook*, SAE Publication No. AE-4, Society of Automotive Engineers, Warrendale, PA
21. Harris, T., 1964, The Endurance of Modern Rolling Bearings, AGMA paper 269.01, Oct. 1964, *Rolling Bearing Analysis*, John Wiley, 1966
22. Harvey, P. D., 1982, *Engineering Properties of Steel*, American Society for Metals, Metals Park, Ohio
23. Hassan, S. K., Polyzois, D., and Morris, G., 1998, Axial fatigue Performance of Cold-Formed Steel Sections, *Journal of Structural Engineering*, Vol. 124, No. 2, pp. 149-157
24. Kilburn, K. R., 1964, An Introduction to Rail Wear and Rail Lubrication problems, *Wear*, Vol. 7, 1964, p 255-269
25. Lamb, S. and Bringas, J. E., 2002, *CASTI Handbook of Stainless Steels & Nickel Alloys*, 2<sup>nd</sup> ed., Casti Publishing Inc, Edmonton, Canada
26. Lampman, S. R., Ed., 1996, *ASM Handbook*, Vol. 19, *Fatigue and Fracture*, The ASM International, Materials Park, OH, USA
27. Lieson, C., and Jurinal, R. C. (1963), *Handbook of Stress and Strength-Design and Material Application*, Collier-MacMillan, London, England
28. Manitoba Hydro, 1986, Design Requirements for Gate Rollers, *Manitoba Hydro Specification No. 1819, Lime Stone G. S. Spillway Gates, B8*
29. McGregor, C. W., and Grossman, N., 1952, Effects of Cyclic Loading on Mechanical Behavior of 24S-T4 and 75S-T6 Aluminum Alloys and SAE 4130 Steel, *NACA TN 2812*, National Advisory Committee for Aeronautics, Washington, DC

30. Milne, I. 1994, The Importance of the Management of Structural Integrity, *Engineering Failure Analysis*, vol. 1, no. 3, pp. 171-181.
31. Mindlin, R. D., (1949), Compliance of Elastic Bodies in Contact, *Journal of Applied Mechanics*, Vol. 6, No. 3, p 259
32. Mitsuda, T., and Bouling, F. G., 1989, Research on Shelling of Crane Wheels, *Iron and Steel Engineer*, v 43, n 4, Apr, 1966, p 106-115
33. Muzeczka, W. J., (1992), Ultimate Load Capacity of Cast Iron Wheels for Vertical Lift Fixed-Wheels Gates, *University of Manitoba, Department of Civil Engineering*, Winnipeg, Manitoba, M. S. thesis
34. Noonan, N. G., and Strange, W. H., (1934) Tests on Rollers, *Technical Memorandum No. 399, U.S. Bureau of Reclamation*, Denver, Colorado, pp. 1-20
35. Park, Y. J., and Stone, D. H., 1981, Cyclic Behavior of Class U Wheel Steel, *Journal of Engineering for Industry*, Vol. 103, American Society of Mechanical engineers, Paper No. 80-WA/Rt-9
36. Polyzois, D. and Muzyczka, W. J., 1993, Ultimate Load Capacity of Cast Iron Wheels for Vertical Lift Fixed-Wheel Gates, *Canadian Society for Civil Engineering, Annual Conference*, June 8-11, 1993, pp. 317-326
37. Polyzois, D. and Muzyczka, W. J., 1994, Behaviour of Cast-Iron Spillway Gate Wheels, *Journal of Materials in Civil Engineering*, Vol. 6, No. 4, pp. 495-512
38. Polyzois, D., Muzyczka, W. J., and Garroni, J. D., 1995, Finite Element Analysis of Cast Iron Spillway Gate Wheels, *Computers and Structures*, Vol. 55, No. 4, pp 741-748

39. Polyzois, D. and Lashari, A. N., 2006, An Investigation on the Fatigue Performance of Hydraulic Gate Wheels, *Fracture of Nano and Engineering Materials and Structures*, Proceedings of the 16<sup>th</sup> European Conference of Fracture, Alexandroupolis, Greece, July 3-7, 2006
40. Roark, R. J., 1989, Roark's Formulas for Stress and Strain, 6<sup>th</sup> Ed., *McGraw Hill*, New York
41. Roark, R. J., 2002, Roark's Formulas for Stress and Strain, 7<sup>th</sup> Ed., *McGraw Hill*, New York
42. Sagar, B. T. A., 1989, Fixed Wheel Gates-Uses and Limitations, *Hydraulics Engineering Proceedings*, 1989 National Conference on Hydraulics Engineering, M.A. Ports, ASCE, New York, N.Y., pp. 1162-1168
43. Seely, F.B., and J.O. Smith, 1955, Advanced Mechanics of Materials, *John Wiley & Sons*, New York
44. Shackelford, J. F. and Alexander, W., Editors, 2000, The CRC Materials Science and Engineering Handbook, 3<sup>rd</sup> ed., *CRC Press*, Boca Raton, FL, USA
45. Shiozawa, K. and Sakai, T., Eds. 1996, Data Book on Fatigue Strength of Metallic Materials, *Elsevier Science Publications*, Amsterdam
46. Sines, G., and Waisman, J. L., 1959, Metal Fatigue, *McGraw-Hill*, New York
47. Skinner, S. J., 1957, *Fixed Wheels for Penstock Intakes*, *Trans., ASCE*, Paper No. 3000, New York, N.Y., p740-771
48. Smith, J. O., 1942, The Effect of Range of Stress on the Fatigue Strength of Metals, *Bulletin No. 334, University of Illinois*, Engineering Experiment Station, Urbana, IL

49. Smith, J. O. and Liu, C. K., 1953, Stresses Due to the Tangential and Normal Loads on an Elastic Solid with Applications to Some Contact Stress Problems, *Journal of Applied Mechanics*, Vol. 20, No. 2, p. 157
50. Smith, W. F., 1993, Structure and Properties of Engineering Alloys, 2nd ed., *McGraw-Hill*, New York
51. Steiner, R., 1996, ASM Handbook, Vol. 1, Properties and Selection, *The ASM International*, Materials Park, OH, USA
52. Stephens, R. I., Fatemi A., Stephens, R. R., and Fuchs, H. O., 2001, Metal Fatigue in Engineering, 2<sup>nd</sup> Ed., *John Wiley & Sons*, New York
53. Swanson Analysis Systems Inc., 2005, *ANSYS® User Manuals*, (21 Volumes), Version 10.0, Southpointe, 275 Technology Drive, Canonsburg, PA, USA
54. Thomas H. R., and Hoersh, V. A., (1930), Stresses Due to the Pressure of One Solid upon Another, *Bulletin of Engineering Experiment Station*, No. 212, University of Illinois, Urbana, Illinois, pp.1-54
55. Tucker, L. E., and Olberts, D. R., 1969, Fatigue Properties of Gray Cast Iron, *Society of Automotive Engineers, Paper No. 690471*, pp. 1-9
56. Wilson, W. M., 1927, Tests on the Bearing Value of Large Rollers, *Bulletin of the Engineering Experiment Station*, No. 162, University of Illinois, Urbana, Illinois
57. Young, J. F., Mindess, S., Gray, R. J., and Bentur, A., 1998, The Science and Technology of Civil Engineering Materials, *Prentice Hall*, New Jersey

## Appendix A Present Method of Computing Stresses for Gate Wheels

Following is a sample calculation illustrating the application of Equation 2.1.

**Case 1:** Given: Wheel loads

Hardness of the wheel or roller path plate (lesser of the two)

Wheel diameter, and crown radius of the wheel

**Find:** Net tread width required to prevent permanent set (flattening)

Maximum shearing stress developed in tread

**Solution:** Assume wheel rim hardened to  $BHN = 375$ , 685.5 mm (27 in.) diameter with a 914 mm (36 in.) crown radius, wheel load is 480.4 kN (108 kips) Normal load, 1272 kN (286 kips) Overload (Muzyczka 1992). Using Eq. 2.1:

Critical Stress =  $(24.5 \times 375) - 2200 = 6988$  *psi* (per inch diameter per inch width)

Required Projected Area (diameter and tread width):

Allowable Stress =  $\frac{6988}{3} = 2329$  *psi* for Normal Loads

Allowable Stress =  $\frac{6988}{2} = 3494$  *psi* for Overloads Loads

$= \frac{108 \text{ kip}}{2.329 \text{ ksi}} = 46.4$  *sq. in.* for Normal Loads,  $= \frac{268 \text{ kip}}{3.49 \text{ ksi}} = 76.7$  *sq. in.* for Overloads

Net tread width required =  $\frac{76.7}{27} = 2.84$  *in.* Say 3 *in.*

**Case 2: Given:** The lesser hardness of the wheel rim or roller path plate

Wheel diameter and wheel tread width

**Find:** Maximum wheel load to prevent permanent set (flattening)

Assume forged steel wheel, rim hardened to  $BHN = 425$ , 685.5 mm (27 in.) diameter with 66.65 mm (2.625 in.) tread width (Muzyczka 1992).

Actual Projected Area =  $27 \times 2.625 = 70.875 \text{ sq. in.}$

From Eq. 2.1:  $\sigma_{cr} = (24.5 \times 425) - 2200 = 8213 \text{ psi}$

Critical Load =  $\sigma_{cr} \times \text{Projected Area} = 8.213 \text{ ksi} \times 70.875 \text{ sq. in.} = \underline{582 \text{ kips}}$

Allowable Normal Load =  $\frac{582}{3} = 194 \text{ kips}$

Allowable Overload =  $\frac{582}{2} = 291 \text{ kips}$

**Check Maximum Shear Stress Developed:** Continuation of Case 1 by computing contact stresses (Muzyczka 1992). Since wheel has a double curvature, assume crossed cylinders with axes at right angles (Roark 1989) p. 651

Diameter of wheel,  $D_1 = 685.5 \text{ mm (27 in.)}$

Crown radius of wheel,  $D_2/2 = 914 \text{ mm (36 in.)}$

Modulus of Elasticity of roller path plate,  $E_1 = 29,500 \text{ ksi}$

Modulus of Elasticity of wheel,  $E_2 = 15,000 \text{ ksi}$

Poisson's ratio for roller path plate,  $\nu_1 = 0.30$

Poisson's ratio for wheel,  $\nu_2 = 0.25$

$$K_D = \frac{D_1 D_2}{D_1 + D_2} = \frac{27 \times 72}{27 + 72} = 19.64, \quad C_E = \frac{1 - \nu_1^2}{E_1} + \frac{1 - \nu_2^2}{E_2} = 9.335 \times 10^{-8}$$

$\alpha$ ,  $\beta$ , and  $\lambda$  depend on geometry of the wheel which is a function of  $\frac{D_1}{D_2} = \frac{72}{27} = 2.667$

$$\alpha = 1.286, \beta = 0.678, \text{ and } \lambda = 0.784, \quad \text{major semi-axes, } a = \alpha (PK_D C_E)^{\frac{1}{3}}$$

$$= 1.286(108,000 \times 19.64 \times 9.335 \times 10^{-8})^{\frac{1}{3}} = 0.749 \text{ in.}$$

Similarly, minor semi-axes,  $b = \beta (PK_D C_E)^{\frac{1}{3}} = 0.395 \text{ in.}$

$$\text{Area of contact patch} = \pi a b = \pi \times 0.749 \times 0.395 = 0.9294 \text{ sq. in.}$$

$$\text{Maximum Compressive Stress } \sigma_c, \text{ (at point of contact)} = \frac{1.5P}{\pi ab} = 174 \text{ ksi (1200 MPa)}$$

$$\text{Maximum Shear Stress } \tau_{max} \text{ developed (at approximately } 0.44a \text{ below the surface)}$$

$$= \frac{\sigma_c}{3} = 58.0 \text{ ksi at } 0.33 \text{ in. below the point of contact.}$$

From Current Manitoba Hydro Specifications: Maximum Shear Stress  $V_u$  shall not exceed:  $350 \times BHN$  for  $BHN < 255$  or  $90 \text{ ksi}$  for  $BHN > 255$ ,  $\tau < V_u$  therefore OK

For Overload:  $P = 268 \text{ kips}$ ,  $a = 1.0148 \text{ in.}$ ,  $b = 0.5349 \text{ in.}$

$$\sigma_c = \frac{1.5 \times 268}{\pi \times 1.0148 \times 0.5349} = 235.7 \text{ ksi}$$

$$\tau = \frac{\sigma_c}{3} = 78.6 \text{ ksi} < 90 \text{ ksi OK}$$

Following is the listing of ANSYS® FE Program R<sub>1</sub>P<sub>1</sub> developed to analyze Roller R1 and roller path Plates P1 and P2.

```

! In the Name of God, Most Gracious, Most Compassionate
! Program R1P1 to analyze roller R1 along with plates P1 & P2
! ANSYS RELEASE 10.0, University Version
! This program is developed by Abdul Nabi Lashari
! Roller R1 along with plate P1, Load Thru Handling Holes
! All dimensions are in mm, E in MPa
/TITLE,Roller R1, Load = 838 KN Through Handling Holes
! this program is divided into following parts:
! Part 1: Scalar Parameters
! Part 2: One Eighth of Actual Roller Geometry
! Part 3: One Quarter of Actual Plate Geometry
! Part 4: Element Types & Material Properties
! Part 5: Meshing
! Part 5a: Components for Meshing
! Part 5b: Meshing Solid Roller Volume
! Part 5c: Meshing Solid Plate Volume
! Part 5d: Meshing Roller Contact Area with TARGET170
! Part 5e: Meshing Plate Contact Area with CONTA175
! Part 6: Boundary Conditions
! Part 7: Solution
! Part 8: Post Processing
! Part 8a: Post Processing Roller Model
! Part 8b: Post Processing Plate Model
!=====
! PART 1: Entering Scalar Parameters
!*SET,X assigns values to user-named parameters
    
```

```

*SET,Er,103420.5 !E for roller R1 is 103420.5MPa=15000ksi
*SET,nur,0.27 !poisson's ratio for roller
*SET,Ep,206841 !E for plate P1 is 206841 MPa=30,000ksi
*SET,nup,0.28 !poisson's ratio for plate
! Roller inside hole diameter D is 152.3334 mm
! Roller hub height is 239.6087 mm
! Radial load on roller R1 applied in laboratory 838.0858 N
! Pressure applied on inside roller hole areas  $p=Force/(h*D)$ 
!  $p=Force/(h*D)=838.0858/(239.6087*152.3334)=22.96100872MPa$ 
*SET,P,22.96100872 !pressure applied on inside roller hole area
*SET,S1,0.7 !element edge length size for volume component R1 in roller
*SET,S2,0.7 !element edge length size for volume component R2 in roller
*SET,S3,0.7 !element edge length size for volume component R3 in roller
*SET,S4,2.5 !element edge length size for volume component R4 in roller
*SET,S5,10 !element edge length size for volume component R5 in roller
*SET,S6,15 !element edge length size for volume component R5 in roller
*SET,T1,0.7 !element edge length size for volume component P1 in plate
*SET,T2,0.7 !element edge length size for volume component P2 in plate
*SET,T3,2 !element edge length size for volume component P3 in plate
*SET,T4,25 !element edge length size for volume component P4 in plate
!=====
! PART 2: Creating One Eighth of Actual Roller Geometry
/PREP7 !enter preprocessor7
K,1,0,0,0 !K,NPT,X,Y,Z defines a keypoint
!NPT: reference number for keypoint
K,2,119.80435,0,0 !If zero, the lowest available number is assigned
K,3,0,76.1667,0
K,4,119.80435,76.1667,0
K,5,119.80435,161.06145,0
K,6,25.3889,174.5494,0
K,7,19.04175,368.1405,0

```

K,8,44.43075,368.1405,0  
 K,9,44.43075,414.4302,0  
 K,10,39.9426,418.9185,0  
 K,11,-39.9426,418.9185,0  
 K,12,0,-494.2087,0 !K12 is used as centre to create crown radius  
 K,999,44.43075,409.4302,0  
 K,991,44.43075,400,0  
 LARC,10,11,12,914.0004 !crown radius of 914.0004mm  
 KDELE,12 !deleting K12  
 LDIV,1,0.5, ,2,0 !dividing line 1 into two equal lines  
 LSTR,3,4 !creating straight line  
 LSTR,4,5  
 LSTR,5,6  
 LSTR,6,7  
 LSTR,7,8  
 LSTR,8,991  
 LSTR,991,999  
 LSTR,999,9  
 LSTR,9,10  
 LSTR,12,3  
 LDELE,2, , ,1 !deleting line 2  
 LFILLT,5,6,15 !creating line fillet b/w lines 5 & 6, r=15 mm  
 LFILLT,6,7,10  
 LANG,12,999,90, ,  
 LANG,15,15,90, ,  
 LANG,1,17,90, ,  
 LANG,17,991,90, ,  
 LANG,14,19,90, ,  
 LANG,22,14,90, ,  
 LANG,24,13,90, ,  
 AL,3,4,5,2,27,26 !creating areas using lines, anti-clockwise numbering

AL,27,6,25,24  
 AL,25,13,20,23,22  
 AL,7,8,21,20  
 AL,21,9,16,17  
 AL,16,10,11,1,19  
 AL,23,17,15,14  
 AL,15,19,18,12  
 CM,A1TO4,AREA !creating area component A1to4  
 !by using following command  
 !creating 1st set of volume by sweeping component A1to4 to 2 deg  
 !along a line thru KPs 1 to 2, Order is important  
 !the last digit is for number of volumes which is one  
 VROTAT,A1TO4, , , , ,1,2,2,1  
 CM,V2DEG,VOLU !creating volume component  
 WPRO, ,2, !rotating WP (XY plane) 2 degrees along +Xaxis  
 CSYS,4 !forcing active coordinate system to follow WP  
 ASEL,S,LOC,Z,0,0 !select areas on (a 2 deg-rotated WP along +Xaxis) XY plane, at z=0  
 !Following component AT2DEG consists of all areas on  
 CM,AT2DEG,AREA !a 2-deg-rotated WP along Xaxis, on XY plane at z=0  
 ALLSEL,ALL,ALL !restore entire selection  
 !by using following command  
 !creating 2nd set of volume by sweeping component AT2DEG to 2 deg  
 !along a line thru KPs 1 to 2, Order is important  
 !the last digit is for number of volumes which is one  
 VROTAT,AT2DEG, , , , ,1,2,2,1  
 CM,V4DEG,VOLU !creating volume component in 4 deg segment  
 WPRO, ,2, !rotating WP (XY plane) 2 degrees along +Xaxis  
 CSYS,4 !forcing active coordinate system to follow WP  
 ASEL,S,LOC,Z,0,0 !select areas on (a 4 deg-rotated WP along +Xaxis) XY plane, at z=0  
 !Following component AT4DEG consists of all areas on  
 CM,AT4DEG,AREA !a 4-deg-rotated WP along Xaxis, on XY plane at z=0

ALLSEL,ALL,ALL

!by using following command

!creating 3rd set of volume by sweeping component AT4DEG to 26 deg

!along a line thru KPs 1 to 2, Order is important

!the last digit is for number of volumes which is one

VROTAT,AT4DEG, , , , ,1,2,26,1

CM,V30DEG,VOLU

WPRO, ,26, !rotating WP (XY Plane) +26 deg more along Xaxis, 30 deg from origin

ASEL,S,LOC,Z,0,0 !areas on XY plane at a distance of 0 from Zaxis

!area component AT30DEG consists of all areas on

!a 30-degree rotated WP from global origin along +Xaxis

CM,AT30DEG,AREA !on XY plane at a distance of 0 from Zaxis

ALLSEL,ALL,ALL

!by using following command

!creating 4th set of volume by sweeping component AT30DEG to 30 deg

!along a line thru KPs 1 to 2, Order is important

!the last digit is for number of volumes which is one

VROTAT,AT30DEG, , , , ,1,2,60,1

CM,V90DEG,VOLU

ALLSEL,ALL,ALL

WPRO, ,-30, !rotating WP -60 deg along Xaxis (back to global origin)

WPAVE,0,0,0 !moving WP to global origin

CSYS,0 !forcing active coordinate system to global origin

! 1/8 of roller without H.hole is complete here

! creating one half handling hole

! this is for applying load thru handling holes

K,125,-10,269.7571,0

KWPAVE,125 !moving WP to KP125

wpro, , ,90 !rotating WP to 90 degrees about y-axis

! creating a half H. hole volume, r=31.736125mm, depth=100mm

! by using following command one can

```

! Create a cylindrical volume anywhere on the working plane
CYL4, , , ,31.736125, ,100
VSBV,V90DEG,33, , !subtracting volume 36 from volume ROLLRV
wpro, , , -90 rotating WP to -90 degrees about y-axis
WPAVE,0,0,0 !moving WP to global origin (0,0,0)
CSYS,0 !forcing active coordinate system to global origin
KDELE,125
VSEL,S, , ,ALL !select all roller volume
CM,ROLLER,VOLU
ALLSEL,ALL,ALL
!=====
! PART 3: creating one quarter of plate geometry
KWPAVE,12 Move working plane origin to K12
CSYS,WP !forcing active coordinate system to follow WP
K,150,0,0,0 !K110 is sitting exactly on top of the K12, a contact pair
K,151,20,0,0 !length of plate 20+20 mm
K,152,40,0,0 !depth of plate 88.86115mm (3.5 inch)
K,153,88.86115,0,0 !thickness of plate 50.7778mm (2 inch)
K,154,0,50.7778,0
K,155,20,50.7778,0
K,156,88.86115,50.7778,0
K,157,0,15.3889,0
K,158,25,25.3889,0
K,159,0,30.3889,0
LSTR,150,151
LSTR,151,152
LSTR,152,153
LSTR,150,157
LSTR,154,155
LSTR,155,156
LSTR,153,156

```

LSTR,151,155  
 LSTR,157,159  
 LSTR,154,159  
 LANG,89,152,90, ,  
 LANG,217,157,90, ,  
 LANG,222,159,90, ,  
 LANG,221,104,90, ,  
 LANG,221,105,90, ,  
 LANG,216,106,90, ,  
 LANG,261,107,90, ,  
 LDIV,40,0.5, ,2,0  
 LDIV,262,0.5, ,2,0  
 LDIV,264,0.5, ,2,0  
 LDIV,220,0.5, ,2,0  
 LSTR,110,125  
 LSTR,125,126  
 LSTR,126,127  
 AL,6,42,223,217  
 AL,-223,218,225,222  
 AL,-225,219,87,224  
 AL,24,217,258,257  
 AL,-258,222,260,259  
 AL,-260,224,89,221  
 AL,40,257,266,269  
 AL,-266,259,267,270  
 AL,-267,221,220,271  
 AL,265,269,262,216  
 AL,-262,270,264,261  
 AL,-264,271,268,263 !I have created above 12 areas on XY plane  
 ! to create a plate I need to sweep above areas in +zaxis  
 ! using following commands: creating plate volume in lentgwise direction

VOFFSET,2,10, , !by sweeping above areas normally to 20 mm in +Zaxis  
VOFFSET,16,10, ,  
VOFFSET,18,10, ,  
VOFFSET,19,10, ,  
VOFFSET,51,10, ,  
VOFFSET,53,10, ,  
VOFFSET,54,10, ,  
VOFFSET,86,10, ,  
VOFFSET,88,10, ,  
VOFFSET,149,10, ,  
VOFFSET,150,10, ,  
VOFFSET,151,10, ,  
VOFFSET,152,10, ,  
VOFFSET,179,10, ,  
VOFFSET,184,10, ,  
VOFFSET,189,10, ,  
VOFFSET,194,10, ,  
VOFFSET,199,10, ,  
VOFFSET,204,10, ,  
VOFFSET,209,10, ,  
VOFFSET,214,10, ,  
VOFFSET,219,10, ,  
VOFFSET,224,10, ,  
VOFFSET,229,10, ,  
VOFFSET,234,10, ,  
VOFFSET,239,10, ,  
VOFFSET,244,10, ,  
VOFFSET,249,10, ,  
VOFFSET,254,10, ,  
VOFFSET,259,10, ,  
VOFFSET,264,10, ,

```

VOFFSET,269,10, ,
VOFFSET,274,10, ,
VOFFSET,279,10, ,
VOFFSET,284,10, ,
VOFFSET,289,10, ,
CMSEL,U,ROLLER !unselect roller volume
CM,PLAT30,VOLU
ALLSEL,ALL,ALL
VOFFSET,294,160.42, ,
VOFFSET,299,160.42, ,
VOFFSET,304,160.42, ,
VOFFSET,309,160.42, ,
VOFFSET,314,160.42, ,
VOFFSET,319,160.42, ,
VOFFSET,324,160.42, ,
VOFFSET,329,160.42, ,
VOFFSET,334,160.42, ,
VOFFSET,339,160.42, ,
VOFFSET,344,160.42, ,
VOFFSET,349,160.42, ,
CMSEL,U,ROLLER !unselect roller volume
CM,PLATE,VOLU
ALLSEL,ALL,ALL
CSYS,0 !forcing active coordinate system to global origin
WPAVE,0,0,0 !moving WP to global origin
!=====
! Part 4: Element Types & Material Properties
ET,1,SOLID45 !element type 1, 8-node brick
ET,2,SOLID95 element type 2, 20-node brick
ET,3,TARGE170 !element type 3 for contact area in roller
ET,4,CONTA175 !element type 4 for contact area in plate

```

```

KEYOPT,4,5,3 !key option for CONTA175, keyoption 5, further option 3
MPTEMP,,,,,,,, !Material properties for roller
MPTEMP,1,0 !Material properties for roller
MPDATA,EX,1,,Er !Modulus of elasticity for roller
MPDATA,PRXY,1,,nur !poisson's ratio for roller
MPTEMP,,,,,,,, !Material properties for plate
MPTEMP,1,0 !Material properties for plate
MPDATA,EX,2,,Ep !Modulus of elasticity for plate
MPDATA,PRXY,2,,nup !poisson's ratio for plate

```

```
!=====
```

```
! Part 5a: Creating components for Meshing
```

```

VSEL,S,,8
CM,R1,VOLU
ALLSEL,ALL,ALL
VSEL,S,,6 !select volume 5
VSEL,A,,7
VSEL,A,,16 !also select volume 13
CM,R2,VOLU
ALLSEL,ALL,ALL
VSEL,S,,5
VSEL,A,,13
VSEL,A,,14
VSEL,A,,15
CM,R3,VOLU
ALLSEL,ALL,ALL
VSEL,S,,1
VSEL,A,,3
VSEL,A,,4
VSEL,A,,9
VSEL,A,,11
VSEL,A,,12

```

VSEL,A, , ,34  
VSEL,A, , ,35  
VSEL,A, , ,36  
VSEL,A, , ,37  
CM,R4,VOLU  
ALLSEL,ALL,ALL  
VSEL,S, , ,17  
VSEL,A, , ,19  
VSEL,A, , ,20  
VSEL,A, , ,21  
VSEL,A, , ,22  
VSEL,A, , ,23  
VSEL,A, , ,24  
CM,R5,VOLU  
ALLSEL,ALL,ALL  
VSEL,U, , ,R1  
VSEL,U, , ,R2  
VSEL,U, , ,R3  
VSEL,U, , ,R4  
VSEL,U, , ,R5  
VSEL,U, , ,PLATE  
VSEL,U, , ,38  
CM,R6,VOLU  
ALLSEL,ALL,ALL  
VSEL,S, , ,2  
CM,P1,VOLU  
ALLSEL,ALL  
VSEL,S, , ,10  
VSEL,A, , ,33  
VSEL,A, , ,47  
CM,P2,VOLU

```

ALLSEL,ALL,ALL
VSEL,S,,PLAT30
VSEL,U,,P1
VSEL,U,,P2
CM,P3,VOLU
ALLSEL,ALL,ALL
VSEL,S,,PLATE
VSEL,U,,P1
VSEL,U,,P2
VSEL,U,,P3
CM,P4,VOLU
ALLSEL,ALL,ALL

```

```
!=====
```

```

! Part 5b: Meshing Roller Volume
SMART,OFF !Deactivate SmartSizing
! current settings of DESIZE will be used
! Elelemnt attributes
TYPE,1 !element type 1, SOLID 45
MAT,1 !material type 1 roller
REAL, real constant nothing (ansys default)
ESYS,0 !element coordinate system 0
SECNUM, !Sets the element section attribute pointer
MSHAPE,0,3D 0-Mesh with hexahedral-shaped elements
! 1-Mesh with tetrahedral-shaped elements
MSHKEY,1 !0-Use free meshing and 1-Use mapped meshing
! Specifies whether free meshing or mapped meshing should be used to mesh a model
ESIZE,S2,, !element edge length size set as S2
VSWEEP,R2,, fills an existing unmeshed volume with elements by sweeping
! the mesh from an adjacent area through the volume
TYPE,2 !element type 2, SOLID 95
MAT,1 !material type 1

```

```

REAL, !real constant nothing (ansys default)
ESYS,0 !element coordinate system 0
SECNUM, !Sets the element section attribute pointer
MSHAPE,0,3D !0-Mesh with hexahedral-shaped elements
! 1-Mesh with tetrahedral-shaped elements
MSHKEY,1 !0-Use free meshing and 1-Use mapped meshing
! Specifies whether free meshing or mapped meshing should be used to mesh a model
ESIZE,S1, ,
VSWEEP,R1 !Fills an existing unmeshed volume with elements by
! sweeping the mesh from an adjacent area through the volume
TYPE,1 !element type 1, SOLID 45
MAT,1 !material type 1
REAL, real constant nothing (ansys default)
ESYS,0 element coordinate system 0
SECNUM, !Sets the element section attribute pointer
MSHAPE,0,3D !0-Mesh with hexahedral-shaped elements
! 1-Mesh with tetrahedral-shaped elements
MSHKEY,1 !0-Use free meshing and 1-Use mapped meshing
ESIZE,S3, ,
VSWEEP,R3, , ,
ESIZE,S4, ,
VSWEEP,38, , ,
VSWEEP,R4, , ,
ESIZE,S5, ,
VSWEEP,R5, , ,
ESIZE,S6, ,
VSWEEP,R6, , ,
!=====
! Part 5c: Meshing solid plate volume
TYPE,1 !element type 1, SOLID 45
MAT,2 !material type 2, plate

```

```

REAL, !real constant nothing (ansys default)
ESYS,0 !element coordinate system 0
SECNUM, !Sets the element section attribute pointer
MSHAPE,0,3D 0-Mesh with hexahedral-shaped elements
! 1-Mesh with tetrahedral-shaped elements
MSHKEY,1 !0-Use free meshing and 1-Use mapped meshing
ESIZE,T2, ,
VMESH,P2 !generates nodes and elements within volume
TYPE,2 !element type 2, SOLID 95
MAT,2 !material type 2, plate
REAL, !real constant nothing (ansys default)
ESYS,0 !element coordinate system 0
SECNUM, !Sets the element section attribute pointer
MSHAPE,0,3D !0-Mesh with hexahedral-shaped elements
! 1-Mesh with tetrahedral-shaped elements
MSHKEY,1 !0-Use free meshing and 1-Use mapped meshing
ESIZE,T1, ,
VMESH,P1
TYPE,1 !element type 1, SOLID 45
MAT,2 !material type 2, plate
REAL, !real constant nothing (ansys default)
ESYS,0 !element coordinate system 0
SECNUM, !Sets the element section attribute pointer
MSHAPE,0,3D !0-Mesh with hexahedral-shaped elements
! 1-Mesh with tetrahedral-shaped elements
MSHKEY,1 !0-Use free meshing and 1-Use mapped meshing
ESIZE,T3, ,
VMESH,P3
ESIZE,T4, ,
VMESH,P4
!=====

```

```

! Part 5d: Meshing roller contact area with Target 170 element
KWPAVE,12 !moving WP to K12 which is the contact point in roller
CSYS,4 !forcing active coordinate system to follow WP
ASEL,S, , ,41 !selecting contact area 41 in roller
NSLA,S,1 !selecting all nodes "attached to" area 41
NSEL,R,LOC,Y,-3,0 !R means selecting only those nodes that are
! attached to above area at a location of Y=0 to -3 mm
CSYS,0 !forcing active coordinate system to global origin
WPAVE,0,0,0 !moving WP to global origin
TYPE,3 !element type 3, TARGET 170
MAT,1 !material type 1 roller
REAL, !real constant nothing
ESYS,0 !element coordinate system 0
SECNUM, !Sets the element section attribute pointer
TSHAP,LINE !Defines simple 3-D geometric surfaces for target elements
ESURF, ,TOP, !Generates target elements
! overlaid on the free faces of existing selected elements
ALLSEL,ALL,ALL

```

```

!=====

```

```

! Part 5e: Meshing plate contact area with CONTA 175 element
KWPAVE,150 !moving WP to KP150 in plate
CSYS,4 !forcing active coordinate system to follow WP
ASEL,S, , ,175 !selecting area 175
ASEL,A, , ,235 !also select area 235
NSLA,S,1 !selecting all nodes attached to above areas
NSEL,R,LOC,Y,0,3 !R means selecting only those nodes
! that are attached to above area at location of Y=0 to 3
CSYS,0 !forcing active coordinate system to global origin
WPAVE,0,0,0 !moving WP to global origin
TYPE,4 !element type is 4, CONTA 175
MAT,2 !material type 2

```

```

REAL,1 !real constant (default)
ESYS,0 !element coordinate system 0
SECNUM, !Sets the element section attribute pointer
TSHAP,LINE !Defines simple 3-D geometric surfaces for target segment elements
ESURF !Generates elements overlaid
! on the free faces of existing selected elements
ALLSEL,ALL,ALL
!=====
! Part 6: Applying Boundary Conditions
ASEL,S,LOC,Z,0,0 !select all areas on XY plane at z=0
CM,XYZ0,AREA !creating component XYZ0 for applying symmetrical BCs
ALLSEL,ALL,ALL
ASEL,S,LOC,X,0,0 !select all areas on YZ plane at x=0
CM,YZX0,AREA !creating component YZX0 for applying symmetrical BCs
ALLSEL,ALL,ALL
ASEL,S,LOC,Y,0,0 !select all areas on XZ plane at y=0
CM,XZY0,AREA creating area component XZY0 for applying coupled DOF constraint
ALLSEL,ALL
KWPAVE,154 !moving WP to K154 in plate
CSYS,4 !forcing active coordinate system to follow WP
ASEL,S,LOC,Y,0,0 !select all areas on XZ plane at Y=0
CM,FXZY0,AREA !creating component FXZY0 for applying FIXED BCs
ALLSEL,ALL,ALL
CSYS,0 !forcing active coordinate system to global origin
WPAVE,0,0,0 !moving WP to global origin
ASEL,S, , ,9
ASEL,A, , ,44
ASEL,A, , ,79
ASEL,A, , ,114
CM,PRS,AREA !Creating component PRS to apply pressure on inside roller hole areas
ALLSEL,ALL,ALL

```

```

ASEL,S, , ,XZY0 !areas on XZ plane at y=0, already defined above
NSLA,S,1 !nodes attached to above area component XZY0
CM,NXZY0,NODE !creating NXZY0, all nodes attached to component XZY0
ALLSEL,ALL,ALL
FINISH !exiting PREP7
/SOL !entering solution processor
DA,XYZ0,SYMM !applying symmet BCs on all XY plane areas at z=0
DA,YZX0,SYMM !applying symmet BCs on all YZ plane areas at x=0
DA,FXZY0,UY,0.0 !applying fixed BCs (0.0) on component FXZY0, defined above
!back of the plate is fixed in Y direction ONLY
SFA,PRS, ,PRES,P !applying pressure on inside roller hole area
CP,1,UY,NXZY0 !coupled DOF constraint to component NXZY0 in Y direction
!1 is refernce number, just arbitrary number
! Part 7: Solution
ANTYPE,STATIC !Perform a static analysis (Valid for all DOF)
NLGEOM,ON !Include large-deflection effects
AUTOTS,OFF !Use automatic time stepping
TIME,100 !time at the end of load step
NSUBST,35,0,0 !Specifies the number of substeps to be taken this load step
!NCNV,0,0,0,0,0 !Do not terminate analysis if solution fails to converge
KBC,0 !Specifies stepped or ramped loading within a load step
! Loads are linearly interpolated (ramped) for each sub-step
! from the values of the previous load step to the values of this load step
!OUTRES,ALL,ALL !Controls the solution data written to the database
!write all solution items
! OUTPR,ALL,ALL !Controls the solution printout
! print all, every thing, in the result file
/STATUS,SOLU!Provides a solution status summary
SAVE, , , ,ALL !save every thing to the current job name file
SOLVE ! Start a solution
FINISH ! Exit from solution processor

```

SAVE, , , ,ALL

/EOF !Stop reading this file and exit from ANSYS, if running in batch mode

!=====

! Part 8: Post Processing

! A maximum of 100 paths can exist within one model

! However, only one path at a time can be the current path

! To change the current path, choose the PATH,NAME command

! Do not specify any other arguments on the PATH command

! The named path will become the new current path

! PATH,2RL12,37,10,10 ! PATH,NAME,nPts,nSets,nDiv

! L is for lab load in Path Name

! Defines a path name and establishes parameters for the path

! The minimum number is two, and the maximum is 1000. Default is 2

! nSets: The number of sets of data which you can map to this path

! You must specify at least four: X, Y, Z, and S. Default is 30

! nDiv: The number of divisions between adjacent points

! Default is 20. There is no maximum number of divisions

!PPATH,POINT,NODE,X,Y,Z,CS

!Defines a path by picking or defining nodes

!or locations on the currently active working plane

!or by entering specific coordinate locations

!PDEF,Lab,Item,Comp,Avglab, Interpolates an item onto a path

!=====

! Part 8a: Post Processing Roller Model

! L12-L14-L22-L235 from K12-K16-K20-K21-K116 deep in Y-axis

! K12 (0,419.7917,0)

! K16 (0,409.4302,0)

! K20 (0,400,0)

! K21 (0,357.8128,0)

! K116(0,301.4932,0)

/POST1 !Enter the database results postprocessor

PATH,1RLY,88, ,  
PPATH,1,41042  
PPATH,2,41917  
PPATH,3,41918  
PPATH,4,41919  
PPATH,5,41920  
PPATH,6,41921  
PPATH,7,41922  
PPATH,8,41923  
PPATH,9,41924  
PPATH,10,41925  
PPATH,11,41926  
PPATH,12,41927  
PPATH,13,41928  
PPATH,14,41929  
PPATH,15,41930  
PPATH,16,41994  
PPATH,17,41995  
PPATH,18,41996  
PPATH,19,41997  
PPATH,20,41998  
PPATH,21,41999  
PPATH,22,42000  
PPATH,23,42001  
PPATH,24,42002  
PPATH,25,42003  
PPATH,26,42004  
PPATH,27,42005  
PPATH,28,42006  
PPATH,29,42007  
PPATH,30,42008

PPATH,31,8584  
PPATH,32,8970  
PPATH,33,8971  
PPATH,34,8972  
PPATH,35,8973  
PPATH,36,8974  
PPATH,37,8975  
PPATH,38,8976  
PPATH,39,8977  
PPATH,40,8978  
PPATH,41,8979  
PPATH,42,8980  
PPATH,43,8981  
PPATH,44,8982  
PPATH,45,8969  
PPATH,46,170959  
PPATH,47,170960  
PPATH,48,170961  
PPATH,49,170962  
PPATH,50,170963  
PPATH,51,170964  
PPATH,52,170965  
PPATH,53,170966  
PPATH,54,170967  
PPATH,55,170968  
PPATH,56,170969  
PPATH,57,170970  
PPATH,58,170971  
PPATH,59,170972  
PPATH,60,170973  
PPATH,61,170974

PPATH,62,170975  
PPATH,63,171489  
PPATH,64,171490  
PPATH,65,171491  
PPATH,66,171492  
PPATH,67,171493  
PPATH,68,171494  
PPATH,69,171495  
PPATH,70,171496  
PPATH,71,171497  
PPATH,72,171498  
PPATH,73,171499  
PPATH,74,171500  
PPATH,75,171501  
PPATH,76,171502  
PPATH,77,171503  
PPATH,78,171504  
PPATH,79,171505  
PPATH,80,171506  
PPATH,81,171507  
PPATH,82,171508  
PPATH,83,171509  
PPATH,84,171510  
PPATH,85,171511  
PPATH,86,171512  
PPATH,87,171513  
PPATH,88,171400  
PDEF,S1,S,1 !principal stress 1  
PDEF,S2,S,2 !principal stress 2  
PDEF,S3,S,3 !principal stress 3  
PDEF,SI,S,INT !stress intensity

PDEF,SE,S,EQV !von Mises or equivalent stress  
 PCALC,ADD,OCTN1,S1,S2, , , !do not use this value  
 PCALC,ADD,OCTN,OCTN1,S3,1/3,1/3, !Octahedral normal stress  
 !PCALC,OPERR,LABR,LAB1,LAB2,FACT1,FACT2,CONST  
 !Forms additional labeled path items by operating on existing path items  
 PCALC,ADD,OCTS,SE, ,0.47140452, , ! OCTAHEDRAL SHEAR STRESS  
 PCALC,ADD,PS1,S2,S3, ,-1, , ! (S2-S3) do not use these values  
 PCALC,ADD,PS2,S1,S3, ,-1, , ! (S1-S3) do not use these values  
 PCALC,ADD,PS3,S1,S2, ,-1, , ! (S1-S2) do not use these values  
 PCALC,ADD,PSH1,PS1, ,0.5, , ! Principal shearing stress 1  
 PCALC,ADD,PSH2,PS2, ,0.5, , ! Principal shearing stress 2  
 PCALC,ADD,PSH3,PS3, ,0.5, , ! Principal shearing stress 3

=====

!from K12-K18-K10 in X-axis

! K12 (0,419.7917,0)

! K18 (29.69613,419.3091,0)

! K10 (39.9426,418.9185,0)

PATH,1RLX,100, ,

PPATH,1,41042

PPATH,2,41972

PPATH,3,41971

PPATH,4,41970

PPATH,5,41969

PPATH,6,41968

PPATH,7,41967

PPATH,8,41966

PPATH,9,41965

PPATH,10,41964

PPATH,11,41963

PPATH,12,41962

PPATH,13,41961

PPATH,14,41960  
PPATH,15,41959  
PPATH,16,41958  
PPATH,17,41957  
PPATH,18,41956  
PPATH,19,41955  
PPATH,20,41954  
PPATH,21,41953  
PPATH,22,41952  
PPATH,23,41951  
PPATH,24,41950  
PPATH,25,41949  
PPATH,26,41948  
PPATH,27,41947  
PPATH,28,41946  
PPATH,29,41945  
PPATH,30,41944  
PPATH,31,41943  
PPATH,32,41942  
PPATH,33,41941  
PPATH,34,41940  
PPATH,35,41939  
PPATH,36,41938  
PPATH,37,41937  
PPATH,38,41936  
PPATH,39,41935  
PPATH,40,41934  
PPATH,41,41933  
PPATH,42,41932  
PPATH,43,41931  
PPATH,44,41021

PPATH,45,41020  
PPATH,46,41019  
PPATH,47,41018  
PPATH,48,41017  
PPATH,49,41016  
PPATH,50,41015  
PPATH,51,41014  
PPATH,52,41013  
PPATH,53,41012  
PPATH,54,41011  
PPATH,55,41010  
PPATH,56,41009  
PPATH,57,41008  
PPATH,58,41007  
PPATH,59,41006  
PPATH,60,41005  
PPATH,61,41004  
PPATH,62,41003  
PPATH,63,41002  
PPATH,64,41001  
PPATH,65,41000  
PPATH,66,40999  
PPATH,67,40998  
PPATH,68,40997  
PPATH,69,40996  
PPATH,70,40995  
PPATH,71,40994  
PPATH,72,40993  
PPATH,73,40992  
PPATH,74,40991  
PPATH,75,40990

PPATH,76,40989  
PPATH,77,40988  
PPATH,78,40987  
PPATH,79,40986  
PPATH,80,40985  
PPATH,81,40984  
PPATH,82,40983  
PPATH,83,40982  
PPATH,84,40981  
PPATH,85,8765  
PPATH,86,8779  
PPATH,87,8778  
PPATH,88,8777  
PPATH,89,8776  
PPATH,90,8775  
PPATH,91,8774  
PPATH,92,8773  
PPATH,93,8772  
PPATH,94,8771  
PPATH,95,8770  
PPATH,96,8769  
PPATH,97,8768  
PPATH,98,8767  
PPATH,99,8766  
PPATH,100,8800  
PDEF,S1,S,1 !principal stress 1  
PDEF,S2,S,2 !principal stress 2  
PDEF,S3,S,3 !principal stress 3  
PDEF,SI,S,INT !stress intensity  
PDEF,SE,S,EQV !von Mises or equivalent stress  
PCALC,ADD,OCTN1,S1,S2, , , !do not use this value

PCALC,ADD,OCTN,OCTN1,S3,1/3,1/3, !Octahedral normal stress  
 !PCALC,OPERR,LABR,LAB1,LAB2,FACT1,FACT2,CONST  
 !Forms additional labeled path items by operating on existing path items  
 PCALC,ADD,OCTS,SE, ,0.47140452, , ! OCTAHEDRAL SHEAR STRESS  
 PCALC,ADD,PS1,S2,S3, ,-1, , ! (S2-S3) do not use these values  
 PCALC,ADD,PS2,S1,S3, ,-1, , ! (S1-S3) do not use these values  
 PCALC,ADD,PS3,S1,S2, ,-1, , ! (S1-S2) do not use these values  
 PCALC,ADD,PSH1,PS1, ,0.5, , ! Principal shearing stress 1  
 PCALC,ADD,PSH2,PS2, ,0.5, , ! Principal shearing stress 2  
 PCALC,ADD,PSH3,PS3, ,0.5, , ! Principal shearing stress 3

=====

! from K12-K42-K62 in Zaxis not straight line

! K12 (0,419.7917,0)

! K42 (0,419.536,14.65052)

! K62 (0,418.7691,29.28319)

PATH,1RLZ,64, ,

PPATH,1,41042

PPATH,2,41022

PPATH,3,41023

PPATH,4,41024

PPATH,5,41025

PPATH,6,41026

PPATH,7,41027

PPATH,8,41028

PPATH,9,41029

PPATH,10,41030

PPATH,11,41031

PPATH,12,41032

PPATH,13,41033

PPATH,14,41034

PPATH,15,41035

PPATH,16,41036  
PPATH,17,41037  
PPATH,18,41038  
PPATH,19,41039  
PPATH,20,41040  
PPATH,21,41041  
PPATH,22,41973  
PPATH,23,41974  
PPATH,24,41975  
PPATH,25,41976  
PPATH,26,41977  
PPATH,27,41978  
PPATH,28,41979  
PPATH,29,41980  
PPATH,30,41981  
PPATH,31,41982  
PPATH,32,41983  
PPATH,33,41984  
PPATH,34,41985  
PPATH,35,41986  
PPATH,36,41987  
PPATH,37,41988  
PPATH,38,41989  
PPATH,39,41990  
PPATH,40,41991  
PPATH,41,41992  
PPATH,42,41993  
PPATH,43,8689  
PPATH,44,8648  
PPATH,45,8649  
PPATH,46,8650

PPATH,47,8651  
 PPATH,48,8652  
 PPATH,49,8653  
 PPATH,50,8654  
 PPATH,51,8655  
 PPATH,52,8656  
 PPATH,53,8657  
 PPATH,54,8658  
 PPATH,55,8659  
 PPATH,56,8660  
 PPATH,57,8661  
 PPATH,58,8662  
 PPATH,59,8663  
 PPATH,60,8664  
 PPATH,61,8665  
 PPATH,62,8666  
 PPATH,63,8667  
 PPATH,64,8647  
 PDEF,S1,S,1 !principal stress 1  
 PDEF,S2,S,2 !principal stress 2  
 PDEF,S3,S,3 !principal stress 3  
 PDEF,SI,S,INT !stress intensity  
 PDEF,SE,S,EQV !von Mises or equivalent stress  
 PCALC,ADD,OCTN1,S1,S2, , , !do not use this value  
 PCALC,ADD,OCTN,OCTN1,S3,1/3,1/3, !Octahedral normal stress  
 !PCALC,OPERR,LABR,LAB1,LAB2,FACT1,FACT2,CONST  
 !Forms additional labeled path items by operating on existing path items  
 PCALC,ADD,OCTS,SE, ,0.47140452, , ! OCTAHEDRAL SHEAR STRESS  
 PCALC,ADD,PS1,S2,S3, ,-1, , ! (S2-S3) do not use these values  
 PCALC,ADD,PS2,S1,S3, ,-1, , ! (S1-S3) do not use these values  
 PCALC,ADD,PS3,S1,S2, ,-1, , ! (S1-S2) do not use these values

PCALC,ADD,PSH1,PS1, ,0.5, , ! Principal shearing stress 1  
 PCALC,ADD,PSH2,PS2, ,0.5, , ! Principal shearing stress 2  
 PCALC,ADD,PSH3,PS3, ,0.5, , ! Principal shearing stress 3  
 !comparison of results with lab  
 ! K999-K36-K56 rim gauge  
 ! K999 (44.43075,409.4302,0)  
 ! K36 (44.43075,409.1808,14.28891)  
 ! K56 (44.43075,408.4328,28.56041)  
 PATH,1RLRIM,3, ,  
 PPATH,1, ,44.43075,409.4302,0  
 PPATH,2, ,44.43075,409.1808,14.28891  
 PPATH,3, ,44.43075,408.4328,28.56041  
 PDEF,1RLYRIM,EPEL,Y  
 ! K991-K35-K55 rim gauge  
 ! K991 (44.43075,400,0)  
 ! K35 (44.43075,399.7563,13.9598)  
 ! K55 (44.43075,399.0256,27.90259)  
 PATH,1RLRIM,3, ,  
 PPATH,1, ,44.43075,400,0  
 PPATH,2, ,44.43075,399.7563,13.9598  
 PPATH,3, ,44.43075,399.0256,27.90259  
 PDEF,1RLYRIM,EPEL,Y  
 ! K-14-K15 web gauge  
 ! K14 (19.38036,357.8128,0)  
 ! K115 (21.22687,301.4932,0)  
 PATH,1RLWEB,2,500,500  
 PPATH,1, ,19.38036,357.8128,0  
 PPATH,2, ,21.22687,301.4932,0  
 PDEF,1RLYWEB,EPEL,Y  
 !=====

```

! Part 8b: Post Processing Plate Model
! from K150-K157-K159-K154 in Yaxis
! K150 (0,419.7917,0)
! K157 (0,435.1806,0)
! K159 (0,450.1806,0)
! K154 (0,470.5695,0)
PATH,1RLY,4, ,
PPATH,1, ,0,419.7917,0
PPATH,2, ,0,435.1806,0
PPATH,3, ,0,450.1806,0
PPATH,4, ,0,470.5695,0
PDEF,S1,S,1 !principal stress 1
PDEF,S2,S,2 !principal stress 2
PDEF,S3,S,3 !principal stress 3
PDEF,SI,S,INT !stress intensity
PDEF,SE,S,EQV !von Mises or equivalent stress
PCALC,ADD,OCTN1,S1,S2, , , !do not use this value
PCALC,ADD,OCTN,OCTN1,S3,1/3,1/3, !Octahedral normal stress
!PCALC,OPERR,LABR,LAB1,LAB2,FACT1,FACT2,CONST
!Forms additional labeled path items by operating on existing path items
PCALC,ADD,OCTS,SE, ,0.47140452, , ! OCTAHEDRAL SHEAR STRESS
PCALC,ADD,PS1,S2,S3, ,-1, , , ! (S2-S3) do not use these values
PCALC,ADD,PS2,S1,S3, ,-1, , , ! (S1-S3) do not use these values
PCALC,ADD,PS3,S1,S2, ,-1, , , ! (S1-S2) do not use these values
PCALC,ADD,PSH1,PS1, ,0.5, , , ! Principal shearing stress 1
PCALC,ADD,PSH2,PS2, ,0.5, , , ! Principal shearing stress 2
PCALC,ADD,PSH3,PS3, ,0.5, , , ! Principal shearing stress 3
!K150-K151-K152-K110-K153 in Xaxis
! K150 (0,419.7917,0)
! K151 (20,419.7917,0)
! K152 (40,419.7917,0)

```

! K110 (64.43058,419.7917,0)  
 ! K153 (88.86115,419.7917,0)  
 PATH,1RLX,5, ,  
 PPATH,1, ,0,419.7917,0  
 PPATH,2, ,20,419.7917,0  
 PPATH,3, ,40,419.7917,0  
 PPATH,4, ,64.43058,419.7917,0  
 PPATH,5, ,88.86115,419.7917,0  
 PDEF,S1,S,1 !principal stress 1  
 PDEF,S2,S,2 !principal stress 2  
 PDEF,S3,S,3 !principal stress 3  
 PDEF,SI,S,INT !stress intensity  
 PDEF,SE,S,EQV !von Mises or equivalent stress  
 PCALC,ADD,OCTN1,S1,S2, , , !do not use this value  
 PCALC,ADD,OCTN,OCTN1,S3,1/3,1/3, !Octahedral normal stress  
 !PCALC,OPERR,LABR,LAB1,LAB2,FACT1,FACT2,CONST  
 !Forms additional labeled path items by operating on existing path items  
 PCALC,ADD,OCTS,SE, ,0.47140452, , ! OCTAHEDRAL SHEAR STRESS  
 PCALC,ADD,PS1,S2,S3, ,-1, , ! (S2-S3) do not use these values  
 PCALC,ADD,PS2,S1,S3, ,-1, , ! (S1-S3) do not use these values  
 PCALC,ADD,PS3,S1,S2, ,-1, , ! (S1-S2) do not use these values  
 PCALC,ADD,PSH1,PS1, ,0.5, , ! Principal shearing stress 1  
 PCALC,ADD,PSH2,PS2, ,0.5, , ! Principal shearing stress 2  
 PCALC,ADD,PSH3,PS3, ,0.5, , ! Principal shearing stress 3  
 !K150-K128-K186-K234-K282 in Z-axis  
 ! K150 (0,419.7917,0)  
 ! K128 (0,419.7917,10)  
 ! K186 (0,419.7917,20)  
 ! K234 (0,419.7917,30)  
 ! K282 (0,419.7917,190.42)  
 PATH,1RLZ,5, ,

```

PPATH,1, ,0,419.7917,0
PPATH,2, ,0,419.7917,10
PPATH,3, ,0,419.7917,20
PPATH,4, ,0,419.7917,30
PPATH,5, ,0,419.7917,190.42
PDEF,S1,S,1 !principal stress 1
PDEF,S2,S,2 !principal stress 2
PDEF,S3,S,3 !principal stress 3
PDEF,SI,S,INT !stress intensity
PDEF,SE,S,EQV !von Mises or equivalent stress
PCALC,ADD,OCTN1,S1,S2, , , !do not use this value
PCALC,ADD,OCTN,OCTN1,S3,1/3,1/3, !Octahedral normal stress
!PCALC,OPERR,LABR,LAB1,LAB2,FACT1,FACT2,CONST
!Forms additional labeled path items by operating on existing path items
PCALC,ADD,OCTS,SE, ,0.47140452, , ! OCTAHEDRAL SHEAR STRESS
PCALC,ADD,PS1,S2,S3, ,-1, , ! (S2-S3) do not use these values
PCALC,ADD,PS2,S1,S3, ,-1, , ! (S1-S3) do not use these values
PCALC,ADD,PS3,S1,S2, ,-1, , ! (S1-S2) do not use these values
PCALC,ADD,PSH1,PS1, ,0.5, , ! Principal shearing stress 1
PCALC,ADD,PSH2,PS2, ,0.5, , ! Principal shearing stress 2
PCALC,ADD,PSH3,PS3, ,0.5, , ! Principal shearing stress 3
! comparison of results with lab
! K153-K108 plate central gauge
! K153 (88.86115,419.7917,0)
! K108 (88.86114,435.1806,0)
PATH,1RLPLATE,2,500,500
PPATH,1, ,88.86115,419.7917,0
PPATH,2, ,88.86114,435.1806,0
PDEF,1RLPLATE,EPEL,Y

```

Following is a sample calculation for calculating contact stresses and contact area for Roller R<sub>1</sub> and roller path Plate P<sub>1</sub> using formulae given in (Roark 2002).

<sup>1</sup>Modulus of elasticity of roller path Plate P<sub>1</sub> =  $E_1 = 206.8$  GPa (30,000 ksi)

Modulus of elasticity of Roller R<sub>1</sub> =  $E_2 = 103.4$  GPa (15,000 ksi) (Muzyczka 1992)

Wheel radial compressive load  $P = 838$  kN (188.4 kips)

<sup>1</sup>Poisson's ratio of roller path Plate P<sub>1</sub> =  $\nu_1 = 0.28$

Poisson's ratio of Roller R<sub>1</sub> =  $\nu_2 = 0.27$  (Muzyczka 1992)

Wheel crown radius =  $\frac{D_1}{2} = 914$  mm (36 in.)

Wheel diameter =  $D_2 = 838$  mm (33 in.)

Since roller has a double curvature, assume crossed cylinders and axes at right angles.

According to Roark (2002, p702), the maximum compressive contact stress and contact area is given by:

Maximum Compressive Stress  $\sigma_c = \frac{1.5P}{\pi ab}$ ,      Area of contact patch =  $\pi a b$ , where:

$$a = \alpha (PK_D C_E)^{\frac{1}{3}}, \quad b = \beta (PK_D C_E)^{\frac{1}{3}}, \quad K_D = \frac{D_1 D_2}{D_1 + D_2}, \quad C_E = \frac{1 - \nu_1^2}{E_1} + \frac{1 - \nu_2^2}{E_2}$$

$\alpha$ ,  $\beta$ , and  $\lambda$  are constants and they depend on geometry of the roller which is a function of

$$\frac{D_1}{D_2}. \text{ For } \frac{D_1}{D_2} = \frac{1828}{838} = 2.18, \quad \alpha = 1.193, \quad \beta = 0.717, \quad \text{and } \lambda = 0.798 \text{ (Roark 2002, p702)}$$

<sup>1</sup>(Davis 1996), (Davis 1999) (Gale and Totemeier 2004), (Harvey 1982), (Shackelford and Alexander 2000), (Smith 1993), and (Steiner 1996)

$$K_D = \frac{D_1 D_2}{D_1 + D_2} = \frac{1828 \times 838}{1828 + 838} = 574.514,$$

$$C_E = \frac{1-\nu_1^2}{E_1} + \frac{1-\nu_2^2}{E_2} = 1.342 \times 10^{-5}$$

$$a = \alpha (PK_D C_E)^{\frac{1}{3}} = 1.193 (838000 \times 574.51 \times 1.34 \times 10^{-5})^{\frac{1}{3}} = 22.22 \text{ mm}$$

$$\text{Minor semi-axes, } b = \beta (PK_D C_E)^{\frac{1}{3}} = 13.36 \text{ mm}$$

$$\text{Area of contact patch} = \pi a b = \pi \times 22.22 \times 13.36 = 932.5 \text{ mm}^2 (1.45 \text{ in}^2)$$

$$\text{Maximum Compressive Stress } \sigma_c = \frac{1.5P}{\pi ab} = \frac{1.5 \times 838000}{932.5} = 1348 \text{ MPa (195.5 ksi)}$$

$$\text{Maximum Shear Stress } \tau_{max} = \frac{\sigma_c}{3} = 449.3 \text{ MPa (65.2 ksi)}$$

Table C.1 Contact stresses and areas using formulae given in (Roark 2002)

Specimen	Roller R <sub>1</sub> , Plate P <sub>1</sub>		Roller R <sub>2</sub> -R <sub>3</sub> , Plate P <sub>3</sub>	
	Axial Load	838 kN (188½ kips)	734 kN (165 kips)	814 kN (183 kips)
Maximum Stress, MPa	1348	1290	1742	1683
Contact Area <sup>5</sup> mm <sup>2</sup>	233	213	175	164

<sup>5</sup>Only one-quarter of the contact area is given in order to compare with the one-quarter of the contact area retrieved from FE analysis.